Durham E-Theses

The Dynamics and History of the Milky Way

CALLINGHAM, THOMAS,MICHAEL

The Dynamics and History of the Milky Way

A cosmic tale of dark matter, simulations, and mathematics

Thomas Callingham

A Thesis presented for the degree of
Doctor of Philosophy

Institute for Computational Cosmology
Ogden Centre for Fundamental Physics
Department of Physics
Durham University
United Kingdom

August 2021

The Dynamics and History of the Milky Way

A cosmic tale of dark matter, simulations, and mathematics

Thomas Callingham

Submitted for the degree of Doctor of Philosophy

August 2021

Abstract: This thesis uses a combination of observations, simulations, and dynamical analysis to study the dark matter (DM) halo and accretion history of the Milky Way (MW).

Chapter 2 presents and applies a method to infer the mass of the MW by comparing the dynamics of observed satellites to those in the EAGLE cosmological hydrodynamics simulations. The method is robustly calibrated on mock EAGLE systems and then validated on the independent AURIGA high-resolution simulation suite of 30 MW-like galaxies. The method is shown to recover a galaxy's true mass and associated uncertainties accurately. Using ten classical satellites with 6D phase-space measurements, including updated proper motions from the *Gaia* satellite, the method is applied to the MW. The mass of the MW is estimated to be $M_{200}^{\mathrm{MW}} = 1.17^{+0.21}_{-0.15} \times 10^{12} M_\odot$ (68% confidence limits). This is then combined with recent mass estimates in the inner regions of the Galaxy to infer an NFW halo concentration of $c_{200}^{\mathrm{MW}} = 10.9^{+2.6}_{-2.0}$.

Chapter 3 models the effect of baryonic contraction in DM haloes by first studying the orbital phase-space of DM haloes in the AURIGA simulation suite of MW analogues. The haloes are characterised by their spherical action distribution of the DM particles, allowing a comparison between the dynamical descriptions of DM-only and hydrodynamical simulations of the same haloes. By applying an iterative algorithm, the AURIGA DM haloes are adiabatically contracted to a given baryon density profile and halo mass. Using this algorithm, the AURIGA haloes are contracted to the baryon profile of the MW, inferring the total mass profile and the dynamics of the MW's contracted DM halo. These models allow

the derivation of updated values for the key astrophysical inputs to DM direct detection experiments: the DM density and velocity distribution in the Solar neighbourhood.

Chapter 4 introduces a multi-component chemo-dynamical model for decomposing the Galactic population of Globular Clusters (GCs) into bulge, disc, and stellar halo components. The halo GCs are further split into the major Galactic accretion events, GES, Kraken, Sequoia, Sag, and Helmi streams. The modelling approach is extensively tested using mock GCs built using the AURIGA suite of hydrodynamical simulations. The method is applied to the Galactic GCs data to infer, in a statistically robust and easily quantifiable way, the GCs associated to each MW accretion event. The MW sample contains 170 GCs, including previously uncategorized clusters from *Gaia* EDR3 observations. The number of GCs if each accretion group is then used to infer properties, such as halo and stellar masses, of these defunct satellites of the MW.

Declaration

The work described in this thesis was undertaken between October 2017 and August 2021 while the author was a research student under the supervision of Dr. Alis Deason and Prof. Carlos Frenk in the Institute for Computational Cosmology at Durham University, England. No part of this thesis has been submitted for any degree or qualification at Durham University or elsewhere.

Chapters 2 and 3 have been published as a papers in Monthly Notices of the Royal Astronomical Society (MNRAS):

Callingham T., Cautun M., Deason A., Frenk C. S., Wenting W., Gomez F., Grand R., Marinacci F., Pakmor R. 2019, MNRAS, **484**, 5453

Callingham T., Cautun M., Deason A., Frenk C. S., Grand R., Marinacci F., Pakmor R. 2020, MNRAS, **495**, 12

Chapter 4 is being prepared for publication.

All figures in this thesis were prepared by the author, or have been properly attributed in the figure caption.

without the author's prior written consent and information derived from it should be acknowledged."

Acknowledgements

On my long road leading to writing this thesis I have met many delightfully splendid and unique individuals. This has considerably lightened my load and altogether made everything more enjoyable. I am immensely fond of you all.

First, I must acknowledge that this past year and a half has been difficult for us all. I am grateful to all those that work in the public health system and related research over this period.

I am eternally indebted to my supervisor team, who have not only academically supported me but have cared about my well-being throughout this experience. Despite the many demands for their attention, they have always found time for me. None of my research would be possible without Carlos's scientific vision, Marius's technical support, and Alis's efficient practicality. I am privileged to have been your student.

I thank many friends in the department; the younger years for their energy and enthusiasm, the older years for maintaining an illusion of knowledge, the postdocs and staff for actually possessing knowledge, and those in my year group for being along for the ride.

To old friends from Cambridge and older friends from home; I wish I could see you all more, but it makes a world of difference knowing that you're there.

Being on the Ustinov pool team has allowed me to play a sport within arms reach of a bar and this deserves special recognition.

My time in Durham would be very different without the DU badminton squad. I thank the fine men of the thirds team that I served alongside, and Jack Richings for his friendship

and getting me into the squad in the first place.

To Ho Chi - thank you for every single day of the last three years. In the wise words of an Icelander: "Everything about you, I like".

Finally, I would like to thank my family for their support over the years. My grandparents for lighting my scientific interest, my brothers for making home a timeless escape, and my parents for helping me in my endeavours, every step of the way.

Tom Callingham,

August 2021, Durham UK

The Road goes ever on and on,
Down from the door where it began.
Now far ahead the Road has gone,
And I must follow, if I can.

— J.R.R. Tolkien

Contents

Contents xi

List of Figures

List of Tables

CHAPTER 1

Introduction

The Milky Way dominates our night sky, but it is just one of incalculably many such galaxies in an ever-expanding Universe. Astrophysically speaking, we inhabit a fairly unremarkable planet orbiting a fairly unremarkable star in the stellar disc of a fairly unremarkable galaxy. What is truly remarkable is that, from our limited vantage point, we have assembled such a detailed understanding of the wider cosmos. This knowledge is the integrated sum of centuries of scientific progress, consisting of a few large leaps made by giants and many smaller contributions from the wider scientific community. The work contained in this thesis is but the latest of these labours.

1.1 The Known Universe

In the current cosmological paradigm, Lambda cold dark matter (ΛCDM), the Universe's energy budget is spent on three ingredients: dark energy (68.5%), dark matter (27%) and baryons (4.5%) (Planck Collaboration et al., 2014). Dark energy, denoted Λ, drives the accelerated expansion of the Universe on intergalactic scales. On the galactic scales studied in this thesis, physical matter overcomes this effect and allows structure to form. Dark matter (DM), the dominant mass component, is collisionless non-baryonic matter,

hypothesised to be composed of a weakly interacting massive particle that has evaded direct detection (Peebles, 1982). The cold nomenclature refers to its initial, non-relativistic, velocity distribution in the primordial Universe, which still dictates the nature of structure today. Currently, the only evidence for the existence of DM comes from its gravitational interactions with baryonic matter (e.g. Zwicky, 1937; Rubin & Ford, 1970). As the only visible material, baryons are relied on to infer the unseen but dominant 'dark side' of the Universe, despite accounting for just a sixth of the total matter.

1.1.1 Dark Matter

DM forms the foundations of all structure in the Universe. Initially, small overdensities of DM collapse to form small gravitationally bound clumps, known as haloes. These clumps then grow by accreting diffuse material and merging with other DM haloes, leading to the hierarchical formation of structure. This process is highly non-linear and beyond analytical theory on all but the largest of scales. Instead, our understanding has been built by collisionless N-body simulations, in which both DM and baryons are modelled as a single dissipationless fluid. These are often referred to as 'dark matter only' simulations, hereafter DMO. For a recent review of DM structure, see Zavala & Frenk (2019).

Large cosmological boxes ($\sim 100\,\mathrm{Mpc}$) can follow the formation of large scale structure and the evolution of the halo mass function (Frenk et al., 1988). The bottom-up formation of ΛCDM leaves the present-day Universe rich in small scale structure, unlike the cut-off seen in alternative warm DM variants (e.g. White et al., 1983; Lovell, 2020). Our Galaxy is likely surrounded by an abundance of these subhaloes and satellites (characterised by works such as Springel et al. (2008); Gao et al. (2008); Richings et al. (2020)). These simulations also allow the birth, evolution and internal structure of individual DM halos to be studied, tracing its assembly history with a merger tree (see Fig. 1.1).

A halo's density smoothly decreases into the background matter of the Universe, providing no clear definition for its edge (Deason et al., 2020). Instead, a halo's size is defined as the radius within which its mean density is equal to a factor times the critical density of the
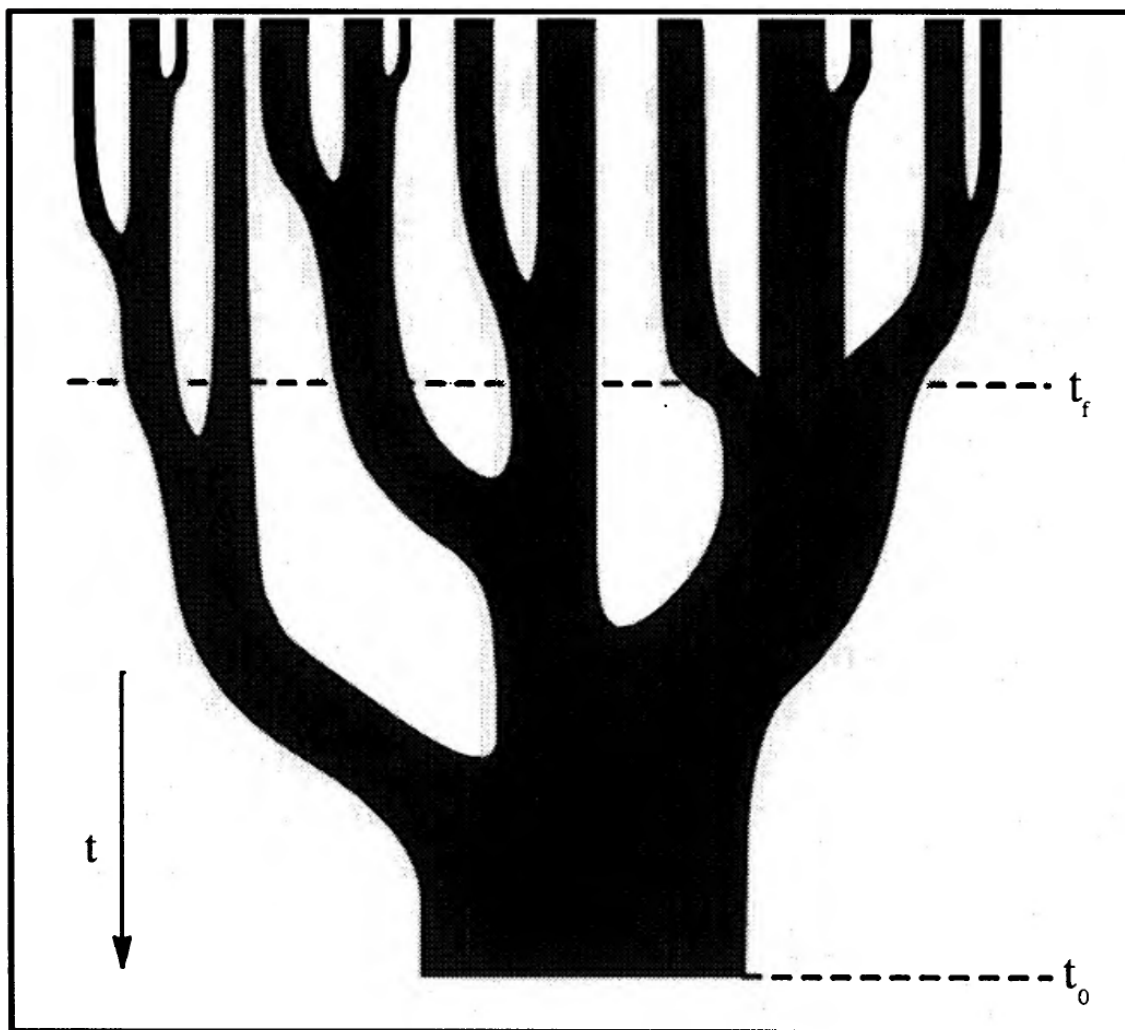
Figure 1.1
A classic schematic representation of a merger tree from Lacey & Cole (1993). The tree depicts the hierarchical growth of a DM halo through a series of mergers. Time increases from top to bottom, and the width of the tree indicates halo mass. t_0 denotes the present day, and t_f denotes the formation time, defined as the time the halo achieved half the mass of the present-day halo.

Universe (Cole & Lacey, 1996). This thesis uses 200 times the critical density, with the halo radius defined as R_{200} and the halo mass contained within this radius denoted as M_{200}. An alternative definition is the virial mass of the halo, approximately the mass contained within the radius that the virial theorem applies (equivalent to a factor of ~ 102 times the critical density at present-day in the Planck Collaboration et al. (2014) cosmology).

DMO haloes have been found to have spherically-averaged density profiles that are universally well fit by a surprisingly simple form, the Navarro, Frenk & White (NFW) profile (Navarro et al., 1996, 1997):

$$\rho\left(r\right) = \frac{\rho_s}{\frac{r}{r_s}\left(1 + \frac{r}{r_s}\right)^2} \, , \tag{1.1.1}$$

This form is characterised by two free parameters: the scale radius, r_s, and the characteristic density, ρ_s. This profile has been found in haloes over 20 orders of magnitude of mass and seems to be only limited by the resolution of the simulation (Wang et al., 2020b). The steep, cuspy centre of this profile ($\rho \propto r^{-1}$) is a fundamental prediction of CDM, and a memory of the DM's phase space in the primordial Universe. Some alternative models, such as self-interacting DM, distinguish themselves from CDM by predicting cores at the halo's centre ($\rho \propto$ constant).

A halo's concentration relates its scale radius to the size of the halo ($c_{200} = R_{200}/r_s$). This quantity roughly correlates with its mass, with larger haloes having lower concentrations (Schaller et al., 2015). However, there is considerable scatter linked to the assembly history of the halo, which can vary significantly between haloes of similar mass (Ludlow et al., 2013, 2014)

The origins of the NFW profile are still debated, with suggestions including a close connection to the halo merger history or an attractor solution to entropy-driven relaxation (e.g. Ludlow et al., 2014; Pontzen & Governato, 2013). DM haloes are, fundamentally, composed of orbiting particles that conspire to give an approximately steady-state profile (Zhu et al., 2016). It is this underlying dynamical system that determines the underlying density profile, and governs how it responds to its environment and new merger events.

1.1.2 Baryons

Galaxies form at the bottom of the gravitational potential well of DM haloes (White & Rees, 1978). Gas falls into haloes and, unlike DM, cools through radiative processes, allowing it to condense at the centre. Once dense and cold enough, the gas clouds fragment and collapse to form stars. Conservation of the initial gas's angular momentum leads to the creation of disc galaxies (Mo et al., 1998). A small fraction of the stars explode as supernovae, releasing heat energy and metal-enriched gas into the interstellar medium. AGN (Active Galactic Nuclei) can form at the galactic centre and drive further baryonic feedback, such as radiation pressure and stellar winds. This stellar feedback disrupts dense gas, inhibiting further star formation and ejecting gas from smaller haloes that cannot gravitationally hold onto their material.

Baryons can substantially affect the DM halo that they inhabit. By accumulating at the centre of the halo, they deepen the galaxy's potential well, increasing the central DM density through an effect known as baryonic contraction (investigated in Chapter 3). The enhanced potential can also affect the distribution of subhaloes surrounding the galaxy, increasing subhalo destruction through strengthening tidal forces and effects such as disc-shocking (e.g. D'Onghia et al., 2010; Sawala et al., 2017; Garrison-Kimmel et al., 2017; Richings et al., 2020). If the feedback is sufficiently strong, rapid changes to the inner baryon profile can transfer energy to the surrounding DM. This mechanism has been proposed to turn cusps into cores in baryon dominated dwarf galaxies (Pontzen & Governato, 2012; Burger et al., 2020).

1.1.3 Success and Tension in ΛCDM

ΛCDM has been undeniably successful on large scales and can consistently describe how structures in the Universe have formed and evolved. ΛCDM simulations have been able to reproduce the structure distribution seen in galaxy redshift surveys (Springel, 2005; York et al., 2000; Colless et al., 2001; Rodríguez-Torres et al., 2016), and duplicated more subtle

cosmological measurements such as anisotropy in the cosmic microwave background and the baryon acoustic oscillations of the matter power spectrum (Komatsu et al., 2011; Cole et al., 2005; Eisenstein et al., 2005; Collaboration et al., 2021a). While the theory has proved remarkably resilient over the past 40 years, it has had historical challenges, with a few tensions remaining areas of active research to this day. Generally, these are motivated by DMO simulations and typically manifest on small scales. On these scales, baryonic effects cannot be neglected, and consequentially their inclusion can give plausible solutions to these tensions. For a more in-depth summary than presented here, see the recent review by Bullock & Boylan-Kolchin (2017).

The missing satellites problem refers to the abundance of substructure predicted in DMO simulation compared to the limited number of dwarf galaxies observed in the MW (Klypin et al., 1999; Moore et al., 1999). Assuming that all DM haloes host stars, the MW should be surrounded by thousands of visible subhaloes. However, it is now known that the effects of feedback and re-ionisation effectively prevent small haloes ($\lessgtr 3 \times 10^8 M_\odot$) from forming stars (Benitez-Llambay & Frenk, 2020). With these effects considered, more recent studies and hydrodynamical simulations now agree with predictions for the MW observed population (e.g. Bose et al., 2018; Sawala et al., 2015).

The too-big-to-fail problem (Boylan-Kolchin et al., 2011) refines the ideas of the missing satellites problem, focusing on the lack of massive haloes around the MW compared to simulations. The haloes cannot be dark, as their size should prevent them from succumbing to baryonic effects and be prevented from hosting stars; they are 'too big to fail'. This problem is alleviated by considering the effect of baryonic feedback slowing the growth rate of DM haloes compared to DMO (Sawala et al., 2016), or if the central densities of the dwarf DM haloes are lowered, such as by the presence of a DM core (Zolotov et al., 2012),

The plane of satellites problem concerns the arrangement of the MW's satellite galaxies, which appear to preferentially lie in a thin plane perpendicular to the galactic disc (Lynden-Bell, 1976; Kunkel & Demers, 1976). This positioning is made more significant by further hints of satellite planes in other galaxies, such as Andromeda (Ibata et al., 2013) and

Centaurus A (Tully et al., 2015; Müller et al., 2018). Whilst this configuration has been found to occur in ΛCDM cosmological simulations, it is only present in a small fraction of disc galaxies ($\sim 1\%$ Shao et al. 2018b). With careful treatment of the statistics, such as considering the look-else-where effect, the tension has lessened (Cautun et al., 2015), but it remains an interesting feature.

The core-cusp problem concerns the disputed claims of DM cores at the centre of dwarf galaxies (Moore, 1994; Read et al., 2016; Battaglia et al., 2013; Genina et al., 2018). If true, it has been suggested that this could be evidence of exotic self-interacting DM. However, as already discussed, in ΛCDM strong baryonic feedback mechanisms have been proposed to create cores (e.g. Navarro et al., 1996; Pontzen & Governato, 2012; Burger & Zavala, 2019). This effect has been replicated in some simulations but is dependant on the implementation of star formation and feedback (Benítez-Llambay et al., 2019).

1.2 Hydrodynamical Galaxy Simulations

Over the past two decades, the field has witnessed the rise of advanced hydrodynamical simulations, hereafter 'Hydro', that are capable of modelling baryons alongside DM (Vogelsberger et al., 2020, review). Such simulations self-consistently implement baryon physics thought to be important in the formation of galaxies, such as gas cooling and heating, stellar winds, chemical evolution and supernova and AGN feedback (e.g. see Somerville & Davé, 2015). Representing an individual star through a single particle is beyond current computational abilities; instead, star particles represent populations of stars. Similarly, astrophysical processes that take place below resolvable scales, such as star formation and the injection of energy into gas from baryonic feedback, must be modelled as 'sub-grid' physics with their effects on resolvable scales approximated analytically.

There are two main hydrodynamical schemes to represent baryons: N-body particles using smoothed particle hydrodynamics (SPH), or cells using adaptive mesh refinement. Current examples of these approaches are the EAGLE project (Schaye et al., 2015; Crain et al., 2015), which is run with a heavily modified GADGET3 SPH code (Springel, 2005), and the Illustris
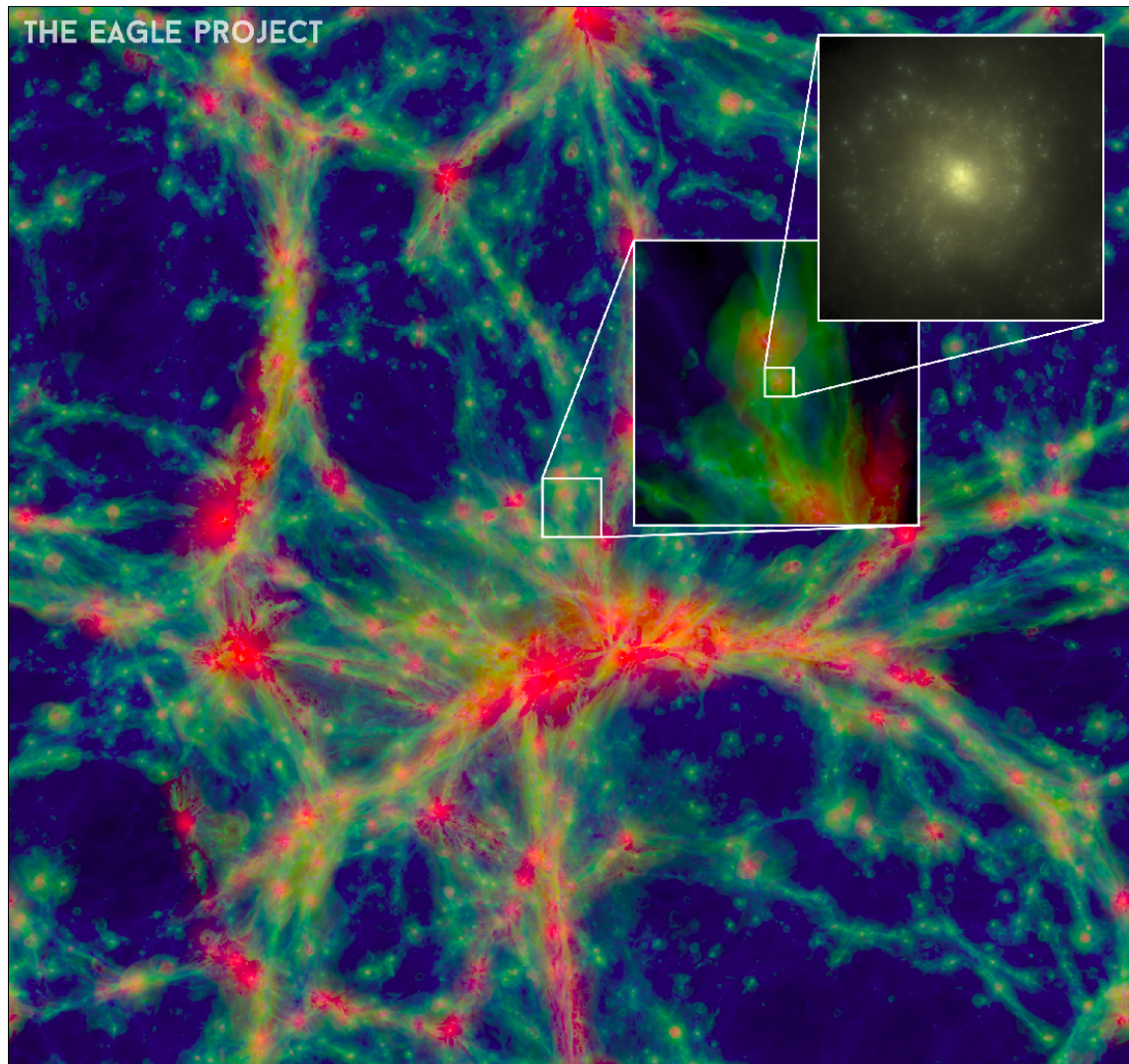
Figure 1.2

The EAGLE simulation box. The colour indicates the density of structure, where red is the most dense. As matter collapses, it forms the cosmic web; a tangle of filaments lined with galaxies. EAGLE can resolve galactic structure such as stellar discs. Credit: The EAGLE project (Schaye et al., 2015).

project (Vogelsberger et al., 2014a,b; Genel et al., 2014), which uses the AREPO (Springel, 2010)) moving mesh scheme. These simulations recover properties observed in the real universe, such as the stellar mass-star formation rate relations, mass-metallicity relations, black hole masses, and the morphology of galaxies.

Modern simulations mostly agree on large scales and integrated properties, particularly where calibrated by observations of the real Universe. However, there are still several areas that are unconstrained, or poorly understood from a theoretical standpoint, that leads to some ambiguity in aspects of subgrid physics. These areas include (to name a few): the stellar-mass to halo-mass relation at lower masses (Behroozi et al., 2019), AGN feedback (Schaye et al., 2010; Scannapieco et al., 2012; Vogelsberger et al., 2013) and the density threshold for star formation (Schaye, 2004; Hopkins et al., 2013). In the future, it is hoped that further observations and theoretical progress will constrain these areas. Increasing computational power and smarter codes continues to push resolution and simulation box sizes up, improving what has emerged as one of the best tools to understand the Universe (Schaller et al., 2018; Borrow et al., 2020).

1.2.1   Zoom-In Simulations

Simulating a single galaxy at high resolution (a zoom-in simulation) can reveal details that would be obscured in a larger cosmological simulation, such as inner DM structure and star formation in dwarf galaxies (e.g. Navarro et al., 2010; Crain et al., 2015). This is especially enlightening if the simulated galaxy has similar properties to the MW. The simulation can then be used to study the processes that formed our Galaxy and give an invaluable method of testing our methodologies. However, forming a MW-like galaxy is challenging due to the chaotic and unpredictable nature of galaxy formation.

One approach to accomplish this is to identify galaxies of interest in large cosmological volumes (Katz & White, 1993; Tormen et al., 1997; Frenk et al., 1999; Bertschinger, 2001; Gao et al., 2005; Hahn & Abel, 2011; Jenkins, 2013). The particles of these are traced back to their initial conditions, which are then re-simulated at higher resolution. The
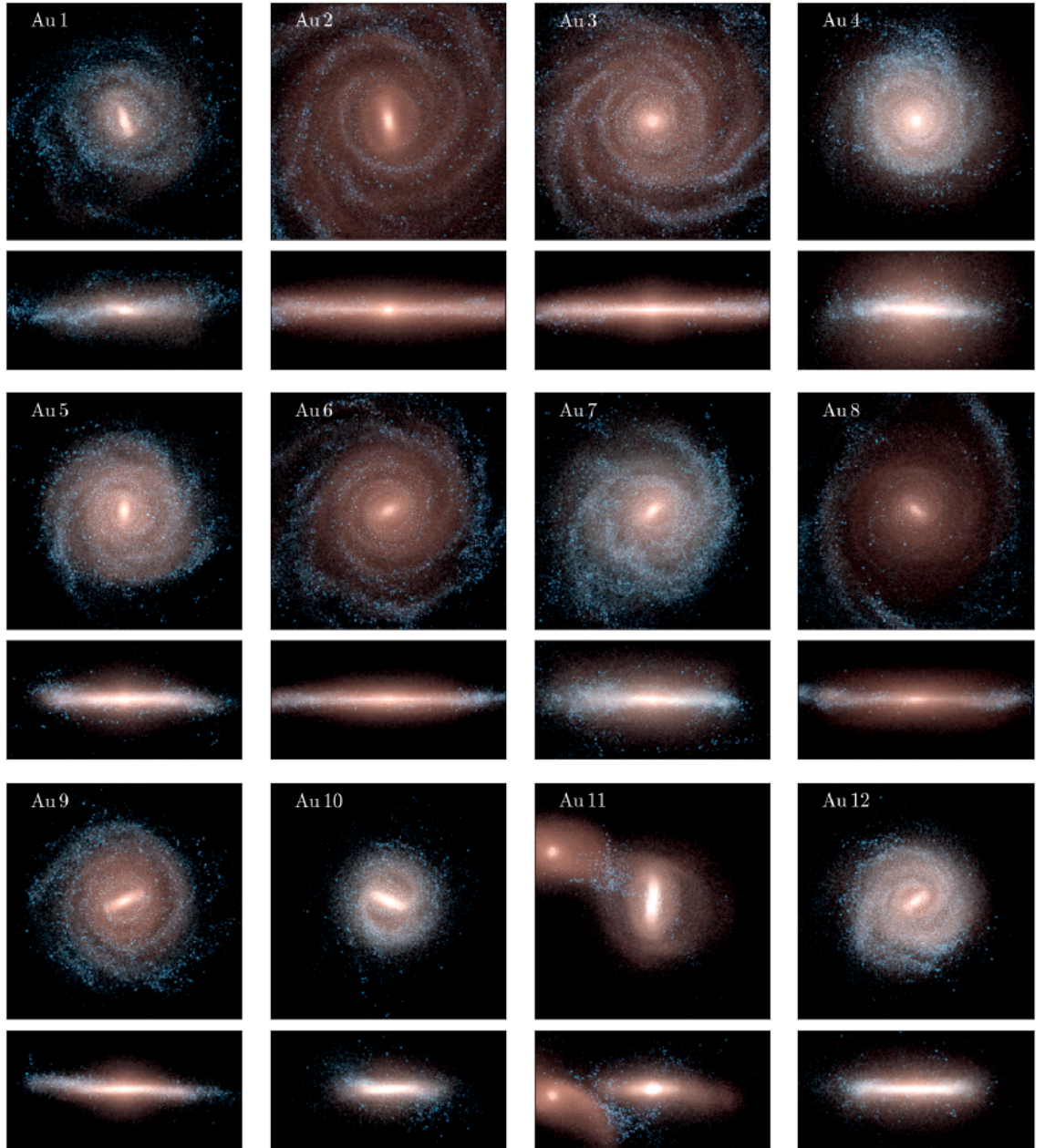
Figure 1.3

Simulated galaxies from the AURIGA project (Grand et al., 2017). These are high resolution, hydrodynamical simulations of MW-like galaxies, containing rich Galactic structure such as discs, spirals and a stellar halo full of substructure.

surrounding regions are re-sampled at lower resolution with massive particles to preserve a realistic tidal field. Alternatively, initial conditions that replicate our local environment can be carefully cultivated through "constrained realisations" (Hoffman & Ribak, 1991; Klypin et al., 2003; Jasche & Wandelt, 2013; Gottloeber et al., 2010; Libeskind et al., 2020).

Modern 'zoom-in' simulations of individual MW-like haloes include the AURIGA simulations (Grand et al., 2017), run with AREPO, and the FIRE simulations (Hopkins et al., 2014), run using a moving mesh code designed for zoom-in simulations. Rather than an individual MW-like halo, the APOSTLE simulations (Sawala et al., 2016; Fattahi et al., 2016) choose to re-simulate a pair of galaxies selected to reproduce Local Group properties.

Typically, the MW analogues are selected to be within the mass range expected of our Galaxy $(0.5, 2) \times 10^{12} \, M_\odot$, and can include further selection criteria in an effort to find MW-like galaxies. It is an open question how well these zoom-in simulations capture the likely properties of the MW and its surrounding environment. In some aspects, the MW is known to be unusual, such as its accretion history and the presence of the LMC (Evans et al., 2020). This may lead to other statistically significant differences between the MW and the average simulated galaxy of a comparable mass, giving rise to unappreciated biases in studies that use them. As our knowledge of the properties of the MW improves, alongside the resolvable details of the simulated galaxies, the criteria for what is MW-like will likely become stricter and make MW analogues harder to find. This demand will be eased by the increasing size and statistics of cosmological simulations, and the growing sophistication of constrained realisations techniques. Hopefully, these continual improvements will allow for better comparisons to the MW Galaxy.

1.2.2 Simulations used in this Thesis

EAGLE

The EAGLE simulation is a large hydrodynamic cosmological simulation (Schaye et al., 2015; Crain et al., 2015). The main $100 \, \text{Mpc}$ cubic volume provides a large sample of

haloes with a wide range of masses and assembly histories (Evans et al., 2020). This suite is used in Chapter 2 to build a sample of satellite dynamics, which is then compared to observations in the MW.

The simulation uses 1504^3 DM particles of mass of $9.7 \times 10^6 M_\odot$ and 1504^3 gas particles of initial mass of $1.81 \times 10^6 M_\odot$. with the Planck cosmological parameters (Planck Collaboration et al., 2014, see Table 9). EAGLE models the relevant baryonic physics processes such as gas cooling, stochastic star formation, stellar and AGN feedback, and the injection of metals from supernovae and stellar winds. The model was calibrated to reproduce the present-day stellar mass function, galaxy sizes and the galaxy mass – black hole mass relation. The friends-of-friends and SUBFIND algorithms are used to identify haloes and subhaloes (Davis et al., 1985; Springel et al., 2001).

AURIGA

AURIGA is a suite of high-resolution, hydrodynamical zoom-in simulations of MW-like systems. These haloes provide an excellent way of testing dynamical methodology before application to the real MW, building an understanding of a methods errors and limitations. Chapter 2, Chapter 3 and Chapter 4 all use AURIGA for this purpose.

The haloes were selected from the $100^3 \, \mathrm{Mpc}^3$ periodic cube of the EAGLE project. The selection criteria were that the haloes have masses between $1 - 2 \times 10^{12} M_\odot$ and to be relatively tidally isolated from neighboring haloes (i.e. not significantly gravitationally interacting with other similarly sized or larger haloes. They were then re-simulated using the N-body and moving mesh magnetohydrodynamic AREPO code (Springel, 2011), using the Planck Collaboration et al. (2014) cosmological parameters. The work in this thesis primarily uses the level 4 resolution of 30 haloes. The simulations have a DM particle mass of $\sim 3 \times 10^5 M_\odot$ and an initial gas resolution element of mass $\sim 5 \times 10^4 M_\odot$; approximately ~30 times higher resolution than EAGLE. AURIGA has been shown to reproduce many properties of the MW and other MW-mass galaxies, such as the satellite luminosity function (Shao et al., 2018a; Simpson et al., 2018), stellar bulge and disc structures (Grand
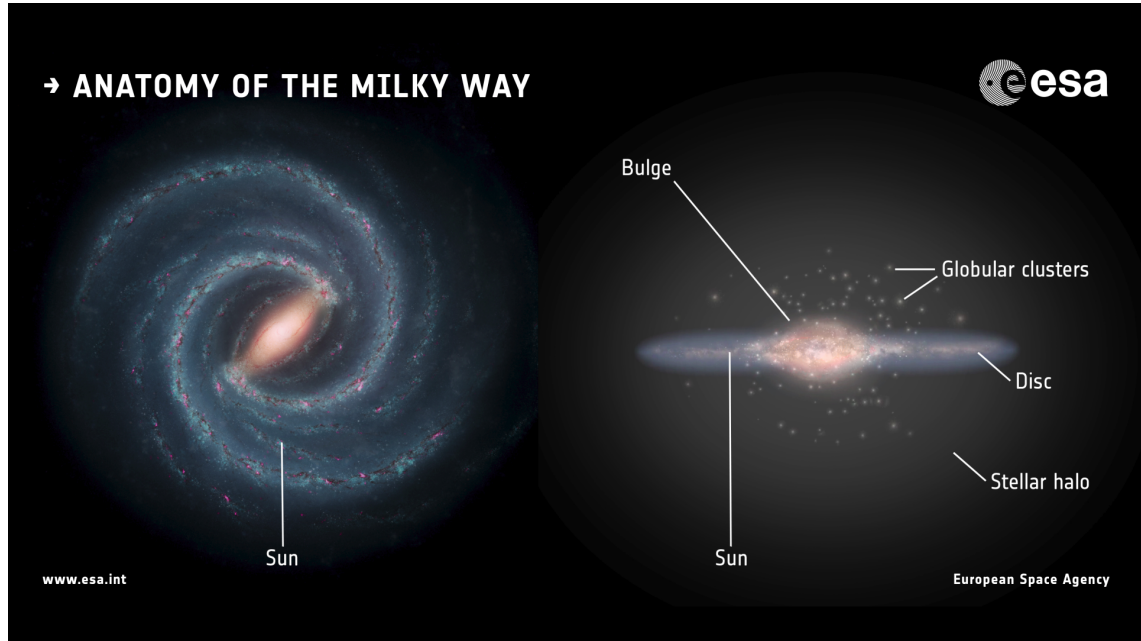
Figure 1.4
   An illustration of the of the structure of the Milky Way galaxy, showing a face on
   and side on view of the stellar disc. Credit: European Space Agency

et al., 2017; Gómez et al., 2017a,b), and stellar halo (Grand et al., 2019; Monachesi et al.,

2019; Fattahi et al., 2019; Deason et al., 2021).

1.3   The Milky Way

The MW is a fairly typical disc galaxy (but not in every aspect, e.g. Evans et al. 2020).

Its stellar material is composed of a few distinct components. The most massive is the

stellar disc ($\sim 4 - 5 \times 10^{10} M_\odot$), home to the Sun at a radius of around $8\,$kpc. The disc

can be further decomposed into the thin disc, containing younger, metal-rich stars on neat

circular orbits within the plane, and the thick disc, containing older, metal-poor stars with

a larger velocity dispersion. The bulge and bar lie within $\sim 2\,$kpc of the galactic centre and

are characterised by their old, metal-rich stellar population. Further out, the diffuse stellar

halo is a roughly spherical distribution of higher energy stars reaching $\sim 10 - 100\,$kpc. It

is dominated by substructure that provided the first strong evidence of hierarchical growth

(Searle & Zinn, 1978). These visible components are enveloped in our DM halo, tens of

times as massive as the stellar disc and a radius likely over $200\,$kpc. This thesis mainly

focuses on the stellar and dark matter haloes, for a recent review of the entire MW, see Bland-Hawthorn & Gerhard (2016).

The MW hosts many orbiting satellite galaxies. The 11 classical satellites (defined as those with luminosity $L > 10^5 \, L_\odot$) range from 16 kpc (Sagittarius) out to around 250 kpc (Leo I). Our largest satellite, the Large Magellanic Cloud, has been proposed to be massive enough ($M \sim 10^{11} M_\odot$) to significantly affect the Galactic potential (Gómez et al., 2015; Peñarrubia et al., 2016; Vasiliev et al., 2021; Erkal et al., 2019), and evidence for its influence has already been seen in the stellar halo (Erkal et al., 2021; Cunningham et al., 2020) With recent improvements in observations, there is now a growing population of previously undiscovered ultra-faint dwarfs ($L < 10^5 \, L_\odot$). With these included, the known satellite population is approximately ~ 60 (Bechtol et al., 2015; Drlica-Wagner et al., 2015; Koposov et al., 2015). In total, 120 satellites brighter than $M_v = 0$ are expected to be within 300 kpc (Newton et al., 2018).

As our window to the wider Universe, correctly interpreting our local environment is central to unravelling some of the biggest mysteries of modern astrophysics and cosmology. The apparent discrepancies with the standard ΛCDM model (as previously discussed), and tests of alternative warm dark matter models, are all based on studies of small scale structure found in the MW and local environment (e.g. Purcell & Zentner, 2012; Wang et al., 2012; Vera-Ciro et al., 2013; Cautun et al., 2014; Kennedy et al., 2014; Lovell et al., 2014). Furthermore, the MW provides a sensitive probe of the key mechanisms of galaxy formation. This is made more enlightening as the behaviour of baryonic feedback undergoes a crucial physical transition around the MW mass (e.g. Bower et al., 2017).

1.3.1 Observations

There is good reason to study our Galaxy – the MW offers the best available galactic data set in the Universe, with kinematics, chemical abundances and ages for individual stars. Since the start of this PhD in 2017, the volume and quality of data available has grown tremendously. In 2018 the *Gaia* mission forever changed the field with the data release
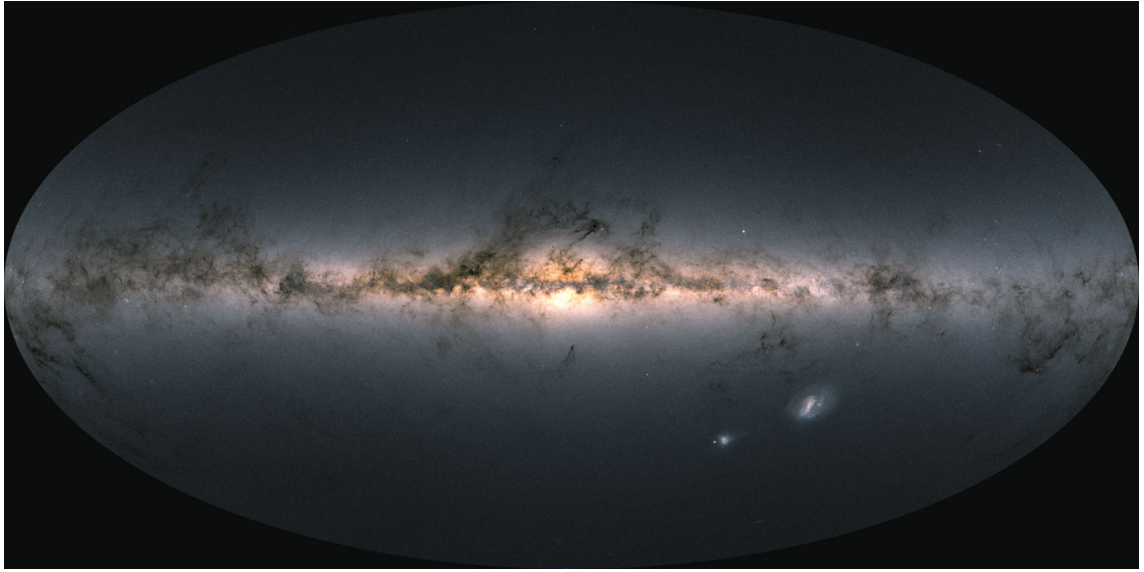
Figure 1.5

The Milky Way, as seen by *Gaia* early data release 3 (Gaia Collaboration et al., 2021b). The lighter areas indicate areas with a higher density of stars. Beneath the disc, the Large and Small Magellanic Clouds can be seen. More than 1.8 billion stars were used by the Gaia Collaboration to make this image.

2 (DR2) catalogue, containing over 1.3 billion stars with positions and proper motions, a considerable increase from 2 million in the previous DR1 catalogue. As a result, there is a growing sample of MW satellites and globular clusters with full 6D phase space information (Helmi et al., 2018b; Fritz et al., 2018; Simon, 2018; Vasiliev & Baumgardt, 2021; Baumgardt & Vasiliev, 2021).

Combined with other surveys (including APOGEE (Majewski et al., 2017), GALAH (Martell et al., 2017), SDSS (Adelman-McCarthy et al., 2007), RAVE (Smith et al., 2007), and *Gaia-ESO* (Gilmore et al., 2012),) the field of Galactic astronomy has been revolutionalised over the past few years (Belokurov et al., 2018; Helmi et al., 2018a; Antoja et al., 2018). In December 2020, the *Gaia* collaboration released the early data release 3 (EDR3) catalogue, which on average halves the proper motion uncertainties of DR2. Future releases promise to continue these trends, driving the field forward into an era of precision Galactic science.
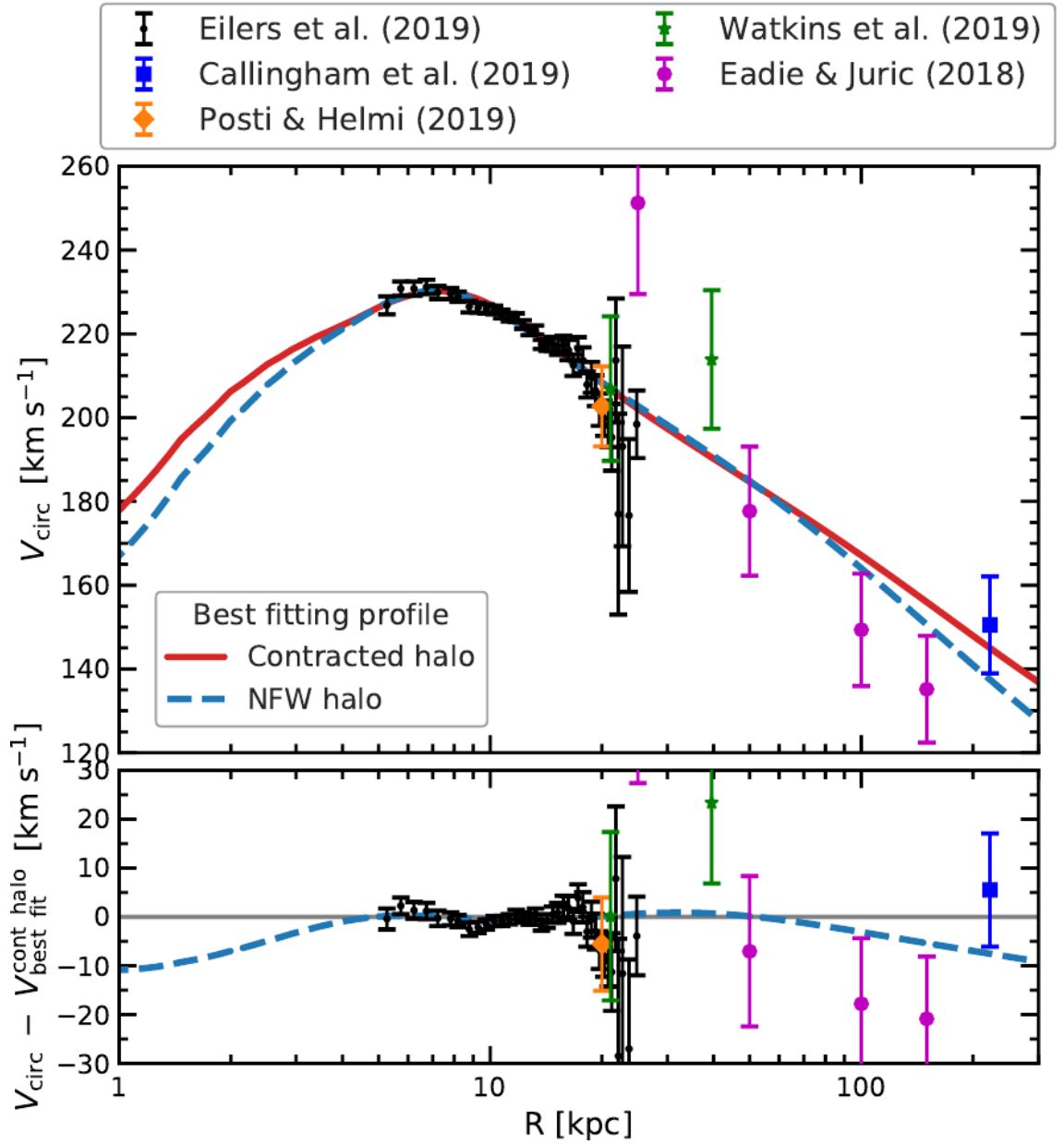
Figure 1.6
A model of the Galactic potential fit to the stellar velocity curve, from Cautun et al.
(2020). The points and error bars show observational constraints. The red line
shows the velocity curve of the fitted Galactic mass distribution.

1.3.2 Galactic Potential and Dark Matter Halo

Whilst observations can tell us an object's position and instantaneous velocity, it is the galactic potential that allows us to put this information into a practical dynamical context. A galaxy's gravitational potential is defined by its mass profile, which is itself the sum of its constituent components. In the outer regions, the potential is dominated by the DM halo. In the inner regions however, the baryonic components cannot be neglected, with the gravitational force of baryon and dark matter approximately even at the solar radius.

The Galactic potential can be inferred the study of the kinematics of various dynamical tracers. The central regions contain numerous visible tracers and constraints such as the circular velocity curve (Eilers et al., 2019), local escape velocity (Deason et al., 2019a), and stellar streams (Sanderson et al., 2015; Reino et al., 2020). To these, various works have fit multi-component models, with individual mass distributions for the bulge, stellar and gas discs, and the DM halo (McMillan, 2011; Bovy, 2015; McMillan, 2017; Cautun et al., 2020). However, models fit to the inner regions of the MW have limited ability to infer the total mass or outer potential of our Galaxy, as most of the DM halo's mass is beyond these tracers.

The total mass of the MW is arguably the single most important quantity describing our Galaxy; dictating the galactic potential and placing the MW into cosmological context within the general galaxy population. Before *Gaia* DR2, the MW mass was commonly quoted to a factor of 2, with most M_{200} mass estimates ranging from 0.5 to $2.5 \times 10^{12} M_\odot$. This considerable uncertainty is arguably the dominant error in the Galactic potential and many other applications, such as constraining the viability of alternative warm DM models (Newton et al., 2018). To infer the total mass with accuracy, and avoid errors induced by extrapolating models from the centre, it is necessary to use tracers from the Galaxy's outer regions. The natural choice is the MW dwarf galaxy population of the MW; the classical satellites are presumed complete out to the Galaxy's R_{200} with relatively small errors for their distance. In Chapter 2, the dynamics of the classical satellites are used to constrain the MW's total mass.
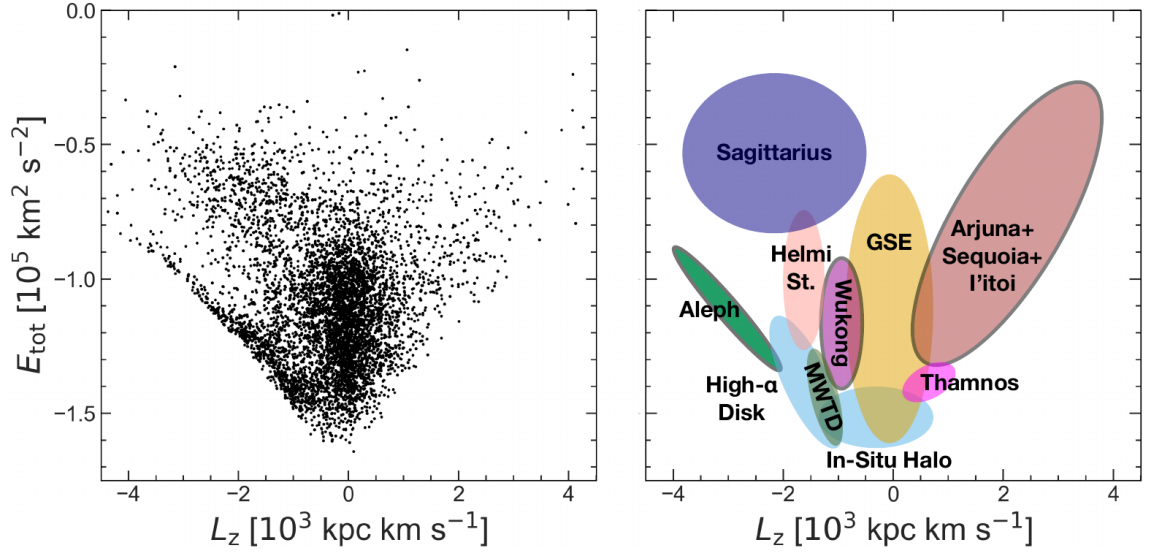
Figure 1.7
An overview of halo star structure in (energy, angular momentum) space from Naidu et al. (2020). The left-hand plot shows halo stars, the right-hand plot shows proposed structure.

As the DM halo cannot be directly observed inferring its properties is intrinsically linked to constraining the Galactic potential. It is commonly assumed that the MW's DM halo can be well-modelled as an NFW density profile. In our baryon-filled Galaxy, this is a mistake as the DM halo suffers baryonic contraction, driven by the more centrally concentrated potential of the baryonic components. (e.g. Blumenthal et al., 1986; Duffy et al., 2010; Schaller et al., 2016). This effect has significant consequences for the mass profile of the MW, approximately doubling the DM density in our solar neighbourhood. Failing to take contraction into account when fitting mass models can lead to an overestimation of the mass of the baryon components to compensate for the lower central DM density (Cautun et al., 2020). However, the contraction effect is hard to predict because of a dependence on the DM halo's internal structure and the nature of the galaxy's baryonic components (Gnedin et al., 2004). This effect, and the consequences for the MW's DM halo, are the focus of Chapter 3.

1.3.3   Assembly History and Stellar Halo

The total mass of the stellar halo is estimated to be approximately $1 - 1.5 \times 10^9 \, \mathrm{M_\odot}$, with around two-thirds accreted material (Deason et al., 2019b; Mackereth & Bovy, 2020). The rest of the stars are *insitu*, born in the MW and somehow dynamically heated out to halo orbits. Thus, our stellar halo is a cosmic graveyard populated with the stars and globular clusters (GCs) of destroyed dwarf galaxies. The bulk of the stellar halo is likely to have come from a few major mergers, which have left scars on our morphology (such as the thick disc, Bekki & Freeman 2003). In its youth, the MW was likely bombarded by smaller galaxies whose remains cannot be easily identified today (Lacey & Cole, 1993; Gottlöber et al., 2001; Fakhouri & Ma, 2009).

When a satellite enters the DM halo of the MW, it begins to experience dynamical friction. The satellite loses energy, and its orbit falls deeper and deeper into our gravitational well. The doomed galaxy is subjected to increasingly strong tidal stripping, first shedding its outer DM before losing its inner stars and gas as it finally breaks apart. The nature of an accretion event is determined by the relative mass of the merging satellite. More massive galaxies experience greater dynamical friction, falling deeper towards the Galactic centre, and can experience a radialising effect of their orbit (Amorisco, 2017). The orbits of smaller satellites take much longer to decay and can remain in our stellar halo over long time periods.

Unravelling this galactic debris to infer the assembly history of the MW is a difficult challenge as ancient mergers have long since phase mixed, effectively erasing the information in physical space. However, in the halo, the dynamical relaxation time is sufficiently long that the materials orbits can retain information of the accretion event (Eggen et al., 1962). Simulation-driven studies have shown that debris from the same progenitor remain on similar orbits, preserving structure in the space of integrals of motion (Bullock & Johnston, 2005; Gómez et al., 2010).

The stars' stellar age and chemistry can also provide further hints of a stars origin. As a galaxy matures, its star-forming gas becomes metal-enriched, with more massive galaxies

enriching faster. This environment is imprinted onto the star at birth, and after accretion, gives a signature of its progenitor. By combining dynamical and chemical clues, it is hoped that enough information is available to allow Galactic archaeologists to reconstruct our galaxy's past.

This task is far more straightforward for recent accretions, such as the Sagittarius dwarf galaxy (Ibata et al., 1994), or events that stay in a stream, such as the Helmi streams (Helmi et al., 1999). With the explosion of recent Galactic data, such as *Gaia*, the field has been able to delve deeper into our Galaxy's past Not long after the release of *Gaia* DR2, evidence for an ancient merger (*Gaia*-Enceladus-Sausage) was identified from an excess of radial velocity and chemical analysis. (Belokurov et al., 2018; Helmi et al., 2018a). In hindsight, hints of this structure have been seen before, such as the break in the power-law describing the stellar halo's density (Deason et al., 2011).

This discovery was followed by a smaller companion accretion event Sequoia, evidence for which centred on the analysis of several key globular clusters (GCs) (Myeong et al., 2018b, 2019; Barba et al., 2019). More recently, the population of GCs has been used to identify another ancient Galactic merger event, the Kraken (Kruijssen et al., 2020). Of the accreted material, GCs have long been recognised as sensitive probes of the accretion history of the MW (Searle & Zinn, 1978). GCs are likely more representative of smaller accretion events of the MW's past (Harris et al., 2015; Amorisco, 2019), and several GCs are suspected to be the nucleus of accreted dwarf galaxies (M54, M4, ω-Centuari, NGC1851). Chapter 4 looks at the history of the MW through the chemodynamics of its globular clusters.

1.4 Galactic Dynamics

Fundamentally, galaxies are composed of matter orbiting in a gravitational potential. To understand galaxies, it is then necessary to tame the mathematics of orbital dynamics. If successful, valuable information can be teased out from the orbits, such as an object's origin and eventual fate, whether it is part of a larger structure, and if so, if that structure is in equilibrium. For a recent review of Galactic dynamics, see Binney (2013).
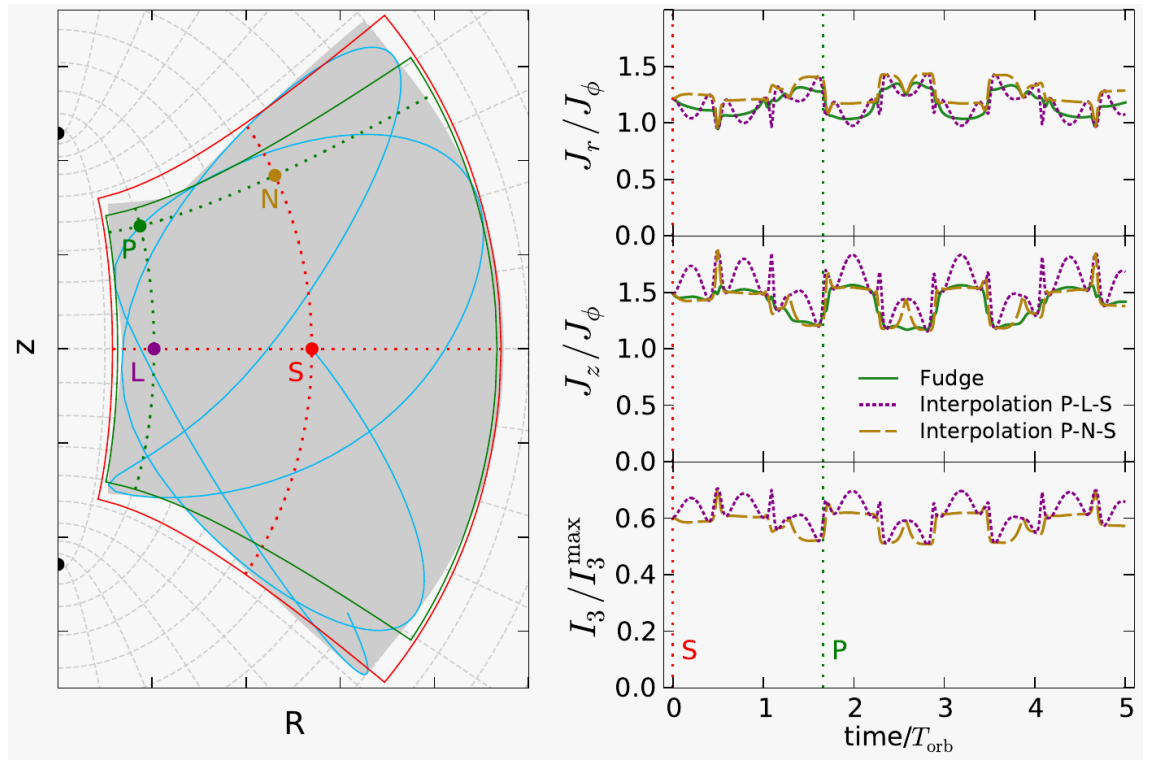
Figure 1.8
In the left panel, the radius and vertical height z of a stellar orbit in a Galactic potential. In the right, the corresponding orbital actions found by Stäckel Fudge technique. Credit: Vasiliev (2019).

Often the goal of such an analysis is to find integrals of motion, constant functions of the orbit dependant on the nature of the potential that have several practical applications. As previously discussed, accreted material typically retains some structure in IoM space, even after phase mixing. Furthermore, the IoM describe the individual orbits and provide a way of dynamically modelling galactic components. By Jeans' theorem, an equilibrium structure can be dynamically described by a distribution of IoMs, providing the orbital blueprints for the structure (Jeans, 1915). Given a potential, the distribution function delivers a complete description of the density profile, velocity distributions and other dynamics. This description forms the basis of self-consistent modelling; where the orbital distribution describes the mass distribution, the mass creates the gravitational potential, and the potential that dictates the orbits of the original distribution.

In a spherical potential, the energy ($E = H$) and the angular momentum vector ($\boldsymbol{L} = \boldsymbol{r} \times \boldsymbol{v}$) are conserved. As the orbit is confined to a plane normal to **L**, only two constants of motion are needed to describe the distribution; the energy and the magnitude of the angular momentum $L = |\mathbf{L}|$. If orbital distribution is isotropic, then it can be described with just an energy distribution. This assumption offers a far simpler description of the Galaxy's dynamics than axisymmetry. Far out from the centre, it is reasonable to assume spherical symmetry (although DM halos more closely resemble ellipsoids). Chapter 2 and Chapter 3 use this approximation.

In the inner regions, galactic potentials are better approximated as axisymmetric and oblate functions due to the influence of the stellar discs. In such a potential, the orbit explores a rosette between fixed extremums whilst the energy and z components of angular momentum are conserved. By numerically integrating orbits in smooth, axisymmetric galactic potentials, it can be demonstrated (for example, by Poincare surfaces of section) that the potential admits three IoM (and are therefore integrable) (Ollongren, 1962). However, finding the third integral of motion is challenging and only calculable for a few analytic potentials.

Arguably the best IoM for galactic dynamics are the action integrals **J**. Formally, for any integrable potential, there exists a canonical transformation between the physical

coordinates $(\mathbf{x}, \mathbf{v})$ and the action-angle coordinates $(\mathbf{J}, \theta)$ (Arnold, 1978). The actions $\mathbf{J}$ succinctly describe the orbit, and the angles θ describe the phase of the orbit whilst increasing linearly in time with a constant frequency. Together these coordinates can be understood as describing a higher dimensional torus. One significant advantage that the actions have over other IoM is that they are adiabatic invariants and thus essentially unchanged by sufficiently 'slow' (defined with respect to the orbital period) changes in the potential (Binney & Tremaine, 2008).

While theoretically attractive, historically, actions have been unfeasible to calculate in realistic galaxy potentials. However, with recent analytical and numerical breakthroughs, such as the 'Stäckel Fudge', this has changed. The Stäckel potentials are a family of separable, ellipsoidal potentials with known analytic expressions for actions. This Fudge works by assuming the Galactic potential is well modelled locally as a Stäckel, allowing fast computation of the actions, but does have inherent errors due to the approximation (Binney, 2012; Sanders & Binney, 2015b). Alternatively, methods based on torus mapping from toy potentials can compute actions to arbitrary accuracy (for non-resonant orbits), but these methods are substantially more computationally expensive (McGill & Binney, 1990; Sanders & Binney, 2015a). For a recent review of the numerical calculation of actions, see Sanders & Binney (2016).

As a result of these technical advances, and the usability of dynamical packages that have implemented these schemes, such as GALPY (Bovy, 2015) or AGAMA (Vasiliev, 2019), the action-angle formalism has grown in popularity over the past decade. Actions (and orbital frequencies) are now commonly used to find structure in observational data-sets and as the base of dynamical models (Myeong et al., 2018a; Fattahi et al., 2019; Piffl et al., 2015). This formalism is used in Chapter 3 to dynamically model the contraction DM haloes and in Chapter 4 to identify accretion groups of globular clusters.

1.4.1 Dynamics within Simulated Galaxies

It is often desirable to model the orbital dynamics within the simulated haloes of N-body simulations. Typically, dynamical methods need a smooth, symmetric potential or equivalently density profile, for which the N-body potential evaluation is unsuitable. There are several methods to derive the required density profile (given the particles positions). One approach is averaging the particles over spherical shells or axisymmetric bins. This can then be fit to by analytic profiles, such as an NFW. In modern dynamical packages, such as AGAMA and GALPY, the density profiles and potentials are expressed in basis expansions. These expansions that allow fast evaluations and conversions between density and the gravitational potential, while describing the profiles accurately

Not all galactic potentials are suitable to model this way, as halos frequently undergo mergers and other violent transient events. After such an event, the halo then takes time to relax back to pseudo-equilibrium. To quantify this, Neto et al. (2007) designed criteria to classify if the haloes are relaxed. A halo is deemed to be relaxed if it meets all of the following criteria:

(i) The total mass of substructure within R_{200} is less than 10 per cent of the total halo mass, M_{200}.

(ii) The distance between the centre of mass and the centre of the potential of the halo is less than $0.07R_{200}$.

(iii) The virial ratio $2T/|U| < 1.35$, where T is the total kinetic energy and U the gravitational potential energy of DM particles within R_{200}.

Of the 30 level 4 AURIGA haloes, 13 are unrelaxed at present-day based on these criteria.

1.5 Thesis Goals and Outline

This thesis aims to further our understanding of the MW's DM halo and accretion history through a combination of observations, simulations and dynamical analysis. The following

work is comprised of 3 science chapters.

Chapter 2: The Mass of the Milky Way from Satellite Dynamics

This chapter develops a method to infer the mass of a host galaxy, by comparing the dynamics of its satellite galaxy population to a sample from the EAGLE simulations. To demonstrate the accuracy of the method, it is first tested on the MW-like galaxies of the AURIGA simulation suite. The method is then applied to the MW, using ten classical satellites.

Chapter 3: The orbital phase space of contracted dark matter halos

This chapter models the baryonic contraction of DM halos described by a distribution of actions. This distribution is effectively preserved under adiabatic contraction, allowing DM haloes to be self-consistently contracted to any given baryon profile with the use of an iterative algorithm. This method is first tested on AURIGA before it is then used to model the MW's contracted DM halo so as to predict the total mass profile and the dynamics.

Chapter 4: The chemo-dynamical groups of the Milky Way's globular clusters

This chapter models the chemo-dynamical groups of a galaxy's GC population, considering the *insitu* and individual accretion groups. This method is first tested on the mock catalogues made from the AURIGA simulations, and then applied to the MW. Once the groups of GCs have been identified, the properties of the MW halo progenitors can be derived.

Chapter 5: Conclusions

This chapter summarises the work of the thesis and outlines areas of future work.

CHAPTER 2

The Mass of the Milky Way from Satellite Dynamics

2.1 Introduction

There have been many attempts to infer directly the MW mass through a variety of methods. The total MW mass is dominated by its dark matter (DM) halo, which cannot be observed directly. Instead, its properties must be inferred from the properties of luminous populations, such as the luminosity function of MW satellites (mostly the Large and Small Magellanic Clouds, e.g. Busha et al., 2011a; González et al., 2013; Cautun et al., 2014) and the kinematics of various dynamical tracers of the Galactic halo. The dynamics of halo tracers are mostly determined by the gravitational potential of the MW halo, and provide a key indirect probe of the total halo mass. Examples of halo tracers used for this purpose are satellite galaxies (e.g. Wilkinson & Evans, 1999; Watkins et al., 2010), globular clusters (e.g. Eadie & Harris, 2016; Binney & Wong, 2017; Sohn et al., 2018; Watkins et al., 2019), halo stars (e.g. Xue et al., 2008; Deason et al., 2012; Kafle et al., 2012, 2014), high velocity stars (e.g. Smith et al., 2007; Piffl et al., 2014a; Fragione & Loeb, 2017; Rossi et al., 2017; Monari et al., 2018) and stellar streams (e.g. Koposov et al., 2010; Newberg et al., 2010;

Gibbons et al., 2014; Küpper et al., 2015; Bowden et al., 2015).

There are a variety of methods for inferring the Galactic halo mass using dynamical tracers. A common approach is to model the tracers as distributions in equilibrium whose parameters are determined by fitting the model to observational data (e.g. Evans et al., 2003; Han et al., 2016). Advances in the calculation of action-angle coordinates (e.g. Vasiliev, 2019) have led to a new generation of analytical galaxy modelling, centred around distribution functions (DFs) in action-angle space. Examples include modelling the MW population of globular clusters (e.g. Posti & Helmi, 2019) or individual DFs of components such as the thick and thin disc, bulge, stellar halo and DM halo (Cole & Binney, 2017). The recent availability of large cosmological simulation has enabled a new class of methods based on comparing the observed properties of MW satellites to those of substructures in cosmological simulations (e.g. Busha et al., 2011a; Patel et al., 2017).

Although over the past decades a large amount of effort has been dedicated to inferring the Galactic halo mass, its value remains uncertain to within a factor of two, with most mass estimates ranging from 0.5 to $2.5 \times 10^{12} M_\odot$ (e.g. Wang et al., 2015, and our Fig. 2.7). While many studies claim uncertainties smaller than this range, the analytical models upon which they rely require several assumptions such as dynamical equilibrium and a given shape of the density or the velocity anisotropy profiles. These assumptions can lead to additional systematic errors, which are difficult to quantify but can be the dominant source of error (e.g. see Yencho et al., 2006; Wang et al., 2015, 2018). This is especially true for the MW halo whose dynamics are likely to be affected by the presence of a very massive satellite, the Large Magellanic Cloud (Gómez et al., 2015; Peñarrubia et al., 2016; Shao et al., 2018a). Furthermore, most methods typically estimate the mass within the inner tens of kiloparsecs, since this is the region where most tracers (such as halo stars and globular clusters) reside, necessitating an extrapolation to the virial radius. This extrapolation requires additional assumptions about the radial density profile of the MW and can lead to further systematic uncertainties.

Large-volume high-resolution cosmological simulations offer a unique test-bed for analytical mass determination methods (e.g. Han et al., 2016; Peñarrubia & Fattahi, 2017; Wang

et al., 2017) and, importantly, enable new methods for inferring the Galactic halo mass with a minimal set of assumptions. The simulations have the advantage of self-consistently capturing the complexities of halo and galaxy formation, as well as the effects of halo-to-halo variation. However, with a few exceptions, the limited mass resolution of current simulations means that they can resolve satellite galaxies but not halo stars or globular clusters (although see e.g. Pfeffer et al., 2018; Grand et al., 2018). This is not a major limitation since satellite galaxies, due to their radially extended spatial distribution, are one of the best probes of the outer MW halo. This is especially true now that the *Gaia* DR2 release has provided a large sample of MW satellites with full 6D phase space information (Helmi et al., 2018b; Fritz et al., 2018; Simon, 2018).

Galactic halo mass estimates that rely on cosmological simulations are relatively recent. Busha et al. (2011b) pioneered the approach of inferring halo properties by finding the best match between the MW satellites and satellites of simulated haloes. The MW mass is then determined by weighting the host haloes according to the quality of the satellite match, a technique known as importance sampling. Busha et al. used the distance, velocity and size of the Large and Small Magellanic Clouds (hereafter LMC and SMC) to constrain the MW mass. The distance and velocity of satellites can vary rapidly, especially when close to the pericentre of their orbit, so very large simulations are needed in order to find enough counterparts to the MW system.

Patel et al. (2017) pointed out that approximately conserved quantities, such as angular momentum, are better for identifying satellite analogues in simulations. This makes it easier to find MW counterparts; applying the criterion to a larger number of satellites results in a more precise mass determination (Patel et al., 2018). A further advance was achieved by Li et al. (2017) who showed that, when scaled appropriately, the DF of satellite energy and angular momentum becomes independent of halo mass. This scaling allows for a more efficient use of simulation data, since any halo can be rescaled to a different mass, and thus a better sampling of halo formation histories and halo-to-halo variation can be achieved. This approach represents a major improvement over importance sampling methods, in which the statistically relevant systems are those in a small mass range.

In this Chapter we improve and extend the Li et al. (2017) mass determination method. We start by constructing the phase-space distribution of satellite galaxies using a very large sample of host haloes taken from the EAGLE (Evolution and Assembly of GaLaxies and their Environments) galaxy formation simulation (Crain et al., 2015; Schaye et al., 2015). We then describe and calibrate three mass inference methods based on the satellite distributions of: i) angular momentum only, ii) energy only, and iii) a combination of both angular momentum and energy. We test these methods by applying them to an independent set of simulations, taken from the AURIGA project (Grand et al., 2017); this is a very stringent test because of the much higher resolution and rather different galaxy formation model implemented in AURIGA compared to EAGLE. Finally, we apply our methods to the latest observations of the classical satellites to determine the MW halo mass; we are able to estimate this mass with an uncertainty of only 20%.

The structure of the Chapter is as follows. Section 2.2 describes the construction of the phase-space DFs using the EAGLE data. Section 2.3 describes our mass inference methods, their calibration and validation with tests on mock systems. In Section 2.4, we apply this method to the observed MW system and discuss our results. Finally, Section 2.5 summarises and concludes the Chapter.

2.2 Construction of the satellite distribution

We now describe how to obtain a phase space distribution of satellites that, when scaled appropriately, is independent of host halo mass. We then introduce the MW observations, and the simulation data that we use for calculating the phase-space distribution function of satellite galaxies.

2.2.1 Theoretical background

We are interested in the energy and angular momentum distribution of Galactic satellites. This can be calculated starting from the observed distance, r^s, tangential velocity, v_t^s, and

speed, v^s, of satellite s, which we use to define the vector:

$$\boldsymbol{x}^s = \left(v^s, v_t^s, r^s\right).$$

(2.2.1)

The specific energy, E, and specific angular momentum, L, of a satellite are given by:

$$E = \frac{1}{2}\left|\mathbf{v}\right|^2 + \Phi\left(r\right)$$

$$L = \left|\boldsymbol{r} \times \boldsymbol{v}\right| = rv_t,$$

(2.2.2)

where $\Phi(r)$ is the gravitational potential at the position of the satellite. This cannot be measured directly in observations, and to calculate it we need to assume a mass profile for the host halo. Here, we assume that the host density profile is well approximated by a spherically symmetric Navarro, Frenk and White profile (hereafter NFW; Navarro et al. 1996, 1997), whose gravitational potential is given by:

$$\Phi_{\text{NFW}}\left(r\right) = -\frac{GM_{200}}{r} \frac{\ln\left(1 + C\frac{r}{R_{200}}\right)}{\ln\left(1 + C\right) - \frac{C}{C+1}},$$

(2.2.3)

where C is the concentration of the halo and M_{200} and R_{200} denotes the halo mass and radius, respectively. The mass, M_{200}, corresponds to the mass enclosed within a sphere of average density 200 times the critical density.

The NFW profile provides a good description of the radial density profile of relaxed haloes in DM-only simulations. The addition of baryons leads to a contraction of the inner region of haloes, and thus to a systematic departure from an NFW profile (e.g. Gnedin et al., 2004). However, at large enough distances (e.g. $r \gtrsim 20\,\text{kpc}$ for a halo mass of $10^{12}\,\text{M}_\odot$) the NFW profile still provides a very good description of the mass distribution even in galaxy formation simulations (e.g. Schaller et al., 2015; Zhu et al., 2016). In this work, we consider only satellites relatively far from the halo centre, where the NFW function represents a good approximation of the mass profile.

DM haloes have several self-similar properties, such as their density profiles (e.g. Navarro et al., 1996, 1997), the substructure mass function (e.g. Wang et al., 2012; Cautun et al., 2014) and the radial number density of subhaloes (Springel et al., 2008; Hellwing et al., 2016). Li et al. (2017) showed that the same self-similar behaviour also holds for the

energy and angular momentum distribution functions of subhaloes. This implies that, when scaled accordingly, satellites around hosts of different mass follow the same energy and angular momentum distribution. The same self-similar behaviour also holds to a good approximation in the EAGLE hydrodynamic simulation (see Appendix 2.6.2).

For a self-similar halo density profile, the satellites' positions and velocities scale with $M_{200}^{1/3}$ (Li et al., 2017). A given host halo and its associated satellite system, can therefore be scaled to a different host halo mass, M_{200}^{Scale}, as:

$$\left(r', v', v'_{\mathrm{t}}\right) = \left(\frac{M_{200}^{\mathrm{Scale}}}{M_{200}}\right)^{\frac{1}{3}} \left(r, v, v_{\mathrm{t}}\right) \ . \tag{2.2.4}$$

This implies that the energy and angular momentum of satellites also scale with halo mass through the relation $E, L \propto M_{200}^{2/3}$. Thus, we can choose characteristic E_0 and L_0 values for each halo mass and use them to rescale the E and L values of each satellite to obtain mass independent quantities. For each halo, we define the scaled specific energy, $\widetilde{E}$, and scaled specific angular momentum, $\widetilde{L}$, as:

$$\left(\widetilde{E}, \widetilde{L}\right) = \left(\frac{E}{E_0}, \frac{L}{L_0}\right) \ , \tag{2.2.5}$$

where the characteristic E_0 and L_0 values correspond to the energy and angular momentum of a circular orbit at R_{200} and are given by:

$$\begin{aligned} E_0 &= \frac{GM_{200}}{R_{200}} \\ L_0 &= \sqrt{GM_{200}R_{200}}. \end{aligned} \tag{2.2.6}$$

This scaling relation preserves the relaxation state, concentration and formation history of the halo, giving scaled properties that are independent of host mass (see Appendix 2.6.2).

2.2.2 Observational data for the MW satellites

We aim to estimate the MW halo mass using the classical satellites since those have the best proper motion measurements. The method we employ is flexible enough to incorporate the ultrafaint dwarfs; however, the EAGLE simulation, which we use for calibration, does not

Table 2.1

Properties of the classical Galactic satellites used in this work. The last two columns give the calculated energy and angular momentum values for each satellite. The energy has been calculated using an NFW profile with a concentration of 8, for a mass, $M_{200}^{\mathrm{MW}} = 1.17 \times 10^{12} M_\odot$, which corresponds to our best MW-halo mass estimate. The distance is with respect to the Galactic Centre. The specific orbital angular momentum, L, and specific energy, E, of the satellites are expressed in terms of the angular momentum, $L_{0;\,\mathrm{MW}}$, and energy, $E_{0;\,\mathrm{MW}}$, of a circular orbit at the virial radius, R_{200}. For the mass and concentration assumed here, we have $L_{0;\,\mathrm{MW}} = 3.34 \times 10^4 \,\mathrm{kpc\,km\,s^{-1}}$ and $E_{0;\,\mathrm{MW}} = 2.28 \times 10^4 \mathrm{km^2\,s^{-2}}$. The errors give the 68% confidence interval based on Monte Carlo sampling of the observational errors (see text for details).

Satellite	Distance [kpc]	$L/L_{0;\,\mathrm{MW}}$	$E/E_{0;\,\mathrm{MW}}$
LMC	51 ± 2	$0.46^{+0.05}_{-0.05}$	$-1.33^{+0.32}_{-0.31}$
SMC	64 ± 4	$0.46^{+0.08}_{-0.08}$	$-1.84^{+0.42}_{-0.37}$
Draco	76 ± 6	$0.30^{+0.03}_{-0.03}$	$-2.40^{+0.10}_{-0.11}$
Ursa Minor	76 ± 6	$0.32^{+0.02}_{-0.01}$	$-2.39^{+0.05}_{-0.05}$
Sculptor	86 ± 6	$0.48^{+0.03}_{-0.03}$	$-1.89^{+0.07}_{-0.07}$
Sextans	86 ± 4	$0.67^{+0.06}_{-0.05}$	$-1.21^{+0.17}_{-0.16}$
Carina	105 ± 6	$0.55^{+0.08}_{-0.08}$	$-1.86^{+0.19}_{-0.19}$
Fornax	147 ± 12	$0.70^{+0.21}_{-0.19}$	$-1.52^{+0.33}_{-0.30}$
Leo II	233 ± 14	$0.96^{+0.30}_{-0.28}$	$-1.20^{+0.29}_{-0.21}$
Leo I	254 ± 15	$0.82^{+0.28}_{-0.26}$	$-0.67^{+0.21}_{-0.15}$

resolve the ultrafaint satellites. Furthermore, we discard any satellites closer than 40 kpc (see section 2.2.3), so we exclude the Sagittarius dwarf from our observational sample. Sagittarius is currently at a distance of 26 kpc, undergoing strong tidal disruption by the MW disc, and is therefore unsuitable as a tracer of the DM halo. This leaves 10 classical satellites with adequate kinematical data (see Table 2.1).

We take satellite positions, distances and radial velocities from the McConnachie (2012) compilation. We use the observed proper motions of the classical satellites derived from the *Gaia* data release DR2 (Helmi et al., 2018b), apart from the most distant satellites, Leo I and Leo II, for which we use the Hubble Space Telescope proper motions (Sohn et al., 2013; Piatek et al., 2016) since these have smaller uncertainties.

To calculate the energy and angular momentum, we transform the satellite positions and velocities from Heliocentric to Galactocentric coordinates using the procedure described in Cautun et al. (2015). The transformation depends on the Sun's position and velocity for which we adopt: $d = 8.29 \pm 0.16$ kpc for the distance of the Sun from the Galactic

Centre; $V_{\text{circ}} = 239 \pm 5 \, \text{km s}^{-1}$ for the circular velocity at the Sun's position (McMillan, 2011); and $(U, V, W) = (11.1 \pm 0.8, 12.2 \pm 0.5, 7.3 \pm 0.4) \, \text{km s}^{-1}$ for the Sun's motion with respect to the local standard of rest, (Schönrich et al., 2010). When transforming to Galactocentric coordinates we account for errors in the distance, radial velocity and proper motion of each satellite, as well as in the Sun's position and velocity, which we model as normally distributed errors. To propagate the errors, we generate a set of 1000 Monte Carlo realizations of the MW system in heliocentric coordinates and transform each realization to Galactocentric coordinates.

2.2.3   EAGLE simulation sample

We select our sample of host haloes and satellite populations from the reference run of the EAGLE project (Crain et al., 2015). The large 100 Mpc volume of the EAGLE simulation provides a large sample of haloes, of a wide range of masses and assembly histories. Our final sample consists of the following host haloes and satellites galaxies.

Selection criteria for hosts haloes:

(i) Halo mass, M_{200}, in the range $10^{11.7} \, \text{M}_\odot$ to $10^{12.5} \, \text{M}_\odot$;

(ii) relaxed systems, that is haloes for which the distance between the centre of mass and the centre of potential is less than $0.07 R_{200}$ and the total mass in substructures is less than 10% (Neto et al., 2007).

Selection criteria of satellite galaxies:

(i) Distance from halo centre in the range $40 \, \text{kpc} < r' < 300 \, \text{kpc}$, where $r' = r(10^{12} \, \text{M}_\odot / M_{200})^{1/3}$ is the rescaled distance of the satellite corresponding to a halo of mass $10^{12} \, \text{M}_\odot$ (see equation 2.2.4); this results in a similar radial distribution as the MW satellites if the MW halo had a mass of $10^{12} \, \text{M}_\odot$;
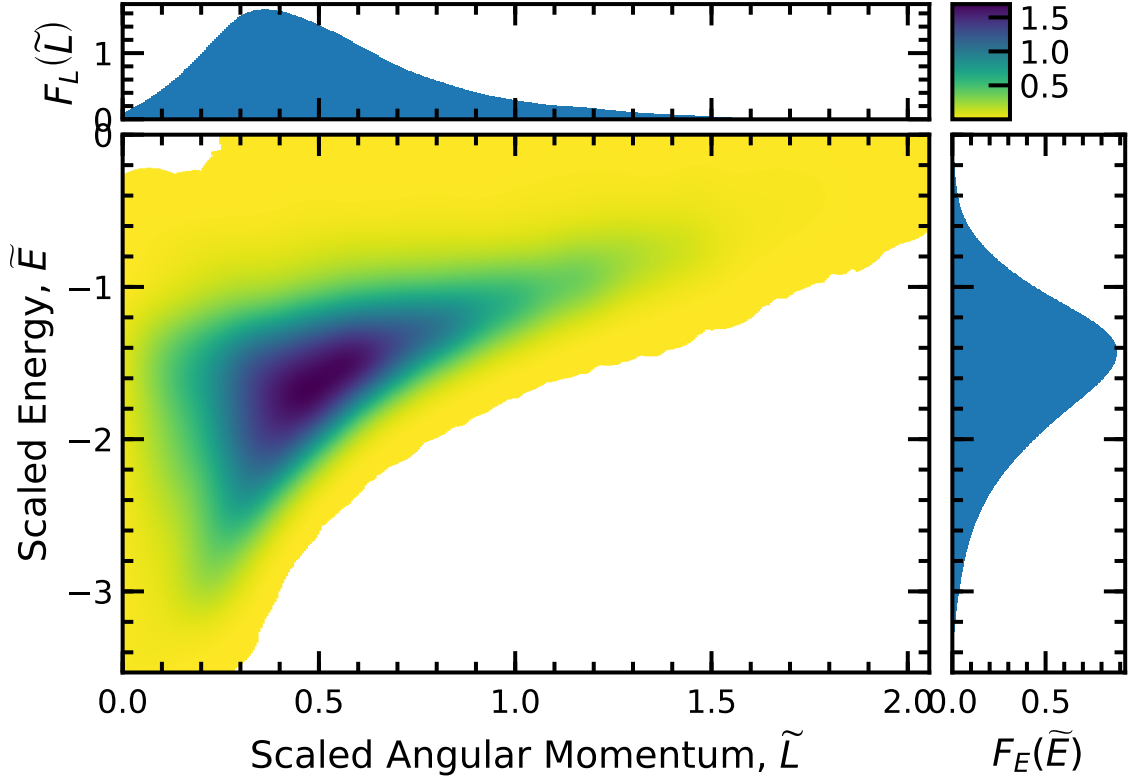
Figure 2.1

The distribution, $F(\widetilde{E}, \widetilde{L})$, of bound EAGLE satellites in terms of the scaled angular momentum, $\widetilde{L}$, and scaled energy, $\widetilde{E}$. The energy and angular momentum are scaled according to equation (2.2.5) to obtain quantities that are independent of host halo mass, M_{200}. The colour gives the number density of satellites, with dark colours corresponding to higher number densities (see colour bar). The two side panels show the one dimensional distributions of the scaled energy $F_E(\widetilde{E})$ (right-hand panel) and scaled angular momentum $F_L(\widetilde{L})$ (top panel) of satellites.

(ii) the satellite is luminous, i.e it contains at least one star particle, which excludes dark subhaloes.

This gives a sample of approximately $\sim 1,200$ host haloes and $\sim 14,000$ satellites. Our mass scaling method allows us to choose haloes in a broad mass range. The restriction on the radial distribution of satellite galaxies is chosen so that the model samples matches the observed one and to ensure that the potential is dominated by DM. Further discussion as to whether the MW satisfies the host criteria can be found in the conclusions section of this Chapter.

In Fig. 2.1 we show the distribution of EAGLE satellites in scaled energy and angular momentum space, $(\widetilde{E}, \widetilde{L})$. For each satellite, we calculate the energy by assuming that

the host halo is well described by an NFW profile individually fitted to each halo as described in Schaller et al. (2015). This procedure is similar to how energy is calculated for observational satellites, and thus allows for a proper comparison between theory and observations. To obtain a continuous DF, we applied a 2D Gaussian smoothing with dispersions $\alpha\sigma_{\widetilde{L}}$ and $\alpha\sigma_{\widetilde{E}}$ for the $\widetilde{L}$ and $\widetilde{E}$ directions, respectively. The symbols $\sigma_{\widetilde{L}} = 0.36$ and $\sigma_{\widetilde{E}} = 0.52$ denote the standard deviation of the $\widetilde{L}$ and $\widetilde{E}$ distributions, respectively. The parameter $\alpha = 0.125$ was chosen as a compromise so as to obtain a locally smooth function without significantly changing the overall shape of the DF.

The distribution in $(\widetilde{E}, \widetilde{L})$ space is not uniform and satellites are most likely to have values around the peak of the DF, $(\widetilde{E}, \widetilde{L}) \approx (-1.5, 0.5)$, which corresponds to the dark coloured region in Fig. 2.1. The $(\widetilde{E}, \widetilde{L})$ distribution is bounded on the lower right hand side by circular orbits. Moving perpendicularly away from this boundary, the orbits become increasingly radial. The $\widetilde{E}$ distribution is bounded by the potential energy of the inner radial cut, and the $\widetilde{L}$ distribution is bounded by a circular orbit at the outer radial cut. In our sample, approximately 1% of the satellites are unbound, i.e. $E > 0$, which is consistent with previous studies (Boylan-Kolchin et al., 2013). However, we note that we do not calculate the exact binding energy of each satellite, but only an approximate value under the assumption that the host halo is spherically symmetric and well described by an NFW profile (see eq. 2.2.3). While not shown in Fig. 2.1, we do keep unbound satellites in our analysis and thus we make no explicit assumption that MW satellites, such as Leo I, are bound. Instead, it is simply improbable that Leo I is unbound, and this is reflected in the individual satellites mass estimates we present in Section 2.4.

There are several advantages to obtaining a composite DF that is averaged over many host haloes instead of calculating individual distributions for each halo, as done by Li et al. (2017). In EAGLE, the mass resolution limits the number of subhaloes that can be identified in each system. As a result, the satellite population of each system represents a poor sampling of their haloes unique DF. The total composite DF contains many possible halo histories, and their multiplicity effectively serves as a prior probability. With further knowledge of the MW's assembly history, it would be possible to restrict the model sample

to have similar assembly histories to the MW. This could reduce the effective halo scatter and potentially result in a more accurate mass estimate. However, in this work we choose not be too restrictive.

2.3 Method

We present three different methods for inferring the mass of the MW, each based on the following satellite properties: i) orbital angular momentum, ii) orbital energy, and iii) both angular momentum and energy. All three methods employ the same principles and steps. We focus the discussion on the third method, which combines both L and E, and which should give the best mass constraints since it uses the largest amount of information. The methods we use are based on the approach of Li et al. (2017), which we have modified to work with a large sample of haloes and our mass independent DF, $F(\widetilde{E}, \widetilde{L})$.

We are interested in determining the mass of a host halo starting from the observed position and velocities of a set of N_{Sat} satellites. Each satellite, s, has a set of observed phase-space coordinates:

$$\boldsymbol{x}^s = \left(v^s, v_{\text{t}}^s, r^s\right) \ \{\boldsymbol{x}^s\}_{s \in [0, N_{\text{Sat}}]} \ , \tag{2.3.1}$$

consisting of the speed, v, the tangential velocity component, v_{t}, and the distance, r, from the host centre. These properties, combined with assumptions about the mass, M_{200}, and the density profile of the host, are sufficient to calculate the energy and angular momentum, $\left\{\widetilde{E}^s, \widetilde{L}^s\right\}\Big|_{M_{200}}$, of each satellite. Varying M_{200} gives a path in the $(\widetilde{E}, \widetilde{L})$ plane for each satellite. As a function of M_{200}, $\widetilde{L}$ scales as $M_{200}^{-2/3}$ and so decreases asymptotically to zero for increasing value of M_{200}. The scaled energy, $\widetilde{E}$, has two terms that scale differently; the kinetic term scales as $M_{200}^{-2/3}$, while the potential term scales as $M_{200}^{1/3}$. With increasing M_{200}, the potential term dominates and $\widetilde{E}$ tends to $-\infty$.

Fig. 2.2 illustrates the path of the Galactic satellites in the $(\widetilde{E}, \widetilde{L})$ plane as we vary the assumed mass of the MW halo. For example, as we increase the value of M_{200}, the LMC dwarf moves from the top part of the plot to the bottom-left corner. This is because both
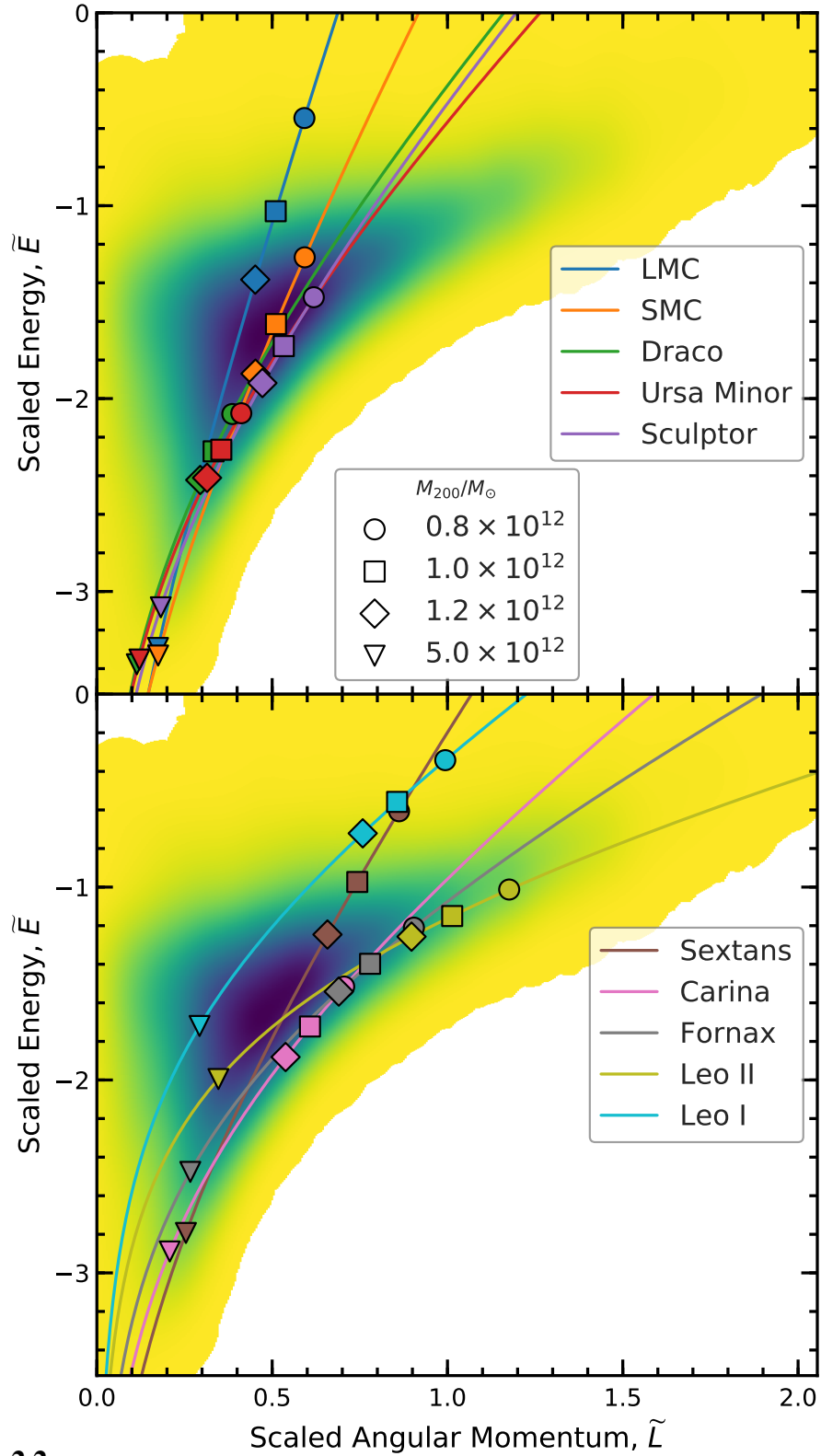
Figure 2.2

The path of the Galactic satellites in scaled energy – angular momentum space, $(\widetilde{E}, \widetilde{L})$, when varying the MW halo mass, M_{200}. Each curve corresponds to a different satellite (see legend). The filled symbols show the location corresponding to the four values of M_{200} given in the legend. The energy has been calculated using an NFW profile with a concentration of 8. The colour scheme is the same as in Fig. 2.1, with darker colours corresponding to higher number densities.

$\widetilde{L}$ and $\widetilde{E}$ decrease with increasing M_{200} values.

The trajectory of the satellites through the 2D plane depends on the satellites' orbital phase. The scaled angular momentum, $\widetilde{L}$, varies as a function of M_{200} uniformly throughout the orbit, but the rate of change of the scaled energy, $\widetilde{E}$, is dependent on the satellites' current radius. Nearer pericentre, the satellites have higher absolute values of kinetic and potential energy components compared to those at larger distances. When increasing M_{200}, the scaled kinetic energy decreases while the absolute value of the scaled potential energy increases, causing the total scaled energy, $\widetilde{E}$, to decrease rapidly and thus results in a more vertical trajectory. The figure also illustrates that when the assumed M_{200} is very high, $\widetilde{L}$ varies slowly and so the paths become nearly vertical.

Fig. 2.2 illustrates how the energy and angular momentum of satellites can be used to determine the host halo mass. The DF in $(\widetilde{E}, \widetilde{L})$ space is not uniform, and as the assumed M_{200} of the host is varied, satellites move between regions of high and low number density in this space. For example, the LMC falls in a high density region for $M_{200} \approx 1.4 \times 10^{12} \, M_{\odot}$, and in lower density regions for higher or lower masses. Thus, the LMC phase space coordinates would prefer a MW halo mass of $\approx 1.4 \times 10^{12} \, M_{\odot}$. In contrast, the Leo I path is nearest to the maximum density for $M_{200} \approx 2.9 \times 10^{12} \, M_{\odot}$, and suggests a higher MW mass.

We now describe how each satellite can be used to obtain a likelihood for the MW halo mass, and how to combine the mass estimates from various satellites. Our aim is to determine the likelihood, $p(M_{200}|\mathbf{x}^s)$, for the host mass given the observed $\mathbf{x}^s$ properties of satellite s.

The likelihood can be calculated from the $\widetilde{E}$ distribution via

$$p(M_{200}|\mathbf{x}^s) = F_E(\widetilde{E}) \left. \frac{\partial \widetilde{E}}{\partial M_{200}} \right|_{\widetilde{E}=\widetilde{E}^s}, \qquad (2.3.2)$$

where the $F_E(\widetilde{E})$ term denotes the DF, while the partial derivative arises from the Jacobian of the transformation from $\widetilde{E}$ to host halo mass, M_{200}. The same procedure can be used to estimate the host mass using only the angular momentum by replacing $F_E(\widetilde{E})$ by the $\widetilde{L}$

distribution function, $F_L(\widetilde{L})$, and by changing the $\widetilde{E}$ derivative term to $\widetilde{L}$, to obtain:

$$p(M_{200}|\mathbf{x}^s) = F_L(\widetilde{L}) \left. \frac{\partial \widetilde{L}}{\partial M_{200}} \right|_{\widetilde{L}=\widetilde{L}^s} . \tag{2.3.3}$$

This expression can be approximately extended to the 2 dimensional case (see Appendix 2.6.1) , where we use both $(\widetilde{E}, \widetilde{L})$ to constrain the halo mass, via

$$p(M_{200}|\mathbf{x}^s) = F(\widetilde{E}, \widetilde{L}) \, M_{200} \left. \frac{\partial \widetilde{E}}{\partial M_{200}} \frac{\partial \widetilde{L}}{\partial M_{200}} \right|_{\widetilde{E}=\widetilde{E}^s; \, \widetilde{L}=\widetilde{L}^s} , \tag{2.3.4}$$

where the additional M_{200} factor is needed to have the correct units. Note that all the $\widetilde{E}$ and $\widetilde{L}$ terms in Eqs. (2.3.2)-(2.3.4) are evaluated at the point $\widetilde{E}^s \equiv \widetilde{E}(\mathbf{x}^s, M_{200})$ and $\widetilde{L}^s \equiv \widetilde{L}(\mathbf{x}^s, M_{200})$. For a detailed derivation of Eqs. (2.3.2)-(2.3.4), and the motivation for the approximation, please see Appendix 2.6.1.

In practice, we actually determine the logarithm of the mass, $\log_{10}(M_{200})$, since the resulting probability distribution function (PDF) in log space is closer to a Gaussian. We determine the most likely host mass as the mass that maximizes the likelihood — the Maximum Likelihood Estimator (MLE) mass, M_{200}^{MLE}. As the uncertainties, we take the 68% confidence limits corresponding to the interval between the 16 and 84 percentiles of the mass PDF. Assuming that the satellites are independent tracers, we can combine the estimates for individual satellites to obtain an overall estimate given a set of observations, $\{\mathbf{x}^s\}$. The combined likelihood is given by:

$$p(M_{200}|\{\mathbf{x}^s\}) = \prod_{s=1}^{N_{\mathrm{Sat}}} p(M_{200}|\mathbf{x}^s) . \tag{2.3.5}$$

The potential energy of satellites has a weak dependence on the host halo concentration, which is an unknown quantity. We have tested that the 10 satellites used here cannot, by themselves, place any meaningful constraints on the concentration of the MW halo. Thus, we proceed to marginalize over the unknown concentration:

$$p(M_{200}|\mathbf{x}^s) = \int p(M_{200}|\mathbf{x}^s, C) \, p(C|M_{200}) \, \mathrm{d}C , \tag{2.3.6}$$

where $p(C|M_{200})$ denotes the distribution of concentrations for haloes of mass, M_{200}, found in the EAGLE simulation, which we took from Schaller et al. (2015). In practice, we

evaluate $p(M_{200}|x, C)$ using 15 evenly spaced values in the range $C \in [5, 20]$. We note that the dependence on concentration is weak, so our results are not affected by the choice of the distribution of concentrations (see Appendix 2.6.3).

2.3.1 Observational errors

While we have perfect knowledge of the phase space coordinates, $\{x^s\}$, of EAGLE satellites, in order to apply the method to the MW satellites we must consider the effects of observational errors. To account for errors, we perform a set of 1000 Monte Carlo realizations that sample the observational uncertainties (see Section 2.2.2 for a detailed description of the procedure). This produces a Monte Carlo sample of allowed phase-space coordinates for each satellite. We first determine the MW mass likelihood for each Monte Carlo realization, and then we average the likelihood of all the Monte Carlo samples. In the limit of a large number of Monte Carlo samples, this is equivalent to marginalizing over the observational errors.

2.3.2 Method calibration using EAGLE

To provide a robust mass estimate of the MW halo, we now explore the accuracy of our methods using tests on mock satellite systems. Since MLE estimates can be biased, we first calibrate the inference methods using a large sample of EAGLE systems. Then, in Section 2.3.3, we validate the methods on an independent, higher resolution set of simulations taken from the AURIGA project.

To calibrate the three mass determination methods we start by applying them to the EAGLE simulations. We select the same EAGLE haloes as in Section 2.2.3, that is haloes of total mass $\sim 10^{12}\,\mathrm{M_\odot}$, and keep only those which contain at least 10 luminous satellites within the distance range quoted in Section 2.2.3. There are ~ 600 haloes satisfying the selection criteria. We then apply each mass determination method to each EAGLE system to obtain the MLE mass, M_{200}^{MLE} of that system. The results are shown in Fig. 2.3, where we compare the MLE masses to the true total halo mass, M_{200}^{True}. The performance of each method
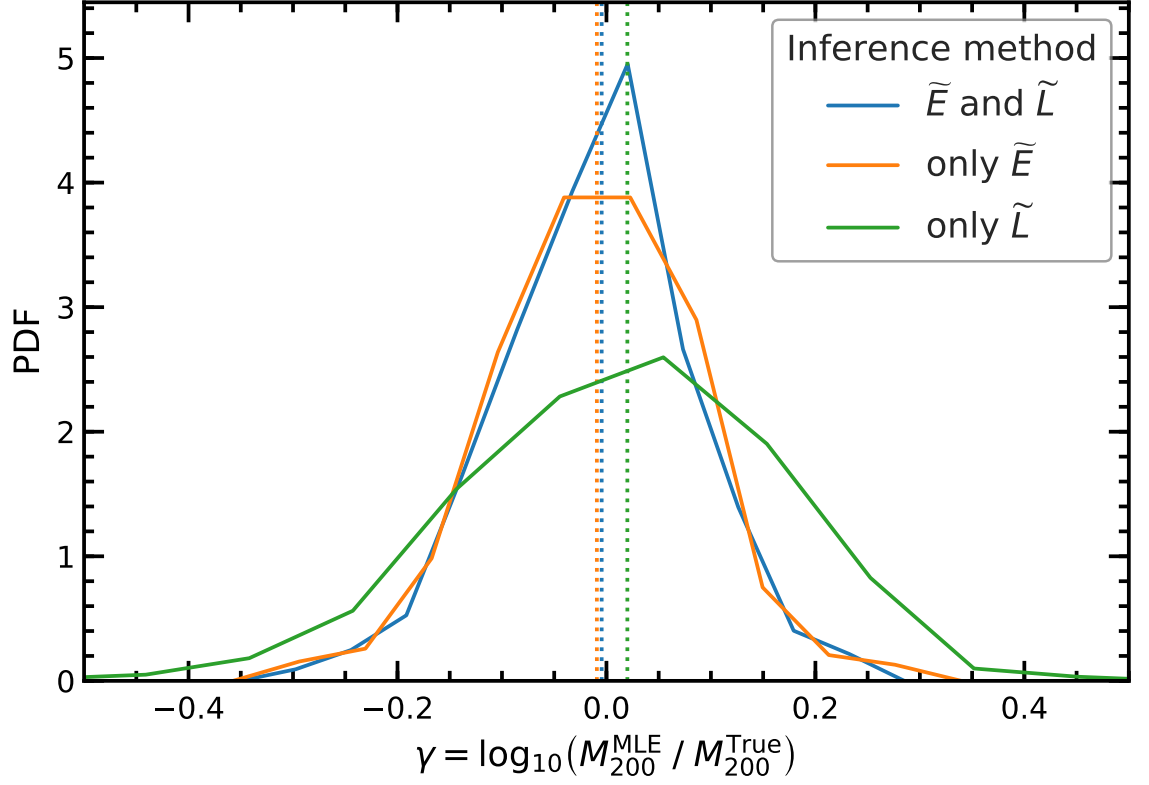
Figure 2.3

The distributions of the ratio of MLE estimate, M_{200}^{MLE}, to the true halo mass M_{200}^{True}, from each of our three inference methods. The results were obtained by applying each mass determination method to a sample of ~ 600 systems from the EAGLE simulation. The vertical dotted lines indicate the median of each distribution, which represents the bias, b, of each method. For subsequent results, we correct the mass estimates by the bias of each method and we denote the corresponding mass by M_{200}^{Esti}.

may be quantified by the ratio, $\gamma = \log_{10}\left(M_{200}^{\text{MLE}}/M_{200}^{\text{True}}\right)$, for each EAGLE system. The median and scatter of the γ distribution give the bias and typical uncertainty of the method, respectively.

Fig. 2.3 shows that our three methods have only small biases compared to their dispersion. The (E, L) and the E only methods have a slight bias with the median of the γ distribution being -0.01, while the method based on L only has an bias of $+0.02$. A consistently biased estimate is not a problem since it can easily be corrected to obtain an accurate result. The bias-corrected mass estimate, M_{200}^{Esti}, is given by:

$$\log_{10}\left(M_{200}^{\text{Esti}}\right) = \log_{10}\left(M_{200}^{\text{MLE}}\right) - b \ . \tag{2.3.7}$$

The dispersion of the γ distributions in Fig. 2.3 reflects the true precision of the method, σ_{True}. Mass estimates based only on the angular momentum have the largest dispersion, $\sigma_{\text{True}} = 0.15$, while both E and (E, L) methods have the same precision, $\sigma_{\text{True}} = 0.09$. Thus, most of the mass information is contained in the satellites' orbital energy. Adding angular momentum data hardly improves the mass estimates, indicating that L does not contain significant information about the host mass beyond the information already contained in the satellites' energy.

Another important point to consider is the confidence interval to be associated with each mass measurement. One possibility is to take the dispersion of γ (see Fig. 2.3), but this suffers from the limitation of assigning the same error to all mass measurements. In practice, the mass of some host haloes can be more precisely determined than the mass of others, and the confidence limits do not need to be symmetrical around the MLE value (e.g. see Fig. 2.4). Thus, the approach of assigning a single error to all measurements is not optimal.

An alternative is to consider the error estimates of the Bayesian method. These should be accurate, except for the effects of an assumption implicit in our method, that all satellites are independent tracers. For example, satellites can fall in groups or filaments, which might result in correlated energy and angular momentum amongst two or more satellite

galaxies. For the brightest 10 satellites, the ones considered here, only a small fraction is expected to have fallen in groups (e.g. Wetzel et al., 2015; Shao et al., 2018a) and, in any case, interactions with other satellites and with the host halo and galaxy are expected to decrease any phase-space correlations present at the time of accretion (e.g. Deason et al., 2015; Shao et al., 2018b). Thus, we would generally expect the assumption of independent tracers to be reasonable. We have checked how realistic the Bayesian error estimates are and found them to be roughly the same as the uncertainties shown in Fig. 2.3. The same will not hold true in future studies when the method will be applied to much larger numbers of satellites (see discussion in Section 2.4.3).

2.3.3 Tests with the AURIGA simulations

In this section we test our mass inference methods by applying them to model galaxies from the AURIGA project. AURIGA is a suite of high-resolution, hydrodynamical zoom-in simulations of MW-like systems. We consider the 30 level 4 systems, which have dark matter and gas mass resolution ~30 times higher than EAGLE (see Grand et al. 2017 for details). AURIGA makes for a perfect test suite since it has higher resolution, uses a different hydrodynamics code and includes a different galaxy formation model than EAGLE. Thus, by applying our inference methods to these completely independent simulations, we can assess our methods' accuracy and quantify any systematic biases that may have been introduced by calibrating our methods on the EAGLE simulations.

For each AURIGA galaxy, we identify the brightest 10 satellites galaxies at a distance between 40 and 300 kpc from the halo centre. These objects represent our mock observational sample of the MW-like satellite systems. We then apply the (E, L) mass determination method to each of the 30 AURIGA systems.

Fig. 2.4 shows the ratio of estimated to true masses, as well as the associated uncertainties for each AURIGA galaxy. We find that for 19 out of the 30 systems, or 63%, the estimated mass agrees with the true value to the 68% confidence interval, approximately as expected from the statistics. This performance is very good especially when taking into account
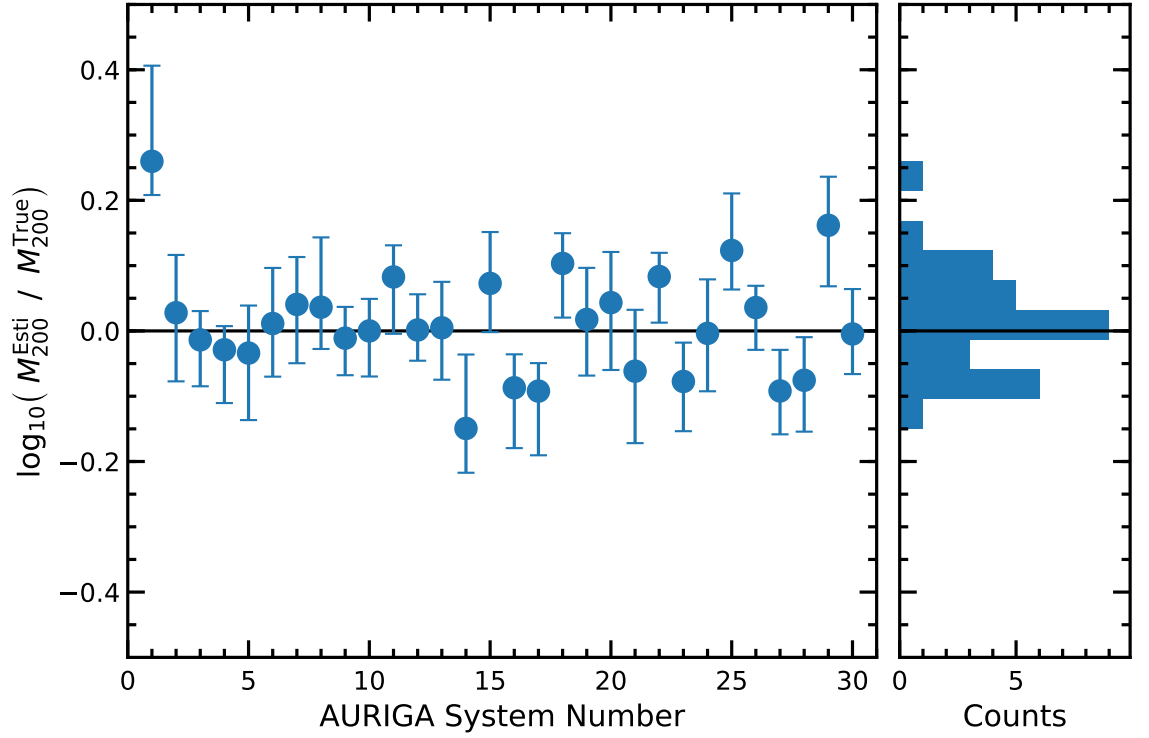
Figure 2.4

Test of the energy – angular momentum halo mass inference method on 30 MW-mass galaxies from the AURIGA galaxy formation simulation project. We show the ratio between the estimated, M_{200}^{Esti}, and the true, M_{200}^{True}, halo masses for each AURIGA system. Note that M_{200}^{Esti} includes the bias correction determined from the EAGLE mock catalogues (see equation 2.3.7). The errorbars correspond to the estimated 68% confidence limit. The AURIGA simulations have much higher resolution and assume different galaxy formation models than EAGLE, and thus provide a rigorous test of the mass inference method. Most mass estimates agree with the true values within the 68% confidence limit, in very good agreement with statistical expectations.

Table 2.2

The MW halo mass, $M_{200}^{\rm MW}$ (the mass enclosed within a sphere of average density 200 times the critical density) estimated from each classical satellite (except Sagittarius), and the combined overall result. The table gives mass estimates using: (i) only the angular momentum, L; (ii) only the energy, E: and (iii) both E and L. We quote 68% confidence limits.

	$M_{200}^{\rm MW}$ $[10^{12} M_{\odot}]$		
Satellite	only L	only E	E and L
LMC	$0.98^{+1.78}_{-0.51}$	$1.23^{+0.65}_{-0.25}$	$1.35^{+0.76}_{-0.28}$
SMC	$0.98^{+1.84}_{-0.52}$	$0.93^{+0.61}_{-0.31}$	$1.00^{+0.68}_{-0.32}$
Draco	$0.51^{+0.94}_{-0.26}$	$0.4^{+0.39}_{-0.09}$	$0.42^{+0.43}_{-0.08}$
Ursa Minor	$0.56^{+1.03}_{-0.29}$	$0.40^{+0.40}_{-0.09}$	$0.42^{+0.43}_{-0.09}$
Sculptor	$1.02^{+1.88}_{-0.52}$	$0.74^{+0.66}_{-0.15}$	$0.76^{+0.74}_{-0.14}$
Sextans	$1.70^{+3.09}_{-0.87}$	$1.35^{+1.01}_{-0.29}$	$1.41^{+1.12}_{-0.28}$
Carina	$1.29^{+2.34}_{-0.69}$	$0.74^{+0.83}_{-0.24}$	$0.69^{+1.02}_{-0.21}$
Fornax	$1.86^{+3.63}_{-1.08}$	$1.12^{+1.68}_{-0.52}$	$1.10^{+1.78}_{-0.52}$
Leo II	$3.02^{+5.63}_{-1.86}$	$1.91^{+4.32}_{-1.01}$	$2.04^{+3.17}_{-1.11}$
Leo I	$2.40^{+4.61}_{-1.49}$	$3.09^{+6.45}_{-1.16}$	$2.88^{+3.43}_{-1.06}$
Combined	$\mathbf{1.20^{+0.42}_{-0.27}}$	$\mathbf{1.10^{+0.21}_{-0.14}}$	$\mathbf{1.17^{+0.21}_{-0.15}}$

that around a third of the AURIGA systems are unrelaxed (see Sec. 2.2.3 for relaxation criteria). We have checked that the other two methods, using only L and only E, are similarly successful. This test demonstrates the accuracy of our method for determining halo masses and confirms that our error estimates are realistic and robust.

2.4   Milky Way Mass Estimates

We now apply our mass estimation methods to data for the 10 MW satellites that satisfy our selection criteria. We begin by obtaining the Galactic halo mass likelihood from each satellite and corresponding uncertainties (calculated with the Monte Carlo sampling technique described in Section 2.3.1). The PDFs of the MW halo mass, M_{200}, obtained from each satellite's data using the (E, L) method are shown in Fig. 2.5; the best estimates and associated 68% confidence intervals are given in Table 2.2.
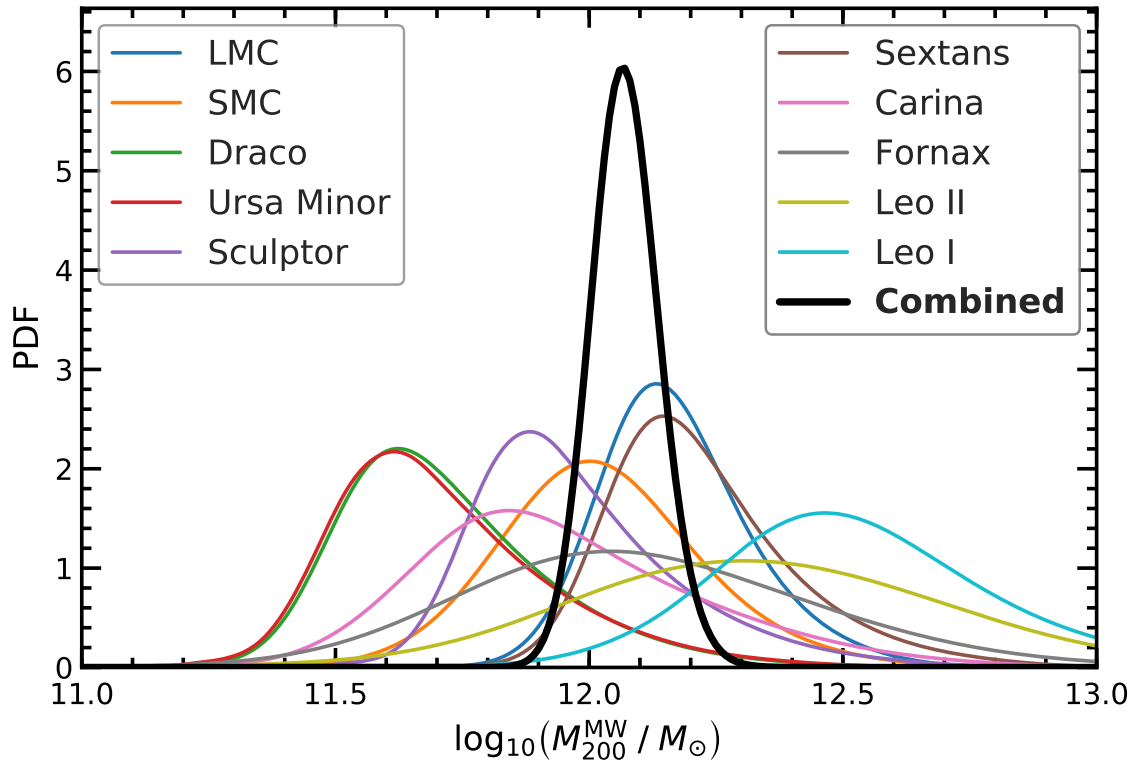
Figure 2.5
   The MW halo mass, M_{200}^{MW}, inferred from the energy and orbital angular momentum of each classical satellite (except Sagittarius). The thick line shows the inferred MW halo mass, $M_{200}^{\mathrm{MW}} = 1.17_{-0.15}^{+0.21} \times 10^{12} M_{\odot}$ (68% confidence limit), obtained by combining the 10 individual estimates. The inferred M_{200}^{MW} values and their corresponding errors are given in Table 2.2.
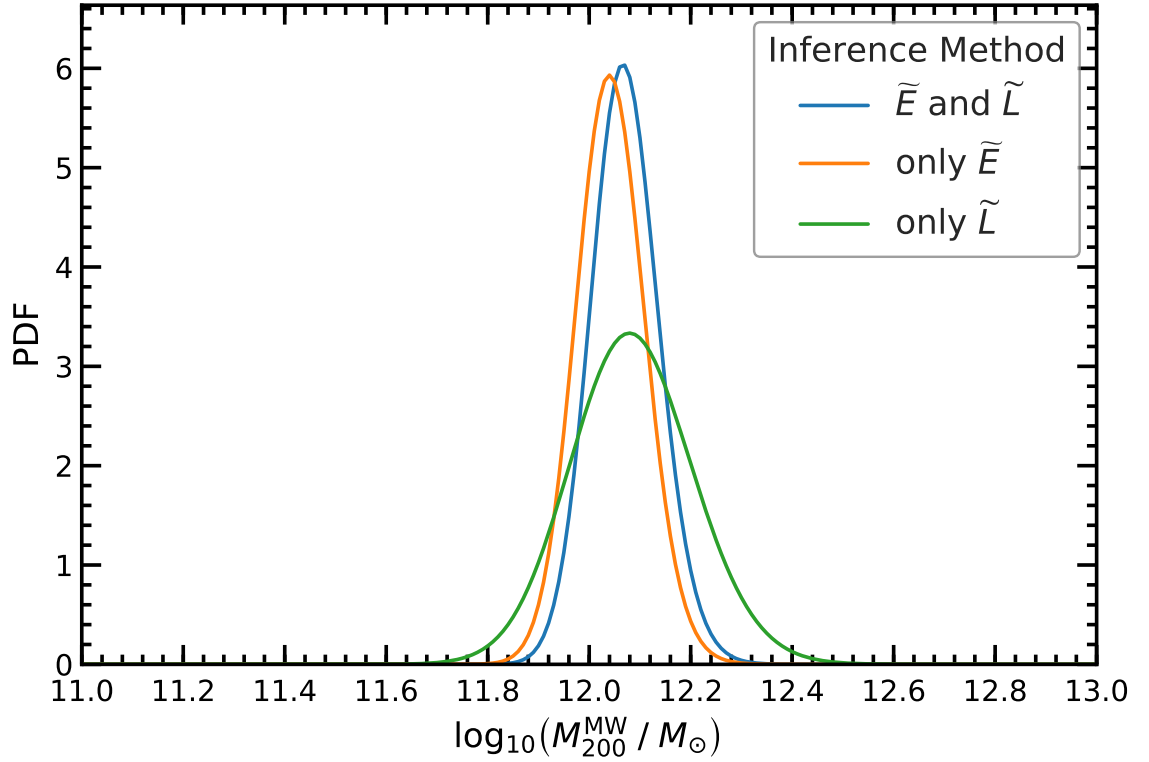
Figure 2.6

Comparison of the MW halo mass inferred using the three methods studied here. The methods use the following satellite data: (i) only the angular momentum, L; (ii) only the energy, E; and (iii) both E and L. The mass estimates and their errors are given in Table 2.2.

Individually, the satellites give a wide range of total masses for the MW. For example, Ursa Minor and Draco favour a very low mass, $M_{200} \approx 10^{11.6}\,M_{\odot}$, which is because both of them have very low total specific energies (see Table 2.1). At the other extreme, Leo I has the highest total energy and favours a halo an order of magnitude more massive, $M_{200} \approx 10^{12.5}\,M_{\odot}$. However, the mass estimate from any one satellite has a broad distribution and does not provide a strong constraint on the MW mass. The true power of the method comes from combining the mass likelihoods from each satellite; the combined result is shown as a thick line in Fig 2.5. The combined estimate for the MW halo mass is $M_{200}^{\mathrm{MW}} = 1.17_{-0.15}^{+0.21} \times 10^{12} M_{\odot}$.

Fig. 2.6 compares the Galactic halo mass determination using the three methods introduced in this study. We find very good agreement amongst the three, with all of them having a very large overlap (see Table 2.2 for the actual values and their uncertainties). Of the three, the method based on angular momentum only is the most uncertain and, of the
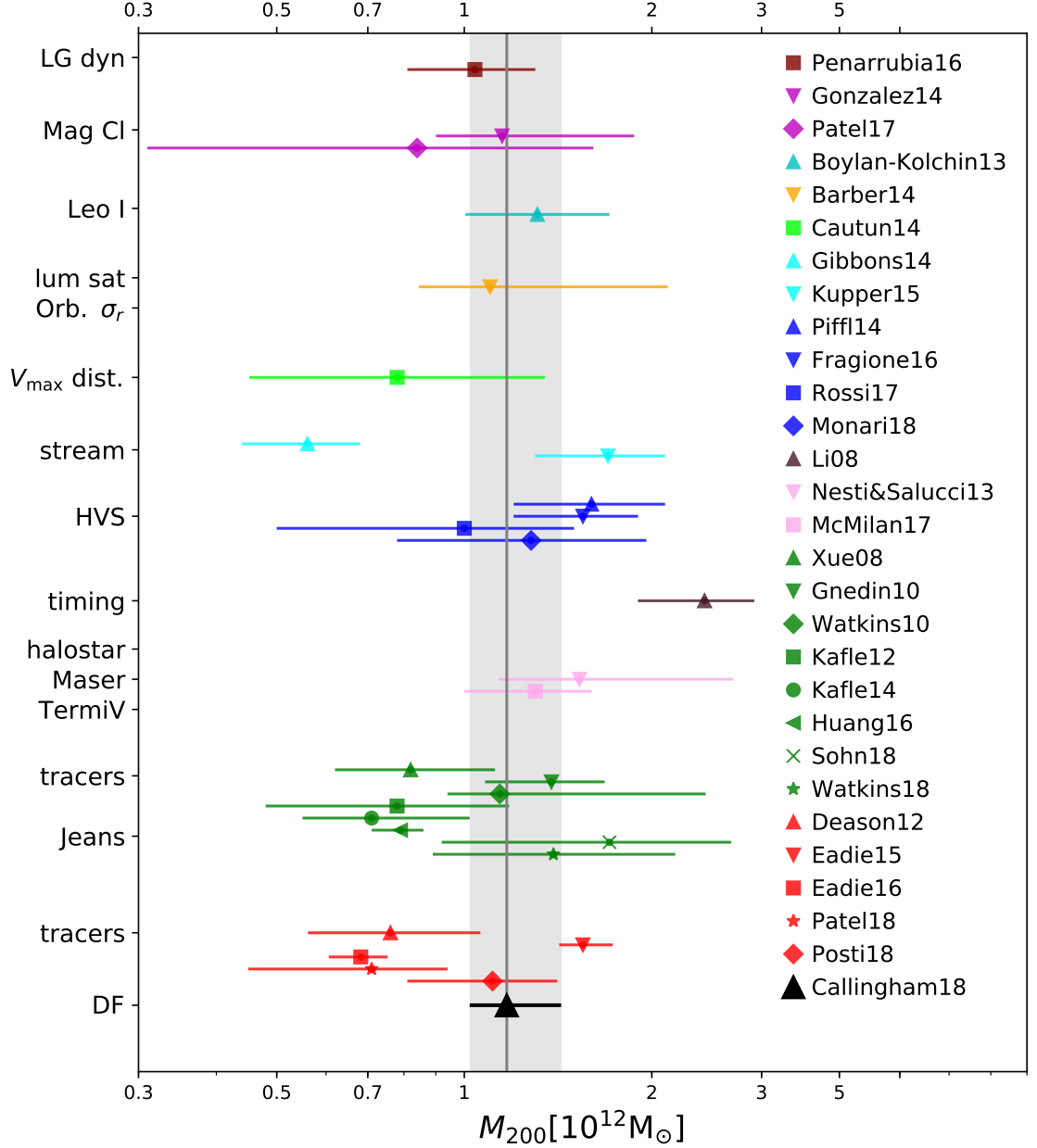
Figure 2.7

Comparison of our inferred MW halo mass with a selection of previous estimates. The vertical line and the shaded region show our M_{200} estimate and its 68% confidence limit. The remaining symbols show previous estimates (see legend), with the horizontal lines corresponding to the quoted 68% confidence limits. The results are grouped according to the methodology employed (see vertical axis). We give the mass, M_{200}, contained within R_{200} (the radius enclosing a mean density equal to 200 times the critical density). Some of the previous estimates were converted to M_{200} by assuming an NFW profile and the mean concentration predicted for that mass.

remaining two, the one based on energy only gives a slightly lower uncertainty. As we saw in Fig. 2.3, adding L data to E data does not produce an improvement in the mass determination, which is what we find here too. In fact, the (E, L) method seems to have slightly larger uncertainties than the E-only method; however, the difference is very small and not statistically significant. We also find that the estimated uncertainties in the MW mass determination are similar to the ones shown in Fig. 2.3, where we tested the methods on the EAGLE simulations. As we will see in Figures 2.10 and 2.11, the uncertainties in the mass are dominated by the small number of satellites, not by their proper motion errors.

It is important to consider possible systematics that may affect our mass determination. For example, the LMC and SMC are believed to have fallen in recently as a pair (e.g. Kallivayalil et al., 2013), and might not encode independent information about the MW halo. We have checked that discarding the SMC from our analysis does not significantly change the median estimate and leads only to a small increase in the uncertainty range. We also know that the classical satellites are atypical in at least two respects: they currently reside in a thin plane, with several orbiting preferentially within it, and they have a very low velocity anisotropy. These two properties place the MW satellite system in the tail of the ΛCDM expectations (e.g. see Pawlowski et al., 2014; Cautun et al., 2015; Cautun & Frenk, 2017). The analysis described in Appendix 2.6.4 shows that the distribution of E and L values of the Galactic satellites is, in fact, consistent with ΛCDM predictions, with no evidence for any tension.

2.4.1 Comparison to previous MW mass estimates

In Fig. 2.7 we compare our total MW halo mass estimate with a selection of results from previous studies. This figure is an update of Figure 1 in Wang et al. (2015) and includes recent estimates, especially those that use *Gaia* DR2 data. Some mass determination methods, such as ours and those based on Local Group dynamics (e.g. Li et al., 2017; Peñarrubia et al., 2016) and satellite dynamics (e.g. Watkins et al., 2010; Boylan-Kolchin et al., 2013; Barber et al., 2014; Eadie et al., 2015), give the total mass directly, but many

others, such as those using globular clusters (e.g. Posti & Helmi, 2019; Watkins et al., 2019) or halo stars (e.g. Xue et al., 2008; Gnedin et al., 2010; Deason et al., 2012; Huang et al., 2016), give the enclosed mass only within an inner region of the MW halo and require an assumption about the MW halo mass profile for extrapolation to the total mass. Despite the wide range of values quoted in the literature, our result is consistent within 1σ with the majority of previous mass estimates. Our errors are significantly smaller than those of most previous estimates and, most importantly, we have rigorously and extensively tested our method on simulated galaxies to produce an accurate, unbiased mass estimate with realistic uncertainties.

Our estimated value of $\sim 10^{12}\,\mathrm{M_\odot}$ for the MW halo mass has important implications for the interpretation of the satellite population of our galaxy, which is often used as a testbed for the ΛCDM model. For example, the "too-big-to-fail" problem (Boylan-Kolchin et al., 2011), which refers to the number of massive, dense satellites in the MW halo, is significantly alleviated. Indeed, Wang et al. (2012) showed that approximately 40% of haloes with mass $M_{\mathrm{halo}} \sim 10^{12}\,\mathrm{M_\odot}$ in ΛCDM dark matter only simulations have three or fewer subhaloes with $V_{\mathrm{max}} > 30$ km/s (the threshold used by Boylan-Kolchin et al. 2011 to define massive failures). For the MW halo mass that we infer, the "too-big-to-fail problem" is not a failure of ΛCDM.

An accurate estimate of the MW halo mass is also crucial in order to address properly the missing satellites problem. The total number of subhaloes depends strongly on the halo mass (doubling the halo mass, roughly doubles the number of subhaloes). Thus, when appealing to baryonic physics solutions to this problem, such as the influence of reionization and stellar feedback, an accurate estimate of the halo mass is a pre-requisite for a realistic model. Moreover, when the halo mass is known, the number of subhaloes may even inform us about these critical processes, such as when the epoch of reionization occured (see e.g. Figure 1 in Bose et al. 2018), or indeed about the identity of the dark matter (Kennedy et al., 2014; Lovell et al., 2014).
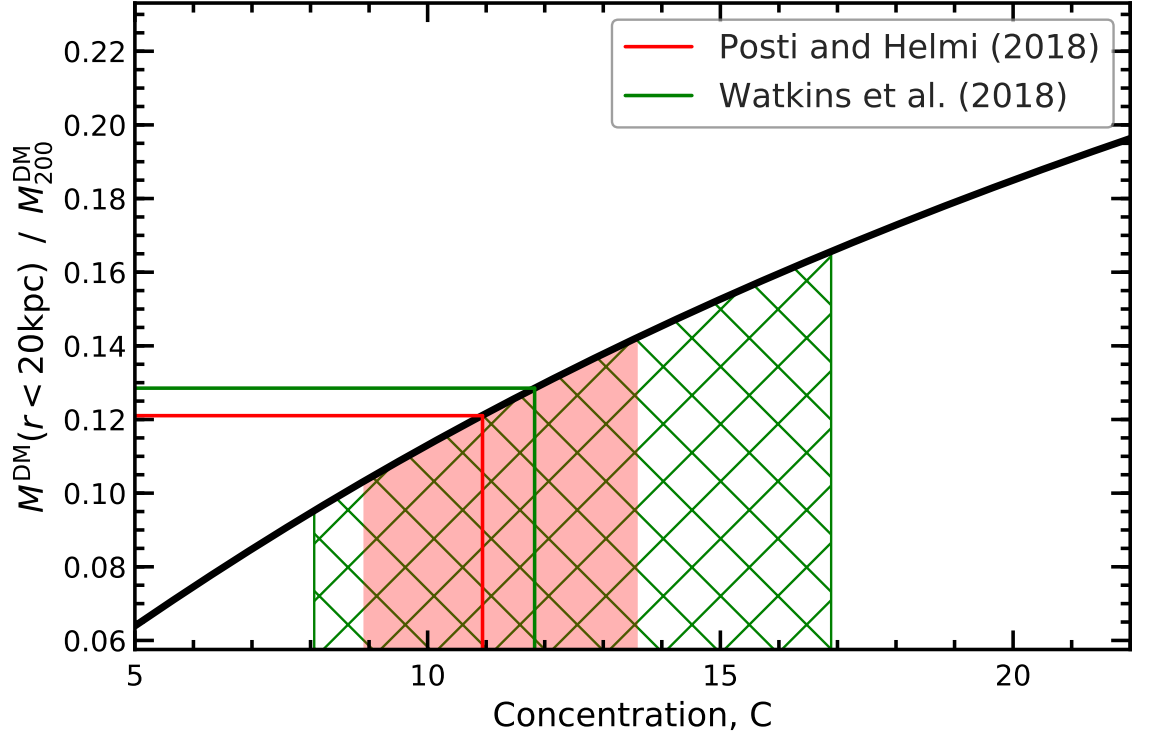
Figure 2.8

The concentration of the MW halo inferred by combining our total mass estimate with previous inner mass estimates. The solid thick curve shows the dark matter (DM) mass fraction, $M^{DM}(< 20 \text{ kpc})/\text{M}^{DM}_{200}$, contained within 20 kpc of the halo centre as a function of concentration, C, for our best estimate of a total halo mass of $M^{DM}_{200} = 1.11 \times 10^{12} M_{\odot}$. The two horizontal lines correspond to the Posti & Helmi (2019) and Watkins et al. (2019) inner mass estimates. The inferred concentrations are shown by the two vertical lines, with the shaded regions corresponding to the 68% confidence ranges. we find $C = 10.9^{+2.6}_{-2.0}$ and $C = 11.8^{+5.1}_{-3.8}$ for the Posti & Helmi and Watkins et al. inner mass estimates, respectively.

2.4.2   The concentration of the MW halo

Alongside mass, the other fundamental property of DM haloes is their concentration. Besides being one of the key parameters of the NFW profile, the concentration encodes crucial information about the halo's formation history (e.g. Wechsler et al., 2002; Lu et al., 2006; Ludlow et al., 2014) and, after halo mass, is the most important property for determining how galaxies populate haloes (e.g. Matthee et al., 2017). Our MW halo mass estimate does not depend on, nor constrain, the MW halo concentration. However, when combined with mass estimates for the inner regions of the Galaxy, we can use our mass estimate to infer the concentration of the MW halo. For this, we use inner mass
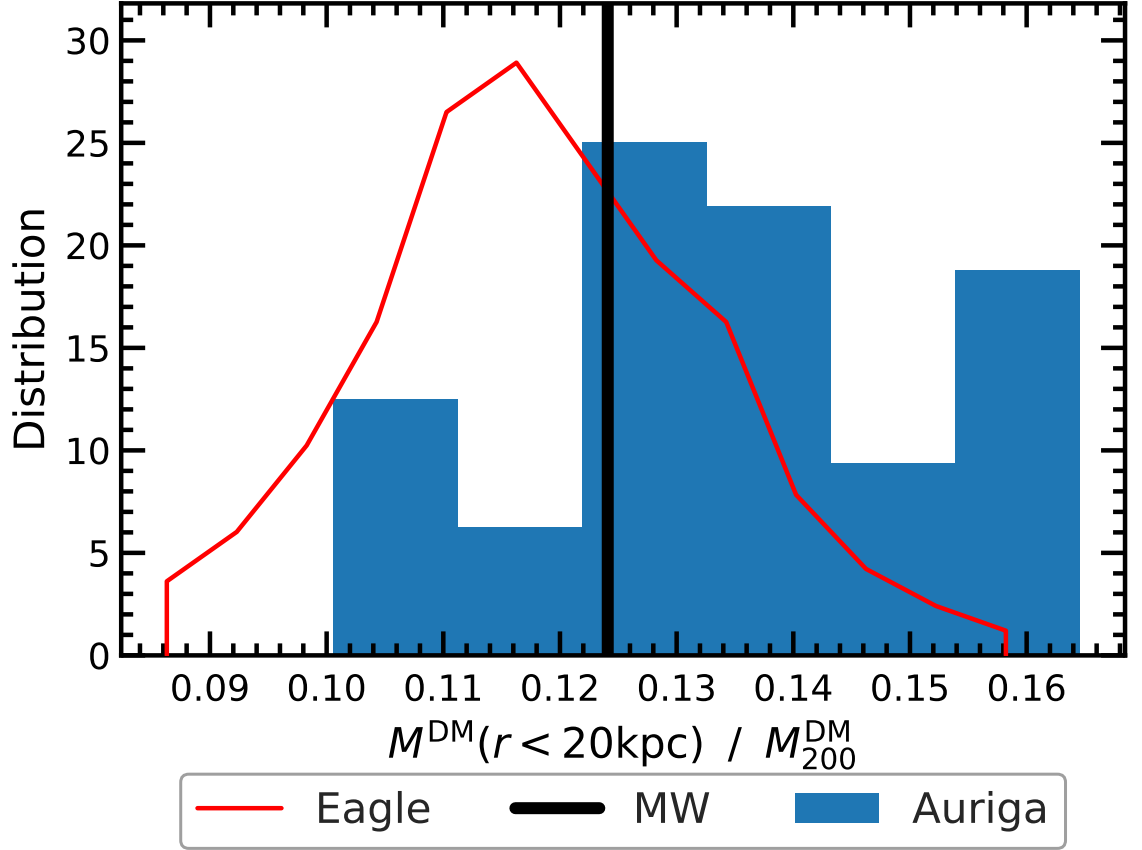
Figure 2.9

The distribution of the DM mass fraction contained within 20 kpc of the halo centre, $M^{\mathrm{DM}}(< 20\,\mathrm{kpc})/\mathrm{M}^{\mathrm{DM}}_{200}$, for MW-sized galaxies in EAGLE and AURIGA. The red line shows the distribution of systems from our EAGLE sample described in Section 2.3, whose M_{200} is within 0.2 dex of our MW mass estimate. The blue histogram gives the distribution of the 30 level 4 AURIGA systems described in Section 3.3. The thick black line shows the MW's DM mass fraction; calculated using our own MW halo mass estimate, M^{DM}_{200}, and $M^{\mathrm{DM}}(< 20\,\mathrm{kpc})$ from Posti & Helmi (2019)

determinations based on the dynamics of the globular cluster population. This population is much more radially concentrated than the satellite galaxy population, and there is a large number of globular clusters with precise *Gaia* DR2 proper motion measurements (**?**). This enabled Posti & Helmi (2019) and Watkins et al. (2019) to estimate the total mass enclosed within ∼20 kpc from the Galactic Centre with high precision.

To determine the concentration we assume that the DM distribution follows the NFW profile, which provides a very good fit to the DM density profiles in both DM-only and hydrodynamic simulations. To determine the enclosed DM mass, we subtract the MW baryonic mass, $M_{\mathrm{MW}}^{\mathrm{baryons}}$, from the total mass measurements within both 20 kpc and R_{200}. We use the McMillan (2017) estimates: a stellar mass of $5.4 \times 10^{10}\,\mathrm{M}_\odot$ and a gas mass of $1.2 \times 10^{10}\,\mathrm{M}_\odot$, which corresponds to $M_{\mathrm{MW}}^{\mathrm{baryons}} = 6.6 \times 10^{10}\,\mathrm{M}_\odot$.

Fig. 2.8 shows the fraction of DM mass enclosed within 20 kpc of the centre as a function of the halo concentration; the solid lines and shaded regions indicate the inferred concentrations and their 68% confidence ranges. The Posti & Helmi (2019) estimate gives a mass ratio, $M^{\mathrm{DM}}(< 20\,\mathrm{kpc})/M_{200}^{\mathrm{DM}} \approx 0.12$, which corresponds to a concentration of $C = 10.9^{+2.6}_{-2.0}$ (68% confidence limits), where the errors were calculated by Monte Carlo sampling of the uncertainties associated with the inner and total mass estimates. The same analysis for the Watkins et al. (2019) inner mass estimate gives $M^{\mathrm{DM}}(< 21.1\,\mathrm{kpc})/M_{200}^{\mathrm{DM}} \approx 0.20$, and a concentration, $C = 11.8^{+5.1}_{-3.8}$. To include the Watkins et al. result in Fig. 2.8, we rescaled their mass estimate to a fiducial distance of 20 kpc.

We find that the MW halo has a high concentration for its mass, with a most likely value of $C \sim 10.9$, which could suggest that the MW halo assembled early. The high MW halo concentration is supported by other studies; for example, the best fit Galaxy model of McMillan (2017) gives $C = 16 \pm 3$. In the EAGLE simulations, the median concentration of a $\sim 10^{12}\,\mathrm{M}_\odot$ halo is ∼8.2 and only ∼23% of haloes have a concentration higher than 10.9 which suggests that the MW halo is an outlier.

However, the presence of central baryonic components causes a contraction of the very inner region of $\sim 10^{12}\,\mathrm{M}_\odot$ mass haloes, increasing the total mass in the inner region. As a result, the inner region is not well described by an NFW profile, and the inferred

concentration is biased high (e.g. Schaller et al., 2015). To overcome this limitation, in Fig. 2.9 we compare the inner DM mass fraction of the MW to that of similar mass haloes in the EAGLE and AURIGA simulations and find that the MW is typical of haloes in both simulations. The systematic difference between the EAGLE and AURIGA distribution reflects the stellar mass content of those objects: compared to abundance matching results, galactic mass haloes in EAGLE have stellar masses that are too low, while equal mass haloes in AURIGA have stellar masses that are too high.

2.4.3   Improving the mass estimate

In this section we discuss the limitations of our method and ways of improving the MW mass estimate. There are two main sources of uncertainty: statistical, from the finite number of satellites; and systematic, from halo-to-halo variation. The former can be reduced by increasing the number of dynamical tracers and/or reducing observational errors, but the latter cannot be reduced.

We begin by investigating the effect of observational errors on the MW halo mass determination. The main source of observational uncertainties are the proper motion measurements. As such, we consider the effect of varying the errors, $\sigma_{\mu_\alpha}^s$ and $\sigma_{\mu_\delta}^s$, associated with the two components of the proper motion. For the MW observations these errors vary from satellite to satellite, from 0.005 mas/year for Sculptor to 0.039 mas/year for Leo II, with a median of ~0.018 mas/year. For simplicity, here we assume the same error for all satellites, that is $\sigma_{\mu_\alpha}^s = \sigma_{\mu_\delta}^s = \sigma_\mu$, and study the effect of observational errors by varying σ_μ. For each σ_μ value, we proceed by taking the current proper motions of each MW satellite and resetting their errors to the target value of σ_μ. Then, we generate a sample of Monte Carlo realizations using the procedure described in Section 2.2.2 and apply the mass estimation method.

Fig. 2.10 shows the MW halo mass estimate inferred from the (E, L) method as a function of the size of the proper motion errors, σ_μ. As we increase σ_μ, we find, as expected, that the uncertainty in the mass determination increases. However, the current proper motion
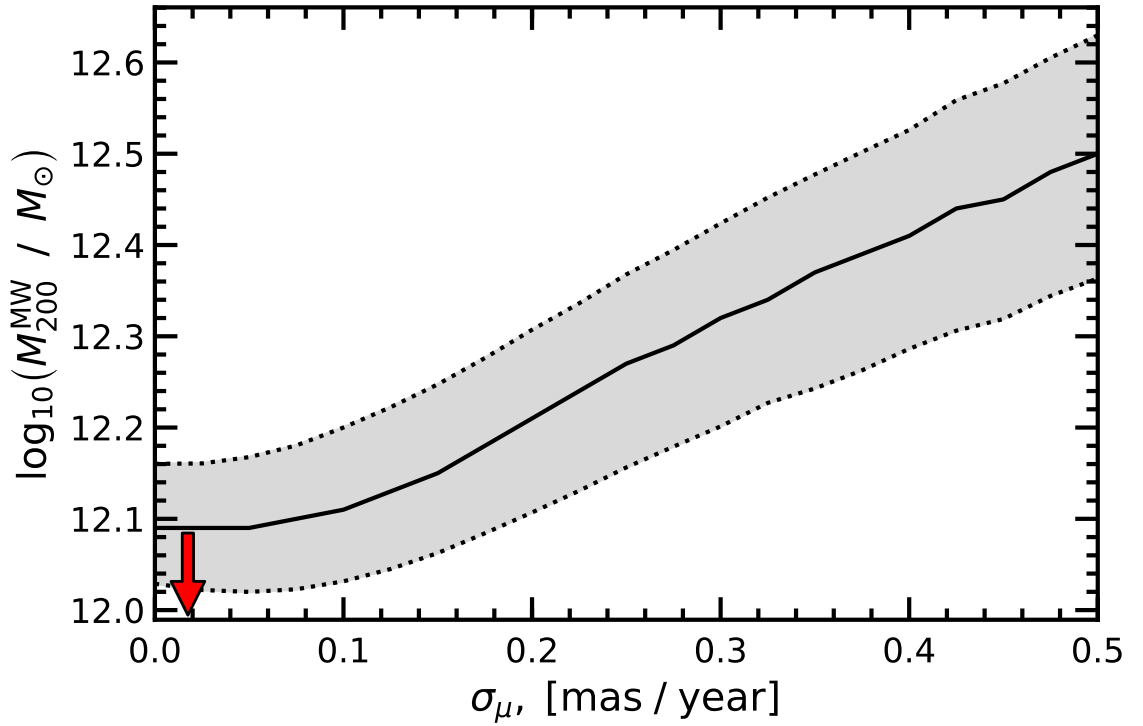
Figure 2.10

The estimated MW halo mass, M_{200}^{MW}, as a function of the size of proper motion errors, σ_μ. Results are shown only for the inference method based on both $\widetilde{E}$ and $\widetilde{L}$ values. The solid line gives the mass estimate while the shaded region shows the 68% confidence interval. Larger values of σ_μ result in more uncertain mass estimates and also in a systematic bias with respect to the true mass. The red arrow shows the median error for our sample of classical satellites.

errors for the classical satellites are so small that they fall in the region where there is hardly any dependence of the mass estimate on σ_μ. Improving the current observational errors will provide little improvement on the mass estimate.

More importantly, we also find a systematic shift in the estimated halo mass, which increases rapidly with the size of the proper motion errors. For example, for $\sigma_\mu \approx 0.35$ mas/year, the estimated mass is a factor of two too high. This comes about because large proper motion errors bias the observed velocities high, thus leading to higher energy and angular momentum values, which, in turn, lead to higher mass estimates. This is not a problem for our current estimate since all the classical satellites have proper motions errors well below 0.1 mas/year, and thus lie in the region where the mass estimate is flat. However, were we to include in the sample ultrafaint dwarf satellites, many of which have large proper motion errors (e.g. Fritz et al., 2018), then we would need to account for the additional bias introduced by the observational errors.

The MW is predicted to have approximately 125 satellites brighter than $M_V = 0$, of which just over 50 have already been discovered (Newton et al., 2018). This means that, in principle, many more satellites can be used to determine the MW halo mass, potentially with a smaller uncertainty. Fig. 2.11 quantifies how the uncertainty in halo mass is reduced as the number of satellite galaxies in the sample increases. Here, we consider the simplified case where there are no observational errors and focus only on the variation arising from the number of tracers, N_{Tracers}.

Using the same sample of EAGLE main haloes as in Section 2.2.3, we determine the host halo mass using the most massive N_{Tracers} subhaloes. To obtain large enough tracer counts in EAGLE, we relax the criteria and consider not only luminous satellites, but also dark subhaloes. Many of these would be the hosts of the ultrafaint dwarfs, but EAGLE lacks the resolution to populate them with stars. However, these dark substructures are well resolved and their orbital properties are reliable. To estimate an average error for each value of N_{Tracers}, we calculate the dispersion in the distribution of $\log_{10}(M_{200}^{\mathrm{Esti}}/M_{200}^{\mathrm{True}})$: the logarithm of the ratio of estimated to true mass. To ensure accurate measures of the average error, we require at least 100 systems that have N_{Tracers} or more tracers; this limits
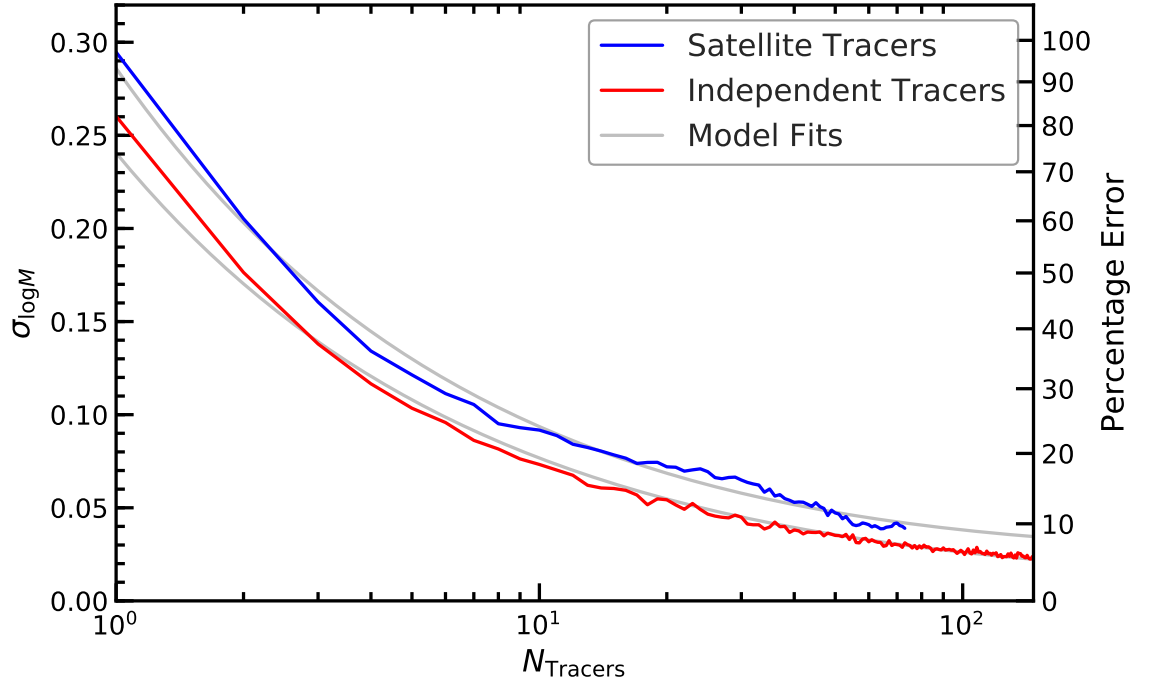
Figure 2.11

The 1σ uncertainty, $\sigma_{\log_{10} M}$, with which we can determine the logarithm of the halo mass as a function of the number of satellite galaxy tracers, N_{tracers}, included in the sample. We show the mean uncertainty for a large number of EAGLE haloes whose mass was determined using the E and L values of their most massive N_{tracers} satellites. The right-hand axis shows the percentage errors in M_{200} corresponding to the $\sigma_{\log_{10} M}$ values. The blue line gives the results using the satellites of EAGLE galaxies. The red line gives the results from idealised cases of independent satellite tracers (see main text) and represents the statistical limit of our method. The two grey lines show the best fitting curves using Eq. (2.4.1).

our analysis to $N_{\text{tracers}} \leq 72$.

The blue line in Fig. 2.11 shows that the expected error in our mass estimate, $\sigma_{\log_{10} M}$, decreases as the number of tracers increases. We would expect that above a certain number of tracers, the mass determination does not improve any more because the error becomes dominated by halo-to-halo variation and systematic effects such as correlations between the kinematics of different satellites (see e.g. Wang et al., 2017, 2018).

To investigate these effects, we construct idealised systems by selecting N_{Tracers} satellites from our samples' DF, $F(\widetilde{E}, \widetilde{L})$, and then scale them to the mass of random host haloes selected from our sample. This gives us a population of systems whose satellites are perfectly described as being independently drawn from our distribution. As an additional advantage, we are not limited to $N_{\text{Tracers}} \leq 72$, and can continue increasing N_{Tracers} as $\sigma_{\log_{10} M}$ asymptotes to zero (Fig. 2.11, red line). The difference between the errors in the two samples is the error due to halo-to-halo scatter, σ_{Scatter}. The dependence of the total error, $\sigma_{\log_{10} M}$, on N_{Tracers} can be modelled as (cf. Li et al. 2017):

$$\sigma^2_{\log_{10} M} = \frac{\sigma^2_{\text{Stat}}}{N_{\text{Tracers}}} + \sigma^2_{\text{Scatter}} \; . \tag{2.4.1}$$

The mass error for the true EAGLE satellite systems is best fitted by $\sigma_{\text{Stat}} = 0.29$ and $\sigma_{\text{Scatter}} = 0.03$, while the error for the idealized systems of independent tracers is best described by $\sigma_{\text{Stat}} = 0.24$ and $\sigma_{\text{Scatter}} = 0.01$. We note that a scatter error, $\sigma_{\text{Scatter}} = 0.03$, equates to an accuracy limit of around 5% and would represent the best mass measurement of the method in the limit of a very large number of tracers. For 10 satellite tracers we obtain a $\sim 20\%$ uncertainty, similar to our MW mass estimate, while the idealised mass estimates give a slightly smaller uncertainty of $\sim 16\%$. The fits suggest that a $\sim 10\%$ determination of the MW mass is achievable by applying our method to around $N_{\text{tracers}} \approx 60$ tracers. The accuracy of our halo mass measurement could be further improved by considering the dependence of the satellite dynamics on the properties and assembly history of the host halo. It is conceivable that by restricting the analysis to a subset of haloes that more closely resembles the MW, such as haloes with a similar assembly history, the halo-to-halo variation could be reduced, leading to an even more precise halo mass determination.

However, at present, the largest benefit would accrue from increasing the number of tracers.

2.5   Conclusions

We have developed a method to determine the total mass of the Milky Way (MW) dark matter (DM) halo by comparing the energy and angular momentum of MW satellites with the respective distributions predicted in the EAGLE galaxy formation cosmological simulations. When scaled appropriately by host halo mass, the energy and angular momentum of the satellites become independent of the host halo mass (see Fig. 2.12). Thus, we can use a large sample of EAGLE haloes, and associated satellites, in our estimate of the MW halo mass. For this, we constructed the satellite distribution function in (E, L) space from the simulations and carried out a maximum likelihood analysis to infer the halo mass from the phase-space properties of the ten brightest satellite galaxies (excluding the disrupting Sagittarius galaxy). Using mock samples from EAGLE we analysed the performance of the method and quantified its statistical and systematic uncertainties.

A key test of our method was to apply it to estimate the masses of the DM haloes of 30 MW analogues simulated in the AURIGA project. These simulations have much higher resolution and employ different baryonic physics models than EAGLE. They produce realistic MW-like galaxies (Grand et al., 2017) and thus provide a rigorous and completely independent external test of our method. We find that our method provides an unbiased estimate of the total halo masses of the AURIGA galaxies, with a precision of $\sim 16\%$, in very good agreement with the expectations from the EAGLE simulations.

Later studies (such as Erkal et al., 2019, 2021) now suggest that the LMC is now generally excepted to be more massive (now around $\sim 1.5 \times 10^{11}$ M$_\odot$) than was believed at the time of the original publishing of this work. The LMC is likely to have affected the dynamics within the MW (such as Cunningham et al., 2020), and it is feasible that this will also apply to the dynamics of the satellite population. Furthermore, this LMC mass suggests that over 10% of the MW's mass is within substructures, violating the selection criteria in Sec 2.2.3. The potential effects and biases of such a large LMC on our methodology

will be the subject of future studies, utilising constrained zoom-in simulations that contain LMC analogues interacting with MW-like galaxies. We note that in this work, we find that the maximum likelihood of our classical satellites is typical of our mock tests, and the results of our methods using only angular momentum or energy are consistent with each other. This suggests that, at the very least, the dynamics of our satellite population is not significantly distinguishable from the likely norm.

Our main conclusions are:

- Applying our method to ten classical MW satellites gives an estimate for the total mass of the MW halo of $M_{200}^{\mathrm{MW}} = 1.17_{-0.15}^{+0.21} \times 10^{12} M_{\odot}$. This result agrees well with most previous estimates in the literature but with a rigorously tested accuracy ($\sim 15\%$) which is better than most other estimates.

- Combining our total DM halo mass estimate with recent estimates of the halo mass within $20\,\mathrm{kpc}$ gives an inner DM mass fraction, $M^{\mathrm{DM}}(< 20\,\mathrm{kpc})/M_{200}^{\mathrm{DM}} \approx 0.12$. Assuming that the MW halo follows an NFW profile, we have inferred a Galactic concentration, $C = 10.9_{-2.0}^{+2.6}$. This is higher than typical EAGLE haloes with masses of $10^{12} M_{\odot}$, which have a median concentration of 8.2, with only $\sim 23\%$ of them having concentrations of 10.9 or higher. The discrepancy likely reflects that an NFW profile is not a good description of the inner region since the Galactic halo has contracted due to the baryonic components. In fact, when comparing the inner DM mass fraction of the MW against the EAGLE and AURIGA simulations, our galaxy is typical of similar mass haloes.

- Our halo mass estimate can be improved by increasing the number of halo tracers and/or reducing the observational uncertainties. We found that the observed proper motions of the ten classical satellites are already so precise that further improvement will make little difference to the halo mass estimate. Increasing the number of satellites, on the other hand, for example by including the ~ 50 currently known satellites in the MW, would reduce the mass errors to $\sim 11\%$. Further improvements would be possible by analysing all ~ 125 satellites that are predicted to reside in the

MW (Newton et al., 2018), which would result in a ∼8% mass uncertainty, a factor of two improvement over our current estimate.

In summary, our MW halo mass estimate is precise and accurate and has been thoroughly tested on realistic model galaxies and their satellite populations. Mass estimates that rely on cosmological simulations are relatively new but the use of simulations enables a robust and testable methodology. Indeed, the accuracy we are now able to achieve ($\sim 15 - 20\%$; see also Patel et al. 2018) is a significant step forward from the factor of two uncertainty that has plagued MW mass estimates for years. This theoretical boost, coupled with the exquisite 6 dimensional data that *Gaia* and complementary facilities are now providing, brings us closer to what may be called the era of "precision" near-field cosmology — when we can go beyond rough estimates of the MW halo mass and, instead, remove this important degree of freedom when making use of the properties of the MW to inform cosmological models and dark matter theories.

2.6 Appendix

2.6.1 Probability distributions

Here we give a short summary on how to calculate the PDF of one variable that is a function of one or more variables with known PDFs. In our case, we want to know the PDF of M_{200} given the distributions of either scaled angular momentum, scaled energy, or both scaled angular momentum and energy.

The PDF, $p(u)$, of a variable u which is a function of x, is given by:

$$p(u) = p(x) \left| \frac{\mathrm{d}x}{\mathrm{d}u} \right| \,, \tag{2.6.1}$$

where $p(x)$ is the probability of variable x and where the derivative corresponds to the Jacobian of the transformation. In our case, the variable u corresponds to the host halo mass, M_{200}, while x corresponds to either the scaled angular momentum, $\widetilde{L}$, or the scaled

energy, $\widetilde{E}$. Replacing these variables into Eq. (2.6.1), we obtain Eqs. (2.3.2) and (2.3.3), that is:

$$p(M_{200}|\mathbf{x}^s) = F_E(\widetilde{E}) \left. \frac{\partial \widetilde{E}}{\partial M_{200}}\right|_{\widetilde{E}=\widetilde{E}^s}, \qquad (2.6.2)$$

$$p(M_{200}|\mathbf{x}^s) = F_L(\widetilde{L}) \left. \frac{\partial \widetilde{L}}{\partial M_{200}}\right|_{\widetilde{L}=\widetilde{L}^s}. \qquad (2.6.3)$$

To constrain M_{200} using both $\widetilde{E}$ and $\widetilde{L}$ we can extend Eq. (2.6.1) to the two-dimensional case. To do this, we approximate the two-dimensional expression by combining the two one-dimensional cases. If the $\widetilde{E}$ and $\widetilde{L}$ variables would be independent then we could just multiply the right-hand side terms of Eqs. (2.6.2) and (2.6.3). However, that is not the case, so we need to take the joint probability, $F(\widetilde{E}, \widetilde{L})$. Furthermore, we also need to obtain the correct units, which we achieve by adding an extra M_{200} factor. Putting everything together, we obtain Eq. (2.3.4), that is

$$p(M_{200}|\mathbf{x}^s) = F(\widetilde{E}, \widetilde{L}) \, M_{200} \left. \frac{\partial \widetilde{E}}{\partial M_{200}} \frac{\partial \widetilde{L}}{\partial M_{200}}\right|_{\widetilde{E}=\widetilde{E}^s, \, \widetilde{L}=\widetilde{L}^s}. \qquad (2.6.4)$$

Note that this result is not exact, but is supported by empirical numerical evidence. We performed extensive tests of the three likelihoods, Eqs. (2.6.2)-(2.6.4), to find that they give very robust estimates of the total mass of haloes. The later work of Li et al. (2020) found an exact solution to a similar problem by transforming from the probability density in energy – angular momentum space to position – velocity space (see paper for further details).

2.6.2   Mass dependence of scaled energy and angular momentum

Here we test the host halo mass independence of the scaled energy and angular momentum of satellites. We take all the luminous satellites in the EAGLE simulation and scale their orbital energy and orbital angular momentum according to Eq. (2.2.5), that is $\propto M_{200}^{2/3}$, where M_{200} is the host mass. The resulting distributions are shown in Fig. 2.12.

We find that, to a very good approximation, the distributions of $\widetilde{E}$ and $\widetilde{L}$ are indeed the same over at least two orders of magnitude in host mass. There are a few small departures
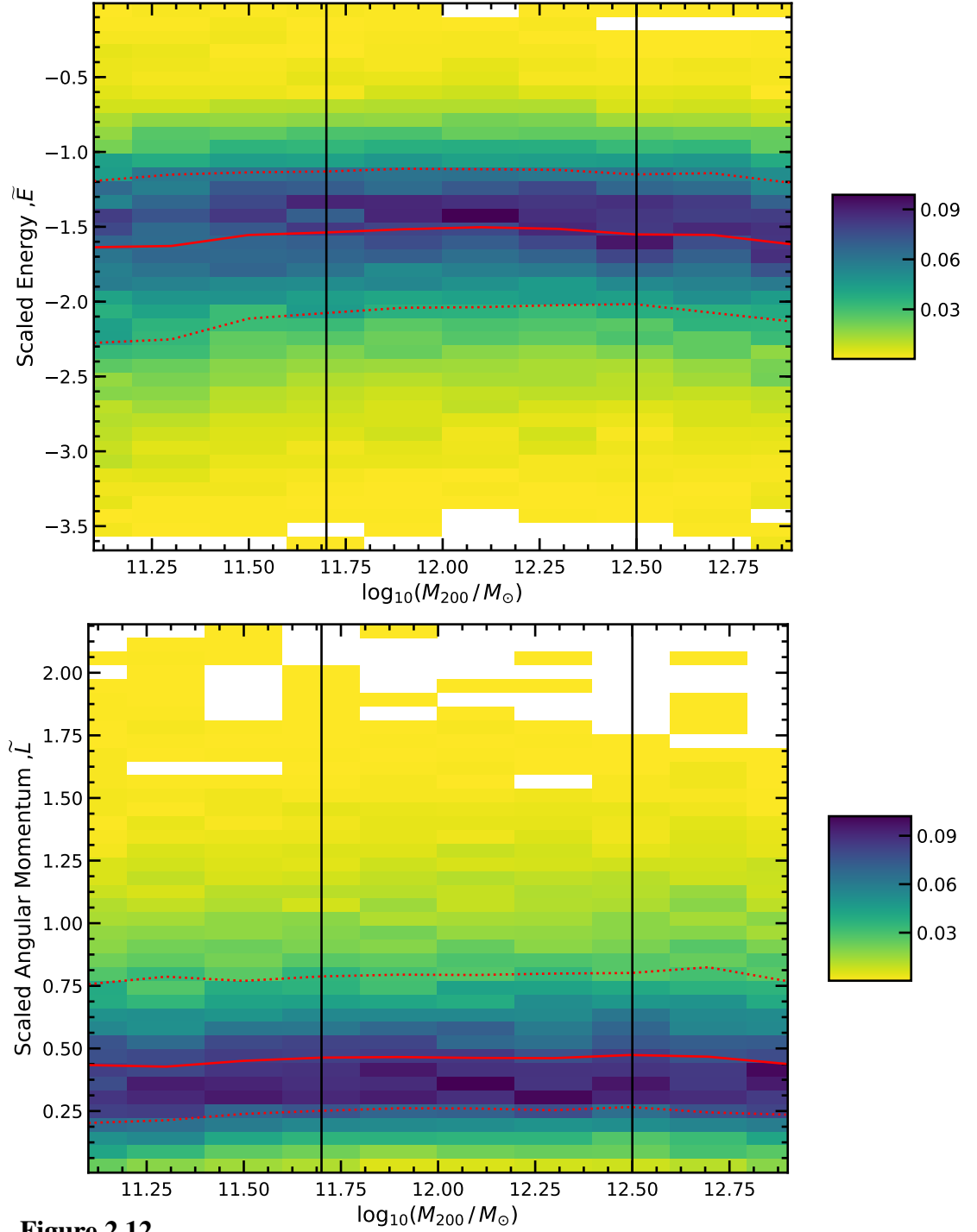
Figure 2.12

The dependence on host halo mass, M_{200}, of the scaled energy, $\widetilde{E}$ (top panel), and scaled angular momentum, $\widetilde{L}$ (bottom panel), of EAGLE satellites. The colour scale shows the density of points, with darker colours corresponding to higher density regions. The distribution is column normalised to each mass bin to allow easy comparison. The solid lines show the median values as a function of M_{200}, while the dotted lines show the 16 and 84 percentiles of the distribution. The two vertical lines delineate the mass range used in our analysis. The plots show that scaling the energy and angular momentum by $M_{200}^{-2/3}$ leads to quantities that are independent of M_{200} to a very good approximation.
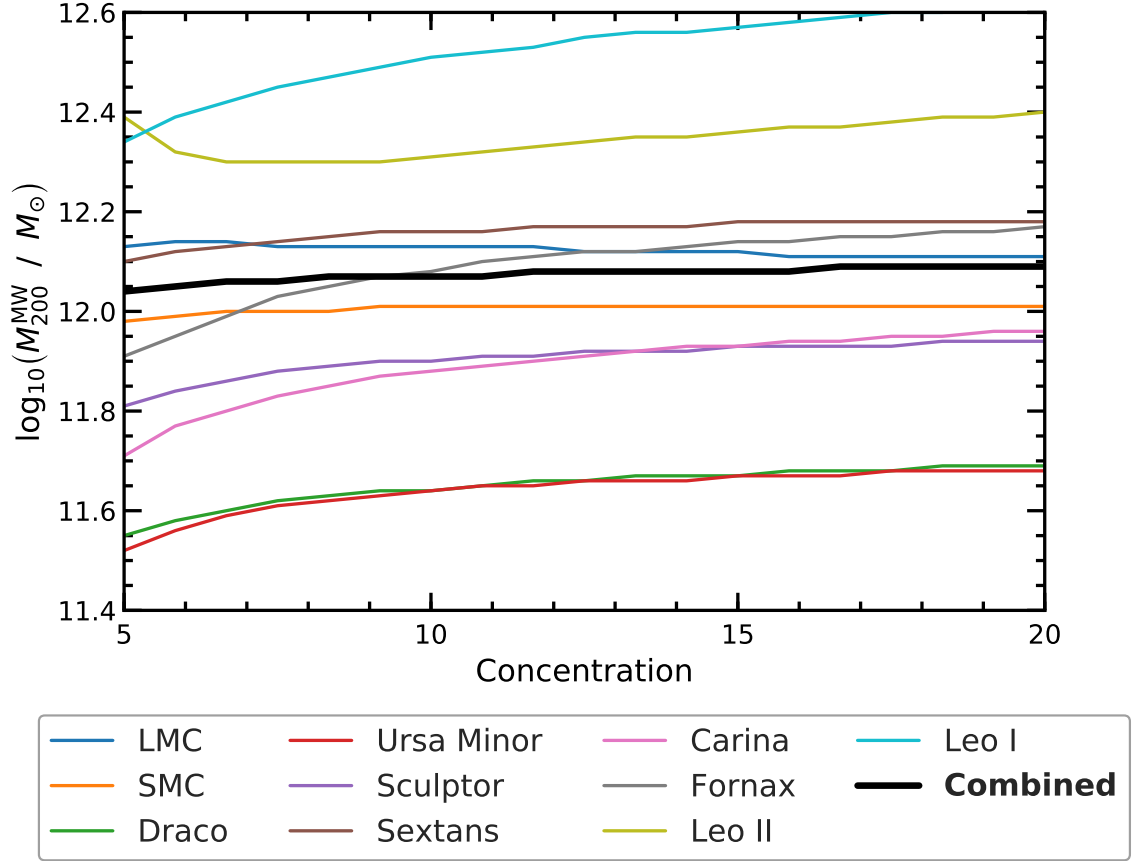
Figure 2.13
The MW total mass estimate, M_{200}^{MW}, as a function of the assumed concentration of the MW halo. The coloured lines show the mass estimates from individual satellites and the black solid line shows the combined mass estimate. There is a very weak dependence on concentration — this is especially true for the combined mass estimate, which remains flat over a wide range of halo concentration.

from universality, especially for low halo masses. This could be a manifestation of the limited resolution of EAGLE, which resolves only a small fraction of the brightest satellites of $10^{11.2}\,\mathrm{M}_\odot$ haloes. However, this small departure from universality does not affect our results since this work is based on hosts with masses in the range $10^{11.7}\,\mathrm{M}_\odot$ to $10^{12.5}\,\mathrm{M}_\odot$, which corresponds to the region between the two vertical lines in Fig. 2.12.

2.6.3   Dependence on concentration

In Fig. 2.13 we show how the MW halo concentration affects our mass estimate. Note that in our method (described in Section 2.3) we marginalise over the concentration parameter. The coloured lines show the mass estimates from individual satellites and the thick black

line the combined mass estimate as a function of the assumed halo concentration. In general, the concentration makes little difference to our estimated masses — this is especially true for the combined mass estimate, which remains flat over a wide range in halo concentration. While not shown, we also find that the maximum likelihood values are largely independent of the assumed concentration. Thus, the 10 classical satellites studied here cannot, on their own, constrain the MW halo concentration. However, as we show in Section 2.4.2, we can estimate the concentration of the MW halo by combining our total halo mass estimate with determinations of the halo mass in the inner regions of the Galaxy.

2.6.4 Distribution of maximum likelihoods

The MW classical satellites have at least two atypical properties: (i) they are distributed on a thin plane with many of the satellites rotating within this plane, and (ii) the satellites have a very low velocity anisotropy indicative of circularly biased orbits. These two characteristics place the MW satellite system in the 5% and 2% tails of the ΛCDM predictions (Cautun et al., 2015; Cautun & Frenk, 2017). This raises the concern that the satellites may also be atypical in terms of their energy or angular momentum distributions. If so, this could lead to biases or untrustworthy MW mass estimates using our method.

A straightforward way to test for this is to compare the maximum likelihood value for the MW with the corresponding values for a large sample of ΛCDM haloes. This is shown in Fig. 2.14, where we plot the distribution of maximum likelihood values for the EAGLE and AURIGA mock satellite systems. We find very good agreement between the EAGLE and AURIGA mocks and, more importantly, the value for the MW lies in the central region of the ΛCDM expectation. This indicates that we can find a range of M_{200} values for the Galactic halo for which the classical satellites have energy and angular momentum values that are fully consistent with the ΛCDM predictions.
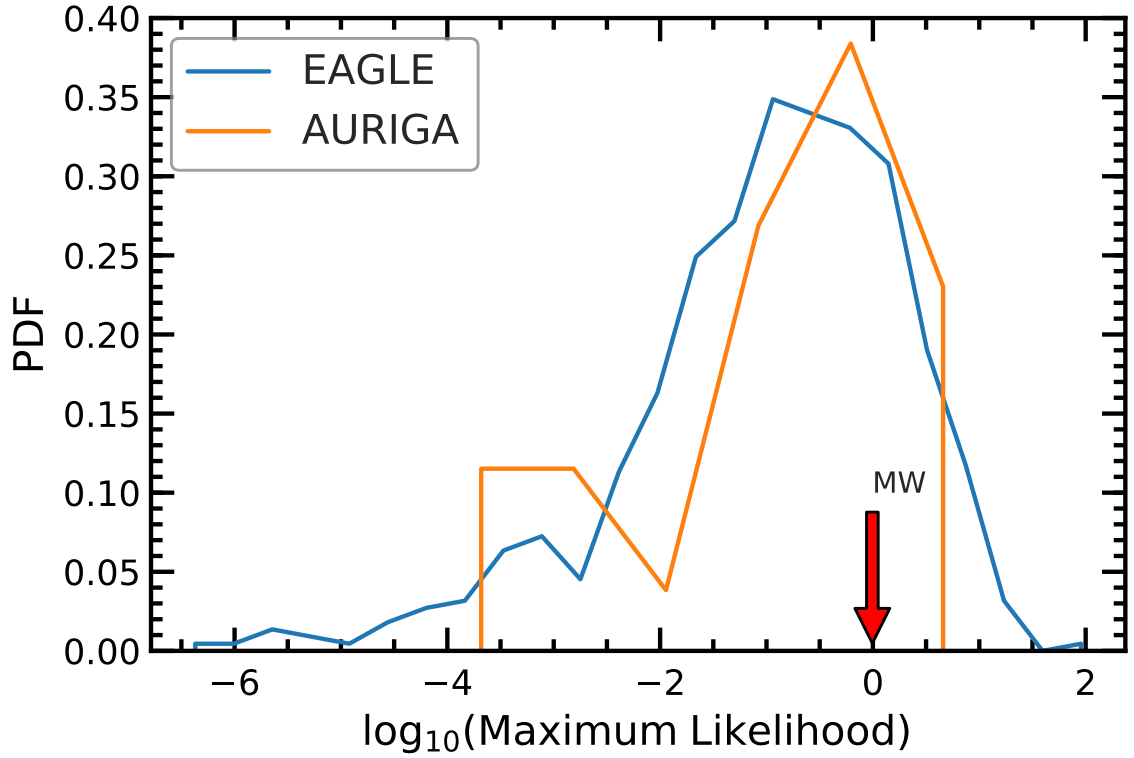
Figure 2.14

The distribution of maximum likelihood values for the mass determination method based on the energy and angular momentum of satellites. We show results for a sample of ~2500 EAGLE systems and for the 30 AURIGA haloes which have a higher resolution and different galaxy formation models than EAGLE. The downward pointing arrow shows the maximum likelihood corresponding to the MW mass determination, which is fully consistent with the EAGLE and AURIGA distributions. This indicates that the MW is not an atypical system in terms of its satellites' energy and angular momentum, and thus we can trust our MW mass determination.

CHAPTER 3

The orbital phase space of contracted dark matter halos

3.1   Introduction

In 'dark matter only' simulations (DMO), it is well known that DM haloes are universally well fit by the NFW profile. This conformity of halos in DMO simulations is broken when baryonic physics are included in fully hydrodynamical simulations (hereafter 'Hydro'). Such simulations include many of the physical processes thought to be important in the formation of galaxies, they thus have a much more complex and rich behaviour than their DMO counterparts. In particular, gas cools and condenses at the halo centre, where it forms stars. This results in DM halos that have higher central densities than a NFW profile, and that are often referred to as having been "contracted". The amount of DM contraction depends on many factors including the mass of the central galaxy, its assembly history and the orbital distribution of DM particles (e.g. Gnedin et al., 2004; Abadi et al., 2010; Duffy et al., 2010; Schaller et al., 2016; Dutton et al., 2016; Artale et al., 2019; Barnes & White, 1984; Blumenthal et al., 1986).

DM halos cannot be observed directly, of course, but some of the properties of the MW

halo can be inferred from observations of tracers of the gravitational potential. The latest *Gaia* data release (DR2) (**?**) provides a remarkable database of full 6D phase-space measurements of stars in the inner regions of the MW. Combined with other datasets, such as SDSS (Abolfathi et al., 2018) and APOGEE (Majewski et al., 2017), the *Gaia* data have been used to place tight constraints on the MW's circular velocity curve (Eilers et al., 2019) and local escape velocity (Deason et al., 2019a, e.g.), and thus have helped constrain the total mass distribution of the MW. The simplest models of the MW assume that the DM halo can be described as an NFW profile. Far from the Galactic Centre, this is a reasonable assumption for the total mass profile (Callingham et al., 2019, hereafter, Callingham19). However, to model the inner regions of our galaxy it is essential to include the mass distributions of its baryonic components such as the thin and thick disks, the bulge and the stellar halo (e.g. McMillan, 2011, 2017). Previous studies (e.g. Deason et al., 2012; McMillan, 2017) have typically found a high halo concentration ($\sim 11 - 12$), which is unusually large compared to the predictions for MW sized halos from cosmological simulations (typically ~ 8 in the EAGLE cosmological simulation; Schaller et al. 2016). This could be a symptom of the neglect of the contraction of the DM halo and underlines the importance of properly accounting for the changes in the DM distribution induced by the baryonic distribution (e.g. see Cautun et al., 2020).

Several methods have been developed to predict the contracted DM halo profile in the presence of baryons. The simplest are different versions of the adiabatic contraction approximation which assumes that particle orbits are adiabatic invariants (Eggen et al., 1962; Barnes & White, 1984). An early example of this approach Blumenthal et al. (1986) effectively assumes that all particles are on circular orbits, a rather crude approximation that leads to excessive compression of the orbits. This method was improved by Gnedin et al. (2004, 2011), who modified it to take into account that DM particles are typically on non-circular orbits. However, these improved versions neglect the fact that DM particles have a distribution of orbits. Cautun et al. 2020, (hereafter, Cautun19) have studied the contraction of DM density profiles in the EAGLE and AURIGA simulations and derived an analytic prescription for the average halo contraction; their approach is unbiased and

recovers the profiles of DM halos in hydro simulations with an accuracy of $\sim 10\%$ that reflects the halo-to-halo scatter.

While these methods are easy to apply, they neglect important information and provide only limited understanding. To model the effects of contraction properly it is necessary to consider the complex dynamics within the DM halo. While often viewed as static profiles, halos are made up of particles moving on various orbits (Zhu et al., 2017) that conspire to give a steady density profile. For a halo in equilibrium it follows from the Jeans theorem that the distribution of the DM particles is solely dependent on integrals of motion (IoM), with no dependence on phase. The halo can therefore be described as a collection of orbits defined by IoM instead of particles. The natural choice for this description are the action integrals $[J_i]_{i=1,2,3}$. One significant advantage that the actions have over other IoM is that they are adiabatic invariants, and thus largely unchanged by sufficiently slow changes in the potential (Binney & Tremaine, 2008).

The distribution function (DF) of DM particle actions, $F(\mathbf{J})$, can be thought of as an orbital blueprint of DM halos that may be use to calculate various halo properties, such as the density and velocity anisotropy profiles. If the growth of the baryonic component is a slow, adiabatic process, then the DM halo is described by the same $F(\mathbf{J})$ as in the absence of baryons, i.e. as in DMO simulations. Given this adiabatic assumption, the differences between halos in DMO and Hydro simulations is induced solely by the deeper gravitational potential of the baryons which are more centrally concentrated in the Hydro than in the DMO simulations. While the halos are composed of DM particles on orbits with the same $\mathbf{J}$ values, the deeper potential compresses the DM orbits to lower radii in physical space, resulting in a higher central density in the Hydro simulations.

The extent to which the adiabatic assumption holds is unclear and depends on the timescale on which the baryons cool and accumulate at the centre. If the cooling timescale is shorter than the free-fall timescale, then the gas undergoes rapid cooling, a non-adiabatic process. Alternatively, if the cooling timescale is much larger than the free-fall timescale, the growth of the baryonic component is adiabatic. There is evidence from analytic arguments (White & Frenk, 1991) and simulations (e.g. Correa et al., 2018) that the MW mass halos are

in the slow cooling regime. Once the baryons have settled in the centre of the halo in a quasi-hydrostatic state they dominate the central gravitational potential. Subsequent violent events, such as gas blowouts, can change the inner mass profile rapidly over short timescales, transferring energy to DM particles in the central region of halos. For halos that host dwarf galaxies, this process could form cores in their DM distribution (e.g. Navarro et al., 1996; Pontzen & Governato, 2012; Benítez-Llambay et al., 2019; Burger & Zavala, 2019).

To perform action angle modelling it is necessary to chose a specific DM action distribution function, $F(\mathbf{J})$. Typically and, in particular, for isolated DMO halos, the DF is derived analytically, often assuming that the DM particle orbits have an isotropic velocity distribution. Under the adiabatic assumption, these orbits can then be combined with a given baryon potential to construct a contracted DM halo. This approach was tested by Sellwood & McGaugh (2005) against N-body simulations that included a slowly grown analytic baryonic component. By using simple action DFs, Sellwood & McGaugh found that radially biased halos resist compression while isotropic distributions end up more compressed (in agreement with the results of Gnedin et al. 2004). In the past decade there have been significant technical advances in the numerical calculation of action angles and in the overall modelling framework (Vasiliev, 2019). More complex action DFs, including one that produces an approximate NFW density profile in isolation, were analytically derived by Posti et al. (2015) and used in a series of papers of increasing complexity, in which the MW is modelled with multiple baryon components (Piffl et al., 2015; Binney & Piffl, 2015). In the most recent study, by Cole & Binney (2017), the DF of Posti et al. was modified assuming a non-adibiatic, baryon driven upscattering of low action orbits, generating a cored DM profile.

Action angle modelling of halos is frustrated by the lack of a standard NFW action distribution; currently there is no well established $F(\mathbf{J})$ model that has been rigorously tested in cosmological simulations. The scatter in DM halo properties, such as concentration and velocity anisotropy (Navarro et al., 2010), adds further complexity to the task of paramaterising a general action DF of a DM halo. This scatter likely causes halos described by

different DFs to undergo different amounts of contraction for a given baryonic profile; it is therefore important to capture the variation with an accurate and flexible parametrisation of the DF. An alternative approach is to use DFs that are directly measured in simulations, especially given the recent increase in the resolution and number of zoom-in simulations of MW mass halos (e.g. Fattahi et al., 2016; Sawala et al., 2016; Grand et al., 2017; Garrison-Kimmel et al., 2017).

In this Chapter, we determine the distribution function, $F(\mathbf{J})$, of DM halos from the AURIGA simulation suite. This allows us to infer accurate DM DFs and, at the same time, sample the breadth of halo-to-halo scatter in cosmologically representative samples of MW-mass halos. Each simulation volume has a DMO and a Hydro simulation. By comparing the halos in one to their counterparts in the other, we can investigate the validity of the *ansatz* that the formation of MW-like galaxies is an adiabatic process. To do so, we first discuss how a halo's density and velocity profiles can be inferred from the action DF, and then test if the halo in the Hydro simulation (hereafter, Hydro halo) can be recovered by adiabatically contracting the DF measured in the corresponding DMO simulation (hereafter, DMO halo).

We illustrate the usefulness of modelling DM halos with an action DF by a few applications targeted at our Galaxy. Our approach has implications beyond the mass profile since it provides accurate predictions for the DM velocity distribution and its moments. Since we use the observed baryonic component of the MW, these predictions are specific to our galaxy and unmatched by conventional approaches. We illustrate this by predicting the density and velocity distribution function (VDF) of DM particles in the Solar neighbourhood, key inputs for direct DM detection experiments (Green, 2010, 2017). In the literature, the VDF is usually given by the standard halo model (SHM), a isothermal DM mass distribution with a Gaussian VDF; however, high-resolution N-body simulations indicate a somewhat different VDF (Vogelsberger et al., 2009). In principle, there is a variety of possible DM DFs, which, in turn, would result in a variety of VDFs at the Solar neighbourhood (e.g. Mao et al., 2013). The sizeable sample of halo DFs that we can measure in the AURIGA simulation suite allows us to characterise the dispersion in the predicted VDF at the Sun's

location, and thus quantify some of the uncertainties in direct DM detection experiments.

The structure of the Chapter is as follows. In Section 3.2 we introduce our sample of halos and compare physical profiles and orbital distributions in the DMO and Hydro cases. In Section 3.3, we construct individual orbits, investigate the effects of compression and develop an iterative method for constructing and contracting physical halos. We apply this to halos in our sample and study the effects of adiabatic contraction in general. In Section 3.4 we contract our halo sample according to the MW baryon distribution and present our main results, including predictions for the properties of the MW's local DM distribution. Finally, in Section 3.5 we summarise our main conclusions.

3.2   Simulated halos

In this Chapter we use a sample of halos from the AURIGA project, a halo. We primarily use the level 4 resolution sample of 30 halos, which we label as Au1 to Au30. In our analysis we treat the halos as being in near spherical equilibrium. The criteria of Neto et al. (2007) identify 13 out of the 30 AURIGA halos as unrelaxed in either the Hydro or the DMO simulations. These halos are included in our sample in order to investigate the dependence and sensitivity of our analysis to departures from equilibrium. Typically, the halos relax from the inside out, and the halo outskirts (approximately around and beyond R_{200}) are the least virialised and phase mixed regions. We have checked that most of the relaxed AURIGA halos are reasonably spherical, especially in the inner regions. For example, the DM particles within $R_{200}/2$ are characterised by the moment of inertia with minor-to-major axes ratio, c/a, of $0.76^{+0.08}_{-0.03}$ in the DMO simulations and $0.87^{+0.03}_{-0.06}$ in the Hydro simulations. The presence of baryons in the Hydro simulations systematically leads to the formation of more spherical halos, as shown by earlier studies (e.g Abadi et al., 2010; Prada et al., 2019; Zhu et al., 2016). Throughout this work we have checked that there are no systematic trends that correlate with the degree of halo asphericity, which suggests that our spherical dynamics treatment represents a reasonable approximation.

While not explicitly shown, we have performed the same analysis on the six AURIGA halos
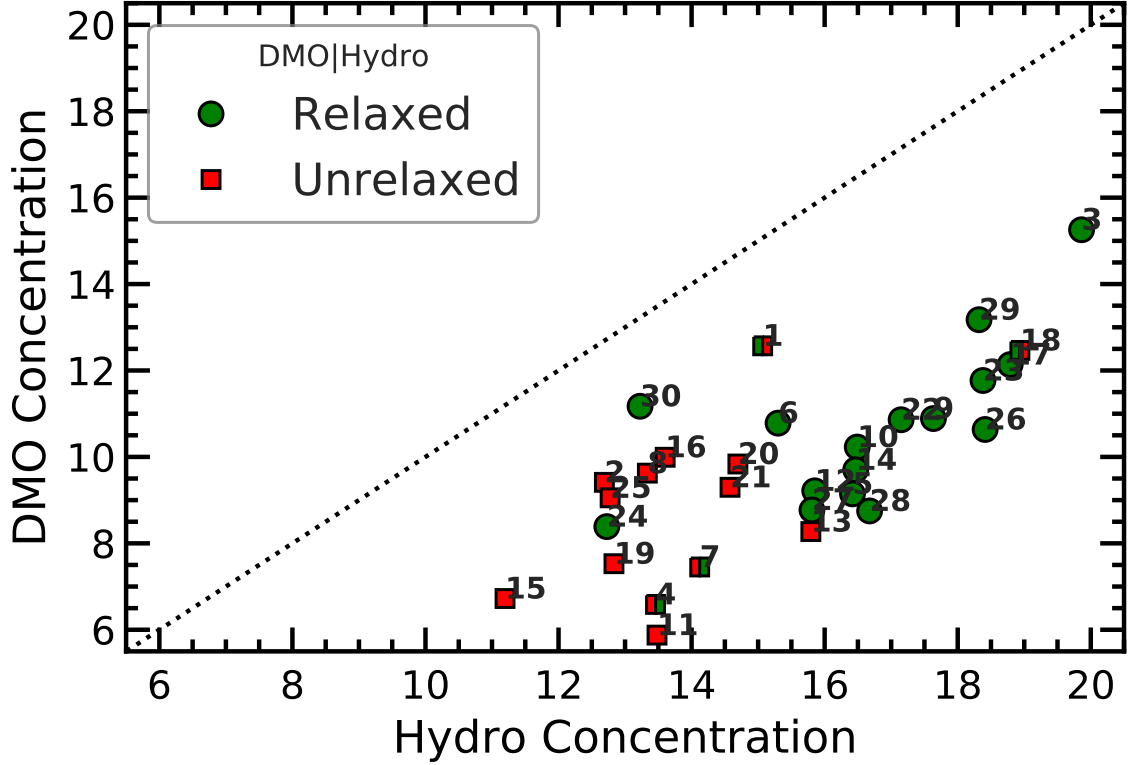
Figure 3.1

The concentrations, $c_{200} = R_{200}/r_s$, of the 30 AURIGA halos in the DMO and Hydro simulations, obtained by fitting an NFW profile to the DM distribution in each case. The points are green circles or red squares if the halos are relaxed or unrelaxed. The contraction of the DM halos in the Hydro simulations increases their concentration relative to the DMO case.

that were simulated at 8 times better mass resolution than the level 4 simulations considered. While the baryon profiles can differ due to the dependence of subgrid physics on resolution and due to stochastic effects, we find the same results as for the level 4 simulations. As such, we have chosen to show the results obtained using the larger level 4 simulation sample to better characterise the halo-to-halo variability.

3.2.1 Halo Properties

We fit NFW profiles to the spherically averaged DM density profile of our halos using least squares fitting in $\log r$ within the range $R_{200}/100 < r < R_{200}$. We find that the NFW profile provides a good fit to the DMO halos, especially the relaxed ones; however it provides a poorer description of the DM distribution in the Hydro simulations (see also e.g. Schaller et al., 2016; Cautun et al., 2020). Nonetheless, for completeness we calculate the best

fitting NFW profile for the dark matter halos in the Hydro simulation as well. In this case, because of the poor fits, the inferred scale radius and concentration can strongly depend on the radial range used for the fitting. The resulting concentrations of the DMO and Hydro halos are shown in Fig 3.1. The concentration of the Hydro halos is systematically higher, indicating an increase in DM density in the inner regions. It can also be seen that unrelaxed halos typically have slightly lower concentration, in agreement with previous studies (Neto et al., 2007).

The effects of contraction may be seen in more detail by comparing the spherically averaged profiles of a halo in the DMO and Hydro simulations. This is shown in Fig. 3.2, which presents the shell mass, $M_{\mathrm{Shell}} = 4\pi r^2 \rho$, the velocity dispersion, σ_V, and the velocity anisotropy, $\beta = 1 - \sigma_T^2/\sigma_r^2$ (where σ_t and σ_r represent the tangential and radial velocity dispersions respectively) for one of the relaxed halos, Au5. The DMO density is scaled by $1 - f_{\mathrm{Baryon}}$ to subtract the cosmic baryon fraction, $f_{\mathrm{Baryon}} = \Omega_{\mathrm{Baryon}}/\Omega_{\mathrm{Matter}}$. As expected, the DMO halo density (top panel) is well fitted by the NFW form, with the best-fit NFW profile shown by the red solid curve. The velocity dispersion (top-middle panel) of the DMO halo peaks just inside the scale radius, which corresponds to the maximum of M_{Shell}. The density at each radius can be interpreted as a measure of the number of different orbits at that radius, so the peak at the scale radius reflects the relatively higher number of orbits that pass through this radius. The velocity anisotropy, $\beta^{\mathrm{DMO}}(r)$, is nearly isotropic in the centre and becomes more radially biased towards the outskirts, again in agreement with previous studies (Tissera et al., 2010; Navarro et al., 2010). While all of our relaxed DMO halos conform to the NFW form, we see significant scatter in their concentrations and variations in their velocity dispersion and velocity anisotropy.

For the Hydro halo, we find a DM profile that is more centrally concentrated (orange line in the top panel of Fig. 3.2). This is due to response of the halo to the baryonic distribution (green line), which is much more centrally concentrated than in the DMO simulation (in which, by construction, the "baryons" have the same profile as the DM, but with a different normalisation). The baryons deepen the central potential, compressing the orbits of the DM particles inwards and significantly increasing the DM density and total velocity
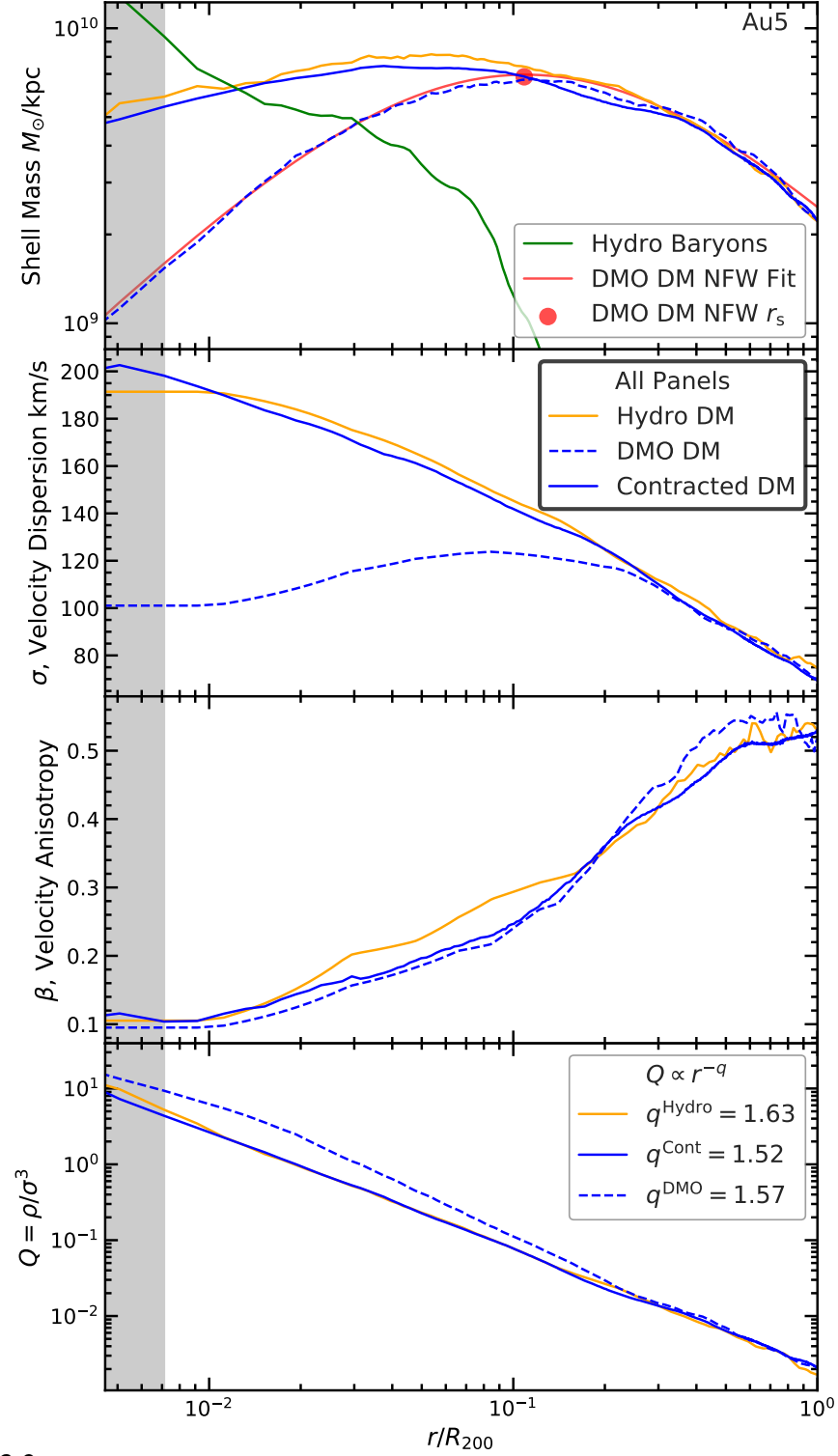
Figure 3.2

An illustration of the density, velocity dispersion and velocity anisotropy profiles of a DM halo (Auriga halo 5) shown for the DMO (dashed blue) and the Hydro (solid orange) versions of the simulation. Compared to the DMO case, the Hydro halo has a higher density in the central regions (top panel), along with an increased velocity dispersion (second panel). The third panel shows only small differences in the velocity anisotropy, β. The bottom panel shows the pseudo-phase-space density, $Q(r) = \rho/\sigma^3$, which we find is well fitted by a simple power law for both DMO and Hydro halos. Also plotted is the contracted DMO halo (solid blue), which was obtained by applying the method described in Sec. 3.3.1. This closely reproduces the Hydro halo. The grey shaded region corresponds to r values below the convergence radius of the simulation (Power et al., 2003).

dispersion in the central regions. The velocity anisotropy, β, profile varies only slightly between the DMO and Hydro halos, with the DMO halos typically having a slightly more radially-biased velocity anisotropy between the scale radius and R_{200} (this is not the case for the Au-5 halo shown in Fig. 3.2), but there is significant halo-to-halo scatter.

The bottom panel of Fig. 3.2 shows the so-called peudo-phase-space density, $Q(r) = \rho/\sigma^3$. Surprisingly, in DMO halos this quantity has been shown to closely follow a simple power law, $Q \propto r^{-q}$, with a theoretically predicted slope, $q \sim 1.875$ (Bertschinger, 1985), that is consistent with our results, $q \sim 1.84^{+0.04}_{-0.07}$. The origin of this relation remains unclear, and whether it is a fundamental feature or a dynamical 'fluke' is debated in the literature (e.g. Ludlow et al., 2010; Navarro et al., 2010; Ludlow et al., 2011; Arora & Williams, 2020). We find that the Hydro halos also conform to this power law (in agreement with Tissera et al. 2010), with similar scatter but with a shallower slope $Q_{\text{Baryon}} \sim 1.62^{+0.08}_{-0.08}$. We leave this interesting observation for future work.

3.2.2   Orbital Phase Space

As we discussed in the introduction, we are interested in describing DM halos in terms of their action distribution, $F(\mathbf{J})$. This provides a complete description of the orbits of particles in the halo, which can be used as the blueprint to reconstruct various halo properties, as we shall see in the next section.

We model halos as spherically symmetric distributions for which the gravitational potential, $\Phi(r)$, is related to the total density profile, $\rho(r)$, by:

$$\Phi(r) = -4\pi G \left(\frac{1}{r} \int_0^r r'^2 \rho(r')\,\mathrm{d}r' + \int_r^\infty r'\rho(r')\,\mathrm{d}r' \right), \qquad (3.2.1)$$

where G is Newton's gravitational constant. Spherical symmetry effectively reduces the number of actions needed to describe each orbit to two as the third action is identically zero and the orbit stays in a plane between its pericentre, r_{min}, and apocentre, r_{max}.

The two nonzero actions are the specific angular momentum, L, and the radial action, J_r,

given by:

$$L = |\boldsymbol{r} \times \boldsymbol{v}| = r v_{\mathrm{t}}$$
$$J_{\mathrm{r}} = \frac{1}{\pi} \int_{r_{\min}}^{r_{\max}} v_r(r) \, \mathrm{d}r \tag{3.2.2}$$

Note that formally $L_z = J_\theta + J_\phi$, where J_θ, J_ϕ correspond to the actions of the angles of the spherical coordinate system. By assuming spherical symmetry, the reference frame can be rotated onto the plane of the orbit such that one action is identically zero and the other is L_z.

An alternative IoM commonly used in dynamical modelling is the (specific) energy, E, defined as:

$$E = \frac{1}{2} |\mathbf{v}|^2 + \Phi(r) \tag{3.2.3}$$

While convenient to calculate, E is not an adiabatic invariant. The energy distribution function, $F(E)$, is therefore expected to differ systematically between the DMO and the Hydro simulations, whereas $F(L)$ and $F(J_{\mathrm{r}})$ are expected to remain approximately the same. Note that in this Chapter all distributions, F, are normalised to integrate to 1.

Here the distributions are found for each halo by selecting, from the centre outwards, the same number of DM particles for each DMO and Hydro counterpart halo, contained within R_{200} of the Hydro halo. In general, halos in the DMO and Hydro simulations are well matched. However, the stochastic nature of galaxy formation, as well as the small inherent numerical efffects, cause small differences in the distributions of DM particles. On average, we find that $\sim 90\%$ of the DM particles within R_{200} in the Hydro case are also found within R_{200} in the DMO case. We have checked that differences in the halos' orbital distributions discussed in this study are not caused by unmatched DM particles between the Hydro and DMO cases; distributions of matched particles differ by similar amounts.

To compare the distributions of different mass halos, the IoMs (of both the Hydro and DMO halos) are rescaled to give values that are independent of the host halo mass (see Zhu et al. 2016; Callingham et al. 2019). The actions, L and J_{r}, are normalised by the characteristic angular momentum of a circular orbit at R_{200}, $L_{\mathrm{h}} = \sqrt{GM_{200}R_{200}}$. The energy is similarly normalised by this orbit's energy, $E_{\mathrm{h}} = GM_{200}/R_{200}$.
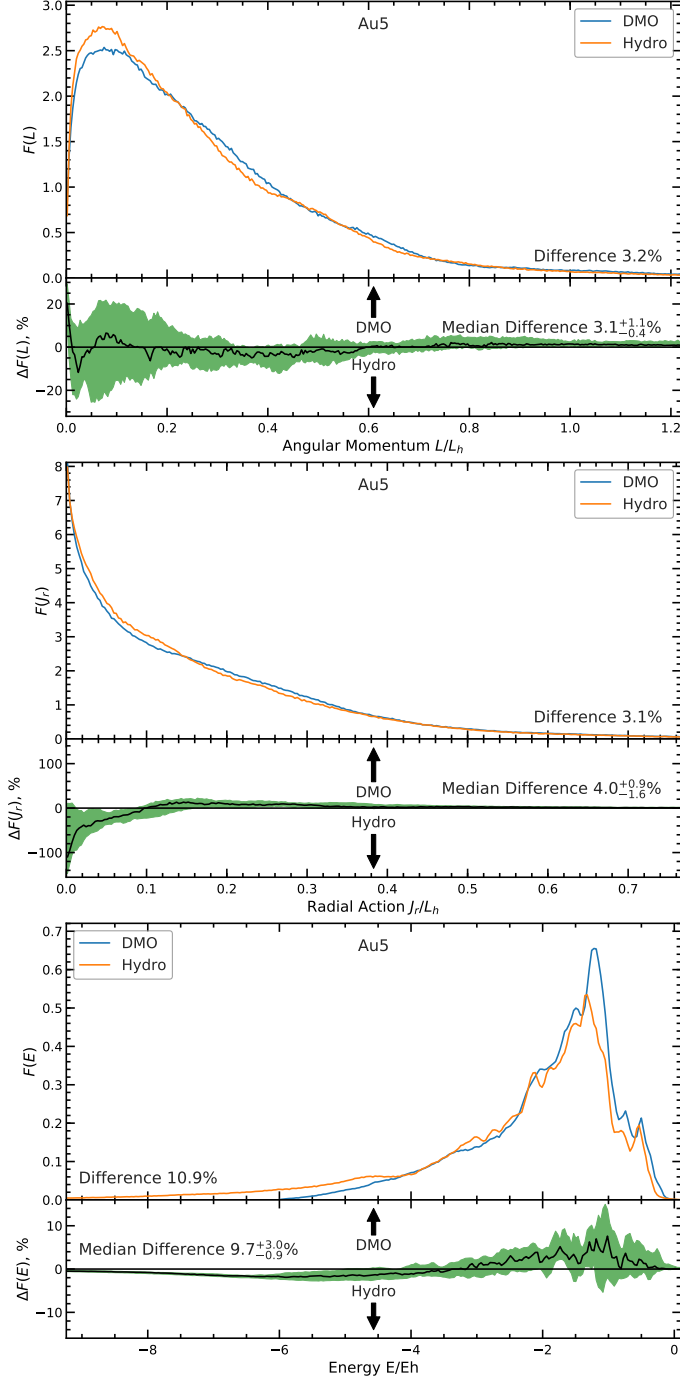
Figure 3.3

The distributions of angular momentum, L, radial action, J_r, and energy, E, of the DM particles in the Hydro and DMO simulations for an example relaxed halo, Au5 (top subpanels). In general, we find small differences between the distribution functions of the adiabatic invariant actions, $F(L)$ and $F(J_r)$, in the DMO and Hydro cases. The distribution of the non-adiabatic invariant energy, $F(E)$, shows larger differences. To check if these differences are systematic, the bottom subpanels show the median (black solid line) and 68 percentiles (green shaded region) of the difference between the DMO and Hydro distributions, $\Delta F = F_{DMO} - F_{Hydro}$, for all relaxed AURIGA halos. To compare different halos, the orbital values are scaled to be independent of halo mass (for further details see the main text). The DM energy distributions (bottom panel) are most affected by the presence of baryons, with about 10% of the particles changing energy. These are mainly inner DM particles shifting to lower energies in the deeper Hydro potential. The distributions of the actions, L and J_r, experience smaller changes, 3% and 4% respectively.

In Fig. 3.3 the distributions of L, J_r and E for one example halo (Au-5) are shown in the top subpanels. The lower subpanels show the difference between the distributions in the DMO and Hydro cases, $\Delta F = F_{DMO} - F_{Hydro}$, for all of the relaxed level 4 AURIGA halos; the solid line is the median and the shaded region indicates the 68 percentiles of the distribution. To estimate the difference between the various distributions, we calculate the overall difference, Δ, which is effectively the fraction of DM particles whose IoM are distributed differently between the Hydro and DMO cases. This is defined as:

$$\begin{aligned} \Delta_X &= \frac{1}{2} \int \left| F_{DMO}(X) - F_{Hydro}(X) \right| \, dX \\ &\equiv \frac{1}{2} \int \left| \Delta F(X) \right| \, dX, \end{aligned} \tag{3.2.4}$$

where X denotes the IoM under consideration, either L, J_r or E. With this normalisation, $\Delta_X = 1$ when the distributions are completely different.

The distributions $F(L)$ (top panel) and $F(J_r)$ (middle panel) are similar to those found in previous simulations (Pontzen & Governato, 2013). Between the DMO and Hydro simulations there is a small, seemingly stochastic difference, in angular momentum ($\Delta_L \sim 3\%$) at low L. The difference in J_r is also small, $\Delta_{J_r} \sim 4\%$, but systematic, with a slight increase towards low J_r for the DM particles in the Hydro case. The energy distributions, $F(E)$ (bottom panel), have distinct peaks and features unique to the individual halo that are not present in the other IoM. These are remnants of a complex merger history, with similar features in the counterpart halo. The energy distributions are most affected by contraction with $\Delta_E \sim 10\%$ as the deeper central potential of the Hydro halo reduces the energy of the inner DM particles.

We saw that the J_r and L one-dimensional distributions are roughly conserved between the Hydro and DMO simulations. But what about the joint two-dimensional $F(J_r, L)$ distribution? Is it also conserved? This question is relevant since we find correlations between J_r and L (as illustrated later in the top panel of Fig. 3.5). These correlations vary between halos and potentially encode important information about the halo's density and velocity profiles. To find the answer, we calculate the differences in the $F(J_r, L)$

distributions between the DMO and Hydro cases; similarly to Eq. (3.2.4), the action difference, $\Delta_{(J_r, L)}$, is defined as:

$$\Delta_{(J_r, L)} = \frac{1}{2} \int \left| F_{\text{DMO}} \left(J_r, L \right) - F_{\text{Hydro}} \left(J_r, L \right) \right| \, dL dJ_r \, . \tag{3.2.5}$$

For relaxed halos, $\Delta_{(J_r, L)} \sim 8 \pm 1\%$. This is larger than the differences in the one-dimensional distributions, but nonetheless it is still rather small indicating that the joint distribution is roughly invariant too. The value of $\Delta_{(J_r, L)}$ is used in the appendix 3.6.2 to study the extent to which differences in action distribution are related to differences between the contracted DMO halos and their Hydro counterparts.

Fig. 3.4 shows the action distributions $F(L)$ and $F(J_r)$ of our relaxed AURIGA halo sample. While the individual action distributions have qualitatively similar form, differences in the peak of the distributions suggest object-to-object scatter in the DFs, which could arise from different halo formation histories. This is to be expected as NFW profiles fit the majority of halos very well, but the concentration and $\beta(r)$ profiles vary from halo to halo. We leave the precise characterisation of these distributions and a potential concentration parameterisation to future work. Here we investigate the effects of halo-to-halo variation by calculating the contracted DM halo using multiple $F(\mathbf{J})$ distributions.

3.3 Constructing the Halo from Particle Orbits

In the previous section we calculated the distribution of DM particle orbits as described by their spherical actions distribution, $F(J_r, L)$. We now calculate the individual orbits in physical space to find their contribution to the structure of the DM halo. We will use this information in the next subsection where we construct the physical properties of the DM halo, such as its density and velocity dispersion profiles, by summing over the orbital distribution, $F(J_r, L)$. Instead of considering a particle as a point contribution to the halo, we consider the physical contribution of its orbit sampled uniformly in phase, i.e. we consider the contribution of the particle spread around its orbit in time. The radial distribution of an orbit, $F(r|J_r, L)$, is defined as the proportion of time that orbit spends
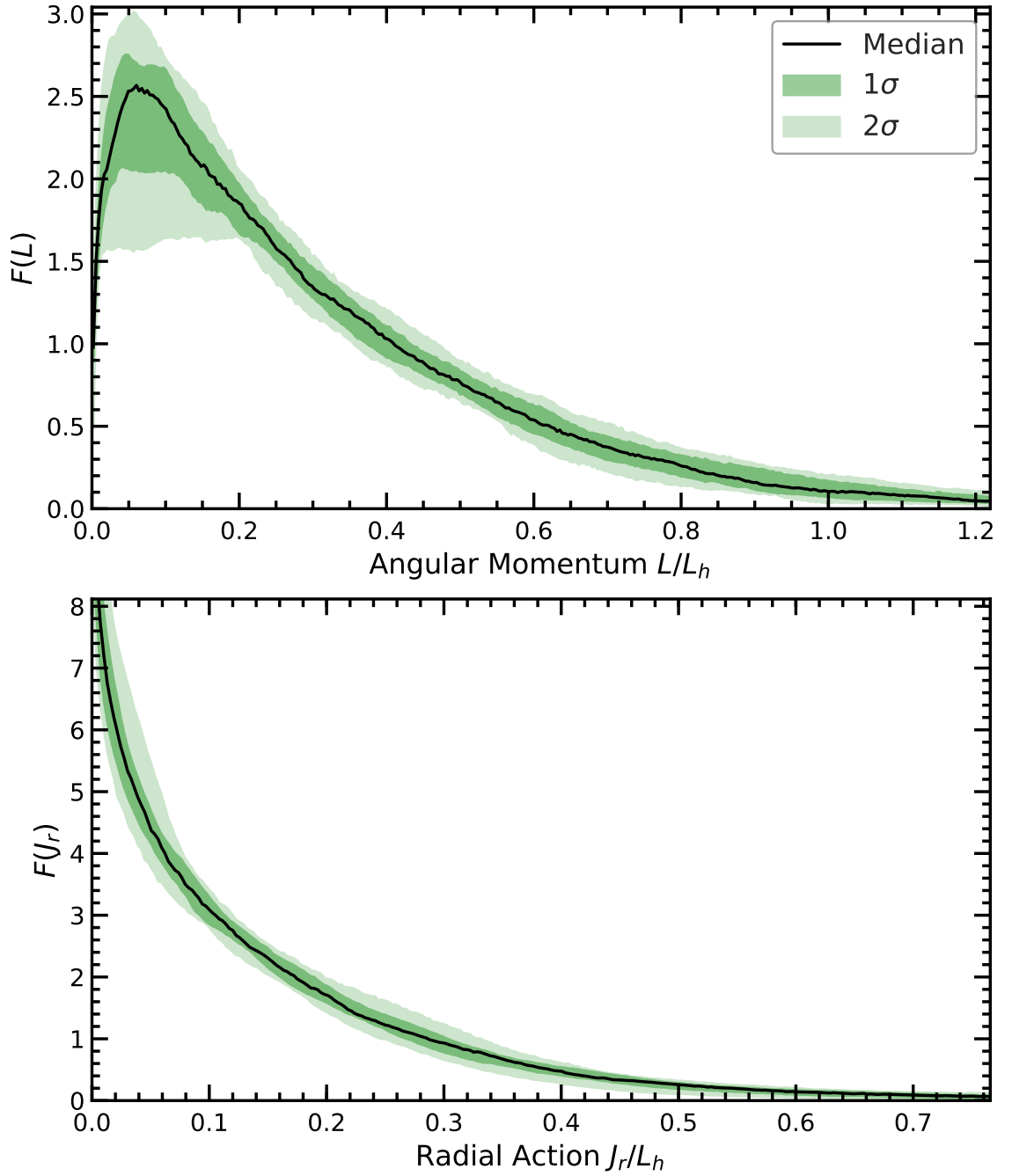
Figure 3.4
The distributions of angular momentum, L, and radial action, J_r, of DM particles in the DMO simulation for our sample of relaxed halos. The black solid line shows the median of our sample and the green shaded region the 68 percentile and full halo-to-halo scatter. To compare halos, L and J_r are scaled to be independent of halo mass (for details see the main text).

at radius r, normalised so that it integrates to unity. This is approximately:

$$F(r|J_r, L) \approx \frac{2}{T|_{J_r, L}} \frac{1}{v_r(r)|_{J_r, L}} \, , \tag{3.3.1}$$

where T is the radial time period and v_r is the radial velocity (see Han et al., 2016). However, this is only an approximation and great care is needed at the endpoints where $v_r \to 0$. For a more detailed derivation and further details please see Appendix 3.6.1. The density can then be reconstructed by integrating over the distribution of these orbits:

$$\rho(r) = \frac{M_{DM}}{4\pi r^2} \iint F(r|J_r, L) \, F(J_r, L) \, dJ_r dL, \tag{3.3.2}$$

where M_{DM} is the total mass of the DM halo.

When contracting a DMO halo to account for its baryon distribution, the cosmic baryon fraction must be removed in order to obtain the correct DM halo mass. That is, the mass of the DM halo in the DMO case is given by $(1 - f_{Baryon})$ times the total halo mass. When constructing the halo, $F(J_r, L)$ must include all DM particles within (and orbits calculated up to) $3R_{200}$ to ensure all significant contributions to the halo are included.

In practice, it is simpler first to construct orbits from a given (E, L) pair and a potential, $\Phi(r)$. The $F(\widetilde{E}, \widetilde{L})$ distribution is derived from $F(J_r, L)$, given a potential Φ. This can be evaluated numerically using the J_r calculated from each (E, L) pair as:

$$F(\widetilde{E}, \widetilde{L}) = F(J_r, L) \frac{dJ_r}{dE} \, , \tag{3.3.3}$$

where $F(J_r, L)$ is evaluated by interpolating the halo action distribution. We can now rewrite Eqn. (3.3.2) in terms of the energy and angular momentum distribution to obtain

$$\rho(r) = \frac{M_{DM}}{4\pi r^2} \iint F(r|E, L) \, F(\widetilde{E}, \widetilde{L}) \, dEdL \, . \tag{3.3.4}$$

To estimate the DM phase-space distribution we sample the (E, L) space using a grid of 500^2 orbits. We find that this grid size is a good compromise between computational time and the sufficiently high orbit density needed to recover a smooth halo profile. We have experimented with different methods for defining the (E, L) grid and have selected the one that gives accurate results for the smallest grid size. This is obtained by first choosing

500 L values, evenly spaced in the cumulative $F(L)$ distribution. Then, for each L bin, We select 500 E values evenly spaced on the allowed phase space, that is in the interval $[E_{\text{Circ}}(L), 0]$. By doing so, we neglect unbound particles, i.e. particles with positive total energy, $E > 0$. However, there is only a small fraction of such particles ($\sim 0.05\%$; see Fig. 3.5) and, in practice, excluding them makes no difference.

We illustrate the transformation from (J_{r}, L) space to (E, L) space in Fig. 3.5. The top panel shows the distribution, $F(J_{\text{r}}, L)$, of the Au5 halo in the DMO simulation. The bottom two panels show the distribution, $F(\widetilde{E}, \widetilde{L})$, for the DMO and Hydro simulations respectively, which have been calculated from the action DF shown in the top panel using the actual gravitational potential measured in each of the two cases. The $F(\widetilde{E}, \widetilde{L})$ distributions are bounded on the lower right edge by circular orbits, which have the minimum energy possible for a given angular momentum. Compared to the DMO case, the Hydro simulation is characterised by more lower energy orbits, a manifestation of the deeper potential well of the Hydro halo.

To gain a better understanding of how a given orbit, (J_{r}, L), changes between the DMO and Hydro potentials, we select 4 orbits with the same angular momentum, $L = 0.12L_h$, and increasing radial action, $J_{\text{r}} = [0, 400, 5000, 15000]$ km kpc s^{-1}. These orbits are shown as colour symbols in Fig. 3.5. The lower the J_{r} of the orbit, the larger the decrease in energy from the DMO to the Hydro potential, as can be determined from the bottom two panels of Fig. 3.5.

The change in energy of the orbits between the DMO and Hydro potentials is accompanied by a pronounced change in the radial range associated with a (J_{r}, L) orbit. This is illustrated in Fig. 3.6, which shows the fraction of time, $F(r|J_{\text{r}}, L)$, that a particle on orbit (J_{r}, L) spends at different distances from the halo centre. The figure shows the same four orbits highlighted in Fig. 3.5. To help interpret the plot, each orbit in Fig. 3.6 is marked with a triangle symbol, which shows the median radial position of the orbit: a particle spends half its orbital time at farther distances than this. Orbit 1 is circular and lies at the scale radius of the DMO halo. With increasing J_{r} the orbits gain radial kinetic energy and become more radial, so their median radial position occurs further out from the circular
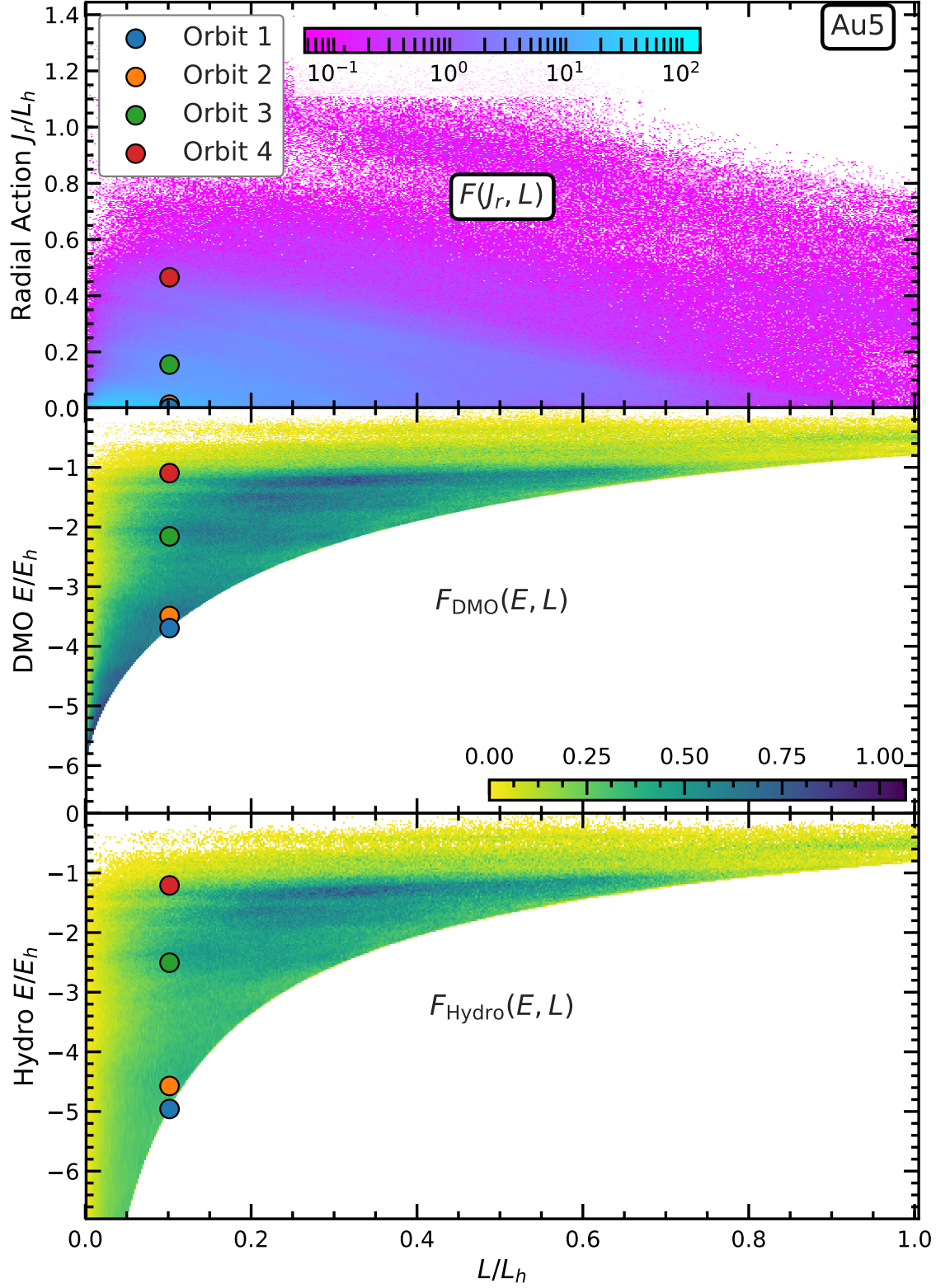
Figure 3.5
The 2D distribution, $F(J_r, L)$, of radial action, J_r, and angular momentum, L, of the DM particles in the DMO simulation of the Au5 halo (top panel). Given a gravitational potential, $F(J_r, L)$ can be used to calculate the 2D distribution, $F(E, L)$, of energy, E, and L. The result is illustrated in the centre and bottom panels, which show $F(E, L)$ for the DMO and Hydro simulations respectively. The deeper potential in the Hydro case leads to overall lower energy orbits. To better illustrate the transformation, the colour symbols show four orbits selected to have the same L, but different J_r values. The radial profiles of these orbits are shown in Fig. 3.6. The actions are given in units of $L_h = \sqrt{GM_{200}}$ and Energy in $E_h = GM_{200}/R_{200}$.
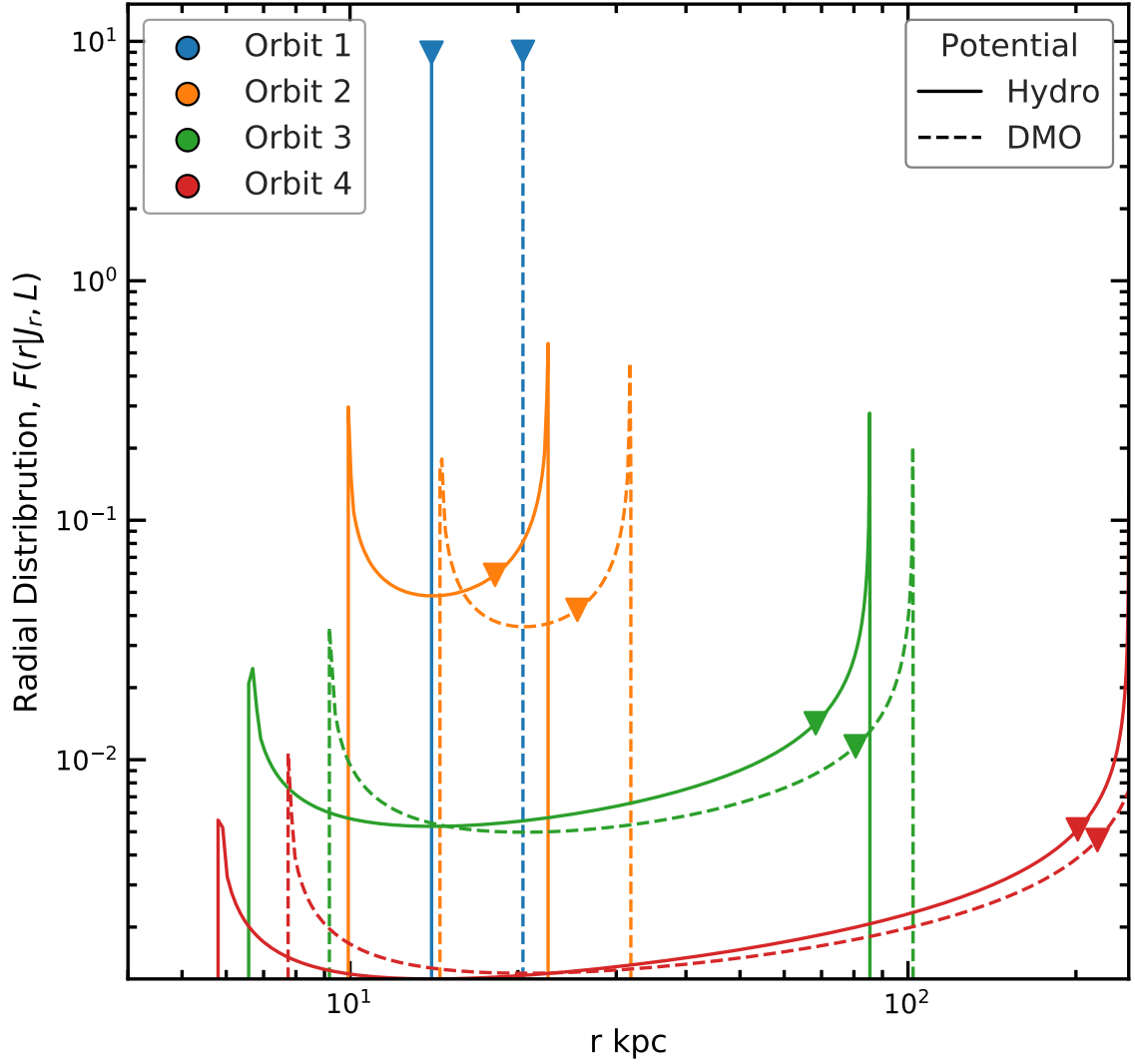
Figure 3.6

The radial distribution, $F(r|J_{\mathrm{r}}, L)$, for four different orbits (each shown by a different colour). This is equivalently the fraction of time that a particle on orbit (J_{r}, L) spends at a given radius, per kpc. The orbits have the same angular momentum, L, but increasing radial action, J_{r} (from Orbit 1 to Orbit 4, where Orbit 1 is circular – see colour symbols in Fig. 3.5). We show the orbits for the gravitational potential of the Au5 halo in the DMO (dashed lines) and Hydro (solid lines) cases. The triangles show the median radius of each orbit. The deeper Hydro potential pulls the orbits to lower radius, affecting the more circular orbits the most.

Create Orbits
(J_r, L)

1 $\Phi_{DM}(r)$
Potential
$(+\Phi_{Baryon})$

2 $F\left(r|J_r, L\right)$
Radial Profiles

**Integrate over
Mass Shells**

**Integrate
over Orbital
Phase Space**
$F(J_r, L)$

3 $\rho_{DM}(r)$
Density
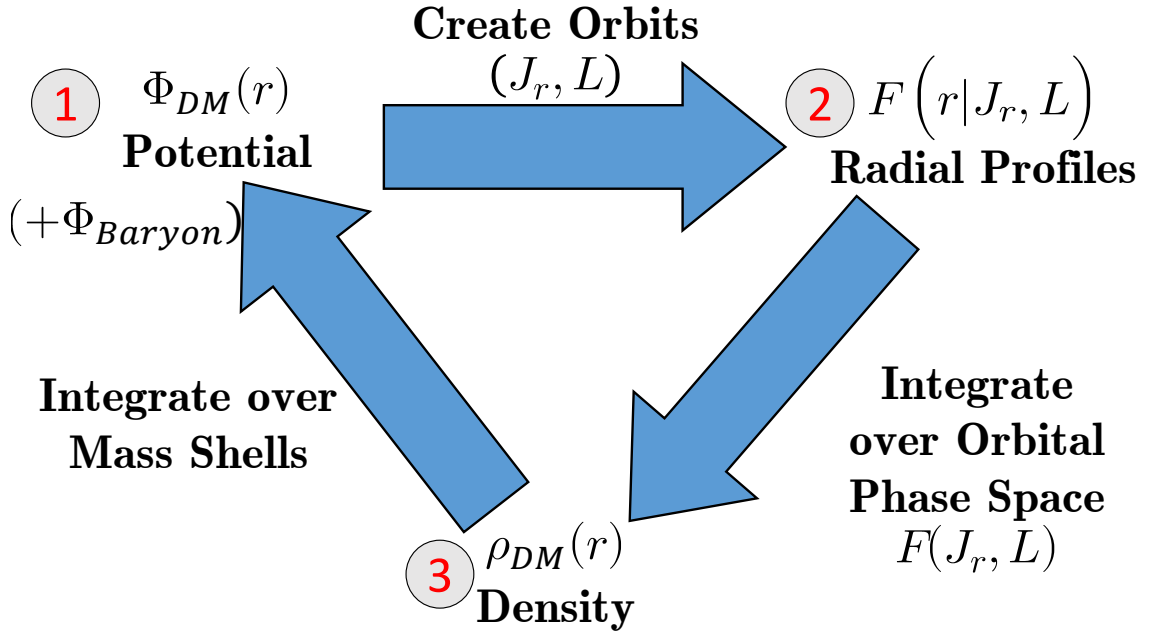
Figure 3.7

Flowchart of an iterative scheme to calculate a halo density profile starting from its action distribution, $F(J_r, L)$. The method proceeds as follows: 1) using a trial gravitational potential for the DM, Φ_{DM}, calculate the radial range, $F(r|J_r, L)$, of each orbit, (J_r, L); 2) integrate over all orbits to calculate the DM density profile, ρ_{DM}; 3) use the inferred DM density to update the DM potential, Φ_{DM}; and repeat from step 1) until convergence is achieved. If required, an additional baryon potential Φ_{Baryon} can be added in step 1) to find a contracted halo.

radius. The orbits spend most of their time at the endpoints, i.e. pericentre and especially apocentre (note the logarithmic y-axis), while they spend the least amount of time at the circular radius for their given angular momentum where v_r is maximal.

Adding baryons deepens the potential well and the orbits are pulled inward, leading to a compression of the DM halo. This can be seen by comparing the DMO orbits (dashed lines) with the Hydro ones (solid lines). The more circular orbits are compressed the most, with fractional decreases in the median radius of orbits from 0.7 for Orbit 1 to 0.9 for the most radial Orbit 4. This is agreement with the suggestion that radial orbits 'resist' compression (Sellwood & McGaugh, 2005; Gnedin et al., 2004).

3.3.1 Finding a Self-consistent Halo

Our aim is to construct a DM halo in physical space, inferring the density and velocity profiles solely from the DM action distribution, $F(J_r, L)$. In the previous Section we

showed that given a fixed potential, Φ, we can obtain the DM density profile, $\rho_{\mathrm{DM}}(r)$, from the action DF by calculating the radial distribution, $F(r|J_{\mathrm{r}}, L)$, of individual orbits that is then integrated over $F(J_{\mathrm{r}}, L)$ to obtain the overall radial distribution of DM particles (see Eq. 3.3.2).

To obtain the true halo density profile we need to know the total gravitational potential, Φ, of the baryonic and DM components. The challenge arises from the fact that the DM gravitational potential needs also to be calculated from the action distribution. Here we describe how this can be done in a self-consistent way using an iterative approach. We first make an initial guess for the potential which, at each iteration, is updated to a value that is ever closer to the true potential.

Our approach is illustrated in Fig. 3.7 and proceeds as follows. First a sensible trial potential, Φ_{DM}^{0}, is chosen, for example, the potential of an NFW halo of average concentration for the target halo mass. When considering the Hydro halo, we typically choose the DM potential from the counterpart DMO halo since this achieves faster convergence. We sum the DM and baryon* potentials to obtain the total potential. The DM density is then calculated using Eqn. (3.3.2), which, in turn, is used to determine the updated DM potential. This is used as the input potential for the next iteration step, which is repeated until convergence is achieved. The convergence criterion is satisfied when the change in DM density between two iterations is small enough. This is quantified in terms of

$$\Delta_{\rho}^{\mathrm{total}} = \left(\log\left(\frac{100}{3}\right)\right)^{-1} \int\limits_{R_{200}/100}^{R_{200}/3} \left|\Delta_{\rho}(r)\right| \, \mathrm{d}\log r \,, \tag{3.3.5}$$

where $\Delta_{\rho}(r)$ is defined as the fractional difference between two density profiles,

$$\Delta_{\rho}(r) = 2\,\frac{\rho_2(r) - \rho_1(r)}{\rho_2(r) + \rho_1(r)} \,. \tag{3.3.6}$$

The quantity $\Delta_{\rho}^{\mathrm{total}}$ characterises the integrated difference between two density profiles

---

*The baryon potential is kept fixed and is an input to the method, e.g. the potential from the stellar distribution of an AURIGA halo or of the MW. The method applies to DMO simulations too, in which case the baryon potential is obtained as the cosmic baryon fraction multiplied by the total potential measured in the simulation. The same result is obtained if instead we take a null baryon potential and assume that the DM constitutes 100% of the mass in the DMO simulation.

in the inner region of the halo, that is for $r \in [\frac{1}{100}, \frac{1}{3}] R_{200}$. When running the iterative approach without a convergence criterion, we find that $\Delta_\rho^{\text{total}}$ reaches a constant small value, $\Delta_\rho^{\text{total}} \in [0.01, 0.005]\%$ (the exact value varies from halo to halo). The final equilibrium state seems to be reached inside out, with the outskirts of the halo converging somewhat more slowly than the inner parts. Based on this, we choose to stop the iterative procedure to determine the potential when $\Delta_\rho^{\text{total}} < 0.02\%$.

We have tested the method by applying it to relaxed AURIGA halos in both the DMO and Hydro simulations. For example, we measured the $F(J_r, L)$ distribution for a DMO halo, which was then used to recover that halo's density profile starting from an initial potential given by an NFW halo of average concentration for its mass. When compared with the 'true' DM halo profile from the simulation we find very good agreement: the density is typically recovered to within ~2% within $R_{200}/2$ with increasing scatter of 5% to 10% towards the outskirts of the halo. Differences mainly arise from assuming steady state halos in which particles are uniformly spread in phase along their orbits. However, recently accreted material and substructures do not satisfy this assumption and can lead to differences between the density profile measured in the simulations and that predicted by our method.

3.3.1.1 Scaling the action distribution to halos of different masses

In this section we show how to scale our results from AURIGA halos to halos of arbitrary mass. We do this within the context of our method for generating a halo from a given $F(J_r, L)$ distribution. The goal is to take the $F(J_r, L)$ distribution measured for a halo of total mass, M_{200}^{initial}, and rescale it so that it can be used to predict the profile of a target halo with total mass, M_{200}^{target}. For this, we exploit the fact that DM halos, at least in DMO simulations, are universal when scaled appropriately (for more details see the discussion in Li et al., 2017; Callingham et al., 2019). As we saw in Fig. 3.3, the action distribution for the DMO and Hydro simulations are very similar so we expect the universality to apply to the action distribution not only in the DMO case, but also when including a baryonic component.

As we are interested in matching the total mass of a target halo with a fixed given baryonic profile, we are only free to rescale the mass of the DM halo, not that of the baryonic component. We define the mass scaling factor, $\lambda = M_{200;\,\mathrm{DM}}^{\mathrm{target}}/M_{200;\,\mathrm{DM}}^{\mathrm{initial}}$, which is the ratio between the DM mass enclosed within R_{200} for the target and initial halos, respectively. For DMO halos, we can rescale the initial halo to the target one by rescaling the positions and velocities by $\lambda^{1/3}$, and the energy and actions by $\lambda^{2/3}$. For Hydro halos, rescaling the position, velocities and energy using the same procedure is not a good strategy, especially in the inner halo regions, where the universality of halos is degraded by the presence of baryons. However, as we discussed earlier, this is not the case for the actions, which scale as in the DMO case.

The rescaled action is given by

$$F'\left(J_{\mathrm{r}}, L\right) \equiv F^{\mathrm{target}}\left(J_{\mathrm{r}}, L\right) = \lambda^{-4/3} F^{\mathrm{initial}}\left(J_{\mathrm{r}}/\lambda^{2/3}, L/\lambda^{2/3}\right), \tag{3.3.7}$$

where F^{target} and F^{initial} denote the action distribution in the target and original halos respectively, and the $\lambda^{-4/3}$ multiplication factor ensures that the new distribution integrates to unity. We then use these new actions, $F'\left(J_{\mathrm{r}}, L\right)$, as input to the method for constructing the halo density profile described in Section 3.3.1.

The total mass, M_{200}^{new}, of the resulting rescaled halo is close to the target mass, $M_{200}^{\mathrm{target}}$, but there can be small differences of order a few percent. These are present when baryons are included since the baryonic distribution can either contract or expand the DM distribution and thus introduce small variations in the total mass within R_{200}. We account for these small differences by applying again the rescaling method, with the actions now rescaled by a new factor, $\lambda' = M_{200;\,\mathrm{DM}}^{\mathrm{target}}/M_{200;\,\mathrm{DM}}^{\mathrm{new}}$, which is typically very close to one. Using the new actions, we calculate again the halo density profile and its total mass, M_{200}^{new}, repeating the procedure until convergence to the target halo mass is achieved.
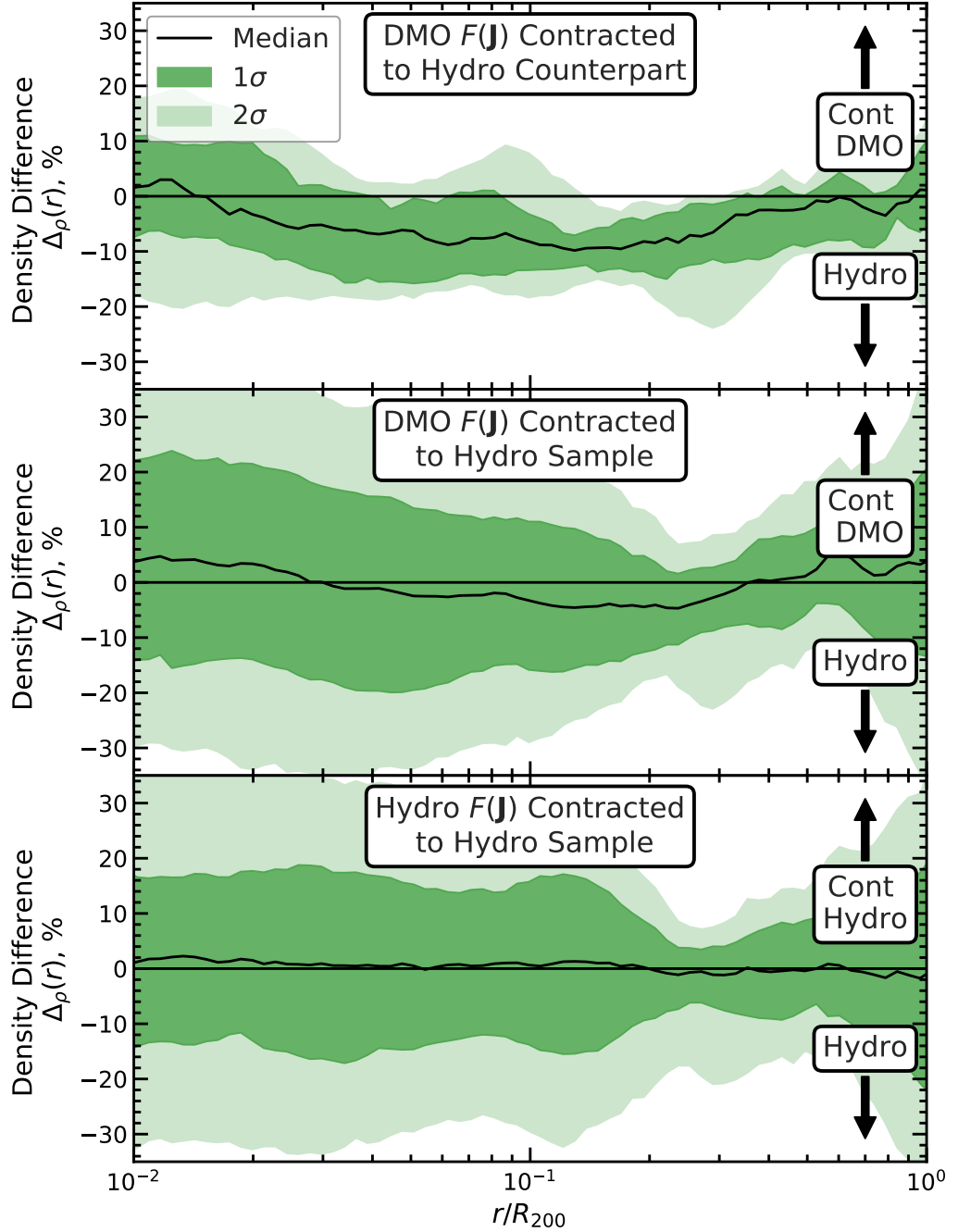
Figure 3.8

The difference in radial density profiles, $\Delta_\rho(r)$, between DM halos described by an action distribution, $F(J_r, L)$, adiabatically contracted according to a given baryonic profile (see main text for details) and the 'true' DM halos in the AURIGA hydrodynamical simulations. We show the results for relaxed halos only. The black line shows the median and the dark and light green regions indicate the 68% and 95% percentiles respectively. In the top panel we compare contracted DMO halos with their Hydro counterparts, highlighting the effects of unadibiatic differences in the action distributions between the DMO and Hydro simulations on the DM halo density profile. In the middle panel we contract each DMO halo in turn to every other Hydro halo in the relaxed sample and compare the resulting density profiles, to additionally see the effects of halo variation. In the bottom panel we contract each Hydro halo in turn to every other Hydro halo across the relaxed sample. This demonstrates the scatter expected when modelling an unknown contracted halo due to halo variation.

3.3.2 Contracting Auriga Halos

We now apply the scheme of Section 3.3.1 to model the DM halos in AURIGA. The action distributions of the DM halos, $F(J_r, L)$, as found in Section 3.2.2, are contracted to a fixed baryon potential, $\Phi_{\mathrm{Baryon}}(r)$, taken from the corresponding counterpart halo in the Hydro simulation.

First, we study if the $F(J_r, L)$ distribution measured in the DMO simulation can be used to predict the DM distribution in the counterpart Hydro halo. We illustrate this for the Au5 halo in Fig. 3.2, which shows the DM density as measured for the Hydro halo (orange line) and the contracted DMO halo (blue line). Although there is good overall agreement between the two, the contracted halo density profile is slightly lower than the true one as measured in the Hydro simulation. This systematic difference is consistently seen in all the relaxed AURIGA halos and is examined further in the top panel of Fig. 3.8, which shows the fractional difference in density profiles between the contracted DMO halo and the actual Hydro DM halo. The contracted halo systematically underpredicts the density profile by $\sim 8\%$ over the radial range, $r \in [1/100, 1/3] R_{200}$, while outside this range the agreement is good. This results in M_{200} masses for the contracted halos that are $5 \pm 2\%$ lower than the true masses. This underprediction suggests a systematic, non-adiabatic, difference between the Hydro and DMO action distributions, as we had already encountered in Fig. 3.3.

To investigate the effects of halo-to-halo variations in action distributions, we contract each of our relaxed DMO halos in turn according to the baryonic distribution of each relaxed Hydro halo. When doing so, we rescale the actions of the DMO halo to the total mass of each target Hydro halo using the procedure described in Section 3.3.1.1, ensuring the final contracted halos have the correct M_{200}. The fractional difference between the density profiles of the contracted and 'true' halos are shown in the middle panel of Fig. 3.8. The variation in the DM halos action distributions, $F(J_r, L)$, produces a greater scatter in the contracted density compared to when each halo is matched with its Hydro counterpart. The scatter is largest in the inner third of the halo beyond which the scatter is noticeably tighter before spreading out again near the outskirts of the halo. This is likely due to

the variation in concentration, which mainly effects the inner regions of the halo, $r \lesssim r_{\rm s}$. Alongside a greater scatter, there is again an underprediction of the contracted density profile, which is slightly reduced by fixing the mass of the contracted halos to be equal to that of the Hydro halos.

We can overcome this systematic difference in the predicted density profile by using the DFs measured in the Hydro halos instead of the DMO halos, as we have done until now, as shown in the bottom panel of Fig. 3.8. The resulting contracted DM profiles are unbiased but they have a rather large, ~15%, halo-to-halo variation. This shows that the small systematic differences we have seen in the actions between the DMO and Hydro simulations (see Section 3.2.2) have measurable effects on the DM density profiles, and that to obtain unbiased contracted DM halos we need to use the action distribution measured in the Hydro simulations. Thus, to obtain an unbiased model of the MW halo, we need to use Hydro derived DFs, and, because of system-to-system variations in the DF, we can predict the MW halo density profile only to 15% accuracy.

We have studied in more detail the most important systematic differences between the action DFs in the DMO and Hydro simulations. The tests and the corresponding results are presented in Appendix 3.6.2. We have found that the small, systematic difference in density profile seen in Fig. 3.8 is predominantly driven by the suppression of $J_{\rm r}$ in the Hydro halos. In the Hydro simulations, some mechanism has caused the DM to lose radial energy in an unadibiatic way. If the systematic decrease of radial action in the Hydro halos was driven by baryons through either feedback or numerical baryon-DMO particle scattering effects we would perhaps expect to see the strongest effects at the centre of the halo, where the baryon density is highest. However, we see no evidence of a radially varying effect, with the $J_{\rm r}$ suppression being, on average, approximately the same at all radial distances from the halo centre and at all angular momentum. Furthermore, the feedback driven cores found in some simulations of dwarf galaxies are formed by increasing the energy of the DM particles, not by reducing it. We leave a more thorough investigation of these non-adiabatic effects to future work.

3.3.3   Local DM Properties in Auriga

As we discussed in the Introduction, a strength of the halo contraction method presented here is that it can be used to predict all DM halo properties, including the velocity distribution. This is in contrast to most other methods (e.g. Blumenthal et al., 1986; Gnedin et al., 2004; Cautun et al., 2020), which apply only to the halo density profile. In this section we study how the contraction method can predict dynamical properties of the DM halo, in particular the DM velocity distribution in the Solar neighbourhood, which is a crucial input into DM direct detection experiments. In preparation for modelling the MW in Section 3.4, we first study the velocity distribution function (VDF) of the relaxed DM AURIGA halos. To validate our methodology, we compare the contracted DMO halos with their Hydro counterparts. Across our sample of different size halos, we define an AURIGA halo's 'Solar radius' as a set fraction of its R_{200}, $0.036R_{200}$, which was obtained by taking the following MW values: $r_\odot = 8$ kpc and $R_{200}^{\mathrm{MW}} \approx 222$ kpc (from Callingham19, corresponding to $M_{200}^{\mathrm{MW}} = 1.17 \times 10^{12} M_\odot$).

We illustrate how well our contraction method recovers the DM velocity distribution in the presence of a baryonic component by studying the AU5 halo. Compared to the DMO case, the Hydro halo has an enhanced density and especially velocity dispersion at the Solar radius, as may be seen in Fig. 3.2, at the radial position, $r \sim 0.04R_{200}$. The contracted DMO halo reproduces well the Hydro halo, in particular, both the velocity dispersion as well as the velocity anisotropy parameter, β. Thus, our contraction technique reproduces local halo properties that are averaged over many DM particles.

In Fig. 3.9 we show that the same technique also reproduces the actual DM velocity distribution. For this, we calculate the velocity distribution of all DM particles found within a radial distance of ± 1 kpc around the Solar radius. As expected, the DM particles in the Hydro case are characterised by higher velocities than in the DMO case. The small irregularities in the distribution are the result of the merger history of the halo. The action distribution of the DMO halo can be used to predict the velocity distribution of the contracted DMO halo. This is similar to the approach taken in Sec. 3.3.1, where we
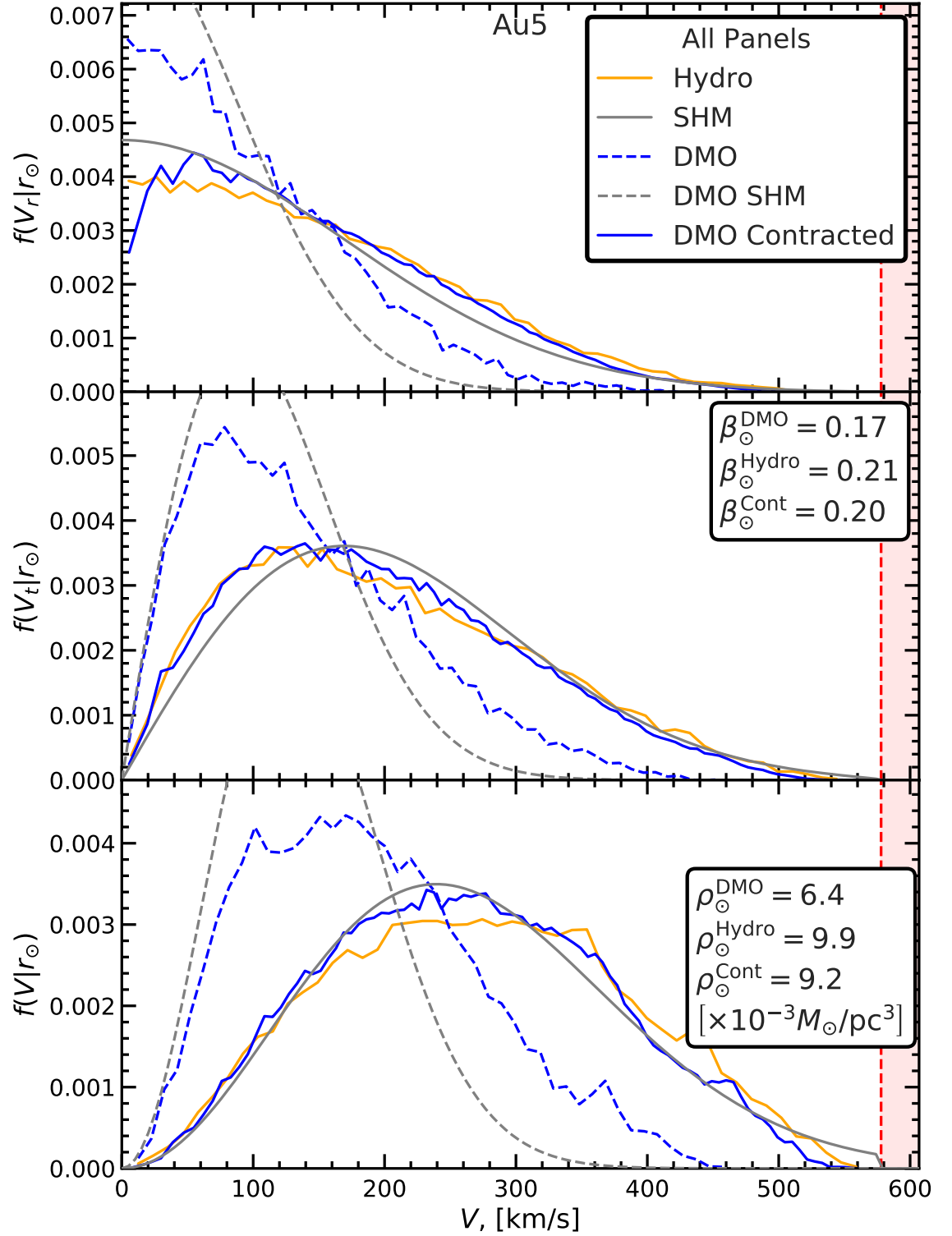
Figure 3.9

The velocity distributions of DM particles at the Solar neighbourhood in the AURIGA Halo 5, AU5. The solid orange line shows the distribution measured in the Hydro halo, the dashed blue line the corresponding quantity in the DMO case, and the solid blue line in the DMO halo contracted with our method to predict the Hydro quantities. In grey we show the predictions of the Standard Halo Model (SHM), based on the assumption of an isotropic isothermal sphere. The top panel shows radial velocity, v_r, the middle panel tangential velocity, v_t, and the bottom panel total velocity, v. The vertical red shaded region shows velocities larger than the escape velocity of the Hydro halo. Estimates for the Solar neighbourhood DM density, $\rho_\odot$, and velocity anisotropy, $\beta_\odot$ are also given (see the two tables enclosed by a thick black line in the right-hand side of the centre and bottom panel).

modelled the density profile. To obtain the VDF, we calculate the velocity components of each $F(r|J_r, L)$ orbit at the solar radius, and then sum over all possible orbits, $F(J_r, L)$ (using a similar weighting to Eqn. 3.6.6). The contracted DMO halo reproduces well the velocity distribution of the Hydro halo, with most differences between the two being stochastic in nature. The only large difference is seen in the radial velocity, v_r, distribution (top panel), where the contracted halo is systematically below the Hydro case for $v_r \to 0$. This is due to the finite number of orbits included in the reconstruction, with none being exactly at apocentre, pericentre or on perfectly circular orbits at this radius. This effect is small and can be reduced by including a greater number of orbits in the reconstruction.

The most popular approach in the field is to model the VDF using the Standard Halo Model (SHM) (e.g. Evans et al., 2019). This is based on the assumption of an isotropic isothermal sphere, and predicts a Gaussian velocity distribution with velocity dispersion, $\sigma = v_{\mathrm{circ}}/\sqrt{2}$, which is truncated at the escape velocity, v_{esc}. The SHM predictions for the DMO and Hydro simulations of Au5 are shown in Fig. 3.9 as dashed and solid grey curves, respectively. The SHM model provides a poor description of the DMO velocity distribution, but performs much better for the Hydro halo. However, we still find important differences between the SHM predictions and the actual Hydro halos. In particular, the sharp truncation of the SHM VDF at v_{esc} is more abrupt than in the simulations and typically leads to an overprediction of high velocity DM particles. Moreover, the SHM assumes isotropic orbits whereas, in this halo and throughout our sample, we find a small, but non zero anisotropy parameter at the Solar neighbourhood, $\beta_\odot^{\mathrm{Hydro}} = 0.21$. Thus, the isotropic SHM slightly underpredicts the v_r and overpredicts the v_t distributions.

3.4 Application to the Milky Way

We can now apply our DM halo reconstruction method to infer the structure of the DM halo of our own galaxy. To do this we need to know: the action DF, $F(J_r, L)$, of the MW halo; the MW baryon distribution; and the total mass, M_{200}^{MW}. The last two quantities can be inferred from observations (e.g. Cautun et al., 2020; Wang et al., 2020a). For the $F(J_r, L)$

distribution, we assume that the MW is a typical ΛCDM halo and that its DF is similar to that of our relaxed AURIGA halos. By considering the range of different DFs for the MW, as spanned by the AURIGA halos, we quantify the extent to which the unknown DM action distribution of our Galactic DM halo affects our predictions. Finally, as we saw in the previous section, there are small systematic differences between the distributions of actions in the DMO and Hydro simulations of MW-mass halos. Thus, to obtain predictions that are as accurate as possible, we use the $F(J_r, L)$ DFs measured in the Hydro simulations of the AURIGA suite.

We adopt the MW baryon density profile advocated by Cautun19, which we model as a spherically symmetric distribution. Cautun19 assumed parameterised density profiles of a thick and thin stellar disc, a stellar bulge, a cold gas ISM and an analytically contracted NFW DM halo. Through an MCMC fitting procedure, these baryonic and DM components were fit to the latest MW rotation curve data derived from *Gaia* DR2 (Eilers et al., 2019); the data cover the radial range 5 to 25 kpc. We also use the total mass of this model, $1.08 \times 10^{12} M_\odot$, with the final mass of our halos set through the scheme in Sec.3.3.1.1. This total mass determination is in very good agreement with other measurements based on *Gaia* DR2 (see Fig. 5 in Wang et al. 2020a), such as the ones based on escape velocity (Deason et al., 2019a; Grand et al., 2019), globular cluster dynamics (Posti & Helmi, 2019; Watkins et al., 2019), rotation curve modelling (Cautun19) and satellite dynamics (Callingham19).

Our inferred properties of the MW DM halo are shown in Fig. 3.10. In the top panel we see that the median of the contracted density profile closely matches that of Cautun19, although some differences are present. This is to be expected since the Cautun et al. results corresponds to a DM halo that, before baryon contraction, had a concentration of 9.4 , while the 17 AURIGA halos studied here have a wide range of concentrations before contraction (averaging 9.7, see Fig. 3.1). Nonetheless, the Cautun et al. result lies well within the 68 percentile scatter of our predictions, indicating good overall agreement. Not knowing the exact $F(J_r, L)$ distribution of the MW halo results in a $\sim 14\%$ scatter (68 percentile range) in the predicted density profile of the contracted halo, in good agreement
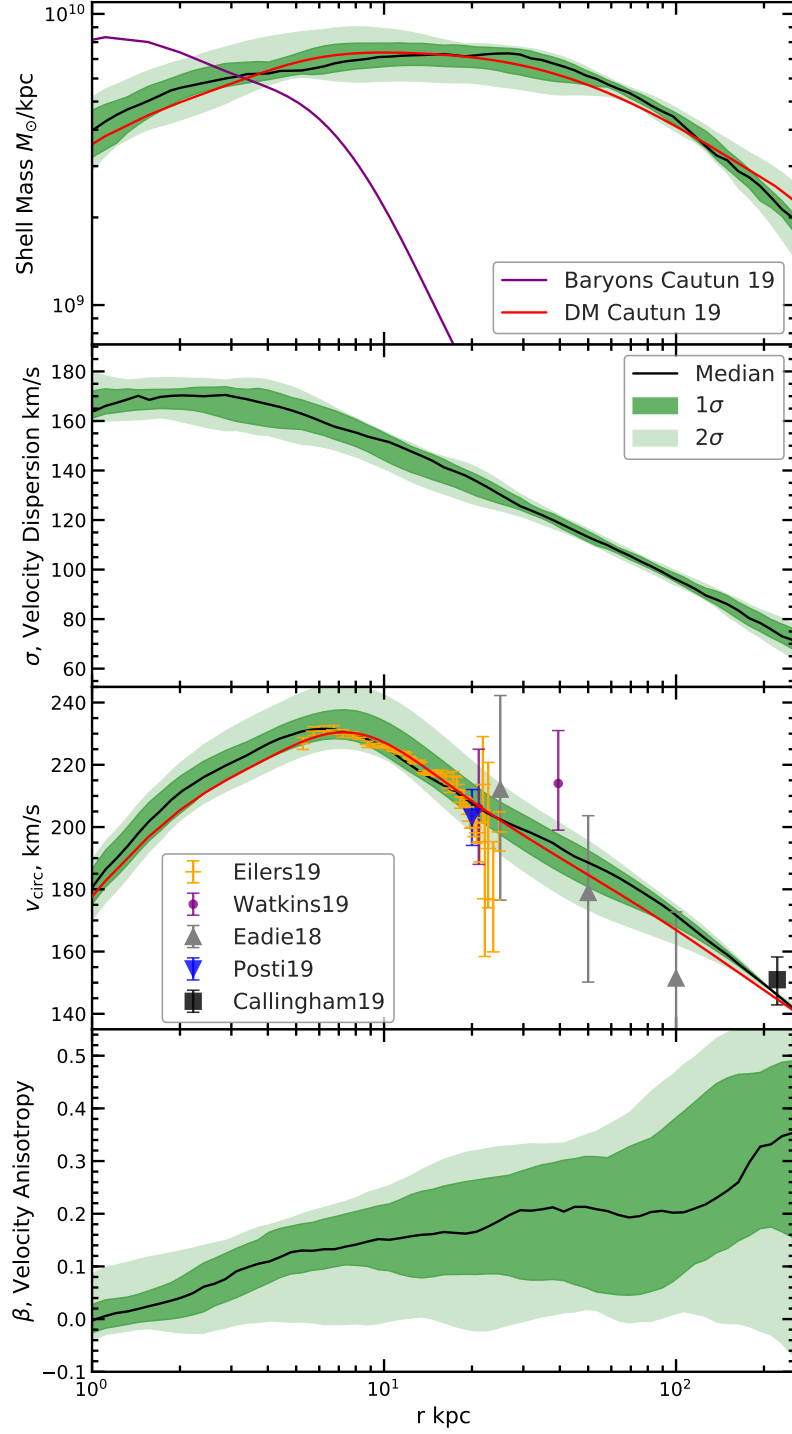
Figure 3.10

From top to bottom: the MW's density, velocity dispersion, circular velocity, and velocity anisotropy radial profiles predicted by our halo contraction method. The DM halos are contracted assuming the Cautun19 MW baryonic model and the action distributions, $F(J_r, L)$, from 17 relaxed halos in the AURIGA Hydro simulations. The black line shows the median prediction of our method, while the dark and light shaded regions show the 68 and 95 percentiles arising from halo-to-halo variation in $F(J_r, L)$. The top panel also shows the Cautun19 baryonic profile (purple) and their best fitting DM profile (red) ; the third panel shows in yellow the Eilers et al. (2019) V_{circ} data and in red the Cautun19 rotation curve for their best fitting MW model. For comparison to other observational estimates of circular velocity, we include data points from Eadie & Jurić (2019), Watkins et al. (2019), Posti & Helmi (2019) and Callingham et al. (2019)

with our AURIGA results. Our model predicts that the DM velocity dispersion is roughly constant at around $160\,\mathrm{km\,s^{-1}}$ in the inner region of our Galaxy, and then decreases rapidly towards the halo outskirts (second panel in Fig. 3.10).

In the third panel of Fig. 3.10, we compare the rotation curve predicted by our model with the actual estimate for the MW as determined by Eilers et al. (2019). we do not fit our model to these data, so the good agreement with observations indicates that our model is making sensible predictions. To compare against the data, we add the rotation curves from both the baryons and the halo. The latter is modelled as a spherically symmetric distribution but for the baryons we need to take into account that their distribution is highly flattened, i.e. most stars and gas are found in a disc, and that the Eilers et al. rotation curve is measured in the plane of this disc. In the plane of the disc, the true axisymmetric profile gives a ~10% greater contribution to the rotation curve than the spherical profile that we use when modelling the contraction of the DM halo.

The distribution of rotation curves across our contracted DM halos are in good agreement with both the Eilers et al. data and the Cautun19 best fitting model. However, we see variation in the curves when using different action DFs. This is to be expected since the MW represents one possible realisation of $F(J_\mathrm{r}, L)$. It is worth stressing that the median result is not necessarily the 'best' model for the MW DM halo, as the MW is unlikely to reside in a typical ΛCDM halo. Instead, the point to emphasise is that we would expect the MW to lie within the range of our halo sample, i.e. within the scatter, which it clearly does. For the data points within 30kpc, we see good agreement with the estimates by Posti & Helmi (2019), Watkins et al. (2019) and Eadie & Jurić (2019). Further out, we find that the Watkins et al. (2019) measurement at 40 kpc lies just outside the 1σ uncertainty of our models, and the lower total mass of Eadie & Jurić (2019) ($0.7 \times 10^{12} M_\odot$) leads to a faster drop off towards R_{200}. Since our total mass is similar, our circular velocity curve matches well that of Callingham19 around R_{200}. For a more detailed discussion see Sec 6. of Cautun19 which presents a comparison with several other Galactic probes.

While the Eilers et al. circular velocity curve data lie comfortably within the 1σ range of our distribution of contracted halos, the individual halo curves are poor fits. This

Table 3.1

A list of MW properties in the Solar neighbourhood inferred from our DM halo contraction model. The third and fourth column column gives the corresponding values from Cautun19. The velocity dispersion's and anisotropy of these columns are not found directly in Cautun19. Instead these values, denoted by *, are calculated by applying the SHM and SHM++ DM models to the Cautun19 MW mass distribution (see sections 3.3.3 and 3.4.1 for further details).

Property	This work	Cautun19 + SHM*	Cautun19 + SHM++*	Units
$\rho_\odot$	$8.5^{+1.6}_{-0.6}$	9.2	9.2	$10^{-3} M_\odot/\mathrm{pc}^3$
	$0.32^{+0.05}_{-0.02}$	$0.34^{+0.02}_{-0.02}$	$0.34^{+0.02}_{-0.02}$	$\mathrm{GeV/cm}^3$
$\sigma_{V,\odot}$	155^{+5}_{-6}	153*	153*	km/s
$\sigma_{V_r,\odot}$	162^{+9}_{-8}	153*	170*	km/s
$\sigma_{V_t,\odot}$	151^{+4}_{-5}	153*	142*	km/s
$\beta_\odot$	$0.14^{+0.06}_{-0.03}$	0 (isotropic)*	0.3*	–
$V_{\mathrm{Circ},\odot}$	231^{+8}_{-2}	230	230	km/s
$V_{\mathrm{Esc},\odot}$	554^{+12}_{-10}	549	549	km/s
M_{200}^{Total}	1.08	1.08	1.08	$10^{12} M_\odot$
M_{200}^{DM}	0.97	0.97	0.97	$10^{12} M_\odot$
$M_{200}^{\mathrm{Baryons}}$	0.11	0.11	0.11	$10^{12} M_\odot$

shortcoming could be overcome by using the observations to find out which $F(J_r, L)$ distribution best describes the MW data. This can be achieved with a MCMC approach in which we sample different action DFs and concurrently constrain the MW baryonic distribution (e.g. similar to the approach of Cautun19). It is important to marginalise over the MW baryonic distributions, since these are uncertain and, as Cautun19 have shown, there is a degeneracy between the baryon content and the DM halo structure when modelling the MW rotation curve. This approach is beyond the scope of this Chapter and we leave it for future work.

3.4.1 MW Local DM Distribution

Having inferred the likely structure of the MW DM halo by applying the results of Section 3.3 based on analysis of 17 AURIGA galactic halos, we now investigate the implications
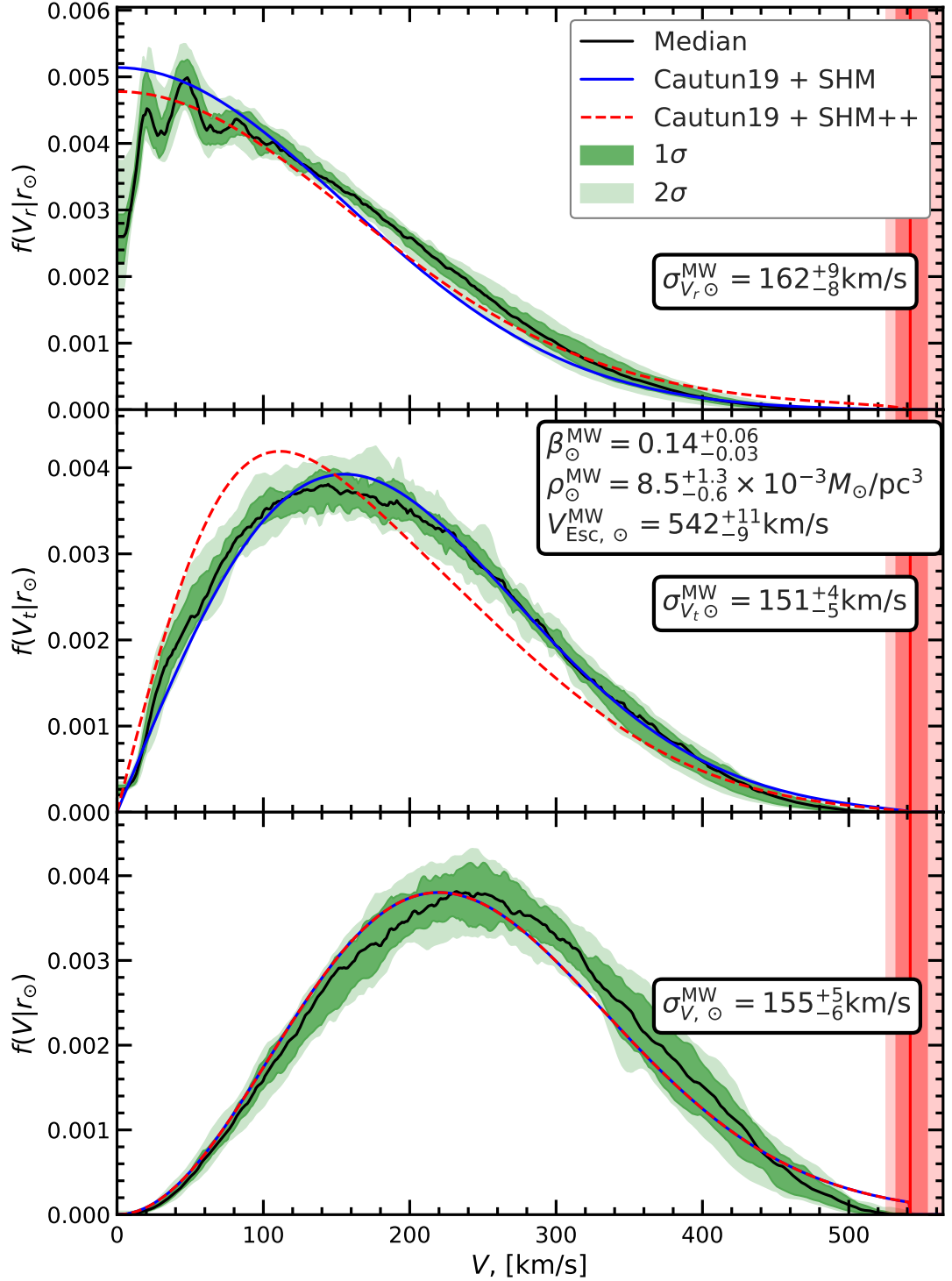
Figure 3.11

The DM velocity distribution at the Solar radius, $r_\odot = 8\,\text{kpc}$, as predicted by our halo contraction model. The velocities are with respect to the Galactic Centre. The radial, tangential, and total velocity distributions are shown in the top, middle and bottom panels, respectively. The median is indicated with a solid black line and the 68 and 95 percentiles are shown in shaded green. The blue curve illustrates the velocity distributions given by the Standard Halo Model (SHM) and the dashed red curve shows the 'SHM++' variant of Evans et al. (2019), both using $V_{\text{Circ},\odot}$ and $V_{\text{Esc},\odot}$ of the Cautun19 MW mass model. We also give several DM properties at the Solar radius (see text inserts in the panels) as predicted from our model: the local DM density, $\rho_\odot$; the components of the velocity dispersion, $\sigma_\odot$; the velocity anisotropy, $\beta_\odot$; and the escape velocity, $V_{\text{Esc},\odot}^{\text{MW}}$ (whose value is also shown as the red shaded region).

for the key astrophysical inputs to direct DM detection experiments: the density and velocity distribution of the DM in our own solar neighbourhood.

From the DM density profile shown in the top panel of Fig. 3.10 we find that our models predict $\rho_\odot = 8.5^{+1.3}_{-0.6} \times 10^{-3} M_\odot/\text{pc}^3$ (equivalently $\rho_\odot = 0.32^{+0.05}_{-0.02}/\text{GeV}/\text{cm}^3$). This values are in good agreement with previous estimates (see the compilation by Read, 2014). The somewhat large uncertainties in our estimate of $\rho_\odot$ could be significantly reduced if we were to restrict our analysis to those DFs that best fit the MW rotation curve, or individually fit the MW baryon distribution for each DM halo as discussed at the end of the previous section. We find a local speed escape velocity 542^{+11}_{-9}km/s, which is consistent with the recent *Gaia* DR2 measurements of Deason et al. (2019a) and Grand et al. (2019).

In Fig. 3.11 we highlight the DM velocity distributions at the Solar position predicted by our MW models. These were derived using the method described in Section 3.3.3 where, for each model, we sum the orbits of all DM particles to find the distribution of radial, tangential and total velocity components. The resulting VDFs have very similar forms to those previously discussed for the Au5 halo (see Fig. 3.9) and many of the conclusions reached for that example apply here too. In particular, we predict a small radial bias in the velocity anisotropy, $\beta_\odot = 0.14^{+0.06}_{-0.03}$, with the radial and tangential velocity dispersions being $\sigma^{\text{MW}}_{V_r,\odot} = 162^{+9}_{-8}$km/s and $\sigma^{\text{MW}}_{V_t,\odot} = 151^{+4}_{-5}$km/s. These and other values are summarised in Table 3.1, where we also compare our results to those from the recent MW mass model of Cautun19. In this table the velocity dispersion's and anisotropy given for Cautun et al. and the results of applying the SHM with the parameters inferred from the Cautun et al. MW mass model. See Sec. 3.3.3 for further details and discussion on the SHM.

The SHM is in good overall agreement with our inferred velocity distribution, although we find large fractional deviations in the high velocity tail of the distribution, the region to which DM direct detection experiments are most sensitive (Bozorgnia et al., 2020). The SHM model assumes an isotropic velocity distribution, at odds with the value of $\beta_\odot \sim 0.14$ in our model. As a result, the SHM does not perform as well when compared against the radial and tangential velocity distribution of our model.

We also give the predictions of the SHM^{++} model of Evans et al. (2019) in the fourth

column of Table 3.1 and as the red dotted line in Fig. 3.11. This is a SHM model modified to include a secondary, highly radial distribution of DM, inspired by evidence that the MW experienced a strongly radial major merger in the past (Belokurov et al., 2018). Alongside a normal isothermal SHM velocity distribution, a fraction of the DM, $f_\mathrm{S} \approx 0.2$, is modelled as a highly radial component, $\beta_\mathrm{merger} \approx 0.9$, as an approximation of the contribution from the radial merger (see Evans et al. 2019 for further details). The resulting overall distribution has a radial anisotropy of $\beta_\odot^{++} = 0.3$, which is more highly anisotropic than any of our Auriga halos. While not explicitly split into separate distributions, the action distributions of our DM halos reflect the accumulated merger history of each halo. Our analysis of these halos suggests that, typically, DM halos are inherently likely to have a slightly radially biased velocity distribution in the solar neighbourhood. Modelling individual contributions to the final DM halo as separate distributions is an interesting possibility but is beyond the scope of this Chapter, and is left to future work.

3.5 Conclusions

We have used the AURIGA suite of hydrodynamical simulations of Milky Way (MW) analogues to investigate the orbital distribution of DM particles in MW-mass halos and to study how this distribution changes when including baryonic physics in the simulations. We have characterised the DM halos in terms of the distribution of spherical actions: radial action, J_r, and angular momentum, L. We have studied these action DFs for all our relaxed halos and have described how the actions can be used to (re)construct the density and velocity distribution of the simulated DM halos. This can be achieved using an iterative method that, starting from a fixed baryonic distribution and an initial guess for the gravitational potential, constructs a DM halo density profile. At each step in the iteration the potential is updated from the DM mass profile obtained in the previous step until convergence is achieved.

The actions J_r and L are useful quantities for describing DM halos since they are conserved during adiabatic changes (i.e. on long timescales) in the gravitational potential. Many

galaxy formation processes, although not all, are thought to be adiabatic and this suggests that halos in dark matter only (DMO) and Hydro simulations should have similar $F(J_\mathrm{r}, L)$ distribution functions. This idea motivated us to investigate if indeed the action DF is conserved in the AURIGA suite between the DMO simulations and the simulations that include galaxy formation physics. We have found good agreement between the actions in the DMO and Hydro halos, with differences at the $5 - 10\%$ level. Most of these differences are due to statistical fluctuations; however, we also find systematic variations, with J_r being lower in the Hydro halos. This difference in radial action leads to an $\sim 8\%$ underprediction of the DM density profile when adiabatic contraction of a DMO halo is assumed. The J_r systematic difference is the same at all radii, suggesting that it is unlikely to be caused by effects associated with baryonic feedback which would mainly affect the central region of a halo.

If we know the $F(J_\mathrm{r}, L)$ actions of a halo in a DMO simulation, we can predict the density and velocity profile of its counterpart in the hydrodynamical simulation with a precision of $\sim 5\%$ (not withstanding the systematic effects discussed above). Most of the scatter is due to stochastic effects as well as to small deviations from the steady state assumption implicit in our method. This object-to-object scatter is a factor of two lower than for other methods, such as that of Cautun19. However, if we do not know the exact $F(J_\mathrm{r}, L)$ distribution, we recover the density profiles only with $\sim 15\%$ precision, with the major limitation being the halo-to-halo scatter in the action distributions.

We have illustrated the contraction of a DM halo in the presence of baryons by decomposing the halo into individual orbits of DM particles. The deeper potential in the Hydro case leads to a contraction, i.e. an inward shift, of the orbits. For a fixed orbital angular momentum, circular orbits contract the most while highly elliptical orbits contract the least. The DM halo is specified by the sum of all orbits as given by the $F(J_\mathrm{r}, L)$ distribution. This property can be used to determine both the density and velocity distribution profiles of a halo.

We have applied our DM halo construction method to the halo of the MW. Starting from the $F(J_\mathrm{r}, L)$ distribution of relaxed AURIGA Hydro halos, in combination with the Cautun19

stellar and gas model of the MW and the value of the MW mass of Callingham19, we have predicted the density and velocity distribution of our galaxy's DM halo. This resulted in 17 models for the Galactic DM halo, which span possible DM distributions given the MW's baryonic component. We find good consistency between our inferred DM halo density and that inferred by Cautun19, and between the circular velocity curve predicted by our models and the one measured from *Gaia* DR2 data (Eilers et al., 2019). The consistency with the Cautun19 results provides an independent check that their DM halo contraction model gives a good description of the Galactic DM distribution.

A major advantage of our halo (re)construction method is that it can predict the velocity distribution of DM particles. We have tested this aspect of our method by comparing directly against measurements of the AURIGA halos and found very good agreement. In particular, our method does better than the Standard Halo Model (SHM) at reproducing the high tail of the velocity distribution, a key input into direct DM detection experiments. We have applied the same analysis to the MW to predict the distribution of DM particle velocities and their components in the solar neighbourhood. Our results are in good agreement with the literature (e.g. Evans et al., 2019), and predict that the DM particles have a preference for radial orbits, with $\beta_\odot = 0.14^{+0.07}_{-0.03}$, and that the SHM overpredicts the high velocity tail of the velocity distribution. Furthermore, by using multiple action distributions, we have characterised the halo-to-halo scatter in the velocity distribution, which is important for understanding how robust are the constraints inferred from direct DM detection experiments.

A potential improvement to this work would be to extend the formalism to axisymmetric models, which provide a better description of disc galaxies such as the MW. In this case, the DM halo is described by the 3D action distribution, $F(J_R, L_z, J_z)$, where (R, z) denote the coordinates in the plane of the disc and perpendicular to it. (For an example of axisymmetric modelling, see Cole & Binney (2017).) As already discussed, the inner regions of DM halos in hydrodynamical simulations are close to spherical, much more so than in their DMO counterparts, and within this work we have found no obvious correlation between the shape of the DM halos and the results of our contraction method. we therefore

expect the effects of including axisymmetry to be subdominant to the effects of halo-to-halo scatter.

Our work leaves open an important question: which baryon processes are responsible for the systematic difference in the action distribution between the DMO and the Hydro halos? While such effects are small, about a few percent, they produce a measurable effect on the density profile and velocity distribution. To overcame this systematic when modelling the MW, we have used the $F(J_{\rm r}, L)$ distribution measured directly in the Hydro simulations. It remains to be seen if the same systematic deviations between DMO and Hydro halos are present in other simulations and if the size of the effect varies between the various subgrid galaxy formation models implemented in different simulations.

In this work, when making predictions specifically for the MW, we employ a range of possible action distribution functions of a MW-mass halo as predicted by the AURIGA project. However, given the observations, e.g. the MW rotation curve, some distributions are more likely than others. This raises the question of which is the best fitting $F(J_{\rm r}, L)$ distribution for the MW, which we leave for future work. To address this will require modelling the still uncertain MW baryon mass distribution self-consistently alongside the DM distribution, since this is degenerate when predicting the inner ($\lesssim 50$ kpc) rotation curve (for details see Cautun19). Such a study is very worthwhile and timely, especially given the wealth of Galactic data available in the current and future *Gaia* data releases.

The method we have presented here provides a very comprehensive tool for modelling DM halos in the presence of baryons and, furthermore, it can easily account for cosmological halo-to-halo variations in halo properties. In the age of precision MW astronomy it is no longer possible to neglect the contraction of the Galactic DM halo or the diversity of DM distributions that form a halo. Our method provides an elegant and robust approach to incorporate these effects.

3.6   Appendix

3.6.1   Radial distribution of orbits

Here we describe how to construct the probability distribution that a particle on a orbit defined in terms of (J_r, L) is found at radial distance, r. We denote this radial probability distribution as $F\,(r|J_\mathrm{r}, L)$. For simplicity, in the following we will work with the (E, L) actions (and thus calculate $F\,(r|E, L)$), which, given a gravitational potential, can be uniquely mapped to (J_r, L) space and *vice-versa* (see main text for details).

Consider an orbit defined by (E, L) in the potential $\Phi\,(r)$. The velocity components at r are defined as:

$$v|_r = \sqrt{2\,(E - \Phi\,(r))}$$
$$v_t|_r = L/r \tag{3.6.1}$$
$$v_r|_r = \sqrt{v|_r^2 - v_t|_r^2},$$

where for the radial velocity component we only consider its absolute value. A tracer on that orbit could have either negative or positive v_r depending on whether it is approaching or receding from the halo centre. The two points where $v_r = 0$ correspond to the peri- and apocentre of the orbit, r_min and r_max, with particles on the orbit spanning the radial range, $r_\mathrm{min} < r < r_\mathrm{max}$.

As described in the main text, the radial distribution of an orbit, either $F\,(r|E, L)$ or $F\,(r|J_\mathrm{r}, L)$, is defined as the proportion of time an orbit spends at radial distance, r, normalised to unity. To calculate this, we first consider the amount of time, $\mathrm{d}t$, taken by a test particle to travel from $r \rightarrow r + dr$. By Taylor expansion, we have

$$r + \mathrm{d}r = r + v_r \mathrm{d}t + \frac{1}{2}\ddot{r}\mathrm{d}t^2 + o\left(\mathrm{d}t^3\right)\,, \tag{3.6.2}$$

where $\ddot{r}$ denotes the radial acceleration, i.e. the second derivative of r with respect to time. By neglecting dt^3 and higher order terms, we can solve for $\mathrm{d}t$ to obtain

$$\mathrm{d}t = \frac{-v_r + \sqrt{v_r^2 + 2\ddot{r}\mathrm{d}r}}{\ddot{r}}\,. \tag{3.6.3}$$

Away from the endpoints, $v_r^2 \gg 2\ddot{r}\mathrm{d}r$ for small $\mathrm{d}r$. Then $\mathrm{d}t \approx \mathrm{d}r/v_r$, that is the time spent at r is inversely proportional to the radial velocity component, as expected. As the test particle approaches the endpoints, $v_r \to 0$ and the radial acceleration terms can no longer be neglected. Then, the fraction of time spent at r, i.e. the radial distribution $F(r|E, L)$, can be written as

$$F(r|E, L)\, \mathrm{d}r = \frac{2}{T|_{E,L}} \mathrm{d}t|_r \, , \tag{3.6.4}$$

where the factor of 2 accounts for the fact that a particle is found at the same r value twice along its orbit, i.e. once when approaching and once when receding from the halo centre. The normalisation factor, $T|_{E,L}$, is the radial time period, which is given by

$$T|_{E,L} = 2 \int_{r_{\min}}^{r_{\max}} \mathrm{d}t|_r \mathrm{d}r. \tag{3.6.5}$$

To calculate $F(r|E, L)$ we use a radial grid with 1500 cells defined in the range $[0, 3R_{200}]$; this corresponds to a grid spacing, $\mathrm{d}r = R_{200}/500 \sim 0.5\mathrm{kpc}$. Special treatment is required at the endpoints of the orbit where better spatial resolution is needed to track the orbit properly. The radial distribution and properties around 1kpc of the end points of each orbit are then recalculated at a higher radial resolution of $\mathrm{d}r^* = 5\mathrm{pc}$.

Averaged radial properties, such as the velocity dispersion or the velocity components, can be evaluated at a given radius using $F(r|J_r, L)$ as a weight. Any general orbital property depending on radius, $X(r)|_{J_r,L}$, can be calculated as

$$\langle X \rangle (r) = \frac{1}{\rho(r)} \frac{M}{4\pi r^2} \iint X(r)|_{J_r,L} F(r|J_r, L)\, dJ_r dL \, . \tag{3.6.6}$$

3.6.2 Systematic Differences in Action between DMO and Hydro

Differences between DM halos, such as in the $\rho(r)$, $\sigma(r)$ and $\beta(r)$ profiles, can be attributed to differences in their action distributions, $F(J_r, L)$. It is natural to expect that the greater the action difference, $\Delta_{(J_r,L)}$, between our DMO and Hydro halos, the greater the difference in the contracted DM density profile. We explore this correlation in Fig. 3.12, which shows the integrated difference in the density profiles, $\Delta_\rho^{\text{total}}$, between
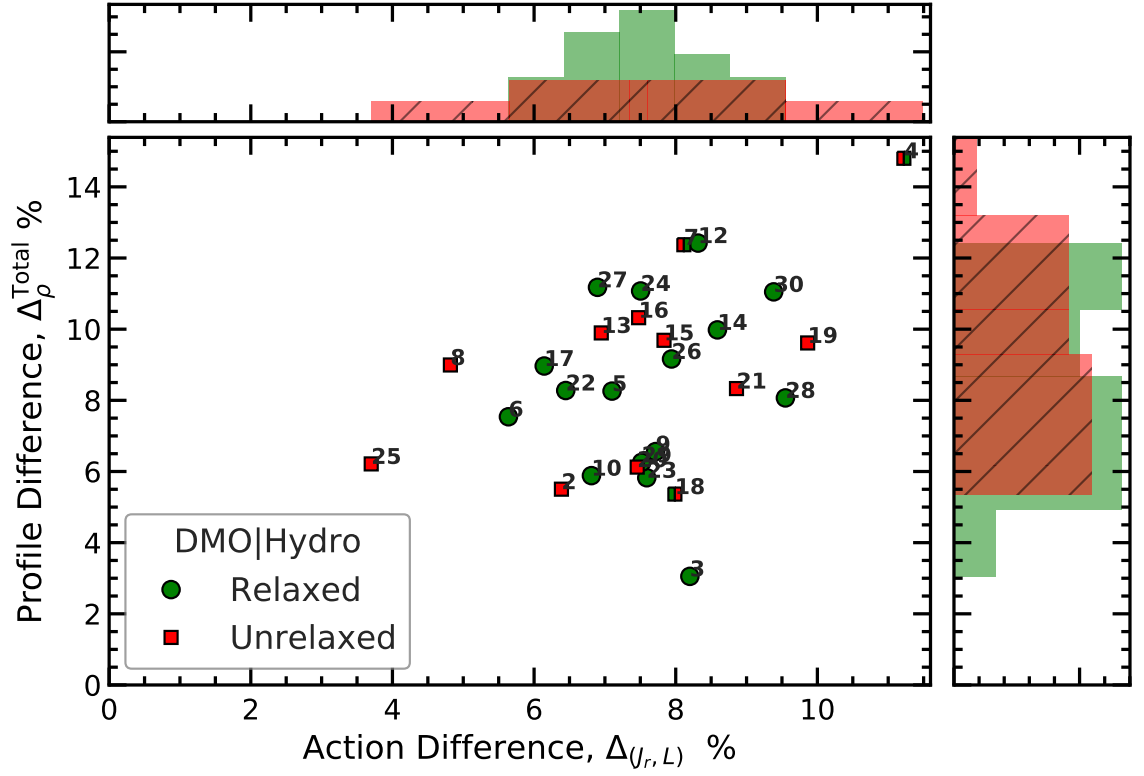
Figure 3.12

An exploration of the extent to which galaxy formation in the AURIGA suite is an adiabatic process. The *x*-axis show the difference in the action distributions, $\Delta_{(J_r,L)}$, of DM halos between the DMO and corresponding Hydro simulations. An adiabatic process would conserve the action, i.e. $\Delta_{(J_r,L)} = 0$. The *y*-axis shows the integrated difference, Δ_ρ^{total}, in the DM density profiles between the contracted DMO halo and the Hydro halo. Each symbol represents one AURIGA system and the green circle or red square indicate if the halo is relaxed or unrelaxed. (See text for definitions and further details.) In the relaxed sample, the $\Delta_{(J_r,L)}$ and Δ_ρ^{total} quantities show only a slight correlation (0.16), suggesting a complex relationship between differences in action distributions and differences in the final contacted profile.

the contracted DMO halo and the Hydro halo as a function of the difference in the action, $\Delta_{(J_r,L)}$, between the two halos. In the relaxed halo sample, the $\Delta_\rho^{\text{total}}$ and $\Delta_{(J_r,L)}$ quantities are characterised by a small correlation of only 0.16. This suggests a complex relationship between action distributions and the physical halo. The relaxed sample has consistent differences of $\Delta_\rho^{\text{total}} \sim 8\% \pm 3\%$, while the unrelaxed sample has a a wider scatter and a higher median $\Delta_\rho^{\text{total}} \sim 10^{+10}_{-3}\%$ (a histogram of the results may be seen in the side panel of Fig. 3.12).

To better understand the effect of systematic differences in the $F(J_r, L)$ distribution between the DMO and Hydro simulations, we proceed to compare in Fig. 3.13 the radial profiles of several halo properties. in the main text, when constructing the DM density profile given a $F(J_r, L)$ distribution, we find the self-consistent gravitational potential given the action distribution. However, differences in actions can lead to differences in potentials that would further enhance differences in DM halo properties. To control for changes in potential, the results in Fig. 3.13 are obtained by constructing the DM halos using the same fixed potential, Φ_{Hydro}, measured in the Hydro simulation. This allows a direct comparison of the orbital structure in physical space, providing insight into the dependence of the differences in density profile on the differences in action distributions. The potential mechanisms behind non-adiabatic effects can also be explored through the radial dependence of the action differences.

In Fig. 3.13 we consider the fractional differences in the density and average actions as a function of radius. In the top panel we see a $\sim 5\%$ underprediction of the DM density when using actions of the DMO halo compared to the Hydro. The slightly changed potential generated with this density profile causes the density difference to grow with the iteration to $\Delta_\rho^{\text{total}} \sim 8\%$ in the final self consistent profile. For L, we find very small systematic differences, but nonetheless the Hydro simulations tend to have slightly higher L values in the very inner regions and for $r \sim 0.3R_{200}$. In contrast, the energy distribution is characterised only by small stochastic differences.

The J_r in the DMO halos is systematically higher at all radii away from the very centre $r \gtrsim 0.1R_{200}$ (second panel). For a single orbit, increasing J_r causes the median position
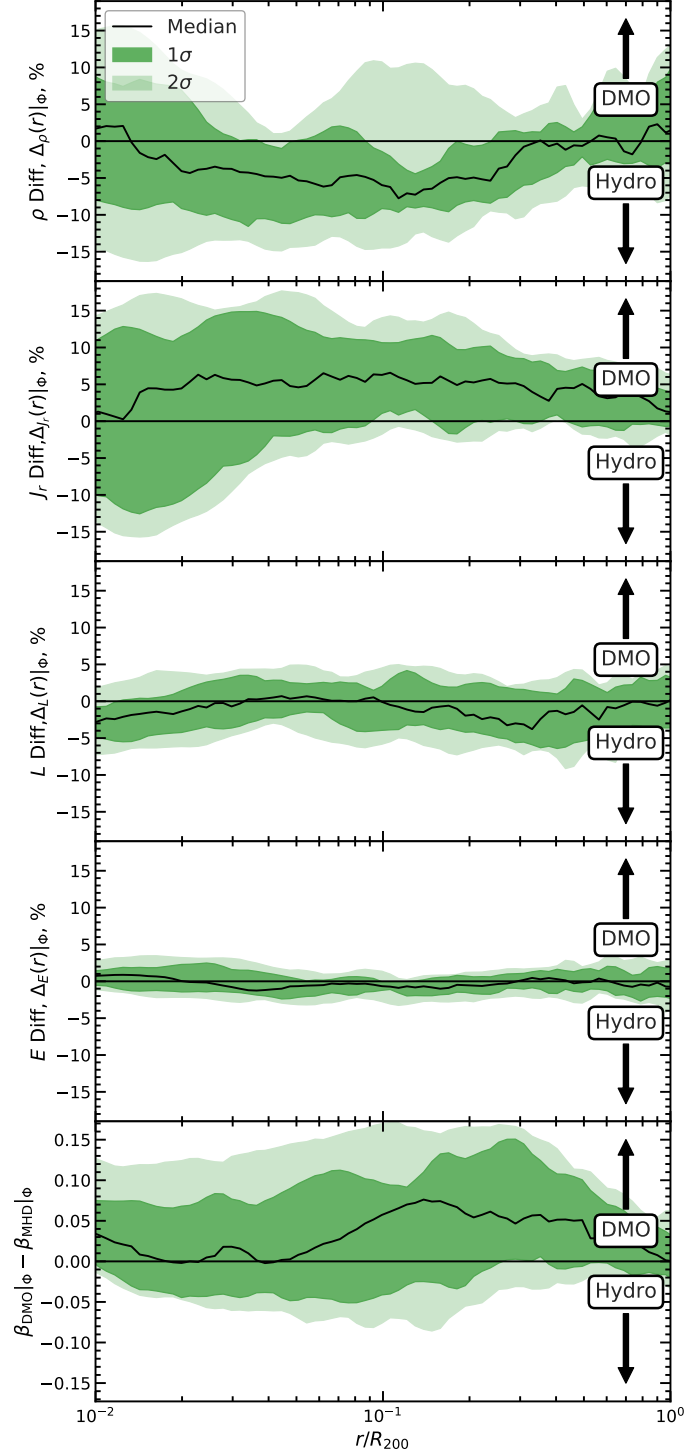
Figure 3.13

The fractional differences in selected halo properties as a function of radial distance. We plot the difference between halo quantities calculated using the $F(J_r, L)$ distribution measured in the DMO and in the counterpart Hydro simulation. When reconstructing the halo properties we use *the same fixed potential*, Φ_{Hydro}, measured in the Hydro simulation; in this way any difference in the plotted quantities are due to variations in the action distribution between the DMO and Hydro halo, and not to changes in the potential. We show, from top to bottom, the differences in the radial profile of: density, average radial action, average angular momentum, average energy, and average velocity anisotropy. The black line gives the median for our sample of relaxed AURIGA halos, and the dark and light green regions the 68 and 95 percentiles, respectively. The DMO density profile, ρ (top panel), is systematically lower than in the Hydro counterpart, driven by a systematic suppression of radial action in the Hydro halo at every radius (second panel).

of an orbit $\langle r \rangle |_{\mathrm{Orbit}}$ to move radially outward, and mass to move from the radial centre of the orbit to its endpoints, as seen in Fig. 3.6. This effect across all orbits seems to drive the difference in density profile (top panel): the density is higher in the Hydro halos at intermediate radii, but the density is higher in the DMO halos at the centre and near R_{200}. The higher radial action gives more radial orbits in the DMO case, increasing β_{DMO} (see bottom panel of Fig. 3.13).

For a discussion of how the results shown in Fig. 3.13 can be used to understand the effects driving the non-adiabatic change in DM actions between the AURIGA DMO and Hydro simulations, we refer the reader to the last paragraph of Section 3.3.2.

CHAPTER 4

The chemo-dynamical groups of the Milky Way's globular clusters

4.1 Introduction

Of the accreted material in the stellar halo, GCs have long been recognised as sensitive probes of the accretion history of the MW (Searle & Zinn, 1978). Several GCs are suspected to be the nucleus of accreted dwarf galaxies (M54, M4, ω-Centuari, NGC1851), directly showing where the cores of fallen progenitors come to rest. Furthermore, while major mergers dominate the stellar halo, it has been shown that GCs are more representative of smaller accretion events of the MW's past (Harris et al., 2015; Amorisco, 2019). When studying the origin of the MW's GC system, it is necessary to identify which of the MW's GCs were born natively in our Galaxy (insitu GCs) and which formed in dwarf galaxies and later accreted.

On average, in the MW, there is a rough trend of metal-poor GCs at higher radius, while metal-rich GCs are more centrally concentrated. However, this is not enough to distinguish populations on chemistry alone (Trujillo-Gomez et al., 2020). With precise age metallicity data now available for many GCs, it has been discovered that the MW GCs age-metallicity

relation (AMR) is composed of two branches: a metal-poor one characterised by halo-like kinematics and a metal-rich branch whose GCs have centralised orbits, suggesting an insitu origin (Forbes & Bridges, 2010; Marín-Franch et al., 2009; Leaman et al., 2013). This behaviour can be understood using simple models, such as a leaky-box chemical enrichment model, in which the stellar birth environment in dwarf galaxies enriches slower than larger galaxies such as our own.

The recent explosion in Galactic data, such as those from the *Gaia* mission (**?**), APOGEE (Majewski et al., 2017), the H3 survey (Conroy et al., 2019), and GALAH (Martell et al., 2017) have revolutionised the field of Galactic astronomy. In particular, they have revealed evidence of an ancient major merger, *Gaia*-Enceladus-Sausage (GES) (Belokurov et al., 2018; Helmi et al., 2018a). Combined with previous discoveries such as the stellar stream of the Sagittarius dwarf galaxy (Ibata et al., 1994) and the Helmi streams Helmi et al. (1999) there is a wealth of known structure present in the Galactic stellar halo (Naidu et al., 2020). Characterising the properties of the progenitors of these structures is challenging, since they represent extended and diffuse stellar distributions. One solution is to identify the GCs associated with these structures, since the GCs are compact and bright objects whose properties and orbits can be measured more accurately.

There have been multiple works that have tried to associate GCs to stellar halo structures. The Sagittarius dwarf galaxy is currently being disrupted (Ibata et al., 1994), and its material and GCs can be found as an identifiable stream (Bellazzini et al., 2020; Antoja et al., 2020; Law & Majewski, 2010; Peñarrubia & Petersen, 2021). The works of Myeong et al. (2018a,c) have associated GCs to GES debris, Koppelman et al. (2019a) identified seven GCs as part of the Helmi streams, and Myeong et al. (2018b, 2019); Barba et al. (2019) have investigated the retrograde GCs FSR1758 and ω-Centuari, which they have speculated to be part of a new accretion event dubbed Sequoia.

A significant development has taken place with the work of Massari et al. (2019), hereafter Massari19, that has studied a large sample of 160 Galactic GCs to identify all the major GCs groups. They have done so by defining selection boxes in energy and angular momentum space that are based on 'known' accretion groups and expanding to include all likely GCs

members. GCs leftover from this process without a clear accretion origin were divided into a high energy group, which is likely a collection of smaller accretion events, and a lower energy group that was thought to potentially be a signature of an ancient accretion event. This GC grouping has been improved further by Horta et al. (2020), hereafter Horta20, which have added APOGEE alpha element abundances for 46 inner GCs make minor revisions.

The Low Energy group of Massari19 is in good agreement with the Kraken event, predicted in Kruijssen et al. (2019b, 2020) to be the MW's most ancient merger. This work identified the structure by comparing the observed distribution of MW GCs with the predictions of the EMOSAICs hydrodynamic simulations for GC formation and evolution (Pfeffer et al., 2018; Kruijssen et al., 2019a). This merger is probably the same as the Koala event of Forbes (2020), hereafter Forbes20, and the Inner Galaxy System (or later Heracles) of Horta et al. (2021).

Once the accretion groups have been identified, the number of GCs, the age-metallicity relation and the dynamics can all give clues about the progenitor galaxy. For example, the Massari19 results have been used by Forbes20 and Trujillo-Gomez et al. (2020) to reverse engineer the assembly history of the MW. The GC AMR relation provides clues on the formation time and the chemical enrichment of the progenitor dwarf (Forbes20). Using the age metallicity spread, Kruijssen et al. (2020) suggests that the MW has experienced 2-3 major mergers, and at least 15 mergers for GCs total. Using the dynamics of accreted GCs, Pfeffer et al. (2020) predicts that groups with small apocentres indicate an ancient or massive merger.

The number of GCs in a progenitor galaxy is related to its mass. For LMC-mass and more massive galaxies, observations have revealed a linear relationship between the number and total mass of GCs and the halo mass of the host galaxy (Forbes et al., 2018). Theoretical models reproduce this trend (such as Boylan-Kolchin, 2017; Burkert & Forbes, 2020; Bastian et al., 2020). However, it is unclear if this relation holds for dwarf galaxies with stellar masses below 10^9 M$_\odot$ Observationally it is difficult to measure the halo mass of such systems, and theoretical predictions in this range do not agree. At lower masses, analytical

models based on hierarchical clustering predict a continuation of the linear relation between GC mass and total halo mass (e.g. Boylan-Kolchin, 2017), while the EMOSAICs project predicts a linear relation with stellar mass instead of halo mass (Bastian et al., 2020).

One limitation of the current GC groups is that they are defined via a rather subjective approach, mostly by eye. This methodology raises questions if the current groupings are statistically robust and physically relevant. Furthermore, subjective methods are very difficult to test using mock catalogues, but this represents an essential analysis step to trust their results (e.g. see Wu et al., 2021). Alternatively, recent work has seen the use of clustering algorithms to find structures in the halo. (such as Ostdiek et al., 2020; Necib et al., 2020; Koppelman et al., 2019b; Helmi et al., 2017; Myeong et al., 2018b). These should give more objective, quantifiable results, but as noted in Naidu et al. (2020), it can be challenging to tune these clustering methods to our astrophysical problem. A few studies have looked at applying these techniques to GCs specifically. Examples include using a friends-of-friends clustering algorithm to associate GCs to the Sequoia merger (Myeong et al., 2018c) and the decomposition of GCs in the centre of our galaxy into bulge, disc and halo components (Pérez-Villegas et al., 2019). However, we know of none that have yet been applied to the total Galactic population of GCs.

In this paper, we develop an objective methodology combining chemo-dynamical information to identify the likely progenitors of the full population of Galactic GCs. By fitting models to both the dynamical distribution in action space and age-metallicity relation of the accreted galaxy, we calculate membership probabilities for each globular cluster and statistically link them to particular accretion events. We do so by modelling the GCs as a combination of bulge, disc, and halo components, the latter representing the subject of our research. The stellar halo is further decomposed into the massive merger events that built it, such as GES, Kraken, and Sagittarius, and an ungrouped component that represents contributions from lower mass mergers that did not contribute enough GCs be robustly identified. This methodology is extensively tested and characterised using mock GC catalogues built from the AURIGA suite of hydrodynamical simulations (Grand et al., 2017). We apply the method to the Galactic GCs and fully account for observational errors

to identify the most likely GCs associated to each merger event. Using this membership, properties of the progenitor galaxies, such as halo and stellar masses, are derived.

The structure of the paper is as follows. Section 4.2 describes our chemo-dynamical mixture model. In Section 4.3 we describe the construction of our mock globular GCs catalogues from AURIGA haloes, and in Section 4.4 we apply our method to the mocks. In Section 4.5 we apply our method to the MW and discuss the individual cluster fits, comparing to the literature. We discuss the implications for the MW's accretion history in Section 4.6. Finally, Section 4.7 summarises and concludes the paper.

4.2 Multi-component model for the Galactic GC population

We model the MW's population of GCs as a combination of a bulge, disc, and stellar halo components. The latter is the main focus of our work and is further split into subgroups that correspond to all known major accretion events, such as GES and Kraken. The decomposition is performed using an expectation-maximization algorithm using chemo-dynamical data, that is combining age-metallicity information with orbital integrals of motions (i.e. action space). This section presents a detailed description of the decomposition method and its motivation.

For a general space X, which represents a combination of metalliticy and action quantities, each GC component is modelled as a distribution $F_c(\mathbf{X}) \equiv F(X|\boldsymbol{\theta}_c)$ specified in terms of a set of model parameters, $\boldsymbol{\theta}_c$, whose details will be given when discussing each model component. $F_c(\mathbf{X})$ is normalised to integrate to 1 over the space $\mathbf{X}$. Then, the multi-component model describing the overall population of GCs is given as the sum over each individual component,

$$F(\mathbf{X}) = \sum_c^{\text{Com}} W_c F_c(X) \,, \tag{4.2.1}$$

where W_c denotes the weight of component c and specifies the fraction of the GC population that is contributed by each component. The total distribution, $F(\mathbf{X})$, normalises to unity

over the space, which implies that:

$$\sum_{c}^{\text{Com}} W_c = 1 \ . \tag{4.2.2}$$

The probability of the i-th GC to belong to component c, which is often referred to as the responsibility in multi-component models, such as Gaussian mixture models, is given by

$$r_{ic} = \frac{W_c F_c(X_i)}{\sum_{c'} W_{c'} F_{c'}(X_i)} \equiv \frac{p_{ic}}{\sum_{c'} p_{ic'}} \ , \tag{4.2.3}$$

where X_i denotes the coordinates of the i-th GC in the chemo-dynamical space used to identify the different populations. For brevity, we also introduced the notation, $p_{ic} \equiv W_c F_c(X_i)$, which gives the value of the F_c distribution at X_i multiplied by the weight of that component. The total log-likelihood, $\ln \mathcal{L}$, of the mixture model is given as:

$$\ln \mathcal{L} = \sum_{i}^{\text{GCs}} \ln F(X_i) \equiv \sum_{i}^{\text{GCs}} \ln \left(\sum_{c'}^{\text{Com}} p_{ic'} \right) , \tag{4.2.4}$$

where in the right-most term the first sum is over all the GCs in the system and the second sum is over all components of the model. To find the maximum likelihood estimate, we need to find the maximum of $\mathcal{L}$ for the set of parameters $\{\boldsymbol{\theta}_c\} \equiv \{\boldsymbol{\theta}_{c=1}, \boldsymbol{\theta}_{c=2}, ..., \boldsymbol{\theta}_{c=K}\}$, where K is the number of components and each $\boldsymbol{\theta}_c$ is in turn a set of multiple parameters. For example, if we model a component as a Gaussian distribution, then $\boldsymbol{\theta}_c$ is the combination of peak position along each coordinate axis in X-space and the corresponding covariance matrix. The maximization procedure is further complicated by the fact that the W_c weights that appear in the $p_{ic'}$ expression depend on the values of all the $\{\boldsymbol{\theta}_c\}$ parameters which makes for a very non-linear and multi-dimensional maximization procedure.

To solve this challenge, we use the expectation-maximization approach. This algorithm is often used to efficiently fit Gaussian mixture models. As explained below, our methodology is similar, but adapted to include relevant astrophysics such as the AMR of the component. The algorithm represents an iterative approach of finding the maximum likelihood and has the following steps:

(i) Initialisation:

An initial guess is made for the responsibilities, r_{ic}. The outcome can be sensitive to this initial choice, especially when the components are considerably overlapping. We discuss and test this aspect in the mock test section.

(ii) <u>Maximisation Step:</u>

In this step, we assume that the responsibilities, r_{ic}, are known and we find the $\{\boldsymbol{\theta}_c\}$ parameters that maximize the log-likelihood, $\ln \mathcal{L}$, for fixed r_{ic} values. The advantage is that once r_{ic} are known, maximising $\ln \mathcal{L}$ reduces to a much simpler problem in which the parameters of one component are independent of the parameters of the remaining components. For component c, $\ln \mathcal{L}$ is maximal for the $\boldsymbol{\theta}_c$ values that maximize the expression:

$$\sum_i^{\text{GCs}} r_{ic} \log F_c(\boldsymbol{X}_i) \; . \tag{4.2.5}$$

In the above equation each data point contributes with a weight r_{ic}, which is why r_{ic} is called the responsibility.

(iii) <u>Expectation Step:</u>

The values of the responsibilities are updated using the $\{\boldsymbol{\theta}_c\}$ parameters found in the previous step.

(iv) <u>Iteration:</u>

Repeat the maximisation and expectation steps until $\ln \mathcal{L}$ is converged. In practice, we assume convergence when $\ln \mathcal{L}$ changes between consecutive steps by less than 0.01 times the number of globular clusters.

The space $\mathbf{X}$ we use to identify the components of the GC population is a combination of orbital dynamical quantities, which we denote with $\mathbf{Y}$, and age-metallicity information, which we denote with $\mathbf{Z}$. We assume that the orbital quantities are uncorrelated with the chemistry of GCs, which implies that the distribution function of each component can be split into two independent distributions:

$$F_c(\mathbf{X}) = F_c^{\text{dyn}}(\mathbf{Y}) \, F_c^{\text{AMR}}(\mathbf{Z}) \tag{4.2.6}$$

In the following, we describe how we model the distribution of dynamical quantities, $F_c^{\text{dyn}}(\mathbf{Y})$, and of the age-metallicity relation, $F_c^{\text{AMR}}(\mathbf{Z})$, where we drop the superscripts for brevity. These functions are independent, and so can be fit by maximising their respective likelihoods (with Eq. 4.2.5) independently.

4.2.1   Dynamical Modelling

In this work, we primarily consider a four-dimensional dynamical space consisting of the orbital energy and the three orbital actions: the component of the angular momentum perpendicular on the disc plane, L_z, the radial action, J_R, and vertical action, J_z. The integrals of motions, $\mathbf{J}$, completely describe the orbit, which determines the orbital energy (for more information see Binney & Tremaine (2008)). This means that in the $(E, \mathbf{J})$ four-dimensional space the GCs lie on a three-dimensional surface. This suggest that the energy only contains redundant information about the orbits, however tests on mock catalogues (more on this in section 4.4) show that the combined $(E, \mathbf{J})$ space leads to a more accurate identification of GCs populations than $(\mathbf{J})$ space, justifying the choice.

4.2.1.1   Accreted GCs

The accreted components are modelled as multivariate Gaussian distributions in the $\mathbf{Y} = (E, L_z, J_R, J_z)$ space via

$$
\begin{aligned}
F_c(\mathbf{Y}) &= N(\mathbf{Y}|\boldsymbol{\mu}, \boldsymbol{\Sigma}) \\
&= \frac{1}{\sqrt{(2\pi)^k |\boldsymbol{\Sigma}|}} \exp\left(-\frac{1}{2}(\mathbf{Y} - \boldsymbol{\mu})^T \boldsymbol{\Sigma}^{-1}(\mathbf{Y} - \boldsymbol{\mu})\right)
\end{aligned}
\tag{4.2.7}
$$

where $k = 4$ is the number of dimensions of the space $\mathbf{Y}$, $\boldsymbol{\mu}$ is the mean, and $\boldsymbol{\Sigma}$ is the covariance matrix. The values of these parameters that maximize the total model likelihood can be found analytically from Eq. (4.2.5) by calculating moments of the distribution.

In reality, the accreted material is unlikely to be well represented by a Gaussian distribution. We find that due to the relatively small number of GCs, alternative 'assumption free'

distributions, such as density kernels, do not work effectively, and it necessary to assume a form for the distribution. The limitations, and possible biases, of this assumption are discussed in the conclusions section of this Chapter.

If the number of points, N_{points}, that a multivariate Gaussian distribution is fit to is equal to or less than k then the covariance matrix becomes degenerate with some eigen values equalling zero, giving infinitesimal width in the corresponding principle axes. For example, in 2-dimensional space two points will be fit as a line. For our model, in principle all data points contribute to each component, although some points can have very low responsibilities. On average, each component fits $N_{\text{points}} = W_c \times N_{\text{total}}$ points where N_{total} is the total number of GCs. If the weight of the component is such that $N_{\text{points}} < k$ then Σ tends towards being degenerate within machine precision. This causes the responsibility of the GCs to tend to one and the fit is unable to evolve. To prevent this, after calculating the covariance matrix we change the $\lfloor k - N_{\text{points}} \rfloor$ smallest eigen values to half of the smallest non degenerate value. If N_{points} drops below 1.5, we set the eigen value to be 0.05 (note that internally the space is scaled (by the $25 - 75\%$ range to be dimensionless). If N_{points} drops below 0.5, the cluster is then considered extinct, and the normalisation weight is set to zero. We note that that the weights of the MW groups generally do not decrease sufficiently when performing the multi-component fit to cause this issue. This process only effects a few groups from the mock samples.

4.2.1.2 Ungrouped GCs

Some GCs cannot be attributed to any known accretion event, such as the High Energy group in the Massari19 analysis. This could be as they fell in as small groups that do not contain enough information to be robustly identified. Our model accounts for such GCs which are classified as the 'Ungrouped' component.

The Ungrouped component is modelled as a uniform background distribution, normalised to integrate to one over the volume, V, of the dynamical space filled by the GCs. That is

$$F_{\text{Ung}} = \frac{1}{V} \, , \tag{4.2.8}$$

where V is calculated by SciPy's convex hull module (Virtanen et al., 2020).

4.2.1.3 Insitu Components

In the MW, we cannot be certain if the GCs are accreted or have an insitu origin. We therefore need to model also include models of the bulge and disc components. The dynamics of these components are not well described by Gaussian components and instead we model them as distribution functions in action space using implementations in AGAMA (Vasiliev, 2019).

When modelling the bulge and disc components in $(E, \mathbf{J})$ space, we assume that the energy distribution can be separated from the action distribution, that is:

$$F(E, \mathbf{J}) = F(E) F(\mathbf{J}) \tag{4.2.9}$$

In principle, the energy distribution can be calculated numerically from the action distribution. In practice, it is simpler and far less computationally expensive to fit a separate distribution.

We find that the energy distributions of the insitu components are well described by an isothermal sphere:

$$F(E) = \begin{cases} \exp\left(\frac{(E_0 - E)}{\sigma_E}\right) & E > E_0 \\ 0 & 0 \le E \le E_0 \end{cases}, \tag{4.2.10}$$

where E_0 is fixed to the value of the potential at the centre of the galaxy, which for practical purposes we take to be the energy of the lowest energy GC, and σ_E is a free parameter that describes how centrally concentrated the GCs are.

We originally modelled the bulge as a double power law with cut off as introduced in Posti et al. (2015). In practice, we have found that the fitting converges on values consistent with the simpler exponential fit:

$$F_{\text{Bulge}}(\mathbf{J}) = \frac{4}{J_{\text{Cut}}^3 \sqrt{3\pi^3}} \exp\left[-(J_{\text{Tot}}/J_{\text{cut}})^2\right] \tag{4.2.11}$$

where $J_{\text{Tot}} = J_R + |L_z| + J_z$ and J_{cut} is a free parameter that controls the steepness of the

cutoff.

The disc is modelled using the quasi-iso-thermal disc, first described in Binney (2010). This is also used to model GCs in Posti & Helmi (2019), whose assumptions we follow. The action distribution is given as:

$$F_{\text{Disc}}(\mathbf{J}) = \frac{\Sigma \nu \Omega}{2\pi^2 \kappa \sigma_R^2 \sigma_z^2} f_{\pm,d} \exp\left(-\frac{\kappa J_R}{\sigma_R^2} - \frac{\nu J_z}{\sigma_z^2}\right)$$

$$\Sigma = \exp\left[-R_c(L_z)/R_d\right] \qquad\qquad, \qquad (4.2.12)$$

$$f_{\pm,d} = \begin{cases} 1 & L_z \geq 0 \\ \exp\left(2\Omega L_z/\sigma_R^2\right) & L_z < 0 \end{cases}$$

where Σ describes the disc surface density and $f_{\pm,d}$ controls the rotation of the disc. The circular, radial and vertical epicycle frequencies, are denoted by Ω, κ and ν respectively, and are evaluated at the radius of the circular orbit $R_c = R_c(J_{\text{Tot}})$ with angular momentum $J_{\text{Tot}} = J_R + |L_z| + J_z$. The radial velocity dispersion is given as $\sigma_R = \sigma_{R0} \exp\left(-R_c/R_\sigma\right)$, and the vertical velocity dispersion is fixed at constant scale-height $\sigma_z = \sqrt{2}h_d\nu$. The disc is chosen to match the thick disc of Piffl et al. (2014b); with $R_\sigma = 13\text{kpc}$ and $h_d = 0.2R_d$. This leaves two free parameters; the disc scale-length R_d and the central radial dispersion $\sigma_{R,0}$.

4.2.2 Age-Metallicity Relation

We use the leaky-box chemical evolution model to describe the age-metallicity relation for GCs, as given in Forbes (2020):

$$[\text{Fe/H}] = -p_{\text{yield}} \log\left(\frac{t}{t_f}\right) , \qquad (4.2.13)$$

where p_{yield} is a measure of how quickly the system enriches and t_f is the formation time of the system. Larger galaxies enrich metallicity quicker, giving a higher p_{yield} and steeper evolution track. Note this is equivalent to the equation of Kruijssen et al. (2019a), with re-arranged and re-named constants and similar to the relation of Massari et al. (2019).

We proceed by fitting Eq. (4.2.13) to the GCs associated to each component taking into

account the weights, i.e. responsibilities, associated to each object. The fitted relation can be inverted to obtain the expected age as a function of metallicity, which we denote as t_{fit} ([Fe/H]). The probability of the GCs observed age being part of the modelled relation is then given by a normal distribution, centred on the expected age with dispersion equal to the error in age, σ_t, i.e.

$$F_c^{\text{AMR}} ([t, [Fe/H]]) = N (t|\mu = t_{\text{fit}} ([Fe/H]), \sigma = \sigma_t) \ . \tag{4.2.14}$$

For the GCs that do not have age-metallicity data, we assume that they have a constant probability of one to be assigned to the component in the age-metallicity space. For the Ungrouped component, we do not expect all group members to be from a single accretion event or follow the same age-metallicity relation. The probability is then taken as a constant value as if there was no age-metallicity data.

4.2.3 Observational Errors

To effectively model the MW it is necessary to include the statistical uncertainty from observational errors. For this, we use the Monte Carlo sample described in Sec. 4.5.1 that sample the uncertainties in the measured velocity and position of GCs. The Monte Carlo samples of a single cluster are treated as independent points, with their own responsibilities and are fit independently. When the model has converged, the final probabilities of cluster i is given as:

$$p_{ic} = W_c \sum_{j}^{\text{MC}} F_c \left(X_i^j \right) \tag{4.2.15}$$

where $\mathbf{X_i^j}$ is j-th Monte Carlo realisation of the i-th GC and the sum is over all the Monte Carlo samples of the GC. These probabilities are then used to calculate the responsibilities of the final results, following Eq. (4.2.3).

4.3   Mock Catalogues of Globular Clusters

Here we use the AURIGA hydrodynamical simulations to build mock GCs catalogue (see Introduction for details). We use the 30 haloes of the level 4 resolution sample, which we label as Au1 to Au30. Of these haloes, 13 are unrelaxed at present day based on the criteria of Neto et al. (2007). These unrelaxed haloes are poorly modelled by static, axisymmetric potentials. As such, we restrict our subsequent analysis to the 17 relaxed haloes.

The AURIGA simulations do not 'natively' contain GCs so, to create mock GCs samples, we assign GCs to old accreted stars similar to the work of Halbesma et al. (2020). We create mock GCs only for the accreted component since the goal is to test the challenging part of our methodology: how to split the stellar halo into its individual GC groups. For each accretion event we identify the accreted stars and randomly assigned GCs to a subsample of these stars based on the properties of the progenitor galaxy. Using this approach, we create 1000 mock GC catalogues for every AURIGA halo.

To assign GCs, we select only the accreted halo stars that are older than 10 Gyrs in age, and require them to be within within R_{200} of the host galaxy at present day. This is motivated by age estimates of the MW GCs that are, with a few exceptions, older than 10 Gyrs (see Fig. 4.8). To determine the origin of our stars, we use the same accretion catalogue of stars as Fattahi et al. (2019). The birth place of the star is defined as the subhalo in which it resides the first simulation snapshot after its formation. If the star is born in the main halo, it is defined as an insitu star. If the star is born outside of the main halo, its origin is defined to be the last subhalo it was in before the main halo. This process will classify accreted stars to be associated with the accretion event that brought them into the main halo. The few stars that formed from the gas of infalling satellites in the main halo are classified as insitu.

4.3.0.1 The GCs population

As discussed in the introduction, the relationship between the number or total mass of a GC system and the mass of the host galaxy is actively discussed in the literature, especially for dwarf galaxies. Here we are interested to test the multi-component analysis framework and the exact way in which the number of GCs relates to progenitor properties is not very relevant since it does not enter our model. To generate the mocks, we adopt the Burkert & Forbes (2020) model in which the number of GCs is proportional to the total mass. The mean number of GCs, N_{GC}, for an accretion event of mass M_{Host} is given by:

$$N_{\mathrm{GC}} = \frac{M_{\mathrm{Host}}}{5 \times 10^9 M_{\odot}} \ . \tag{4.3.1}$$

Using this halo mass - number of GC relation ($M_H - N_{GC}$) we generate 1000 GCs mocks for each accreted satellite to increase our sample statistics. For each mock, the number of GCs will be a Poisson distribution with mean given by Eq. (4.3.1). This makes it rather difficult to compare between each random realisation of a given accretion event, so, to keep the analysis as clear as possible, each random realisation has an equal number of GCs given by the mean expectation, which is rounded to the nearest integer.

Whilst the expected number of GCs from a single small accretion event (objects of mass less than $5 \times 10^9 M_{\odot}$) is less than one, we estimate that on average the expected total number of GCs from small accretion events is typically ~5. This population of small accretion events bring in individual, ungrouped GCs. To account for these objects, we assign individual GCs starting from the largest 'small' accretion event until the expected population is accounted for.

The resulting population of GCs in our mocks is compared to the observed Galactic GCs in Figs. 4.1 and 4.2. The former shows that the number of accreted GCs in our mocks is in agreement with the MW estimates. For the MW data, we take the total mass estimate from Callingham et al. (2019) and the number of accreted GCs that we find in Sec. 4.5. The number of GCs in the mocks grows with halo mass, as expected from observations and theoretical models (see discussion in Sec. 4.1). The AURIGA mocks with total mass
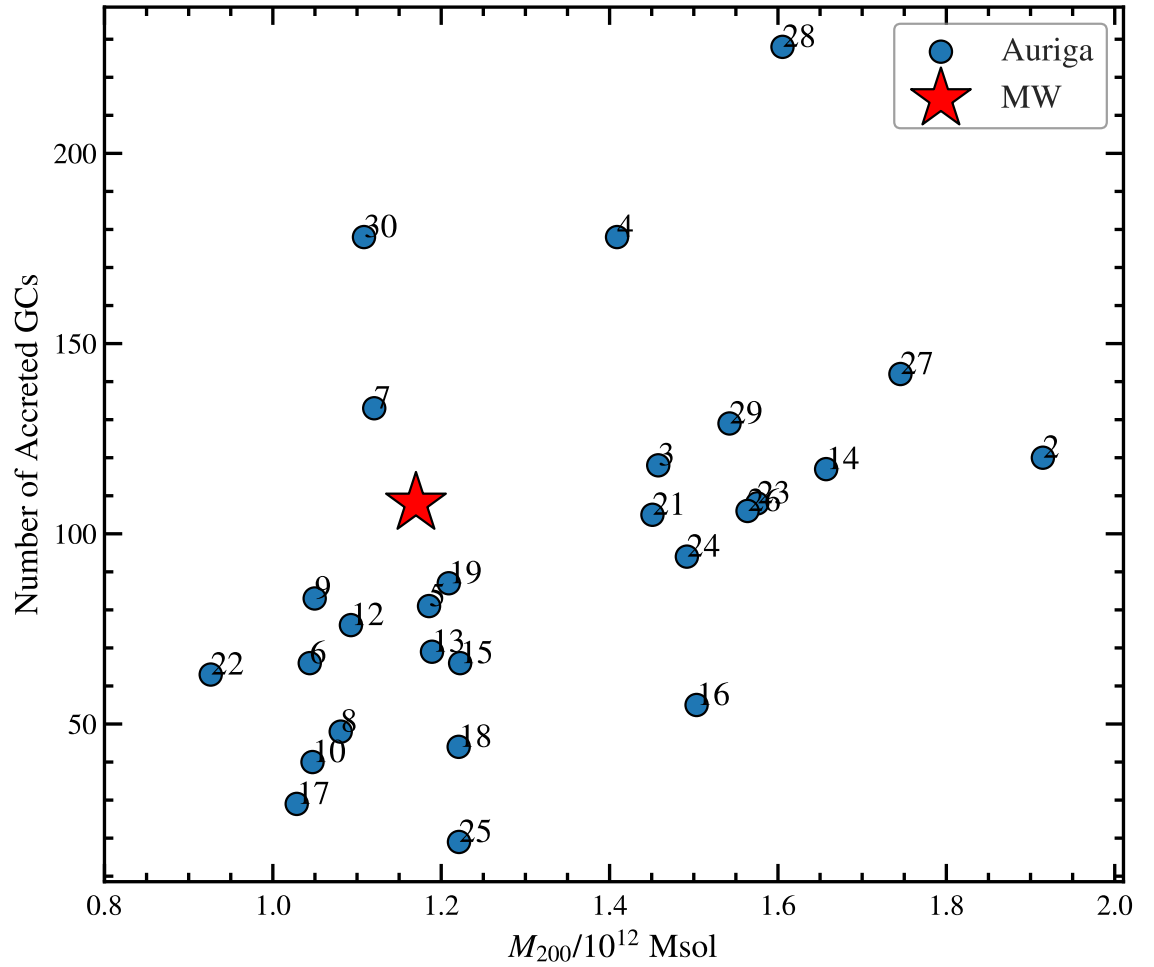
Figure 4.1
The relation between total mass, M_{200}, and the number of accreted GCs for our AURIGA mock catalogues (blue symbols) and for the MW (red star).
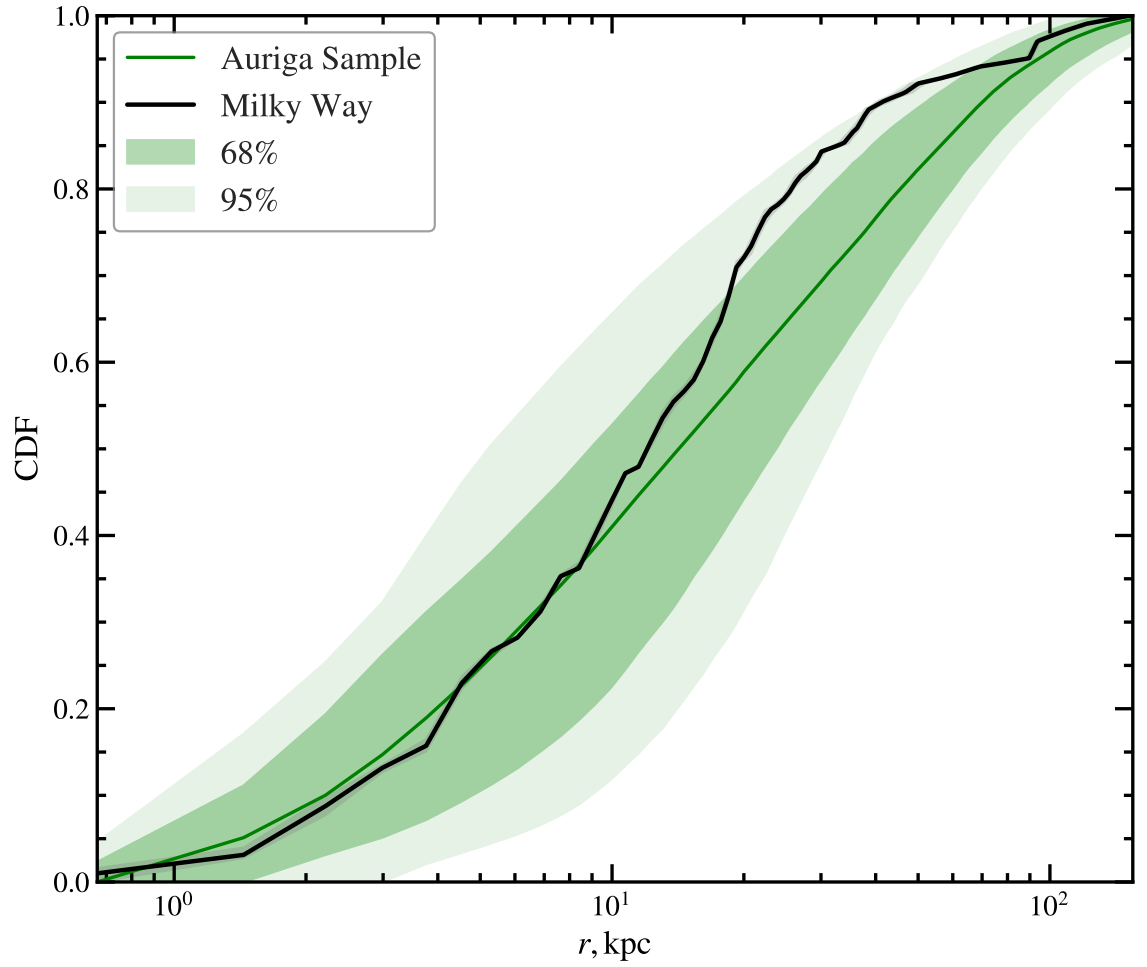
Figure 4.2
   The cumulative radial distribution of accreted GCs in our AURIGA mock catalogues
   and in the MW (black line). The green solid line show the median in the mocks,
   and the shaded regions give the 68 and 95 percentile regions.

$\sim 1.2 \times 10^{12}$ M$_\odot$ have slightly fewer GCs than the MW, but the scatter is rather large and there are at least two systems with more GCs.

Fig. 4.2 compares the radial distribution of GCs, where the distance of the GCs in the AURIGA mocks was scaled by $R_{200}^{\mathrm{MW}}/R_{200}^{\mathrm{AURIGA}}$ to account for the different sizes of the AURIGA systems. For this, we used $R_{200}^{\mathrm{MW}} = 222$ kpc from Callingham et al. (2019). The radial distribution of GCs in our mocks is similar to the observed one, although the MW is slightly more centrally concentrated in the $20 - 30$ kpc region than most of our AURIGA sample. This could potentially reflect that the Galactic stellar halo is mostly built from a few massive early accretion events (e.g. Kruijssen et al., 2019b) whose remains are mostly found in the inner region of our galaxy.

For our mock catalogues we have chosen to only include the accreted component. In principle, we could select insitu stars as mock GCs However, typically galaxies from the AURIGA simulations have higher stellar masses for a given halo mass (Monachesi et al., 2019). This discrepancy is lessened when only considering the accreted stellar halo. Furthermore, the stellar discs of the galaxies are typically larger than those expected of MW-like galaxies. This could be corrected with a selection function, but it is simpler to omit the insitu component and focus on the accreted component.

The orbital dynamics (including the energy, pericentres, apocentres, actions, angles and frequencies) for all stars in the main AURIGA halo at present day are calculated using the AGAMA package (Vasiliev, 2019). The potential is modelled from the $z = 0$ simulation snapshot as an axisymmetric cubic spline.

4.3.0.2 Age-Metallicity Relation

Hydrodynamical simulations face difficulties in reproducing the metallicity of dwarf galaxies and their GCs (e.g. Halbesma et al., 2020), which is potentially due to uncertainties in stellar yield models. To mimic the observed age-metallicity relation of GCs we assign new metallicity values to our mock GCs using the relation given in Eq. (4.2.13). For each accretion event we first choose an age-metallicity relation, setting a formation time that

is equal to the oldest star in that galaxy and a yield determined by the yield-stellar mass relation described in Forbes (2020). The AURIGA galaxies have a somewhat high stellar mass for their halo mass, so to mitigate this aspect we recalculate the progenitor stellar masses using the halo mass at infall and the stellar-mass-halo-mass relation of Behroozi et al. (2019). This gives yields more comparable with those predicted for the MW than if we would have used the original stellar mass of AURIGA. To mimic observational uncertainties, we add normally distributed 1 Gyr errors to the age estimates, which corresponds to the average errors for the MW's GCs.

4.4 Mock tests of the mixture model

We continue by testing our multi-component model for the GC population using our mock catalogues. These tests were used to select the optimal dynamical quantities to identify GC groups and to characterize the extent to which our modelling approach recovers the true GC groups as predicted by cosmological simulations.

First consider an example of our models chemo-dynamical fit of a mock catalogue. Fig. 4.3 shows the (E, J) distribution, and Fig. 4.4 shows the AMR fits, of the six accretion events with the largest halo masses, for the AURIGA 5 halo. These events are numbered from 0 to 5 in descending order of their total mass at accretion and are the systems with four or more GCs. The remaining GCs, i.e. from accretion events that brought three of less objects, are labeled as 'ungrouped'. The figure shows that the GC groups overlap in all the three panels and that identifying the groups using just dynamical information is not an easy task. It highlights the need for realistic mocks to test any approach that tries to decompose the stellar halo into its various accretion components. In this fit, our model agrees with 58/85 groups. The smaller groups at higher energy seem to be better recovered as they are more distinct. The groups at lower energy, which includes the larger groups, seem to overlap more.
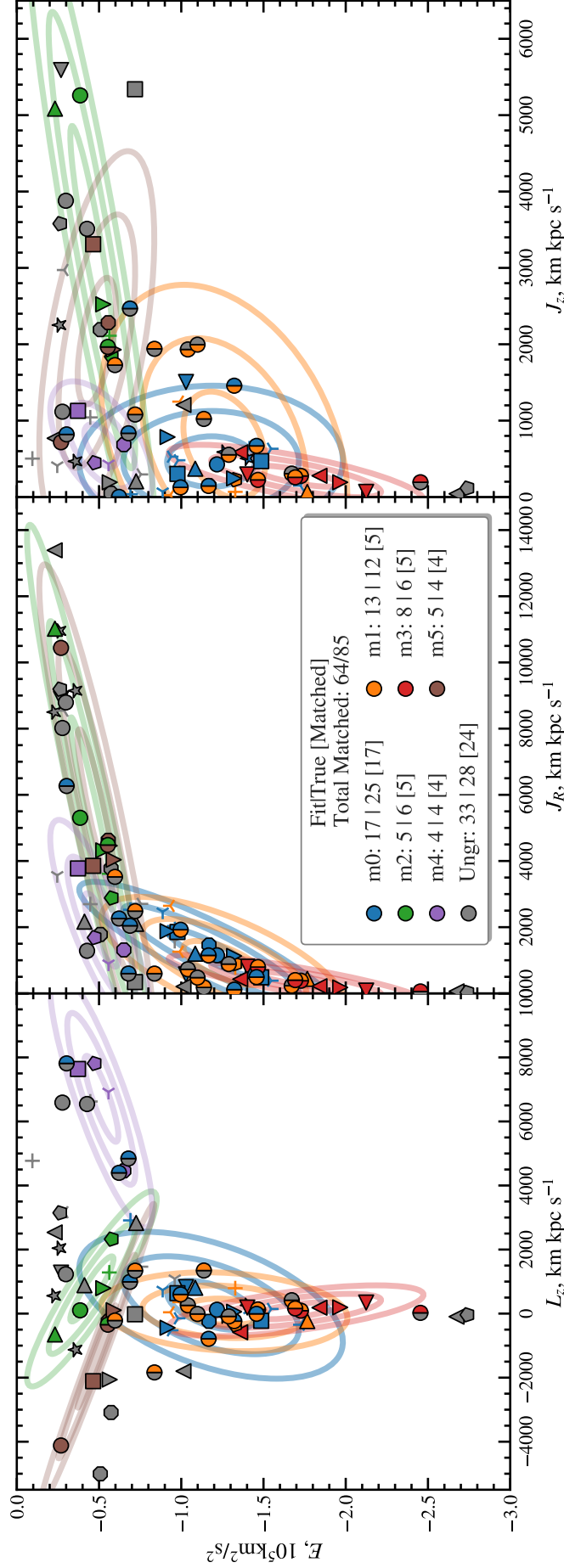
Figure 4.3

Our chemo-dynamical model fit to the AURIGA 5 mock sample of GCs. The axes show the dynamical component of the fit in energy (E) and action space (angular momentum L_z, radial action J_R, vertical action J_z). The accompanying age-metallicity fit is given in Fig. 4.4 GCs are represented by symbols, which are consistent for each object between the three panels to help identify individual GCs. Different colours represent the different accretion groups, labelled m0 to m5 in decreasing accretion mass. The groups are modelled as Gaussian distributions, with the contours giving the one, two and three sigma areas. The ungrouped group contains GCs that do not fit well in other groups, or contain less than 4 members in the true groups. Solid colours where the model and the agrees with the true grouping. Split groups show the original true grouping on the right hand side, and the assigned group on the left hand side.
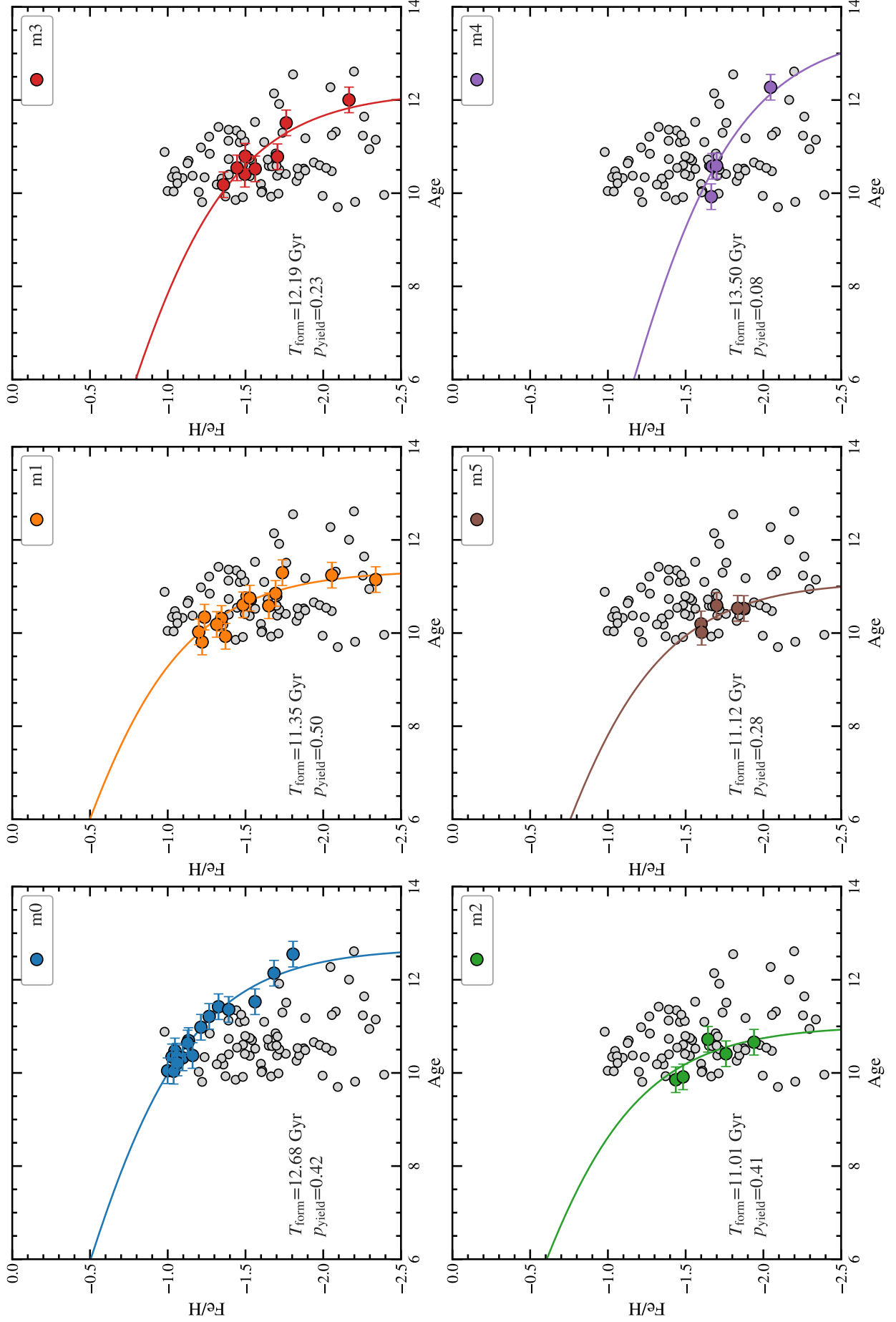
Figure 4.4

The age-metallicity relation for the AURIGA 5 GC mock catalogue. The different panels show the position of the different GC groups as identified by our method and the age-metallicity relation fit to them (see main text for details).

4.4.1 Initial Groups

One of the important choices in our multi-component analysis is the choice of starting groups. This is the case since, as can be appreciated from Fig. 4.3, most accretion events show considerable overlap in energy-action space. This makes it difficult to identify the true groups since potentially the model likelihood has multiple maxima. We have experimented extensively with different methodologies to generate the initial groups, including using other clustering algorithms and seeding the groups with random GCs and over densities. However, none of them returned satisfactory results.

To overcome this challenge, we have chosen to initialize the expectation-maximization algorithm using the true GC groups as measured in the simulations. This is motivated by our application to the Galactic data, where there is already a rough decomposition of GCs into accretion events with the main limitation being that the boundary between these groups is rather subjectively defined (e.g. Massari19). Our goal is to motivate a more robust and statistically based methodology of splitting the groups rather than cuts by eye. We tested the robustness of the initialization step in mocks by randomly assigning a fraction of the GCs from known groups to the ungrouped category. The outcome is robust to such changes as long as the reassigned fraction is $\lesssim 20\%$, with the smaller groups being the most effected. When analysing the MW sample, with known groups larger than 9, this suggests that having a modest fraction of mislabeled GCs, does not impact strongly the outcome.

4.4.2 Testing on Mock Samples

We now apply our method across the relaxed AURIGA sample, with each halo having 1000 mock realisations. To score how well the method performs across our samples, we quantify the success of our method with the following quantities. For a fit group of population N_{fit}, the true group of population N_{true} and their intersection $N_{\cap}$. We then define the purity P
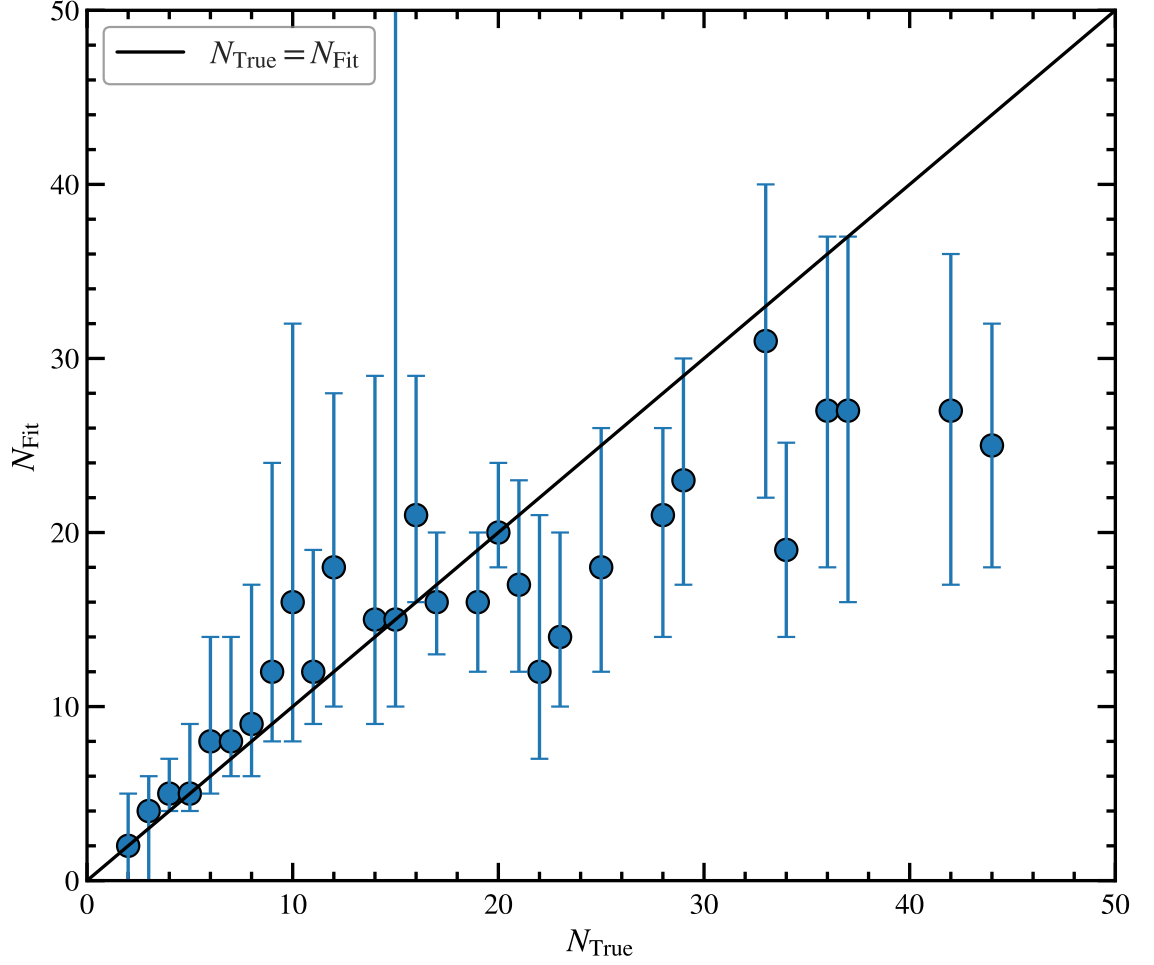
Figure 4.5

The true group of population N_{true} against the fit group of population N_{fit} for our mock GC sample. We bin the results in N_{true}, showing the median and $16\% - 84\%$ range with the errors bars for the distribution of N_{fit}. The black line shows where the populations would be correctly recovered, $N_{\text{true}} = N_{\text{fit}}$.

and completeness C of a fit as:

$$P = N_{\cap}/N_{\text{fit}} \tag{4.4.1}$$

$$C = N_{\cap}/N_{\text{true}} \tag{4.4.2}$$

$$\tag{4.4.3}$$

We find that the larger groups have greater spread in phase space, and tend to exist at lower energy. This is expected; the larger groups have a higher internal velocity dispersion before accretion and suffer from greater dynamical friction. The smaller groups tend to be more densely distributed in phase space, and typically to exist at higher energies (unless
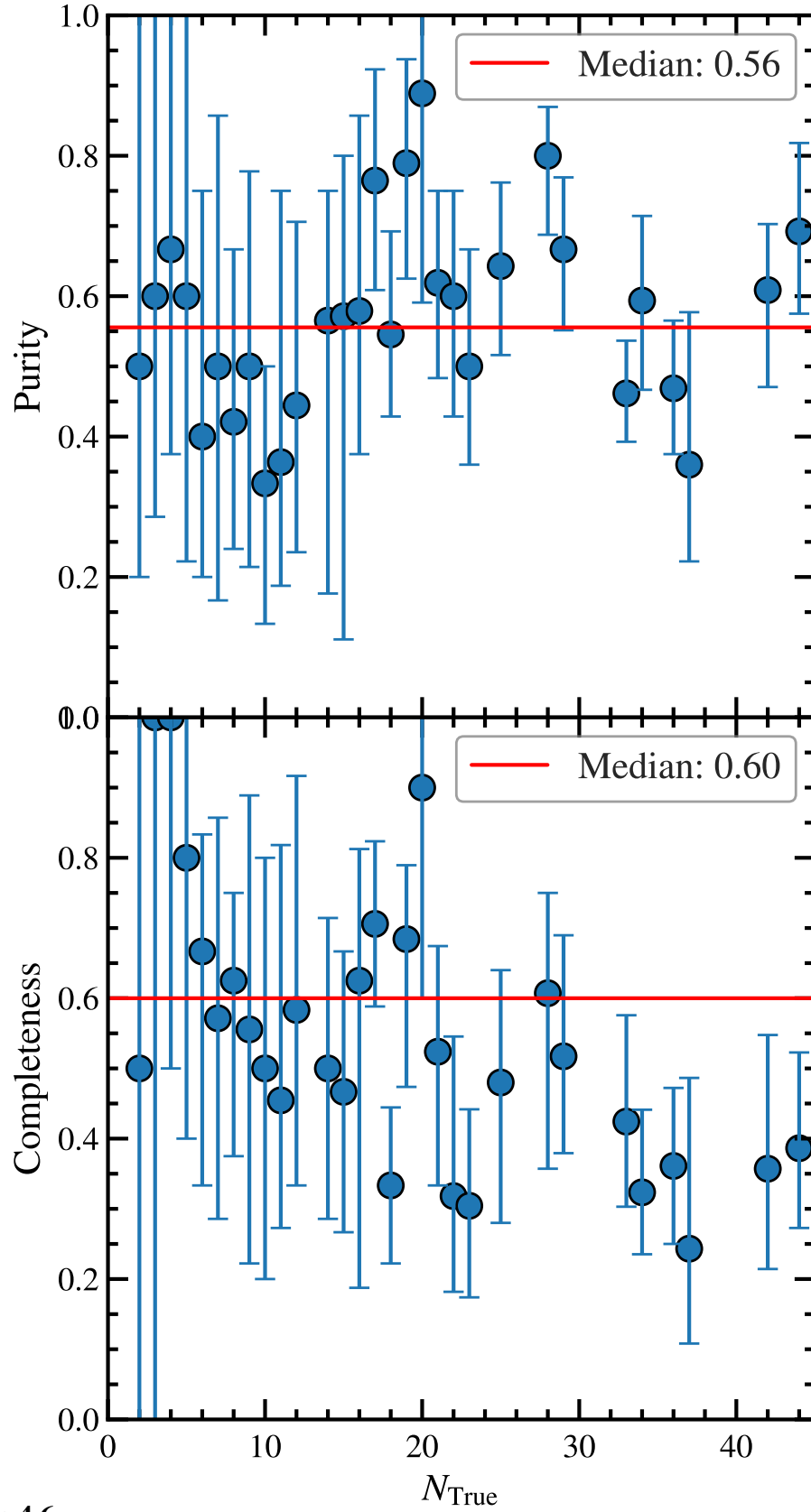
Figure 4.6

The true group of population N_{true} against the purity P and completeness C (defined in the main text) of our fitted mock GC sample. We bin the results in N_{true}, showing the median and $16\% - 84\%$ range with the errors bars for the distribution of N_{fit}. The red line shows the median of the purity and completeness of all the fitted groups.

accreted at early time). These effects are driven by the mass of the accretion event, and so correlate with the true population of the group. This appears to directly impact our recovery of the groups.

First consider the true group population against the fit populations in Fig. 4.5. On average, we recover the populations accurately. However, for the smaller populations ($\lesssim 15$), over estimation in the groups population, matched with a underestimation bias for the larger groups ($\gtrsim 20$). This is particularly true for the largest merger events for each halo, which on average we underestimate by a factor of 25%.

This trend is continued if we instead consider the purity and completeness of our fits against the true group population in Fig. 4.6. We find that on average, despite recovering the population of the groups, we only achieve a purity and completeness of 60%. There is a slight trend in decreasing completeness as the group number increases. This likely due to the merger debris increasing spread in phase space. Furthermore, as the group size increase, the average energy decrease, where there is greater overlap of the groups.

The ungrouped component has a low average purity of around $\sim 40\%$, suggesting that there exists a population of clusters that cannot be associated with the rest of their accretion group. These are typically apart from the rest of their accreted group in phase space, where it is difficult to identify them and so they fall into the ungrouped component.

We also used the mocks to test which dynamical spaces recover best the true GC groups, which we identify as the space that returns the highest purity and completeness for the identified groups. We found that the $(E, \boldsymbol{J})$ space is best at recovering the true groupings, performing better than $\boldsymbol{J}$ space alone, or combinations between E and angular momentum, $\boldsymbol{L}$, components, such as $(E, \boldsymbol{L})$, and (E, L_z, L_p), where L_p is the $\boldsymbol{L}$ component in the disc plane. The (E, L_z, L_p) space is the one used by Massari19 to identify GCs groups.

4.5   Fitting the Galactic GCs

We now proceed to apply the multi-component model described and tested in the previous sections to the Galactic GCs data.

4.5.1   Observational Data

We make use of the largest Galactic GC sample to date, which consists of the 170 GCs studied in Vasiliev & Baumgardt (2021) that have 6D phase space (i.e. position and velocity) data. The GCs proper motions are based on the *Gaia* Early Data Release 3 (EDR3) and represent an improvement in precision by roughly a factor of 2 compared to the previous *Gaia* Data Release 2 (DR2) measurements (Gaia Collaboration et al., 2021b). Where available, we updated the Vasiliev & Baumgardt GC distances with those from Baumgardt & Vasiliev (2021), which are based on a combination of *Gaia* EDR3, Hubble Space Telescope, and literature data.

To transform the observations to a Galactocentric reference frame we assume a Local Standard of Rest, LSR=232.8 km/s (McMillan, 2017), a solar radius of $R_\odot = 8.2$kpc, a a solar height of $z = 0$pc (assumed negligible), and a local solar motion of $(U, V, W) = (11.1, 12.24, 7.25)$km/s Schönrich et al. (2010).

To calculate the dynamics of the GCs, we use the AGAMA package (Vasiliev, 2019) and use the McMillan (2017) potential of the MW, as implemented in AGAMA. We calculate a range of dynamical quantities for the analysis, including the energy, actions, and angular momentum of the GCs' orbits.

To account for measurement errors in the positions and velocities of GCs, we create a Monte Carlo sample of 1000 points in observed space (i.e. radial distance and velocity, and celestial proper motions) using the quoted measurement errors which we model as Gaussian errors for each measured quantity. These are then transformed into positions and velocities with respect to the Galactic Centre, and fed into AGAMA to generate a Monte Carlo sample of dynamical quantities. The precision of these phase-space coordinates is typically limited by distance uncertainties.

The age-chemistry data are taken from a compilation of literature sources compiled in Kruijssen et al. (2019b), giving ages and [Fe/H] for 96 GCs. This values are averaged from values derived in Forbes & Bridges (2010), VandenBerg et al. (2013), Dotter et al. (2010), Dotter et al. (2011). We neglect measurement uncertainties in metallicity since

they are considerably smaller than the errors in age determination. We assume that in this data errors in metallicity are subdominant to errors in age.

4.5.2 Fitting the Milky Way

We now apply our model to the Milky Way. We performed extensive tests of the starting groups to initialise our expectation-maximisation algorithm to ensure that we find the best fitting model given current estimates for possible GC groups. First, we consider several different initial groups from the literature, primarily from Massari19, Horta20 and Forbes20. We have also tried a bootstrap inspired approach, relabeling each GC as 'ungrouped' at a time and refitting the model to further check for a higher likelihoods model. In general, for these small changes we find little dependence on the final groups.

The results we present in the following is for the maximum likelihood model over all these variations in the initialization of the expectation-maximization algorithm. The final fit can be seen in Fig. 4.7 and Fig. 4.8. The derived properties of the groups can be found in Tab. 4.2, and the cluster memberships are discussed for every component in the next subsection.

We find good general agreement with previous work, with all groups showing to be distinct in either chemical or dynamical space. At the center of our Galaxy, we find overlap between the two insitu components and the Kraken group in dynamical space. This is the area where we see most change from the initial groups. To separate these groups with confidence, we rely on the age-metallicity space for the GCs that have the data. However, the insitu and accreted tracks overlap for old, low metallicity GCs and cannot be distinguished. In this region we find, there is not enough information to confidently separate the groups.

We find that Sequoia and GES cannot be convincingly fit by a single group. While there is no clear difference in the age-metallicity space, the dynamics of the two groups seem to be distinct. The possibility that Kraken is the core of GES, is briefly discussed in Horta et al. (2021). We agree with their conclusions that Kraken and GES are unlikely to have the same origin. The dynamics of the two groups seem to be distinct, and Kraken has a steeper metallicity enrichment (higher p_{yield}) than GES.

We find no clear evidence of the Wukong structure as suggested in Naidu et al. (2020), containing ESO280, NGC5024, NGC5053. When we model these GCs as a separate group we find that the group becomes extinct as the GCs become members of the GES group. However, we note that this group is in the regime where the number of points is less than the dimensions of the space, and thus the groups are poorly modelled (see Sec 4.2.1.1 for details). As such, we stress that this is not conclusive.

4.5.3 Component Fits and Membership

We now discuss the specific groups. The membership of the groups can be found in Table 4.2, whilst the individual membership probabilities is compiled in Table 4.3. We generate a Monte Carlo sample our groups population by drawing a GCs membership based on its membership probability. From this sample of groups, we find the expected membership and the one sigma errors.

4.5.3.1 Insitu

We find that 56 of our GCs likely have an insitu origin, with the bulge group containing an expected number of 33 ± 2 GCs, and the disc group contains an expected number of 23^{+2}_{-1} GCs. This is comparable with Massari19 who find 36 Bulge and 26 Disc GCs and Kruijssen et al. (2019b) who predict 67 out of their 157 have an insitu origin.

The bulge GCs lies below an energy of $-2 \times 10^5 \, \mathrm{km}^2/\mathrm{s}^2$ and apocentres below 5 kpc. This component does not have any significant rotation and has an AMR track that is slightly steeper than the disc. The disc extends to high energy, but all of the GCs have $z_{\mathrm{max}} < 6 \, \mathrm{kpc}$, an eccentricity $e < 0.6$ and circularity > 0.5. In the very centre of the galaxy the disc overlaps with the bulge, leaving a hole in the middle of the radial distribution, with no GCs having an apocentre $< 4 \, \mathrm{kpc}$.

Here we list some other observations about the insitu GCs:

- We find that 10 GCs previously associated to the disc instead are probable Kraken
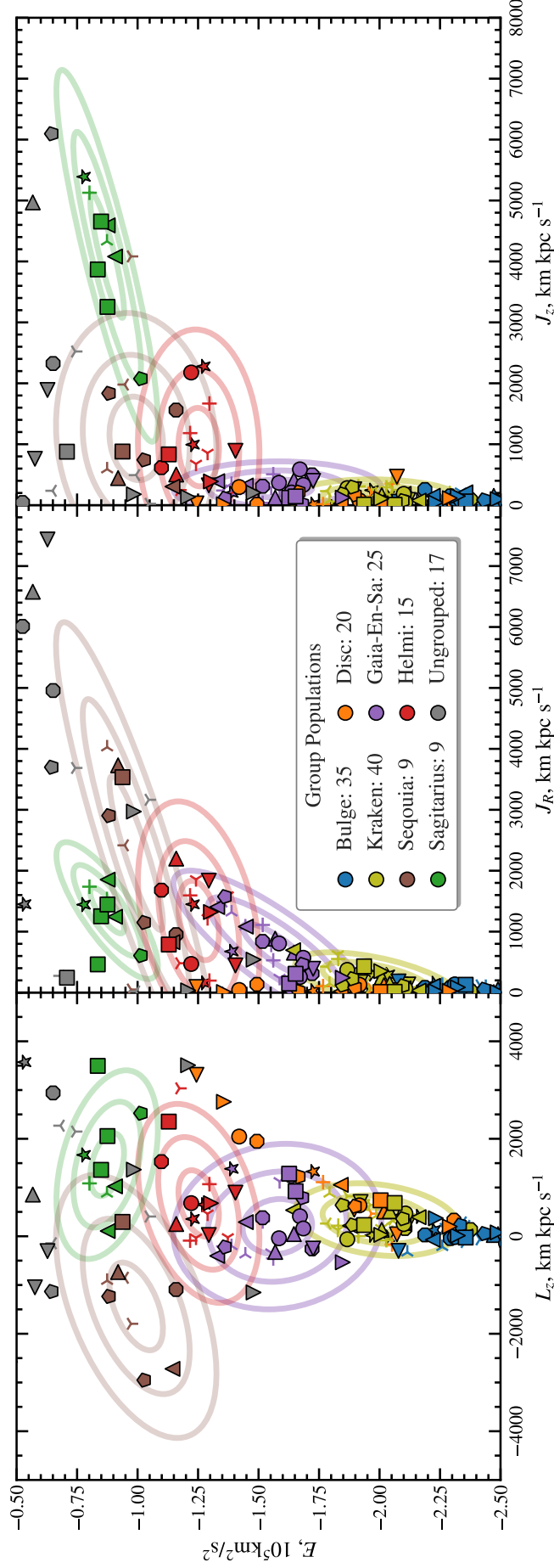
Figure 4.7

Dynamical groups in energy-action space as inferred by our chemo-dynamical model of the Galactic GC population. The companion age-metallicity modelling can be found in Fig. 4.8. Symbols are the observed GCs, the symbol is consistent between panels to help identify individual GCs. Different colours show the different groups modelled, with each cluster coloured by its most likely group. Accreted components are modelled as Gaussian distributions, with the 1, 2 and 3 sigma areas given by the contours. Insitu components, Bulge and Disc are at the inner regions of the galaxy and typically contained the most bound GCs. The Ungrouped component is modelled as a uniform distribution and contains objects accreted in small groups that cannot reliably be identified. Note that a few high energy GCs are beyond the axes limits and are not shown.
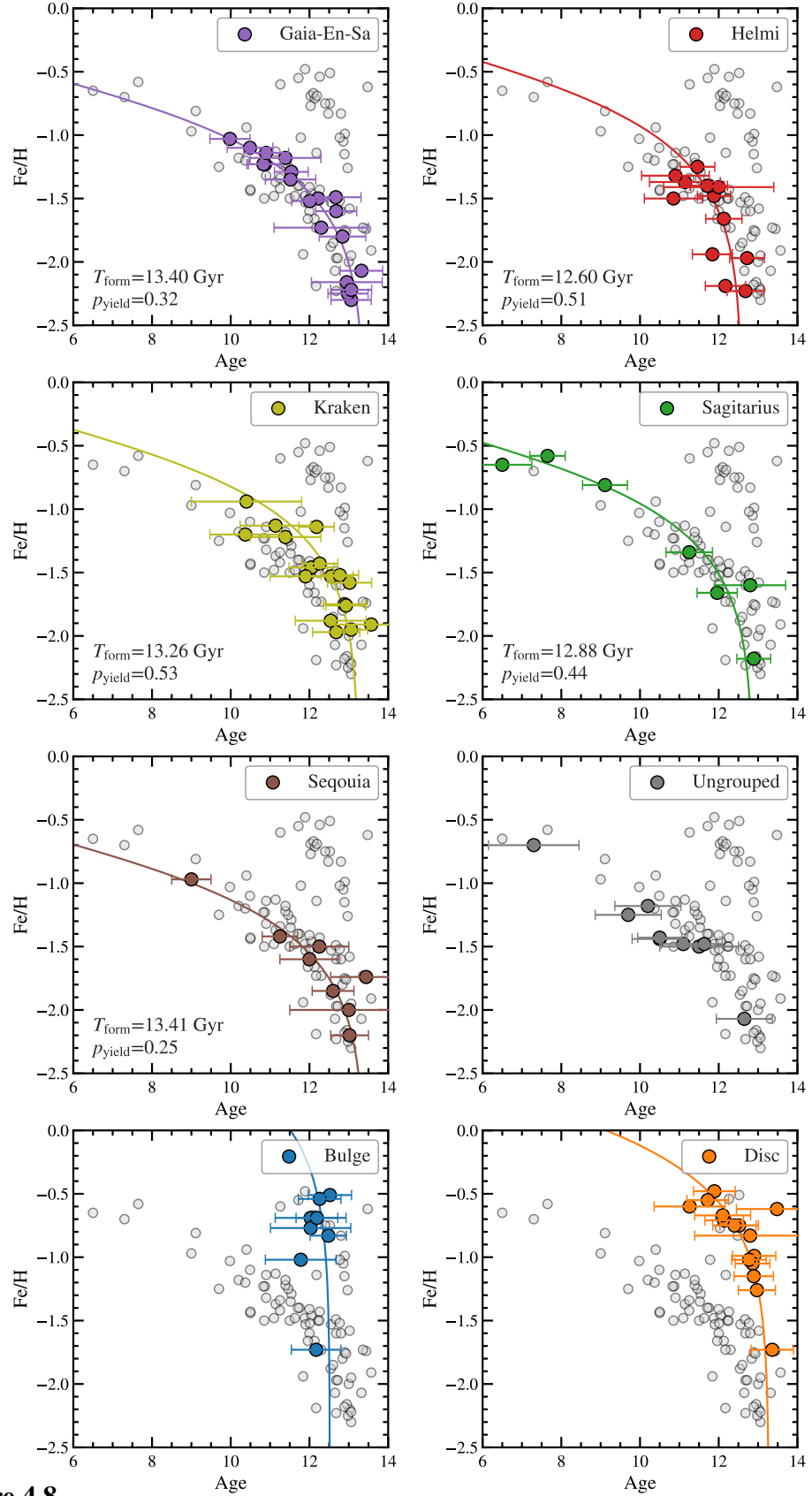
Figure 4.8

The age-metallicity relation for the Galactic GCs split according to the component they are associated to. The solid lines show the age-metallicity relation fit to the GCs associated to each component (see main text for details).

Table 4.1

The GC members of the accretion groups of the MW. Note that these are the most probable memberships. To see the membership probability of individual GCs, see Tab. 2.

Component	Membership
Bulge	NGC6535, Djorg2 (ESO456), NGC6388, NGC6380 (Ton1), Terzan6 (HP5), Terzan2 (HP3), Liller1, NGC6440, NGC6642, NGC6401, NGC6325, NGC6638, Terzan5 (11), Pal6, Terzan9, 1636-283 (ESO452), NGC6528, NGC6624, NGC6558, HP1 (BH229), Terzan4 (HP4), NGC6453, NGC6266 (M62), NGC6355, NGC6626 (M28), NGC6652, NGC6522, Terzan1 (HP2), NGC6293, NGC6342, NGC6304, NGC6637 (M69), VVVCL001, NGC6517, NGC6540 (Djorg)
Disc	NGC5927, NGC6838 (M71), NGC6352, NGC6362, NGC6496, NGC104 (47Tuc), NGC6366, ESO93, BH176, NGC6441, NGC6218 (M12), Pal10, Lynga7 (BH184), NGC6144, E3, NGC6171 (M107), NGC6723, NGC6717 (Pal9), NGC6256, IC1276 (Pal7)
Gaia-En-Sa	NGC6205 (M13), NGC362, NGC6779 (M56), NGC6341 (M92), NGC2298, NGC7089 (M2), NGC1851, NGC7099 (M30), NGC2808, NGC5286, ESO-SC06 (ESO280), NGC1261, NGC288, NGC6864 (M75), NGC5897, NGC5139 (oCen), NGC7078 (M15), NGC6656 (M22), NGC6235, BH140, Ryu879 (RLGC2), NGC6426, Pal11, IC1257, Pfleiderer
Helmi	NGC5904 (M5), NGC4147, NGC5634, NGC5053, Pal5, NGC5272 (M3), NGC7492, NGC5024 (M53), NGC6229, NGC4590 (M68), NGC6981 (M72), Rup106, NGC6584, Bliss1, NGC1904 (M79)
Kraken	NGC6254 (M10), NGC6712, NGC6544, NGC6287, NGC6681 (M70), NGC6809 (M55), NGC5986, NGC5946, NGC4833, NGC6541, Terzan10, NGC6121 (M4), NGC6752, NGC6402 (M14), UKS1, NGC6760, NGC6397, FSR1735, NGC6749, Mercer5, NGC6316, NGC6284, Pal8, NGC6539, Terzan3, Ton2 (Pismis26), FSR1716, Terzan12, Djorg1, NGC4372, NGC6273 (M19), BH261 (AL3), NGC6569, NGC6553, NGC6333 (M9), NGC6356, NGC6093 (M80), VVVCL002, Gran1
Sagittarius	Terzan8, NGC6715 (M54), Arp2, Terzan7, Pal12, Whiting1, NGC5824, Munoz1, Kim3
Sequoia	NGC5466, NGC6101, NGC3201, NGC7006, IC4499, Pal13, NGC5694, Pal15, AM4
Ungrouped	Ryu059 (RLGC1), Ko2, NGC6934, Crater, Pal3, Pyxis, Pal14, AM1, Eridanus, Pal1, Segue3, Pal4, NGC2419, Laevens3, Pal2, FSR1758, Ko1

members. All these GCs are without age-metallicity data or [Fe/H] < −1.5. This highlights the overlapping nature of the insitu and lower energy components.

- VVVCL001, previously uncategorized, is a likely Bulge member, but could also plausibly fit into the Kraken group.

- ESO93, previously uncategorized is almost certainly a member of the Disc

- Liller1 and NGC6388 are very likely to be part of the Bulge, in agreement with Horta20.

- E3 (ESO37-1) has previously been associated with the Helmi streams (Koppelman et al., 2019a). We find it has over a 94% prob of being a disc member, driven by its place on the insitu AMR track (in agreement with Kruijssen et al. 2020).

4.5.3.2 Kraken

We expect 39 ± 2 GCs in the Kraken group, a substantial increase from Massari19's population of 25. Compared to Massari19's groups, there is a net 7 contribution from the disc and 4 from the GES component. We also find that two previously uncategorized GCs, UKS1 and Mercer5, are highly likely to be Kraken members and VVVCLOO2 and Gran1 are split between Kraken and the bulge.

Our model predicts that the Kraken groups energy is approximately normally distributed with a mean of $-2 \times 10^5 \, \mathrm{km^2/s^2}$ and one sigma values of $0.1 \times 10^5 \, \mathrm{km^2/s^2}$ (in shorthand, $E \sim -(2 \pm 0.1) \times 10^5 \, \mathrm{km^2/s^2}$). This is higher than other selections in the literature, who typically have selections below $E < -2 \times 10^5 \, \mathrm{km^2/s^2}$ (such as Massari19, Horta et al. (2021)). Notably, our Kraken group seems to have bridged the gap seen in stars in Horta et al. (2021) at energies $-2 < E/10^5 \, \mathrm{km^2/s^2} < -1.85$. Furthermore, unlike previous results, our Kraken group has net prograde motion, with Lz distributed as $\sim 340 \pm 250 \, \mathrm{kpc \, km/s}$. This prograde bias possibly indicates some disc GCs have been included in the group.

For GCs without metallicity, or those that have low metallicity where the insitu and accreted branches overlap, we have found distinguishing their origin to be difficult. In the future

further chemistry information will hopefully allow us to distinguish better the accreted and insitu components at low energy.

4.5.3.3   Sagitarius

Our Sagitarius group contains an expected population of 9^{+1}_{-0} GCs. Due to recent accretion and tidal stripping its material is an easily identifiable stream. This allows 7 GCs to be identified with a higher degree of certainty as being associated to the Sagittarius dwarf: Terzan7, Arp2, Terzan8, Pal12, NGC5824, Whiting1 and M54 (NGC6715), which is believed to be the nucleus of Sagittarius. (Bellazzini et al., 2020; Antoja et al., 2020; Law & Majewski, 2010; Peñarrubia & Petersen, 2021). We find that these GCs have a near certain membership. We also find that two new GCs, Munoz1 and Kim3, also have over 90% probability of membership. These high probabilities are driven by a high group density in dynamical space and a distinct age-metallicity branch.

Several other GCs have been tentatively linked to Sagitarius in the literature, but we find no other likely members. Compared to the literature, we find:

- Pal2, has been proposed to lie on the trailing arm of the stream (Bellazzini et al., 2020; Law & Majewski, 2010). However we find that it has a 82% probability of being a ungrouped and 13% of being associated with Sequoia

- NGC2419 is commonly linked to Sagittarius (Antoja et al., 2020; Bellazzini et al., 2020; Peñarrubia & Petersen, 2021). but find that it is almost certainly ungrouped. Its orbit is more radial than the average more vertical Sagitarius orbit.

- NGC5634 and NGC5053 have been proposed as lying on ancient wraps of the stream Bellazzini et al. (2020). We find that they are not likely members (in agreement with Law & Majewski (2010)); they are a near certain member of the Helmi group.

- AM4 was attributed to Sagittarius by Forbes20 based on chemistry as at the time AM4 did not have *Gaia* kinmatics (for this reason Massari19 did not assign the cluster to a group). We find that as a prograde cluster its orbit is incompatible with

the Sagittarius orbit. Instead, we find that it is a likely member of Sequoia, but has a 15% chance of being ungrouped.

- Before Koposov 1 and 2 (Ko1,Ko2) had radial velocities, Paust et al. (2014) suggested that they could plausibly lie on the Sagittarius stream. Improved observations by Vasiliev & Baumgardt (2021) have placed Ko1 as a likely member, but Ko2 not. We find that Ko1 is evenly split between Sagittarius and ungrouped, but confirm that Ko2 is almost certainly ungrouped.

4.5.3.4 Gaia-Enceladus-Sausage (GES)

Our analysis infers 25^{+1}_{-2} GCs in the GES structure, in good agreement with Massari19 (25) and Forbes20 (28). The GES group is consistent with no net rotation and is distributed as $E/10^5 \, \mathrm{km^2/s^2} \sim -1.5 \pm 0.2$. This approximately agrees with previous literature selections: $-1.75 < E/10^5 \, \mathrm{km^2/s^2} < -1.3$ in Horta et al. (2021) , and $-1.86 < E/10^5 \, \mathrm{km^2/s^2} < -0.9$ in Massari19. Massari19 also notes that the apocentres are mostly below 25 kpc in good agreement with Deason et al. (2018). We also find that our GES GCs apocentres are between 10kpc and 20kpc.

- The previously uncategorised clusters Ryu879 (RLGC2) and Pfleiderer are likely to be members of GES, but also could be associated with Kraken. BH140 is a near certain GES cluster

- In contrast to Myeong et al. (2019), we infer that NGC4147, NGC6584 and NGC6981 (M72) are part of the Helmi Streams and NGC7006, Pal15 and NGC5694 are associated to Sequoia.

- 4 GCs that have been previously associated with GES are now primarily associated with the Kraken structure (NGC4833, NGC6284, Djorg1 and Terzan10).

- ω-Centuari is almost certainly a GES cluster, in agreement with a tentative categorization by Massari19, who found it ambiguous between GES and Sequoia. This

cluster has been claimed to be the nucleus of Sequoia by Myeong et al. (2019), and is discussed more in the Sequoia section.

- Pal2 is likely to be ungrouped, despite being linked to GES by Massari19 and Forbes20. We find it is at higher energy $(-1.1 \times 10^5 \, \mathrm{km^2/s^2})$ than the rest of the GES group.

4.5.3.5 Sequoia

We predict 9^{+1}_{-0} members in the Sequoia group, comparable to the 7 attributed in Myeong et al. (2019) and Massari19, and the 9 in Forbes20.

We find that the group has a slim distribution in energy space $E/10^5 \, \mathrm{km^2/s^2} \sim -1 \pm 0.1$ and a wide prograde distribution in angular momentum space $L_z/\mathrm{kpc \, km/s} \sim -1400 \pm 900$. The is noticeably smaller than other selections in the literature, such as Myeong et al. (2019) (and used in Massari19) selection of $-1.5 < E/10^5 \, \mathrm{km^2/s^2} < -0.7$ and $-3700 < L_z \, \mathrm{kpc \, km/s} < -850$. The distribution in J_z and J_R is very broad, stretching across the space.

FSR1758 was characterized in Barba et al. (2019), and gave the name to the Sequoia structure in Myeong et al. (2019). We find that FSR1758 has a 30% of being associated with Sequoia, with a 60% of being associated with GES. This is primarily driven by its position at lower energy than the rest of Sequoia. This finding is in agreement with Romero-Colmenares et al. (2021), who have suggested that FSR1758 belongs to GES.

ω-Centuari is another cluster that has been previously attributed as a key Sequoia member. We find it has a near certain GES membership. Due to its peculiar chemistry, ω-Centuari has long been identified as the nucleus of a dwarf galaxy (Bekki & Freeman, 2003), believed to be of mass on the order of $\sim 10^{10} M_\odot$ (Valcarce & Catelan, 2011). Forbes20 and Myeong et al. (2019) believed this to be Sequoia, based on its retrograde orbit. As noted in Myeong et al. (2018b), ω-Centuari could have sank to lower energy due to dynamical friction.

As briefly discussed in the Sagitarius section, the AM4 cluster has before been tentatively been linked to Sagitarius, but we find it is likely a Sequoia member. If true, it is the

youngest Sequoia member with a age of ~9 Gyr, ~ 2 Gyr younger than the rest of the group. its position in energy-action space is unusual for Sequoia; while at the centre of the angular momentum distribution, it has negligible radial action and is primarily on a vertical orbit, in agreement with Sagitarius. We flag this cluster as a potential outlier.

4.5.3.6 Helmi Streams

We infer 14 ± 1 GCs in the Helmi streams group. Koppelman et al. (2019a) identifies 7 GC members, (NGC4590, NGC5272 NGC5904, NGC5024, NGC5053, NGC5634, NGC6981). We find that these are very likely members. Our Helmi stream structure has a slim energy distribution $E/10^5 \, \mathrm{km^2/s^2} \sim -1.2 \pm 0.08$, and wide angular momentum distribution $Lz/ \, \mathrm{kpc \, km/s} \sim 700 \pm 700$. This is in approximate agreement with the rest of the literature (Koppelman et al., 2019a; Massari et al., 2019; Naidu et al., 2020).

- We find that the previously uncategorized cluster Bliss1 is likely a Helmi member.

- NGC6441 is almost certainly a member of the Disc and not a Helmi Stream or Kraken member as suggested by Massari19.

- NGC4147 is not part of GES or SGR as it has been previously claimed Myeong et al. (2019); Forbes & Bridges (2010), but instead it is very likely to be a Helmi stream member.

4.5.3.7 Ungrouped

We find 16^{+2}_{-0} GCs that are ungrouped, or do not fall into the other accretion groups. This is collection of GCs from different low mass dwarfs that have otherwise not left significant stellar material to be identified. In their equivalent High Energy group Massari19 (and Forbes20) identify 11 members. We find 4 new GCs (Ryu059, Ko2, Segue3 and Laevens3) that are highly likely to be ungrouped, while Ko1 is evenly split between Ungrouped and Sagitarius. We find no obvious subgroups in these GCs. These GCs are all at high energy apart from Pal1.

Table 4.2

Properties of the Galactic GC accretion groups. The second column gives the expected number of GCs, including one sigma errors, as inferred by our chemo-dynamical model. From this, using the halo mass - number of GCs relation of Burkert & Forbes (2020) we find likely halo mass of the accretion event, including one sigma errors (third column). The halo mass is used to further infer the stellar mass (fourth column) from the stellar mass - halo mass relation of Behroozi et al. (2019).

Accretion Event	Number of GCs	$\log_{10} M_{halo}$	$\log_{10} M_{\star}$
Gaia-En-Sa	25^{+1}_{-2}	$11.08^{+0.60}_{-0.60}$	$8.67^{+1.13}_{-1.17}$
Helmi	15^{+1}_{-1}	$10.86^{+0.51}_{-0.51}$	$8.25^{+0.98}_{-0.99}$
Kraken	39^{+2}_{-2}	$11.28^{+0.68}_{-0.68}$	$9.06^{+1.21}_{-1.33}$
Sagitarius	9^{+1}_{-0}	$10.66^{+0.42}_{-0.42}$	$7.84^{+0.83}_{-0.83}$
Seqouia	9^{+1}_{-0}	$10.65^{+0.42}_{-0.42}$	$7.83^{+0.83}_{-0.83}$
Bulge	33^{+2}_{-2}	-	-
Disc	23^{+2}_{-2}	-	-
Ungrouped	16^{+2}_{-0}	-	-

Pal1 has previously been linked to the Disc (Massari19 and GES Forbes20, but instead we find that it has a very high probability of being ungrouped (in agreement with Kruijssen et al. 2020). it is on circular orbit compatible with the outskirts of the disc, but is young and high [Fe/H] similar to the young Sagittarius GCs Whiting1 and Terzan7. Other hints from its chemistry supports this accreted claim (Sakari et al., 2011). Naidu et al. (2020) identifies Pal1 with a newly identified Aleph structure due to chemo-dynamical similarities.

Cluster NGC2419 has been previously associated with Sagitarius, but we find it is highly likely to have different accretion origin and we associated it to the ungrouped component.

4.6   Inferring the Properties of Accreted Galaxies

With the likely populations of our groups found, we now use the $M_H - N_{GC}$ relation (Eq. 4.3.1) to estimate the mass of our accreted dwarf galaxies. We also include the theoretical uncertainties in this relation (σ_{Ngc}), given in figure 2 of Burkert & Forbes (2020) as

$\sigma_{\mathrm{Ngc}}/N_{\mathrm{GC}} \approx (N_{\mathrm{GC}}/2)^{-1/2}$. To find the halo mass, this error is included in the errors in our expected population numbers. These results are given as probability density functions (PDFs) in Fig. 4.9. Then, using the estimated halo masses (including the uncertainties) we infer the stellar masses using the zero redshift stellar mass - halo mass relation of Behroozi et al. (2019) (see Fig. 4.10. The median and 68% confidence limits of these results are summarised in Table 4.2.

We note that this methodology has significant caveats and limitations, as discussed in Kruijssen et al. (2019b). We do not include any redshift dependence in the $M_H - N_{GC}$ relation, assuming that this is sufficiently flat. The errors assumed on this relation are theoretical, and they and the relation are debated extensively in the literature.

In general, we find good agreement with the literature. Our Kraken group is larger than Massari19 and Forbes20, with a log stellar mass of $9.06^{+1.21}_{-1.33}$, but the uncertainties are significant. This is in agreement better with Horta et al. (2021), who estimated a log stellar mass of 8.7, approximately twice the stellar mass of Gaia-En-Sa.

Recent work has claimed to find an additional 20 plausible GCs in the body of Sagittarius (Minniti et al., 2021a,b). With our analysis, this would suggest a log halo mass of ~ 11.16. This matches well with work by Bland-Hawthorn & Tepper-García (2021), who suggest that the that suggests that the infall mass of Sagittarius has been understimated, due to rapid tidal stripping, and is actually comparable to the LMC with halo mass of $\sim 10^{11} M_\odot$.

4.6.1 Phase Mixing

When groups of GCs are accreted they are initially clumped in their orbital phases. Over time, the differences in orbital frequencies cause the phases to mix, losing information. The time taken for the group to phase mix can be simply estimated as 2π over the spread in the orbital frequencies of the cluster, giving a simple lower bound on the accretion time of a phase mixed group. However, we find that in practice this mixing time is typically under 1 Gyr and is not very constraining.
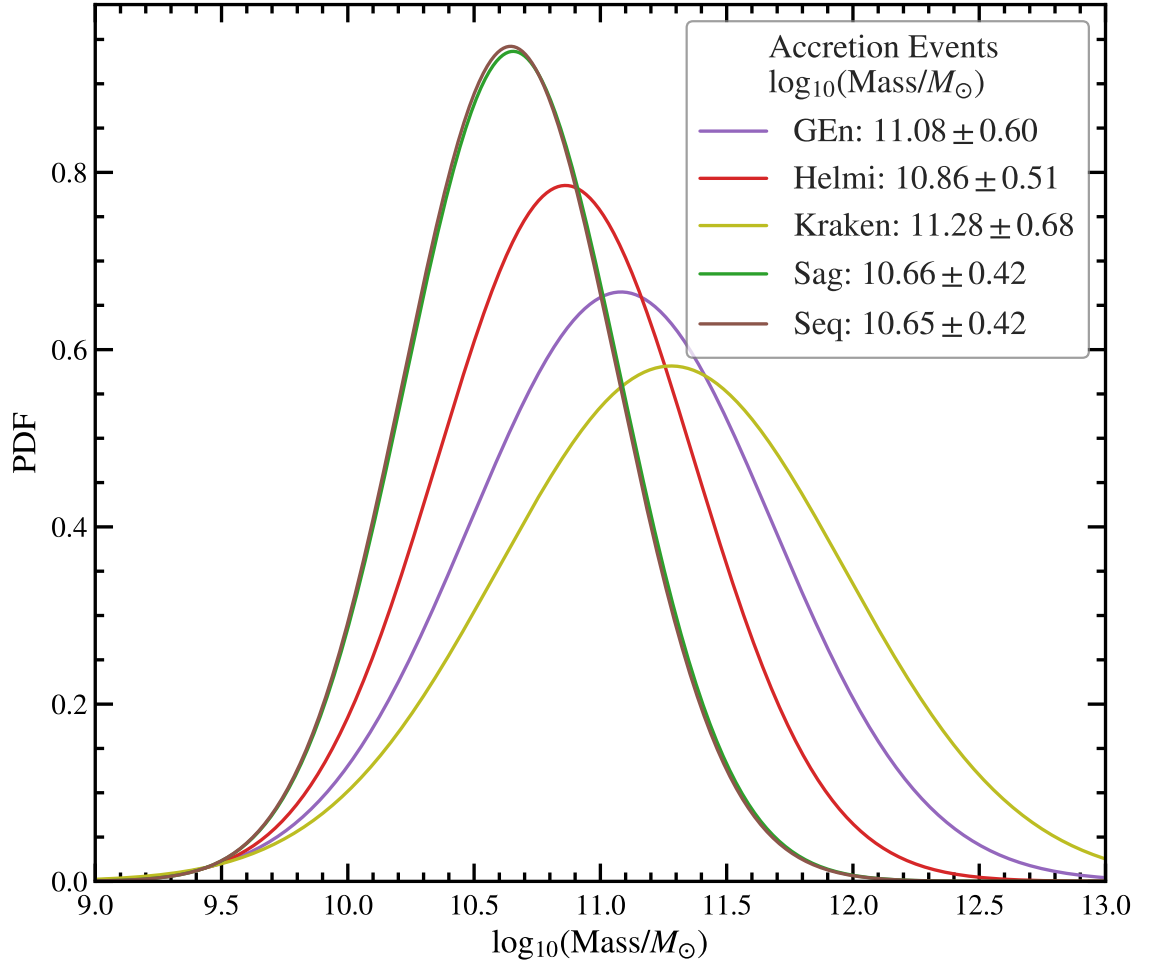
Figure 4.9
 The PDFs of the mass of our accreted galaxies, derived from their probable
 populations of GCs using the halo mass to number of GC relation of Burkert &
 Forbes (2020). This includes uncertainties from grouping the clusters, and the
 theoretical uncertainties from the relation.
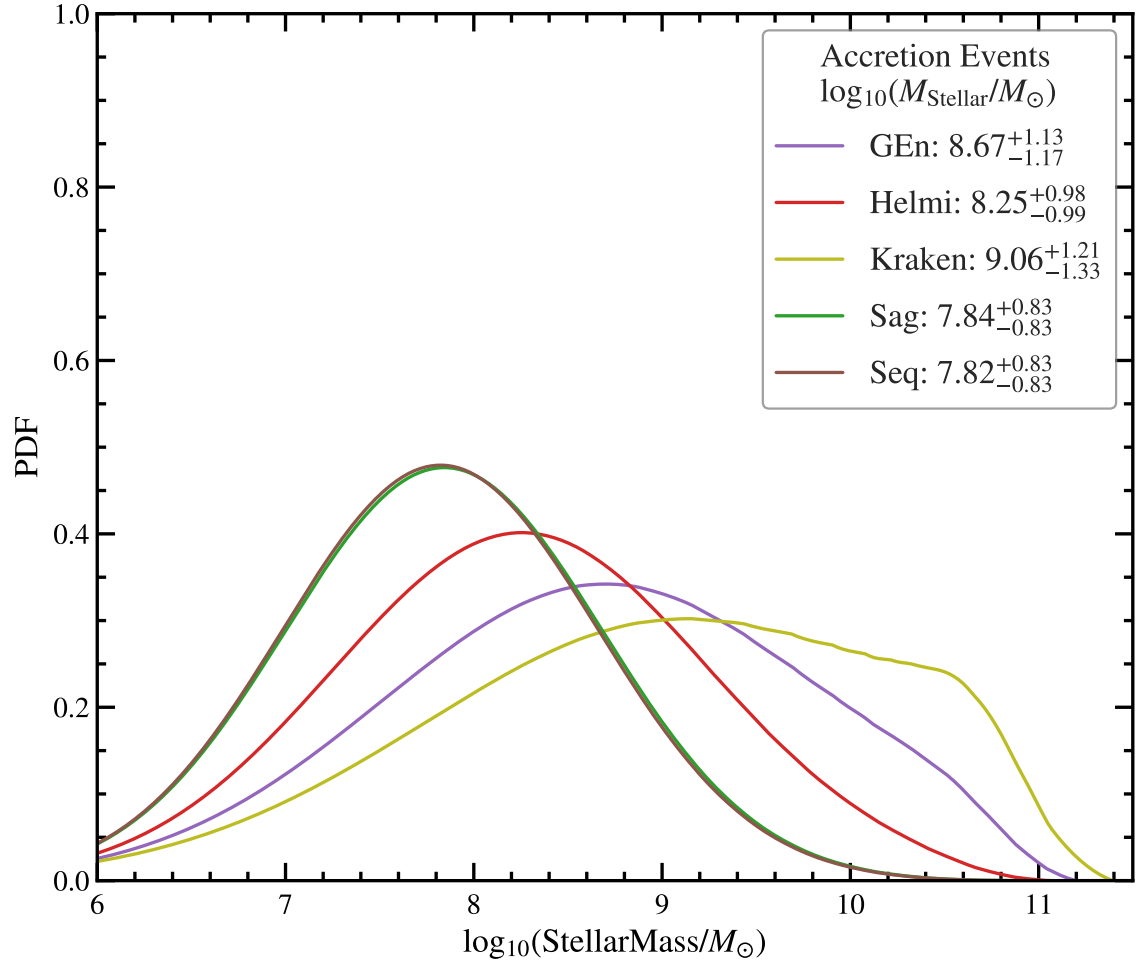
Figure 4.10
The PDFs of the stellar mass of our accreted galaxies. These were calculate by assuming the redshift zero stellar mass to halo mass relation of Behroozi et al. (2019) to transform the halo mass PDFs of Fig. 4.9.

We define two statistical tests to study if our GCs groups are phase mixed. If we find the groups are not phase mixed, this could indicate recent accretion or dynamical information contained in the phase distribution. This could also suggests selection effects or a cluster being categorized in the incorrect group. We can also test if the distributions are axisymmetric, such as by testing that ϕ, the angle in the plane of the disc, is also uniformly distributed with a Kuiper test. Similar to the more commonly used KS test, the Kuiper test can be used to quantify if the cumulative of two distributions are statistically compatible, but is particularly suited to testing distributions of modular variables as the statistic is invariant under cyclic transformations to the random variable (Kuiper, 1960).

If the group is phase mixed then z, v_z and v_R should be evenly distributed between positive and negative values. Using a binomial test on the distribution of each quantity, we can assign p-values which are then combined using the Fisher method to give a final p-value for the hypothesis that a given group is phase mixed. This test is independent of potential.

We also consider tests based on the angles of the action angle coordinates, $\left[\theta_R, \theta_\phi, \theta_z\right]$, which do depend on the assumed MW potential. If the groups are phase mixed, then the angles should be uniformly distributed in the $[0, 2\pi]$ interval. As a uniform distribution modulo 2π, we test this hypothesis using a Kuiper's test. The p-values can be calculated for every angle and then combined via the Fisher method. By remapping the θ_R and θ_z angles a finer test of the potential can be achieved (see appendix 4.8.1 for details).

GES, Kraken, Sequoia are all consistent with being phase mixed, with no detectable structure in action angles or evidence against axisymmetry. This is consistent with the components being ancient accretions. We also find that as a component, our Ungrouped GCs are consistent with the hypothesis. Sagitarius is not consistent with being phase mixed, with a p-value ~ 0.001. This is to be expected, as it is recently accreted. We estimate it to phase mix in $5 - 6$ Gyrs.

We find that the Helmi streams distribution of GCs in z have a p-value of 0.04, with 11/15 GCs are at positive height above the disc. Kepley et al. (2007) find a bimodal distribution in v_z of Helmi stars, splitting the selected stars into a positive and negative moving groups. This was thought to be a selection effect of our local neighbourhood seeing multiple tidal

wraps; stars on a vertical orbit necessarily have high v_z near the plane that we observe. The asymmetry of the moving groups is discussed in Koppelman et al. (2019a), and used to estimate the accretion time 6-9 Gyrs ago. However, we would expect the GCs to be complete and not subject to selection effects like the stars. This is weak evidence of structure persisting in phase space.

We expect the insitu components to be completely phase mixed. Both the disc and bulge individually and together are consistent with our binomial tests. However, both components distribution of remapped vertical angle are incompatible with uniformity, with p-values below 0.01. This indicates that there are too many near the maximum height of their orbit above the plane. This could suggest that the disc potential that we use (McMillan, 2017) is too heavy, making it seem like orbits are closer to their maximum. We note that recent potentials such as Cautun et al. (2020) have lighter discs, which we would anticipate alleviating this tension. Alternatively, we could have an incomplete sample, with GCs in the plane not being observed.

We find both insitu components are not consistent with being axisymmetric, with p-values of 0.004 for the disc 0.04 for the bulge, and 0.004 for the combined sample. This is consistent with an overabundance of GCs on the near side of the Galactic Centre. Binning the GCs into quarter slices with the Sun at $\phi = 0$, we find that our 55 insitu clusters are angular distributed as: 23 GCs in $-\pi/4 < \phi \leq \pi/4$, 10 GCs in $\pi/4 < \phi \leq 3\pi/4$, 14 GCs in $-3\pi/4 < \phi \leq -\pi/4$, 8 GCs in $\phi \leq -3\pi/4, 3\pi/4 < \phi$. In the grouping of Massari19, out of the 62 insitu clusters 30 GCs exist in $-\pi/4 < \phi < \pi/4$, with the rest evenly distributed. These results suggests either incomplete observations, with on the order 30 missing insitu clusters, or this suggests otherwise undiscovered structure in the GCs identified as insitu.

4.7 Conclusions

We have introduced a multi-component model for the population of GCs that splits into three individual components: bulge, disc, and stellar halo. The latter component is further decomposed into the large accretion events that build the Galactic stellar halo. The

identification of the various components has been performed in a chemo-dynamical space, where we combine GC information on the age-metallicity relation with orbital energy, E, and action, J. The aim of our study has been to obtain an objective and statistically robust identification of accreted GCs groups. These have been modelled as multivariate Gaussian distributions in (E, J) space that follow the age-metallicity relation proposed by Forbes (2020).

We have extensively tested our methodology using GCs catalogues built using the AURIGA suite of zoom-in simulations of MW-like galaxies. The mocks roughly reproduce the number, radial distribution, and, by construction, the age-metallicity relation of GCs in our galaxy, which makes them ideal samples to test our multi-component model. Our approach recovers the correct number of GCs associated with each merger event on average, however, the associated GCs are not always the true objects brought by that merger even. This corresponds to a mean purity and completeness of ~60%. The low completeness and purity values are due to the large overlap between various accretion events, which makes it difficult to associate unequivocally most GCs to a single accretion group.

We then have applied this methodology to Galactic GCs observations, accounting for measurement errors. The result is a decomposition of the GC population into: bulge, disc, GES, Kraken, Sagittarius, Sequoia, and Helmi groups, with 16 left-over GCs that follow a uniform background distribution likely consisting of many smaller accretion events that do not contain enough members to be robustly identified. The resulting populations of GCs have been combined with the halo to GCs number relation of Burkert & Forbes (2020) to infer the progenitor halo mass for each accretion event. Then, the halo masses combined with the stellar to halo mass relation of Behroozi et al. (2019) have been used to infer the progenitor stellar masses. We also have discussed the degree of phase mixing of the various GCs groups and their likely infall time into our galaxy.

The age-chemistry could in principle be expanded to include more detailed models of chemical evolution. The obvious choice for this would be to include the α abundances, following the work of Horta et al. (2020). This could be crucial in determining the insitu and Kraken groups. However, this is information is currently only available for a small

subset of GCs, which limits the viability of effective fitting and useful constraints from the GCs alone. Our methodology could be expanded to use more information about the GCs.

In the dynamical transformation from position and velocity space to orbital constants we have neglected the phase of the orbits; we have considered what orbits the GCs are on but not where on those orbits they are. For the most recent infalling objects, we would expect the GCs to be close together in phase, corresponding to being on similar orbits and close together in physical space. Combined with frequency analysis, it may be possible to find more information in orbital phase space.

The methodology could be extended to include stellar halo stars. Our methodologies automated and statistical nature are well placed to handle the increasing numbers, as well as the much higher observational errors. Increasing the number of dynamic tracers by several orders of magnitude will allow for a much stronger inference of the MW's accretion history.

A limitation of this work is in assuming a Gaussian distribution for the accreted GCs in space. Due to the limited number of GCs in every accretion group, we find it necessary to make some assumptions to allow any kind of fitting. With more points, we hope that a density based algorithms that does not require a distribution to be assumed will be possible. The areas most effected by this assumption in $(E, \mathbf{J})$ space are likely the distributions on more circular orbits, particularly where the distribution is extended in energy space (due to the nature of the energy - angular momentum boundary). Notable GCs in these regions include Omega Centauri and FSR1758. Further work is needed to explore the biases in these regions.

This work has developed a methodology to combine the available dynamical and chemical information, in a statistically robust manner. A crucial part of this work has been the mock tests, where we have highlighted the difficulties of this important problem. In the face of considerable uncertainties due to the messy nature of accretion, we believe that this philosophy represents an improvement on previous work. In the future, with further development and the availability of more information, this will allow for much stronger inference of the MW's accretion history.

4.8 Appendix

4.8.1 Phases as a Potential Probe

The angle θ_R is at pericenter at 0, apocenter at π and back at apocenter at 2π. Consider the mapping:

$$\tilde{\theta}_R = \begin{cases} \theta_R & \theta_R < \pi \\ 2\pi - \theta_R & \theta_R > \pi \end{cases} \tag{4.8.1}$$

$\tilde{\theta}_R$ is then uniformly distributed on $[0, \pi]$, and near pericenter at 0, and near apocenter at π, regardless of the sign of v_R. If the we see a bias of over abundance of orbits near pericenter, it can be seen as evidence that the potential is too weak and vice versa.

The angle θ_z is at $z = 0$ with $v_z > 0$ at 0, $z = z_{\max}$ at $\pi/2$, $z = 0$ with $v_z < 0$ at π, $z = -z_{\max}$ at $3\pi/2$, and back at $z = 0$ at 2π. Consider the mapping:

$$\tilde{\theta}_{z1} = \begin{cases} \theta_z & \theta_z < \pi \\ 2\pi - \theta_z & \tilde{\theta}_{z1} > \pi \end{cases}$$

$$\tilde{\theta}_z = \begin{cases} \tilde{\theta}_{z1} & \tilde{\theta}_{z1} < \pi/2 \\ \pi - \tilde{\theta}_{z1} & \tilde{\theta}_{z1} > \pi/2 \end{cases} \tag{4.8.2}$$

$\tilde{\theta}_z$ is then uniformly distributed on $[0, \pi/2]$, and near the center of the plane at 0, and near $z_{\max}$ at $\pi/2$. If the we see a bias of over abundance of orbits near z_{max} it can be seen as evidence that the potential in z is too strong.

Table 4.3

The membership probability of individual GCs, as found by our chemo-dynamical model. We give the most likely group and probability of each cluster, and the second most probable alternate group. We also give the groupings from the literature were possible: M19 corresponds to Massari et al. (2019), F20 corresponds to Forbes (2020), and H20 corresponds to Horta et al. (2020).

Name	Alternative	Main Group	Prob	Alt Group	Alt Prob	M19	F20	H20
NGC6535	-	Bulge	1.00	-	-	Kraken/Seq	Seq	-
Djorg2	ESO456	Bulge	1.00	-	-	Bulge	-	-
NGC6388	-	Bulge	0.99	Disc	0.01	Bulge	-	Seq/Bulge
NGC6380	Ton1	Bulge	0.99	Disc	0.01	Bulge	-	Bulge
Terzan6	HP5	Bulge	0.99	Disc	0.01	Bulge	-	-
Terzan2	HP3	Bulge	0.99	Disc	0.01	Bulge	-	Bulge
Liller1	-	Bulge	0.99	Disc	0.01	-	-	Ungr
NGC6440	-	Bulge	0.98	Disc	0.02	Bulge	-	-
NGC6642	-	Bulge	0.98	Disc	0.02	Bulge	-	-
NGC6401	-	Bulge	0.98	Disc	0.02	Kraken	Kraken	-
NGC6325	-	Bulge	0.96	Disc	0.02	Bulge	-	-
NGC6638	-	Bulge	0.96	Disc	0.04	Bulge	-	-
Terzan5	11	Bulge	0.95	Disc	0.05	Bulge	-	-
Pal6	-	Bulge	0.94	Kraken	0.03	Kraken	-	Kraken
Terzan9	-	Bulge	0.94	Disc	0.06	Bulge	-	-
1636-283	ESO452	Bulge	0.94	Disc	0.06	Bulge	-	-
NGC6528	-	Bulge	0.94	Disc	0.06	Bulge	-	-
NGC6624	-	Bulge	0.93	Disc	0.07	Bulge	-	-
NGC6558	-	Bulge	0.92	Disc	0.08	Bulge	-	-
HP1	BH229	Bulge	0.91	Disc	0.09	Bulge	-	Bulge
Terzan4	HP4	Bulge	0.91	Disc	0.09	Bulge	-	-
NGC6453	-	Bulge	0.89	Disc	0.10	Kraken	Kraken	-
NGC6266	M62	Bulge	0.88	Disc	0.12	Bulge	-	-
NGC6355	-	Bulge	0.87	Kraken	0.11	Bulge	-	-
NGC6626	M28	Bulge	0.86	Disc	0.14	Bulge	-	-
NGC6652	-	Bulge	0.85	Disc	0.15	Bulge	-	-
NGC6522	-	Bulge	0.83	Disc	0.17	Bulge	-	Bulge
Terzan1	HP2	Bulge	0.81	Disc	0.19	Bulge	-	-
NGC6293	-	Bulge	0.76	Kraken	0.22	Bulge	-	-
NGC6342	-	Bulge	0.76	Disc	0.24	Bulge	-	-
NGC6304	-	Bulge	0.76	Disc	0.24	Bulge	-	-
NGC6637	M69	Bulge	0.75	Disc	0.25	Bulge	-	-
VVVCL001	-	Bulge	0.63	Kraken	0.36	-	-	-
NGC6517	-	Bulge	0.60	Kraken	0.32	Kraken	Kraken	-
NGC6540	Djorg	Bulge	0.53	Disc	0.47	Bulge	-	Bulge
NGC5927	-	Disc	1.00	-	-	Disc	-	-
NGC6838	M71	Disc	1.00	-	-	Disc	-	Disc
NGC6352	-	Disc	1.00	-	-	Disc	-	-
NGC6362	-	Disc	1.00	-	-	Disc	-	-
NGC6496	-	Disc	1.00	-	-	Disc	-	-
NGC104	47Tuc	Disc	1.00	-	-	Disc	-	Disc
NGC6366	-	Disc	1.00	-	-	Disc	-	-

Name	Alternative	Main Group	Prob	Alt Group	Alt Prob	M19	F20	H20
ESO93	-	Disc	1.00	-	-	-	-	-
BH176	-	Disc	1.00	-	-	Disc	-	-
NGC6441	-	Disc	0.99	-	-	Kraken	-	Kraken
NGC6218	M12	Disc	0.99	Kraken	0.01	Disc	-	Disc
Pal10	-	Disc	0.98	GEn	0.02	Disc	-	Disc
Lynga7	BH184	Disc	0.97	Bulge	0.02	Disc	-	-
NGC6144	-	Disc	0.95	Bulge	0.05	Kraken	Kraken	-
E3	-	Disc	0.94	Ungr	0.06	Helmi/?	-	-
NGC6171	M107	Disc	0.93	Bulge	0.07	Bulge	-	Bulge
NGC6723	-	Disc	0.81	Bulge	0.19	Bulge	-	Bulge
NGC6717	Pal9	Disc	0.77	Bulge	0.23	Bulge	-	-
NGC6256	-	Disc	0.68	Bulge	0.32	Kraken	Kraken	-
IC1276	Pal7	Disc	0.64	Kraken	0.28	Disc	-	-
NGC6205	M13	GEn	1.00	-	-	GEn	GEn	GEn
NGC362	-	GEn	1.00	-	-	GEn	GEn	GEn
NGC6779	M56	GEn	1.00	-	-	GEn	GEn	-
NGC6341	M92	GEn	1.00	-	-	GEn	GEn	GEn
NGC2298	-	GEn	1.00	-	-	GEn	GEn	-
NGC7089	M2	GEn	1.00	-	-	GEn	GEn	GEn
NGC1851	-	GEn	1.00	-	-	GEn	GEn	GEn
NGC7099	M30	GEn	1.00	-	-	GEn	GEn	-
NGC2808	-	GEn	1.00	-	-	GEn	GEn	GEn
NGC5286	-	GEn	1.00	-	-	GEn	GEn	-
ESO-SC06	ESO280	GEn	1.00	-	-	GEn	-	-
NGC1261	-	GEn	1.00	-	-	GEn	GEn	-
NGC288	-	GEn	1.00	-	-	GEn	GEn	GEn
NGC6864	M75	GEn	1.00	-	-	GEn	GEn	-
NGC5897	-	GEn	1.00	-	-	GEn	GEn	-
NGC5139	oCen	GEn	1.00	-	-	GEn/Seq	Seq	-
NGC7078	M15	GEn	0.99	Disc	0.01	Disc	-	Disc
NGC6656	M22	GEn	0.96	Disc	0.04	Disc	-	Disc
NGC6235	-	GEn	0.95	Kraken	0.05	GEn	GEn	-
BH140	-	GEn	0.95	Disc	0.04	-	-	-
Ryu879	RLGC2	GEn	0.93	Kraken	0.06	-	-	-
NGC6426	-	GEn	0.80	Helmi	0.20	Ungr	Ungr	-
Pal11	-	GEn	0.74	Disc	0.25	Disc	-	-
IC1257	-	GEn	0.60	Helmi	0.39	GEn	GEn	-
Pfleiderer	-	GEn	0.55	Kraken	0.27	-	-	-
NGC5904	M5	Helmi	1.00	-	-	Helmi/GEn	Helmi	GEn/Helmi
NGC4147	-	Helmi	1.00	-	-	GEn	GEn	-
NGC5634	-	Helmi	1.00	-	-	Helmi/GEn	Helmi	-
NGC5053	-	Helmi	1.00	-	-	Helmi	Helmi	Helmi

Name	Alternative	Main Group	Prob	Alt Group	Alt Prob	M19	F20	H20
Pal5	-	Helmi	1.00	-	-	Helmi/?	Helmi	Helmi
NGC5272	M3	Helmi	1.00	-	-	Helmi	Helmi	Helmi
NGC7492	-	Helmi	1.00	-	-	GEn	GEn	-
NGC5024	M53	Helmi	1.00	-	-	Helmi	Helmi	Helmi
NGC6229	-	Helmi	1.00	-	-	GEn	GEn	GEn
NGC4590	M68	Helmi	1.00	-	-	Helmi	Helmi	Helmi
NGC6981	M72	Helmi	1.00	-	-	Helmi	Helmi	-
Rup106	-	Helmi	0.95	Ungr	0.05	Helmi/?	Helmi	-
NGC6584	-	Helmi	0.93	GEn	0.07	Ungr	Ungr	-
Bliss1	-	Helmi	0.88	Ungr	0.11	-	-	-
NGC1904	M79	Helmi	0.63	GEn	0.37	GEn	GEn	GEn
NGC6254	M10	Kraken	1.00	-	-	Kraken	Kraken	Kraken
NGC6712	-	Kraken	1.00	-	-	Kraken	Kraken	-
NGC6544	-	Kraken	1.00	-	-	Kraken	Kraken	Kraken
NGC6287	-	Kraken	1.00	-	-	Kraken	Kraken	-
NGC6681	M70	Kraken	1.00	-	-	Kraken	Kraken	-
NGC6809	M55	Kraken	1.00	-	-	Kraken	Kraken	Kraken
NGC5986	-	Kraken	1.00	-	-	Kraken	Kraken	-
NGC5946	-	Kraken	1.00	-	-	Kraken	Kraken	-
NGC4833	-	Kraken	1.00	-	-	GEn	GEn	-
NGC6541	-	Kraken	1.00	-	-	Kraken	Kraken	-
Terzan10	-	Kraken	1.00	-	-	GEn	GEn	-
NGC6121	M4	Kraken	0.99	Bulge	0.01	Kraken	-	Kraken
NGC6752	-	Kraken	0.99	GEn	0.01	Disc	-	Disc
NGC6402	M14	Kraken	0.99	Bulge	0.01	Kraken	Kraken	-
UKS1	-	Kraken	0.98	GEn	0.01	-	-	-
NGC6760	-	Kraken	0.98	Disc	0.02	Disc	-	Disc
NGC6397	-	Kraken	0.98	Disc	0.01	Disc	-	Disc
FSR1735	-	Kraken	0.98	Disc	0.01	Kraken	Kraken	-
NGC6749	-	Kraken	0.98	Disc	0.02	Disc	-	-
NGC6139	-	Kraken	0.98	Disc	0.01	Kraken	Kraken	-
Mercer5	-	Kraken	0.98	Disc	0.02	-	-	-
NGC6316	-	Kraken	0.98	Bulge	0.01	Bulge	-	-
NGC6284	-	Kraken	0.97	GEn	0.03	GEn	GEn	-
Pal8	-	Kraken	0.97	Disc	0.02	Disc	-	-
NGC6539	-	Kraken	0.97	Disc	0.03	Bulge	-	Bulge
Terzan3	-	Kraken	0.96	Disc	0.04	Disc	-	-
Ton2	Pismis26	Kraken	0.96	Disc	0.04	Kraken	Kraken	-
FSR1716	-	Kraken	0.96	Disc	0.04	Disc	-	-
Terzan12	-	Kraken	0.94	Disc	0.05	Disc	-	-
Djorg1	-	Kraken	0.93	GEn	0.06	GEn	GEn	-

Name	Alternative	Main Group	Prob	Alt Group	Alt Prob	M19	F20	H20
NGC4372	-	Kraken	0.92	GEn	0.05	Disc	-	-
NGC6273	M19	Kraken	0.91	Bulge	0.09	Kraken	Kraken	-
BH261	AL3	Kraken	0.88	Disc	0.11	Bulge	-	-
NGC6569	-	Kraken	0.85	Disc	0.13	Bulge	-	-
NGC6553	-	Kraken	0.83	Disc	0.17	Bulge	-	Bulge
NGC6333	M9	Kraken	0.80	GEn	0.20	Kraken	Kraken	-
NGC6356	-	Kraken	0.78	GEn	0.22	Disc	-	-
NGC6093	M80	Kraken	0.66	Disc	0.29	Kraken	Kraken	-
VVVCL002	-	Kraken	0.52	Bulge	0.41	-	-	-
Gran1	-	Kraken	0.47	Bulge	0.46	-	-	-
Terzan8	-	Sag	1.00	-	-	Sag	Sag	-
NGC6715	M54	Sag	1.00	-	-	Sag	Sag	-
Arp2	-	Sag	1.00	-	-	Sag	Sag	-
Terzan7	-	Sag	1.00	-	-	Sag	Sag	-
Pal12	-	Sag	1.00	-	-	Sag	Sag	-
Whiting1	-	Sag	1.00	-	-	Sag	Sag	-
NGC5824	-	Sag	0.99	-	-	Sag	Sag	-
Munoz1	-	Sag	0.97	Ungr	0.03	-	-	-
Kim3	-	Sag	0.92	Ungr	0.07	-	-	-
NGC5466	-	Seq	1.00	-	-	Seq	Seq	Seq
NGC6101	-	Seq	1.00	-	-	Seq/GEn	Seq	-
NGC3201	-	Seq	1.00	-	-	Seq/GEn	Seq	Seq
NGC7006	-	Seq	1.00	-	-	Seq	Seq	-
IC4499	-	Seq	1.00	-	-	Seq	Seq	-
Pal13	-	Seq	0.99	Ungr	0.01	Seq	Seq	-
NGC5694	-	Seq	0.98	Ungr	0.02	Ungr	Ungr	-
Pal15	-	Seq	0.96	Ungr	0.04	GEn/?	GEn	-
AM4	-	Seq	0.84	Ungr	0.15	-	Sag	-
Ryu059	RLGC1	Ungr	1.00	-	-	-	-	-
Ko2	-	Ungr	1.00	-	-	-	-	-
NGC6934	-	Ungr	1.00	-	-	Ungr	Ungr	-
Crater	-	Ungr	1.00	-	-	Ungr	Ungr	-
Pal3	-	Ungr	1.00	-	-	Ungr	Ungr	-
Pyxis	-	Ungr	1.00	-	-	Ungr	Ungr	-
Pal14	-	Ungr	1.00	-	-	Ungr	Ungr	-
AM1	-	Ungr	1.00	-	-	Ungr	Ungr	-
Eridanus	-	Ungr	1.00	-	-	Ungr	Ungr	-
Pal1	-	Ungr	1.00	-	-	Disc	GEn	-
Segue3	-	Ungr	1.00	-	-	-	-	-
Pal4	-	Ungr	1.00	-	-	Ungr	Ungr	-
NGC2419	-	Ungr	0.98	Seq	0.02	Sag	Sag	-
Laevens3	-	Ungr	0.94	Seq	0.06	-	-	-

Name	Alternative	Main Group	Prob	Alt Group	Alt Prob	M19	F20	H20
Pal2	-	Ungr	0.82	Seq	0.13	GEn	GEn	-
FSR1758	-	Ungr	0.63	Seq	0.29	Seq	Seq	-
Ko1	-	Ungr	0.53	Sag	0.47	-	-	-

Conclusions

This thesis has developed several dynamical methods to infer properties of the MW, focusing on its DM halo and accretion history. A crucial part of this process has been the use of simulations of MW-like galaxies. Through study, these galaxies have provided excellent sources of inspiration, and provide an invaluable testbed for methodologies. Combined with the latest observations of the MW, this approach has proven to be very effective, allowing progress on several significant, longstanding problems in astrophysics.

Chapter 2 presented and applied a method to infer the mass of the Milky Way by comparing the dynamics of observed satellites to the theoretical predictions for the energy and angular momentum distributions of orbits from the EAGLE cosmological hydrodynamics simulations. This research estimated the mass of the Milky Way to be $M_{200}^{\mathrm{MW}} = 1.17^{+0.21}_{-0.15} \times 10^{12} M_\odot$ (68% confidence limits), approximately $\sim 20\%$ accuracy. This result is a substantial improvement on pre-*Gaia* estimates, where the total mass was only known to a factor of two (see Fig. 2.7). Previous studies have struggled to understand systematic effects in their methodology, leading to an underestimate of errors. This challenge was overcome by rigorously testing the method on the MW-like galaxies of the AURIGA project, thus demonstrating its accuracy. This research developed a technique that produced a robust, precise MW mass estimate that remains competitive with later post-Gaia mass measurements (see

Fig. 2.7).

Chapter 3 studied the effect of baryonic contraction in dark matter haloes in the AURIGA simulation suite. Describing the haloes by their spherical action distribution, an iterative algorithm was developed to adiabatically contract AURIGA DM halos to a given baryon mass profile. With the correct action distribution, the density profiles of the DM halos is recovered to within a few percent. In general, halos are recovered to around 15% due to halo-to-halo variation such as concentration. This technique was used to model the contracted DM halo of the MW, inferring the total mass profile and the dynamics of the DM halo. The DM velocity distributions are encoded in the model DM halo's orbital structure, offering a substantial improvement on simpler models, such as the 'Standard Halo Model', that particle physicists commonly assume (see Fig. 3.11). This methodology shows promising potential as a way to model our MWs contracted DM halo while considering the effects of cosmological variation in DM halos.

Chapter 4 developed an objective methodology combining chemo-dynamical information to identify the likely progenitors of the entire population of Galactic GCs. By fitting models to both the dynamical distribution in action space and age-metallicity relation of the accreted galaxy, the membership probabilities for each globular cluster were calculated, allowing them to be statistically linked to particular accretion events. This data was then used to infer properties of the progenitors of the MW's stellar halo, such as the halo and stellar masses. This method was first tested on the mock catalogues made from the AURIGA simulations before being applied to the MW, including previously categorised clusters from *Gaia* EDR3. This showed that reliably identifying the groupings of GCs as very challenging, as consequence of the complex nature of accretion and the large degree of overlap between groups in the phase space. The objective statistical nature of this method, combining chemistry and dynamics whilst including observational errors, is arguably a substantial improvement on previous work in the literature. In the future, to make more confident predictions, more observational information, such as further chemistry information, are needed.

5.1   Future Work

The field is now entering the era of precision near-field cosmology. The next *Gaia* data releases are already on the horizon and promise to push the boundaries of our knowledge further still. To make full use of the dynamics found in this exquisite data, it will be necessary to reduce the uncertainty introduced from the (unknown) Galactic potential, which is becoming comparable to those from observational errors.

5.1.1   The Mass Profile of the Milky Way

There is still significant uncertainty in the potential and the radial profile or shape of the dark matter matter distribution has not yet been robustly constrained. To reduce uncertainty in the inner density profile, the satellite-based methodology of Chapter 2 can be extended to include inner tracers, such as GCs and halo stars. In addition, a more robust inference on the total mass can be made by using ultra-faint satellites, for which observational incompleteness is a critical aspect that needs to be accounted for. By increasing the numbers of dynamical tracers, the precision can be pushed towards 10% (see Fig. 2.11).

In recent years, it has been shown that the LMC has significantly perturbed the MW (Cunningham et al., 2020). To overcome this and other systematic errors, it is of the utmost importance to test any inference techniques on simulations of MW-like galaxies that replicate our local environment, such as those from the new MAGPIE project (Shao et al. in prep).

5.1.2   The Core of the MW

A fundamental prediction of CDM is the steep, cuspy central density profiles of DM halos. A cored DM halo would have implications for cosmology (the core-cusp problem) and change the inner structure of our Galaxy, implying $\sim$ 5 times less DM density at the solar radius than cuspy models. Cole & Binney (2017) claims to find evidence supporting a DM

core at the centre of the MW itself by constructing an elaborate multi-component dynamical model of our Galaxy. The DM halo, stellar discs and bulge are modelled as a collection of orbits, described by analytically postulated distributions of orbital actions. However, it is unclear how well this idealistic modelling survives the inherent non-equilibrium of realistic galaxies or if the analytically postulated action distributions capture the correct dynamics.

This controversial result can be tested by applying the dynamical methodology used to a variety of MW-like zoom-in simulations, including those with different galaxy formation models and DM cosmologies from the AURIGA and APOSTLE projects. This is an extension of the work of Chapter 3 to study the stellar components of the galaxy; characterising numerical components analytically and comparing them to the proposed analytic distributions. The final model has applications beyond the core-cusp problem; giving DM and baryonic mass profiles for the MW, the total gravitational potential and robustly inferring the dynamics that govern the structures of the MW. This includes the velocity distribution of DM in our local solar neighbourhood. Such an approach will connect the latest analytical techniques with simulations and presents a unique opportunity to probe the structure of the MW and the nature of DM.

5.1.3   The Accretion History of the Stellar Halo

A natural development of the work of Chapter 4 is to extend it to include stellar halo stars. Increasing the number of dynamic tracers by several orders of magnitude will allow for a much stronger inference of the MW's accretion history. However, this also increases the complexity of the problem. Furthermore, individual stars have much higher observational errors than globular clusters, requiring a robust statistical approach. Fortunately, these are perfect conditions for an algorithmic method to excel. The technique can be tested and calibrated on galaxy simulations and *Gaia* mocks, which include observational errors equivalent to EDR3 and future data releases and potentially developed improved models for the chemo-dynamical distribution of the debris of satellite galaxies. This study will

develop a holistic method to probabilistically infer the accretion history of our MW from remnants in the stellar halo.

5.2   Concluding Remarks

Since the start of this PhD, the field of Galactic science has developed significantly and it is the author's good fortune that the duration of this work fell in this prosperous time. Piece by piece, we are assembling an understanding of our own Galaxy and its history. In turn, this is bringing us closer to understanding the wider Universe. Driving this success has been a combination of advancing observations, analytical tools and simulations, as this thesis has demonstrated. As these areas continue to advance, new avenues of discovery will open, and further progress will be made. Future prospects have never looked better.

All we have to decide is what to do with the time that is given us.

— J.R.R. Tolkien

Bibliography

Abadi M. G., Navarro J. F., Fardal M., Babul A., Steinmetz M., 2010, Monthly Notices of the Royal Astronomical Society, 407, 435

Abolfathi B., et al., 2018, The Astrophysical Journal Supplement Series, 235, 42

Adelman-McCarthy J. K., et al., 2007, The Astrophysical Journal Supplement Series, 172, 634

Amorisco N. C., 2017, Monthly Notices of the Royal Astronomical Society, 469, L48

Amorisco N. C., 2019, Monthly Notices of the Royal Astronomical Society, 482, 2978

Antoja T., et al., 2018, Nature, 561, 360

Antoja T., Ramos P., Mateu C., Helmi A., Anders F., Jordi C., Carballo-Bello J. A., 2020, Astronomy and Astrophysics, 635, L3

Arnold V. I., 1978, Mathematical methods of classical mechanics. Springer, `https://ui.adsabs.harvard.edu/abs/1978mmcm.book.....A`

Arora A., Williams L. L. R., 2020, The Astrophysical Journal, 893, 53

Artale M. C., Pedrosa S. E., Tissera P. B., Cataldi P., Cintio A. D., 2019, Astronomy & Astrophysics, 622, A197

Barba R. H., Minniti D., Geisler D., Alonso-Garcia J., Hempel M., Monachesi A., Arias J. I., Gomez F. A., 2019, The Astrophysical Journal, 870, L24

Barber C., Starkenburg E., Navarro J. F., McConnachie A. W., Fattahi A., 2014, Monthly Notices of the Royal Astronomical Society, 437, 959

Barnes J., White S. D. M., 1984, Monthly Notices of the Royal Astronomical Society, 211, 753

Bastian N., Pfeffer J., Kruijssen J. M. D., Crain R. A., Trujillo-Gomez S., Reina-Campos M., 2020, Monthly Notices of the Royal Astronomical Society, 498, 1050

Battaglia G., Helmi A., Breddels M., 2013, New Astronomy Reviews, 57, 52

Baumgardt H., Vasiliev E., 2021, Monthly Notices of the Royal Astronomical Society, 505, 5957

Bechtol K., et al., 2015, The Astrophysical Journal, 807, 50

Behroozi P., Wechsler R. H., Hearin A. P., Conroy C., 2019, Monthly Notices of the Royal Astronomical Society, 488, 3143

Bekki K., Freeman K. C., 2003, Monthly Notices of the Royal Astronomical Society, Volume 346, Issue 2, pp. L11-L15., 346, L11

Bellazzini M., Ibata R., Malhan K., Martin N., Famaey B., Thomas G., 2020, Astronomy & Astrophysics, 636, A107

Belokurov V., Erkal D., Evans N. W., Koposov S. E., Deason A. J., 2018, Monthly Notices of the Royal Astronomical Society, 478, 611

Benitez-Llambay A., Frenk C., 2020, Monthly Notices of the Royal Astronomical Society, 498, 4887

Benítez-Llambay A., Frenk C. S., Ludlow A. D., Navarro J. F., 2019, Monthly Notices of the Royal Astronomical Society, 488, 2387

Bertschinger E., 1985, The Astrophysical Journal Supplement Series, 58, 39

Bertschinger E., 2001, The Astrophysical Journal Supplement Series, 137, 1

Binney J., 2010, Monthly Notices of the Royal Astronomical Society, 401, 2318

Binney J., 2012, Monthly Notices of the Royal Astronomical Society, 426, 1324

Binney J., 2013, New Astronomy Reviews, 57, 29

Binney J., Piffl T., 2015, Monthly Notices of the Royal Astronomical Society, 454, 3653

Binney J., Tremaine S., 2008, Galactic Dynamics: Second Edition. Princeton University Press, `https://ui.adsabs.harvard.edu/abs/2008gady.book.....B`

Binney J., Wong L. K., 2017, Monthly Notices of the Royal Astronomical Society, p. stx234

Bland-Hawthorn J., Gerhard O., 2016, Annual Review of Astronomy and Astrophysics, 54, 529

Bland-Hawthorn J., Tepper-García T., 2021, Monthly Notices of the Royal Astronomical Society, 504, 3168

Blumenthal G. R., Faber S. M., Flores R., Primack J. R., 1986, The Astrophysical Journal, 301, 27

Borrow J., Schaller M., Bower R. G., Schaye J., 2020, arXiv e-prints, p. arXiv:2012.03974

Bose S., Deason A. J., Frenk C. S., 2018, The Astrophysical Journal, 863, 123

Bovy J., 2015, The Astrophysical Journal Supplement Series, 216, 29

Bowden A., Belokurov V., Evans N. W., 2015, Monthly Notices of the Royal Astronomical Society, 449, 1391

Bower R. G., Schaye J., Frenk C. S., Theuns T., Schaller M., Crain R. A., McAlpine S., 2017, Monthly Notices of the Royal Astronomical Society, 465, 32

Boylan-Kolchin M., 2017, Monthly Notices of the Royal Astronomical Society, 472, 3120

Boylan-Kolchin M., Bullock J. S., Kaplinghat M., 2011, Monthly Notices of the Royal Astronomical Society: Letters, 415, L40

Boylan-Kolchin M., Bullock J. S., Sohn S. T., Besla G., Marel R. P. v. d., 2013, The Astrophysical Journal, 768, 140

Bozorgnia N., Fattahi A., Frenk C. S., Cheek A., Cerdeno D. G., Gómez F. A., Grand R. J. J., Marinacci F., 2020, Journal of Cosmology and Astroparticle Physics, 2020, 036

Bullock J. S., Boylan-Kolchin M., 2017, Annual Review of Astronomy and Astrophysics, vol. 55, issue 1, pp. 343-387, 55, 343

Bullock J. S., Johnston K. V., 2005, The Astrophysical Journal, 635, 931

Burger J. D., Zavala J., 2019, Monthly Notices of the Royal Astronomical Society, 485, 1008

Burger J. D., Peñarrubia J., Zavala J., 2020, arXiv:2012.00737 [astro-ph]

Burkert A., Forbes D. A., 2020, The Astronomical Journal, 159, 56

Busha M. T., Marshall P. J., Wechsler R. H., Klypin A., Primack J., 2011a, The Astrophysical Journal, 743, 40

Busha M. T., Wechsler R. H., Behroozi P. S., Gerke B. F., Klypin A. A., Primack J. R., 2011b, The Astrophysical Journal, 743, 117

Callingham T. M., et al., 2019, Monthly Notices of the Royal Astronomical Society, 484, 5453

Cautun M., Frenk C. S., 2017, Monthly Notices of the Royal Astronomical Society: Letters, 468, L41

Cautun M., Frenk C. S., van de Weygaert R., Hellwing W. A., Jones B. J. T., 2014, Monthly Notices of the Royal Astronomical Society, 445, 2049

Cautun M., Bose S., Frenk C. S., Guo Q., Han J., Hellwing W. A., Sawala T., Wang W., 2015, Monthly Notices of the Royal Astronomical Society, 452, 3838

Cautun M., et al., 2020, Monthly Notices of the Royal Astronomical Society, 494, 4291

Cole D. R., Binney J., 2017, Monthly Notices of the Royal Astronomical Society, 465, 798

Cole S., Lacey C., 1996, Monthly Notices of the Royal Astronomical Society, 281, 716

Cole S., et al., 2005, Monthly Notices of the Royal Astronomical Society, 362, 505

Collaboration D., et al., 2021a, arXiv:2107.04646 [astro-ph]

Collaboration G., et al., 2021b, arXiv:2101.05811 [astro-ph]

Colless M., et al., 2001, Monthly Notices of the Royal Astronomical Society, 328, 1039

Conroy C., et al., 2019, The Astrophysical Journal, 883, 107

Correa C. A., Schaye J., Wyithe J. S. B., Duffy A. R., Theuns T., Crain R. A., Bower R. G., 2018, Monthly Notices of the Royal Astronomical Society, 473, 538

Crain R. A., et al., 2015, Monthly Notices of the Royal Astronomical Society, 450, 1937

Cunningham E. C., et al., 2020, The Astrophysical Journal, 898, 4

D'Onghia E., Springel V., Hernquist L., Keres D., 2010, The Astrophysical Journal, 709, 1138

Davis M., Efstathiou G., Frenk C. S., White S. D. M., 1985, The Astrophysical Journal, 292, 371

Deason A. J., Belokurov V., Evans N. W., 2011, Monthly Notices of the Royal Astronomical Society, 416, 2903

Deason A. J., Belokurov V., Evans N. W., An J., 2012, Monthly Notices of the Royal Astronomical Society: Letters, 424, L44

Deason A. J., Wetzel A. R., Garrison-Kimmel S., Belokurov V., 2015, Monthly Notices of the Royal Astronomical Society, 453, 3568

Deason A. J., Belokurov V., Koposov S. E., Lancaster L., 2018, The Astrophysical Journal Letters, Volume 862, Issue 1, article id. L1, <NUMPAGES>5</NUMPAGES> pp. (2018)., 862, L1

Deason A. J., Fattahi A., Belokurov V., Evans N. W., Grand R. J. J., Marinacci F., Pakmor R.,

2019a, Monthly Notices of the Royal Astronomical Society, 485, 3514

Deason A. J., Belokurov V., Sanders J. L., 2019b, Monthly Notices of the Royal Astronomical Society, 490, 3426

Deason A. J., Fattahi A., Frenk C. S., Grand R. J. J., Oman K. A., Garrison-Kimmel S., Simpson C. M., Navarro J. F., 2020, Monthly Notices of the Royal Astronomical Society, 496, 3929

Deason A. J., et al., 2021, Monthly Notices of the Royal Astronomical Society, 501, 5964

Dotter A., et al., 2010, The Astrophysical Journal, 708, 698

Dotter A., Sarajedini A., Anderson J., 2011, The Astrophysical Journal, 738, 74

Drlica-Wagner A., et al., 2015, The Astrophysical Journal, 813, 109

Duffy A. R., Schaye J., Kay S. T., Dalla Vecchia C., Battye R. A., Booth C. M., 2010, Monthly Notices of the Royal Astronomical Society, 405, 2161

Dutton A. A., et al., 2016, Monthly Notices of the Royal Astronomical Society, 461, 2658

Eadie G. M., Harris W. E., 2016, The Astrophysical Journal, 829, 108

Eadie G., Jurić M., 2019, The Astrophysical Journal, 875, 159

Eadie G. M., Harris W. E., Widrow L. M., 2015, The Astrophysical Journal, 806, 54

Eggen O. J., Lynden-Bell D., Sandage A. R., 1962, The Astrophysical Journal, 136, 748

Eilers A.-C., Hogg D. W., Rix H.-W., Ness M. K., 2019, The Astrophysical Journal, 871, 120

Eisenstein D. J., et al., 2005, The Astrophysical Journal, 633, 560

Erkal D., et al., 2019, Monthly Notices of the Royal Astronomical Society, 487, 2685

Erkal D., et al., 2021, Monthly Notices of the Royal Astronomical Society

Evans N. W., Wilkinson M. I., Perrett K. M., Bridges T. J., 2003, The Astrophysical Journal, 583, 752

Evans N. W., O'Hare C. A. J., McCabe C., 2019, Physical Review D, 99, 023012

Evans T. A., Fattahi A., Deason A. J., Frenk C. S., 2020, Monthly Notices of the Royal Astronomical Society, 497, 4311

Fakhouri O., Ma C.-P., 2009, Monthly Notices of the Royal Astronomical Society, 394, 1825

Fattahi A., et al., 2016, Monthly Notices of the Royal Astronomical Society, 457, 844

Fattahi A., et al., 2019, Monthly Notices of the Royal Astronomical Society, 484, 4471

Forbes D. A., 2020, Monthly Notices of the Royal Astronomical Society, 493, 847

Forbes D. A., Bridges T., 2010, Monthly Notices of the Royal Astronomical Society, 404, 1203

Forbes D. A., et al., 2018, Proceedings of the Royal Society A: Mathematical, Physical and Engineering Sciences, 474, 20170616

Fragione G., Loeb A., 2017, New Astronomy, 55, 32

Frenk C. S., White S. D. M., Davis M., Efstathiou G., 1988, The Astrophysical Journal, 327, 507

Frenk C. S., et al., 1999, The Astrophysical Journal, 525, 554

Fritz T. K., Battaglia G., Pawlowski M. S., Kallivayalil N., Marel R. v. d., Sohn S. T., Brook C.,

Besla G., 2018, Astronomy & Astrophysics, 619, A103

Gao L., White S. D. M., Jenkins A., Frenk C. S., Springel V., 2005, Monthly Notices of the Royal Astronomical Society, 363, 379

Gao L., Navarro J. F., Cole S., Frenk C. S., White S. D. M., Springel V., Jenkins A., Neto A. F., 2008, Monthly Notices of the Royal Astronomical Society, 387, 536

Garrison-Kimmel S., et al., 2017, Monthly Notices of the Royal Astronomical Society, 471, 1709

Genel S., et al., 2014, Monthly Notices of the Royal Astronomical Society, 445, 175

Genina A., et al., 2018, Monthly Notices of the Royal Astronomical Society, 474, 1398

Gibbons S. L. J., Belokurov V., Evans N. W., 2014, Monthly Notices of the Royal Astronomical Society, 445, 3788

Gilmore G., et al., 2012, The Messenger, 147, 25

Gnedin O. Y., Kravtsov A. V., Klypin A. A., Nagai D., 2004, The Astrophysical Journal, 616, 16

Gnedin O. Y., Brown W. R., Geller M. J., Kenyon S. J., 2010, The Astrophysical Journal, 720, L108

Gnedin O. Y., Ceverino D., Gnedin N. Y., Klypin A. A., Kravtsov A. V., Levine R., Nagai D., Yepes G., 2011, arXiv e-prints, p. arXiv:1108.5736

González R. E., Kravtsov A. V., Gnedin N. Y., 2013, The Astrophysical Journal, 770, 96

Gottloeber S., Hoffman Y., Yepes G., 2010, arXiv e-prints, p. arXiv:1005.2687

Gottlöber S., Klypin A., Kravtsov A. V., 2001, The Astrophysical Journal, 546, 223

Grand R. J. J., et al., 2017, Monthly Notices of the Royal Astronomical Society, 467, 179

Grand R. J. J., et al., 2018, Monthly Notices of the Royal Astronomical Society, 481, 1726

Grand R. J. J., Deason A. J., White S. D. M., Simpson C. M., Gómez F. A., Marinacci F., Pakmor R., 2019, Monthly Notices of the Royal Astronomical Society, 487, L72

Green A. M., 2010, \jcap, 2010, 034

Green A. M., 2017, Journal of Physics G Nuclear Physics, 44, 084001

Gómez F. A., Helmi A., Brown A. G. A., Li Y.-S., 2010, Monthly Notices of the Royal Astronomical Society, 408, 935

Gómez F. A., Besla G., Carpintero D. D., Villalobos A., O'Shea B. W., Bell E. F., 2015, The Astrophysical Journal, 802, 128

Gómez F. A., White S. D. M., Grand R. J. J., Marinacci F., Springel V., Pakmor R., 2017a, Monthly Notices of the Royal Astronomical Society, 465, 3446

Gómez F. A., et al., 2017b, Monthly Notices of the Royal Astronomical Society, 472, 3722

Hahn O., Abel T., 2011, Monthly Notices of the Royal Astronomical Society, 415, 2101

Halbesma T. L. R., Grand R. J. J., Gómez F. A., Marinacci F., Pakmor R., Trick W. H., Busch P., White S. D. M., 2020, Monthly Notices of the Royal Astronomical Society, 496, 638

Han J., Wang W., Cole S., Frenk C. S., 2016, Monthly Notices of the Royal Astronomical Society, 456, 1017

Harris W. E., Harris G. L., Hudson M. J., 2015, The Astrophysical Journal, 806, 36

Hellwing W. A., Frenk C. S., Cautun M., Bose S., Helly J., Jenkins A., Sawala T., Cytowski M., 2016, Monthly Notices of the Royal Astronomical Society, 457, 3492

Helmi A., White S. D. M., de Zeeuw P. T., Zhao H., 1999, Nature, Volume 402, Issue 6757, pp. 53-55 (1999)., 402, 53

Helmi A., Veljanoski J., Breddels M. A., Tian H., Sales L. V., 2017, Astronomy & Astrophysics, 598, A58

Helmi A., Babusiaux C., Koppelman H. H., Massari D., Veljanoski J., Brown A. G. A., 2018a, preprint

Helmi A., et al., 2018b, Astronomy & Astrophysics, 616, A12

Hoffman Y., Ribak E., 1991, The Astrophysical Journal, 380, L5

Hopkins P. F., Narayanan D., Murray N., 2013, Monthly Notices of the Royal Astronomical Society, 432, 2647

Hopkins P. F., Kereš D., Oñorbe J., Faucher-Giguère C.-A., Quataert E., Murray N., Bullock J. S., 2014, Monthly Notices of the Royal Astronomical Society, 445, 581

Horta D., et al., 2020, Monthly Notices of the Royal Astronomical Society, 493, 3363

Horta D., et al., 2021, Monthly Notices of the Royal Astronomical Society, 500, 1385

Huang Y., et al., 2016, Monthly Notices of the Royal Astronomical Society, 463, 2623

Ibata R. A., Gilmore G., Irwin M. J., 1994, Nature, 370, 194

Ibata R. A., et al., 2013, Nature, 493, 62

Jasche J., Wandelt B. D., 2013, Monthly Notices of the Royal Astronomical Society, 432, 894

Jeans J. H., 1915, Monthly Notices of the Royal Astronomical Society, 76, 70

Jenkins A., 2013, Monthly Notices of the Royal Astronomical Society, 434, 2094

Kafle P. R., Sharma S., Lewis G. F., Bland-Hawthorn J., 2012, The Astrophysical Journal, 761, 98

Kafle P. R., Sharma S., Lewis G. F., Bland-Hawthorn J., 2014, The Astrophysical Journal, 794, 59

Kallivayalil N., Marel R. P. v. d., Besla G., Anderson J., Alcock C., 2013, The Astrophysical Journal, 764, 161

Katz N., White S. D. M., 1993, The Astrophysical Journal, 412, 455

Kennedy R., Frenk C., Cole S., Benson A., 2014, Monthly Notices of the Royal Astronomical Society, 442, 2487

Kepley A. A., et al., 2007, The Astronomical Journal, 134, 1579

Klypin A., Kravtsov A. V., Valenzuela O., Prada F., 1999, The Astrophysical Journal, 522, 82

Klypin A., Hoffman Y., Kravtsov A. V., Gottlöber S., 2003, The Astrophysical Journal, 596, 19

Komatsu E., et al., 2011, The Astrophysical Journal Supplement Series, 192, 18

Koposov S. E., Rix H.-W., Hogg D. W., 2010, The Astrophysical Journal, 712, 260

Koposov S., Belokurov V., Torrealba G., Evans W., 2015, IAU General Assembly, 29, 2256759

Koppelman H. H., Helmi A., Massari D., Roelenga S., Bastian U., 2019a, Astronomy and Astrophysics, 625, A5

Koppelman H. H., Helmi A., Massari D., Price-Whelan A. M., Starkenburg T. K., 2019b, Astronomy & Astrophysics, Volume 631, id.L9, <NUMPAGES>6</NUMPAGES> pp., 631, L9

Kruijssen J. M. D., Pfeffer J. L., Crain R. A., Bastian N., 2019a, Monthly Notices of the Royal Astronomical Society, 486, 3134

Kruijssen J. M. D., Pfeffer J. L., Reina-Campos M., Crain R. A., Bastian N., 2019b, Monthly Notices of the Royal Astronomical Society, 486, 3180

Kruijssen J. M. D., et al., 2020, Monthly Notices of the Royal Astronomical Society, 498, 2472

Kuiper N. H., 1960, Indagationes Mathematicae (Proceedings), 63, 38

Kunkel W. E., Demers S., 1976, Royal Greenwich Observatory Bulletins, 182, 241

Küpper A. H. W., Balbinot E., Bonaca A., Johnston K. V., Hogg D. W., Kroupa P., Santiago B. X., 2015, The Astrophysical Journal, 803, 80

Lacey C., Cole S., 1993, Monthly Notices of the Royal Astronomical Society, 262, 627

Law D. R., Majewski S. R., 2010, The Astrophysical Journal, 718, 1128

Leaman R., VandenBerg D. A., Mendel J. T., 2013, Monthly Notices of the Royal Astronomical Society, 436, 122

Li Z.-Z., Jing Y. P., Qian Y.-Z., Yuan Z., Zhao D.-H., 2017, The Astrophysical Journal, 850, 116

Li Z.-Z., Zhao D.-H., Jing Y. P., Han J., Dong F.-Y., 2020, The Astrophysical Journal, 905, 177

Libeskind N. I., et al., 2020, Monthly Notices of the Royal Astronomical Society, 498, 2968

Lovell M. R., 2020, Monthly Notices of the Royal Astronomical Society, 493, L11

Lovell M. R., Frenk C. S., Eke V. R., Jenkins A., Gao L., Theuns T., 2014, Monthly Notices of the Royal Astronomical Society, 439, 300

Lu Y., Mo H. J., Katz N., Weinberg M. D., 2006, Monthly Notices of the Royal Astronomical Society, 368, 1931

Ludlow A. D., Navarro J. F., Springel V., Vogelsberger M., Wang J., White S. D. M., Jenkins A., Frenk C. S., 2010, Monthly Notices of the Royal Astronomical Society, 406, 137

Ludlow A. D., Navarro J. F., White S. D. M., Boylan-Kolchin M., Springel V., Jenkins A., Frenk C. S., 2011, Monthly Notices of the Royal Astronomical Society, 415, 3895

Ludlow A. D., et al., 2013, Monthly Notices of the Royal Astronomical Society, 432, 1103

Ludlow A. D., Navarro J. F., Angulo R. E., Boylan-Kolchin M., Springel V., Frenk C., White S. D. M., 2014, Monthly Notices of the Royal Astronomical Society, 441, 378

Lynden-Bell D., 1976, Monthly Notices of the Royal Astronomical Society, 174, 695

Mackereth J. T., Bovy J., 2020, Monthly Notices of the Royal Astronomical Society, 492, 3631

Majewski S. R., et al., 2017, The Astronomical Journal, 154, 94

Mao Y.-Y., Strigari L. E., Wechsler R. H., Wu H.-Y., Hahn O., 2013, The Astrophysical Journal, 764, 35

Martell S. L., et al., 2017, Monthly Notices of the Royal Astronomical Society, 465, 3203

Marín-Franch A., et al., 2009, The Astrophysical Journal, 694, 1498

Massari D., Koppelman H. H., Helmi A., 2019, Astronomy & Astrophysics, 630, L4

Matthee J., Schaye J., Crain R. A., Schaller M., Bower R., Theuns T., 2017, Monthly Notices of the Royal Astronomical Society, 465, 2381

McConnachie A. W., 2012, The Astronomical Journal, 144, 4

McGill C., Binney J., 1990, Monthly Notices of the Royal Astronomical Society, 244, 634

McMillan P. J., 2011, Monthly Notices of the Royal Astronomical Society, 414, 2446

McMillan P. J., 2017, Monthly Notices of the Royal Astronomical Society, 465, 76

Minniti D., Fernández-Trincado J. G., Gómez M., Smith L. C., Lucas P. W., Ramos R. C., 2021b, arXiv:2106.01383 [astro-ph]

Minniti D., Gómez M., Alonso-García J., Saito R. K., Garro E. R., 2021a, arXiv:2106.03605 [astro-ph]

Mo H. J., Mao S., White S. D. M., 1998, Monthly Notices of the Royal Astronomical Society, 295, 319

Monachesi A., et al., 2019, Monthly Notices of the Royal Astronomical Society, 485, 2589

Monari G., et al., 2018, Astronomy & Astrophysics, 616, L9

Moore B., 1994, Nature, 370, 629

Moore B., Ghigna S., Governato F., Lake G., Quinn T., Stadel J., Tozzi P., 1999, The Astrophysical Journal, 524, L19

Myeong G. C., Evans N. W., Belokurov V., Amorisco N. C., Koposov S. E., 2018a, Monthly Notices of the Royal Astronomical Society, 475, 1537

Myeong G. C., Evans N. W., Belokurov V., Sanders J. L., Koposov S. E., 2018b, Monthly Notices of the Royal Astronomical Society, 478, 5449

Myeong G. C., Evans N. W., Belokurov V., Sanders J. L., Koposov S. E., 2018c, The Astrophysical Journal Letters, 863, L28

Myeong G. C., Vasiliev E., Iorio G., Evans N. W., Belokurov V., 2019, Monthly Notices of the Royal Astronomical Society, 488, 1235

Müller O., Pawlowski M. S., Jerjen H., Lelli F., 2018, Science, 359, 534

Naidu R. P., Conroy C., Bonaca A., Johnson B. D., Ting Y.-S., Caldwell N., Zaritsky D., Cargile P. A., 2020, The Astrophysical Journal, 901, 48

Navarro J. F., Frenk C. S., White S. D. M., 1996, The Astrophysical Journal, 462, 563

Navarro J. F., Frenk C. S., White S. D. M., 1997, The Astrophysical Journal, 490, 493

Navarro J. F., et al., 2010, Monthly Notices of the Royal Astronomical Society, 402, 21

Necib L., Ostdiek B., Lisanti M., Cohen T., Freytsis M., Garrison-Kimmel S., 2020, The Astrophysical Journal, 903, 25

Neto A. F., et al., 2007, \mnras, 381, 1450

Newberg H. J., Willett B. A., Yanny B., Xu Y., 2010, The Astrophysical Journal, 711, 32

Newton O., Cautun M., Jenkins A., Frenk C. S., Helly J. C., 2018, Monthly Notices of the Royal Astronomical Society, 479, 2853

Ollongren A., 1962, Bulletin of the Astronomical Institutes of the Netherlands, 16, 241

Ostdiek B., et al., 2020, Astronomy and Astrophysics, 636, A75

Patel E., Besla G., Mandel K., 2017, Monthly Notices of the Royal Astronomical Society, 468, 3428

Patel E., Besla G., Mandel K., Sohn S. T., 2018, The Astrophysical Journal, 857, 78

Paust N., Wilson D., van Belle G., 2014, The Astronomical Journal, 148, 19

Pawlowski M. S., et al., 2014, Monthly Notices of the Royal Astronomical Society, 442, 2362

Peebles P. J. E., 1982, The Astrophysical Journal, 263, L1

Peñarrubia J., Fattahi A., 2017, Monthly Notices of the Royal Astronomical Society, 468, 1300

Peñarrubia J., Petersen M. S., 2021, arXiv:2106.11984 [astro-ph]

Peñarrubia J., Gómez F. A., Besla G., Erkal D., Ma Y.-Z., 2016, Monthly Notices of the Royal Astronomical Society: Letters, 456, L54

Pfeffer J., Kruijssen J. M. D., Crain R. A., Bastian N., 2018, Monthly Notices of the Royal Astronomical Society, 475, 4309

Pfeffer J. L., Trujillo-Gomez S., Kruijssen J. M. D., Crain R. A., Hughes M. E., Reina-Campos M., Bastian N., 2020, Monthly Notices of the Royal Astronomical Society, 499, 4863

Piatek S., Pryor C., Olszewski E. W., 2016, The Astronomical Journal, 152, 166

Piffl T., et al., 2014a, Monthly Notices of the Royal Astronomical Society, 445, 3133

Piffl T., et al., 2014b, \aap, 562, A91

Piffl T., Penoyre Z., Binney J., 2015, Monthly Notices of the Royal Astronomical Society, 451, 639

Planck Collaboration et al., 2014, Astronomy & Astrophysics, 571, A1

Pontzen A., Governato F., 2012, Monthly Notices of the Royal Astronomical Society, 421, 3464

Pontzen A., Governato F., 2013, Monthly Notices of the Royal Astronomical Society, 430, 121

Posti L., Helmi A., 2019, Astronomy & Astrophysics, 621, A56

Posti L., Binney J., Nipoti C., Ciotti L., 2015, Monthly Notices of the Royal Astronomical Society, 447, 3060

Power C., Navarro J. F., Jenkins A., Frenk C. S., White S. D. M., Springel V., Stadel J., Quinn T., 2003, \mnras, 338, 14

Prada J., Forero-Romero J. E., Grand R. J. J., Pakmor R., Springel V., 2019, Monthly Notices of the Royal Astronomical Society, 490, 4877

Purcell C. W., Zentner A. R., 2012, Journal of Cosmology and Astroparticle Physics, 2012, 007

Pérez-Villegas A., Barbuy B., Kerber L., Ortolani S., Souza S. O., Bica E., 2019, Monthly Notices of the Royal Astronomical Society, p. stz3162

Read J. I., 2014, Journal of Physics G Nuclear Physics, 41, 063101

Read J. I., Agertz O., Collins M. L. M., 2016, Monthly Notices of the Royal Astronomical Society, 459, 2573

Reino S., Rossi E. M., Sanderson R. E., Sellentin E., Helmi A., Koppelman H. H., Sharma S., 2020,

arXiv:2007.00356 [astro-ph]

Richings J., et al., 2020, Monthly Notices of the Royal Astronomical Society, 492, 5780

Rodríguez-Torres S. A., et al., 2016, Monthly Notices of the Royal Astronomical Society, 460, 1173

Romero-Colmenares M., et al., 2021, arXiv:2106.00027 [astro-ph]

Rossi E. M., Marchetti T., Cacciato M., Kuiack M., Sari R., 2017, Monthly Notices of the Royal Astronomical Society, 467, 1844

Rubin V. C., Ford Jr. W. K., 1970, The Astrophysical Journal, 159, 379

Sakari C. M., Venn K. A., Irwin M., Aoki W., Arimoto N., Dotter A., 2011, The Astrophysical Journal, 740, 106

Sanders J. L., Binney J., 2015a, Astrophysics Source Code Library, p. ascl:1512.020

Sanders J. L., Binney J., 2015b, Monthly Notices of the Royal Astronomical Society, 447, 2479

Sanders J. L., Binney J., 2016, Monthly Notices of the Royal Astronomical Society, 457, 2107

Sanderson R. E., Helmi A., Hogg D. W., 2015, The Astrophysical Journal, 801, 98

Sawala T., et al., 2015, Monthly Notices of the Royal Astronomical Society, 448, 2941

Sawala T., et al., 2016, Monthly Notices of the Royal Astronomical Society, 457, 1931

Sawala T., Pihajoki P., Johansson P. H., Frenk C. S., Navarro J. F., Oman K. A., White S. D. M., 2017, Monthly Notices of the Royal Astronomical Society, 467, 4383

Scannapieco C., et al., 2012, Monthly Notices of the Royal Astronomical Society, 423, 1726

Schaller M., et al., 2015, Monthly Notices of the Royal Astronomical Society, 451, 1247

Schaller M., et al., 2016, Monthly Notices of the Royal Astronomical Society, 455, 4442

Schaller M., Gonnet P., Draper P. W., Chalk A. B. G., Bower R. G., Willis J., Hausammann L., 2018, Astrophysics Source Code Library, p. ascl:1805.020

Schaye J., 2004, The Astrophysical Journal, 609, 667

Schaye J., et al., 2010, Monthly Notices of the Royal Astronomical Society, 402, 1536

Schaye J., et al., 2015, Monthly Notices of the Royal Astronomical Society, 446, 521

Schönrich R., Binney J., Dehnen W., 2010, Monthly Notices of the Royal Astronomical Society, 403, 1829

Searle L., Zinn R., 1978, The Astrophysical Journal, 225, 357

Sellwood J. A., McGaugh S. S., 2005, The Astrophysical Journal, 634, 70

Shao S., Cautun M., Frenk C. S., Grand R. J. J., Gómez F. A., Marinacci F., Simpson C. M., 2018a, Monthly Notices of the Royal Astronomical Society, 476, 1796

Shao S., Cautun M., Deason A. J., Frenk C. S., Theuns T., 2018b, Monthly Notices of the Royal Astronomical Society, 479, 284

Simon J. D., 2018, The Astrophysical Journal, 863, 89

Simpson C. M., Grand R. J. J., Gómez F. A., Marinacci F., Pakmor R., Springel V., Campbell D. J. R., Frenk C. S., 2018, Monthly Notices of the Royal Astronomical Society, 478, 548

Smith M. C., et al., 2007, Monthly Notices of the Royal Astronomical Society, 379, 755

Sohn S. T., Besla G., Marel R. P. v. d., Boylan-Kolchin M., Majewski S. R., Bullock J. S., 2013, The Astrophysical Journal, 768, 139

Sohn S. T., Watkins L. L., Fardal M. A., Marel R. P. v. d., Deason A. J., Besla G., Bellini A., 2018, The Astrophysical Journal, 862, 52

Somerville R. S., Davé R., 2015, Annual Review of Astronomy and Astrophysics, 53, 51

Springel V., 2005, Monthly Notices of the Royal Astronomical Society, 364, 1105

Springel V., 2010, Monthly Notices of the Royal Astronomical Society, 401, 791

Springel V., 2011, Proceedings of the International Astronomical Union, 270, 203

Springel V., Yoshida N., White S. D. M., 2001, New Astronomy, 6, 79

Springel V., et al., 2008, Monthly Notices of the Royal Astronomical Society, 391, 1685

Tissera P. B., White S. D. M., Pedrosa S., Scannapieco C., 2010, \mnras, 406, 922

Tormen G., Bouchet F. R., White S. D. M., 1997, Monthly Notices of the Royal Astronomical Society, 286, 865

Trujillo-Gomez S., Kruijssen J. M. D., Reina-Campos M., Pfeffer J. L., Keller B. W., Crain R. A., Bastian N., Hughes M. E., 2020, arXiv:2005.02401 [astro-ph]

Tully R. B., Libeskind N. I., Karachentsev I. D., Karachentseva V. E., Rizzi L., Shaya E. J., 2015, The Astrophysical Journal, 802, L25

Valcarce A. a. R., Catelan M., 2011, Astronomy & Astrophysics, Volume 533, id.A120, <NUMPAGES>15</NUMPAGES> pp., 533, A120

VandenBerg D. A., Brogaard K., Leaman R., Casagrande L., 2013, The Astrophysical Journal, 775, 134

Vasiliev E., 2019, Monthly Notices of the Royal Astronomical Society, 482, 1525

Vasiliev E., Baumgardt H., 2021, Monthly Notices of the Royal Astronomical Society, 505, 5978

Vasiliev E., Belokurov V., Erkal D., 2021, Monthly Notices of the Royal Astronomical Society, 501, 2279

Vera-Ciro C. A., Helmi A., Starkenburg E., Breddels M. A., 2013, Monthly Notices of the Royal Astronomical Society, 428, 1696

Virtanen P., et al., 2020, Nature Methods, 17, 261

Vogelsberger M., et al., 2009, Monthly Notices of the Royal Astronomical Society, 395, 797

Vogelsberger M., Genel S., Sijacki D., Torrey P., Springel V., Hernquist L., 2013, Monthly Notices of the Royal Astronomical Society, 436, 3031

Vogelsberger M., et al., 2014a, Monthly Notices of the Royal Astronomical Society, 444, 1518

Vogelsberger M., et al., 2014b, Nature, 509, 177

Vogelsberger M., Marinacci F., Torrey P., Puchwein E., 2020, Nature Reviews Physics, 2, 42

Wang J., Frenk C. S., Navarro J. F., Gao L., Sawala T., 2012, Monthly Notices of the Royal Astronomical Society, 424, 2715

Wang W., Han J., Cooper A. P., Cole S., Frenk C., Lowing B., 2015, Monthly Notices of the Royal Astronomical Society, 453, 377

Wang W., Han J., Cole S., Frenk C., Sawala T., 2017, Monthly Notices of the Royal Astronomical Society, 470, 2351

Wang W., Han J., Cole S., More S., Frenk C., Schaller M., 2018, Monthly Notices of the Royal Astronomical Society, 476, 5669

Wang W., Han J., Cautun M., Li Z., Ishigaki M. N., 2020a, Science China Physics, Mechanics & Astronomy, 63, 109801

Wang J., Bose S., Frenk C. S., Gao L., Jenkins A., Springel V., White S. D. M., 2020b, Nature, 585, 39

Watkins L. L., Evans N. W., An J. H., 2010, Monthly Notices of the Royal Astronomical Society, 406, 264

Watkins L. L., van der Marel R. P., Sohn S. T., Evans N. W., 2019, The Astrophysical Journal, 873, 118

Wechsler R. H., Bullock J. S., Primack J. R., Kravtsov A. V., Dekel A., 2002, The Astrophysical Journal, 568, 52

Wetzel A. R., Deason A. J., Garrison-Kimmel S., 2015, The Astrophysical Journal, 807, 49

White S. D. M., Frenk C. S., 1991, The Astrophysical Journal, 379, 52

White S. D. M., Rees M. J., 1978, Monthly Notices of the Royal Astronomical Society, 183, 341

White S. D. M., Frenk C. S., Davis M., 1983, The Astrophysical Journal, 274, L1

Wilkinson M. I., Evans N. W., 1999, Monthly Notices of the Royal Astronomical Society, 310, 645

Wu Y., Valluri M., Panithanpaisal N., Sanderson R., Freese K., Sharma S., 2021, Bulletin of the AAS, 53

Xue X. X., et al., 2008, The Astrophysical Journal, 684, 1143

Yencho B. M., Johnston K. V., Bullock J. S., Rhode K. L., 2006, The Astrophysical Journal, 643, 154

York D. G., et al., 2000, The Astronomical Journal, 120, 1579

Zavala J., Frenk C. S., 2019, Galaxies, 7, 81

Zhu Q., Marinacci F., Maji M., Li Y., Springel V., Hernquist L., 2016, Monthly Notices of the Royal Astronomical Society, 458, 1559

Zhu Q., Hernquist L., Marinacci F., Springel V., Li Y., 2017, Monthly Notices of the Royal Astronomical Society, 466, 3876

Zolotov A., et al., 2012, The Astrophysical Journal, 761, 71

Zwicky F., 1937, The Astrophysical Journal, 86, 217